Investigating the Role of GTP Cyclohydrolase I Mutations and the Tetrahydrobiopterin Pathway in Parkinson's Disease

A thesis submitted to the University College London for the degree of Doctor of Philosophy

January 2020

By

Léa Emma Sophie R'Bibo

Declaration of Authorship

I, Léa Emma Sophie R'Bibo, confirm that the work presented in this thesis is my own. Where information has been derived from other sources, I confirm that this has been indicated in the thesis.

Acknowledgements

This thesis is dedicated to the loving memory of my grandfather Armand. His words of wisdom shaped my mind and soul and his love and teachings will always guide me throughout life.

I would like to express my most sincere gratitude to my primary supervisor Professor Nicholas Wood for offering me the opportunity to pursue my research as both Masters and PhD in his laboratory at the Institute of Neurology and to my secondary supervisors, Doctor Sonia Gandhi and Professor Rickie Patani, for taking me on-board in their adventure to the Crick. To all three, thank you for your guidance and teachings, introducing me to the fascinating yet widely different worlds of genetics, cell biology and developmental neuroscience and supporting my development as an independent researcher.

Thanks to all the members of the Wood, Gandhi and Patani labs, as well as all the people I have met at the Institute of Neurology and the Francis Crick Institute, for countless hours of scientific discussions, teaching, experimental advice..., who altogether contributed to make this PhD a positive and formative experience. A special mention to: Dr. Minee Choi for guiding me through the cell culture, experiments and functional analyses, to Dr. Alan Pittman and Dr. Giulia Tyzack for always answering my scientific and technical questions, to Mike Nalls for helping me make sense of large genetic data, and to Dr. Niccolo Mencacci for helping me starting this journey. And of course to (soon to be Dr.) Heather Ging for going through all these stages with me side-by-side, whose friendship and positivity made this experience enjoyable.

A special thanks to my family. First to my parents Lynda and Philippe, for teaching me the importance of choosing a career that I love, to dream my life and to pursue my goals no matter the difficulties and for having sparkled my interest for science and biology since a very young age. Thanks to my siblings Tanya, Gregor and Mickaël for their unwavering love and support even through great distances; and to my nieces and nephew Naya, Ava, Elodie, Oscar and Amélie, for being my greatest joy. To my grandmother Aurélie who can now add my PhD to her impressive pile of diplomas.

Thanks also to the rest of my family and especially Michael for always being there to help me recharge my batteries and to always supporting my decision to move to London.

Finally, thanks to *mon amour* Ulrich Eberle, also soon to be Dr., for standing by my side every minute of this journey and for being such an inspiration. Thank you for dealing with my stress and frustrations, for celebrating every little victory with me while always pushing me to become better and for always making me laugh. You are an amazing researcher and an inspiration and I just can't wait to start our next great adventure.

Abstract

My thesis investigates the role of GTP cyclohydrolase I (*GCH1*) mutations and the downstream tetrahydrobiopterin (BH4) pathway in Parkinson's disease (PD) using a wide range of methods and human-derived cell models.

First, the burden of mutations in *GCH1* and other genes associated to the *GCH1*-BH4 pathway is analysed in a large PD exome cohort from the IPDGC. This analysis highlights a cumulative role for variants in this pathway with the risk for PD, especially in the genes directly involved in BH4 synthesis as part of the pathway.

Second, functional investigations into the putative functions of the *GCH1*-BH4 pathway are undertaken in several cell models from a family of patients carrying a heterozygous *GCH1* mutation and affected by either PD or Dopa-responsive dystonia (DRD), the latter was first associated with *GCH1* mutations.

Primary investigations make use of patient-derived fibroblasts, with and without GTPCH-inducting cytokine treatment, and observe an effect of the mutation on mitochondrial function and antioxidant levels without changes in superoxide production.

Further, fibroblasts are reprogrammed to induced pluripotent stem cells (iPSC) and these are differentiated into midbrain dopaminergic neural precursors and neurons. Comparisons are made between controls, PD and DRD cells. iPSC-derived neural precursors demonstrate high purity and their functional analysis results are in line with the observations made in fibroblasts. These changes are mainly observed in the DRD lines suggestive of an early phenotype for that disease in my model. Finally, in iPSC-derived midbrain dopaminergic neurons, mitochondrial function and superoxide production are affected differently between disorders with no effect on antioxidants in the cells. The mutation is associated with a higher proportion of cell death in the PD cultures compared to both controls and DRD, suggestive of a recapitulation of the neurodegenerative phenotype in this model.

Impact Statement

By affecting 1-3% of the global population above the age of 65, Parkinson's disease (PD) is the second most common neurodegenerative disease in the world. In the UK alone, approximately 200,000 people live with the condition. Previous research has unravelled a wide variety of genetic factors for PD and understanding the mechanisms underlying them appears not only essential to explain the causes of the disease, but also central to inform the development of therapeutic approaches.

The identification of GTP cyclohydrolase I (*GCH1*) mutations as a genetic risk factor for PD (both sporadic and familial), in addition to its known involvement in Dopa-responsive dystonia (DRD), by Pr. Nicholas Wood's team (Institute of Neurology) offers another opportunity to understand PD pathology. DRD is an early onset type of dystonia in which symptoms respond very positively to low doses of Levodopa, the primary drug used in the treatment of PD. This link first supports a role for *GCH1* and its downstream pathway in the development of PD; and second, offers the possibility to research the differences between PD- and DRD-related deleterious mechanisms to inform on the distinct late neurodegenerative phenotype of PD.

The research project subject to this thesis describes a cumulative role for variants in the *GCH1* pathway on the risk for sporadic PD through the use of the largest known PD exome sequencing dataset from the International Parkinson's disease Genomics Consortium (IPDGC). The method used for this analysis could inform similar future research into the effects of specific pathways in large genetics datasets.
It also presents a human induced pluripotent stem cell (hiPSC)-derived midbrain neuronal model for the in vitro analysis of disease relevant cell functions in the context of PD, developed with Pr. Rickie Patani's team. This human *in vitro* model allows for the study of disease mechanisms and drug-based intervention in both academic and pharmaceutical research.

Table of Contents

Table of Figures

Table of Tables

Chapter 1: General Introduction

I. Parkinson's disease

1. Definition and Symptoms

Parkinson's disease (PD) is the second most common neurodegenerative disease worldwide, after Alzheimer's disease, and is estimated to affect 1-3% of the population over the age of 65 years worldwide (De Rijk et al., 2000). Prevalence for PD has most recently been estimated at 572 per 100,000 at age ≥ 45 years in North America (Marras et al., 2018) and at 218 per 100,000 at age ≥ 40 years in the United Kingdom (including England, Wales, Scotland and Northern Ireland) (Parkinson's UK, 2018). In the UK in 2018, it is estimated that 145,519 patients above 20 live with a diagnosis of PD, with prevalence estimated to rise by 18% by 2025 to 168,582 people, due to both population growth and ageing. By 2065, there could be more than a quarter million people living with PD in the UK only (Parkinson's UK, 2018).

When describing the visible symptoms of the '*Paralysis Agitans*' or 'Shaking Palsy', as observed in his clinic and in the streets of East London some 200 years ago, James Parkinson was probably unaware of the justness of his observations and of the importance his Essay will take in modern medicine. Parkinson's described the symptoms in these terms: "*Involuntary tremulous motion, with lessened muscular power, in parts not in action and even when supported; with a propensity to bend the trunk forward, and to pass from a walking to a running pace: the senses and intellects being uninjured*" (Parkinson, 1817). It is only after his death that Jean-Martin Charcot, the founder of the first neurology clinic in Europe at the hospital of the Pitié-Salpêtrière, and Father of Modern Neurology, renamed the confusingly branded '*Paralysis Agitans*' as "la maladie de Parkinson" (Parkinson's disease). Charcot also importantly added bradykinesia as a cardinal symptom of the disease (Charcot, 1875). Later, Sir William Gowers described male predominance and gave a detailed description of the tremor which is still useful in clinics today: "*The movement of the fingers at the metacarpalphalangeal joints is similar to that by which Orientals beat*

their small drums". Gower's work also included a drawing of the typical Parkinsonian's posture famous to this day (Gowers, 1886) (Figure 1).

Figure 1: The Parkinsonian patient posture. Drawing by Pr. Gowers.

Clinical diagnosis is typically based on the observation of bradykinesia (of which PD is the most common cause) associated with at least one of the following motor symptom: muscle rigidity, rest tremor and/or postural instability (Hughes et al., 1992; Lees et al., 2009; Postuma et al., 2015). However, diagnosis of PD is complicated by the similarity of its symptoms with various other movement disorders. PD is the most common form of Parkinsonism, and Parkinsonism itself is the second most common movement disorder after essential tremor (Louis et al., 1998). PD may be misdiagnosed in cases of atypical parkinsonian syndromes such as multiple system atrophy or other movement disorders such as progressive supranuclear palsy or dystonia (Berardelli et al., 2013; Lees et al., 2009). As a result, diagnostic guidelines add criteria to refine diagnosis: the UK Parkinson's Disease Society Brain Bank (UKPDSBB) clinical diagnostic criteria have added both exclusion criteria of PD diagnosis and supportive prospective criteria for the diagnosis of definite PD (Hughes et al., 1992); while the Movement Disorders Society, include supportive criteria, red flags and absolute exclusion criteria to establish different certainty levels in the diagnosis (Postuma et al., 2015) (Table 1). These diagnostic guidelines are under constant revision, with the input from the progresses of research on the understanding of PD (Berardelli et al., 2013) and the assessment of their sensitivity in detecting PD

in the clinical context, as confirmed by post-mortem brain tissue histopathology investigations (Hughes et al., 2002). Of note, although the UKPDSBB criteria are still most widely used, some aspects such as more than two relatives affected by PD as an exclusion criteria may often be overlooked (Berardelli et al., 2013).

Many non-motor symptoms have also been documented in PD, including but not limited to: insomnia, excessive day-time somnolence, fatigue, rapid eye movement (REM) sleep disorder, constipation, symptomatic orthostasis, erectile dysfunction (in men), hyposmia, depression, anxiety, hallucinations, pain (Noyce et al., 2012; Postuma et al., 2015). These symptoms are of importance as they can appear decades before the onset of motor symptoms and have a significant impact on the quality of life of patients (Martinez-Martin, 2011). Some of these symptoms, like constipation and hyposmia, also progress with disease duration (Ramjit et al., 2010). As both prodromes and markers of disease duration, non-motor symptoms in PD are likely to represent a manifestation of changes associated with disease progression. They represent the first phenotypic manifestations of the disease, reflecting the yet non-motor function-impairing underlying neurodegeneration and accumulation of LBs (Schapira et al., 2017). As such, they are used in longitudinal observational studies with the aim of defining how their association and progression may foretell the onset and progression of subsequent PD. They may, ultimately, help the development of neuroprotective strategies for the slowing or stopping of disease progression by identifying populations at high risk of PD for clinical trials (Noyce et al., 2017).

Criteria	UKPDSBB clinical diagnostic criteria	MDS Clinical diagnostic criteria
Diagnosis criteria	Bradykinesia associated with at least one of: Muscular rigidity 4-6Hz rest tremor Postural instability not associated with other dysfunctions	Bradykinesia associated with either or both rest tremor and rigidity
Exclusion criteria	History of repeated strokes or head injury or definite encephalitis Oculogyric crises Neuroleptic treatment >1 affected relative Sustained remission Strcitly unilateral features after 3 years Suprenuclear gaze palsy Cerebellar signs Early severe autonomic involvement or dementia with disturbances of memorey, language and praxis Babinski sign Cerebral tumour Negative response to large doses of levodopa MPTP exposure	Unequivocal cerebellar abnormlities Supranuclear gaze palsy Probable behavioural FTD diagnosis or primary progressive aphasia in the first 5years of disease Parkinsonian features restricted to lower limbs >3 years Drug-induced parkinsonism Absence of levodopa response in high dosage Unequivocal cortical sensory loss Normal functional neuroimaging presynaptic dopaminergic system Alternative condition plausibly connected to patient symptoms and known to produce parkinsonism Also includes red flags criteria
Supportive criteria	Unilateral onset Rest tremor onset Progressive disorder Persistent asymmetry affecting side of onset most Excellent response to levodopa Severe levodopa-induced chorea Levodopa response for 5 or more years Clinical course of 10 or more years	Clear beneficial response to dopaminergic therapy Presence of levodopa-induced dyskenisia Rest tremor of a limb Presence of either: olfactory loss, cardiac sympathetic denervation or MIBG scintigraphy

Table 1: Simplified UKPDSBB diagnosis criteria for Parkinson disease.

2. Neuropathology

Specific loss of the dopaminergic neurons of the substantia nigra pars compacta (SNpc) and their striatal expansion by neurodegeneration and the presence of Lewy bodies in surviving cells are the main hallmarks of PD pathology (Figure 2). Both lesions are observable in post mortem brain tissue and often used for the confirmation of PD diagnosis. Importantly, these lesions appear gradually and are present before the onset of motor symptoms (Braak et al., 2003; Fearnley and Lees, 1991; Gibb and Lees, 1989) (Figure 3). As such, they have been suggested to underlie the appearance of prodromal symptoms long before the possibility of a clinical diagnosis of PD (Johnson et al., 2018). The onset of motor symptoms is thought to coincide with a threshold of neurodegeneration, reportedly with the loss of 50% of the dopaminergic neurons of the SNpc and of 80% of striatal dopamine (Bernheimer et al., 1973). However these estimates may not be accurate and larger post-mortem studies have demonstrated a variable decrease of striatal dopamine of 44-98% in advanced PD (Johnson et al., 2018).

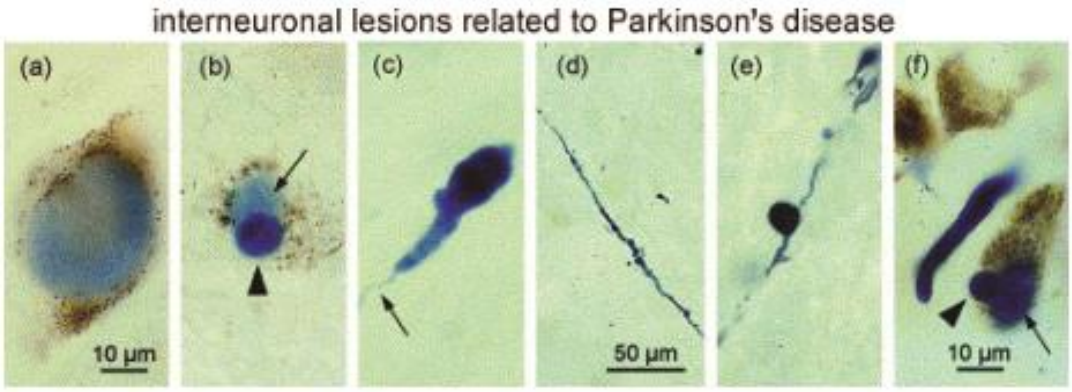

Figure 2: PD-related intraneuronal lesions. Extracted from Braak et al., 2003. Large pale body (a); combination of a pale body (arrow) with a small Lewy body (arrow head) in a melanized projection in the SN (b and f); thread-like Lewy neurite terminating in an enlarged shape (c); filiform Lewy neurite with small spine-like expansions (d) or a large globular swelling (e). Scale bar in (a)is valid for (b) and (c); scale bar in (d) is valid for (e).

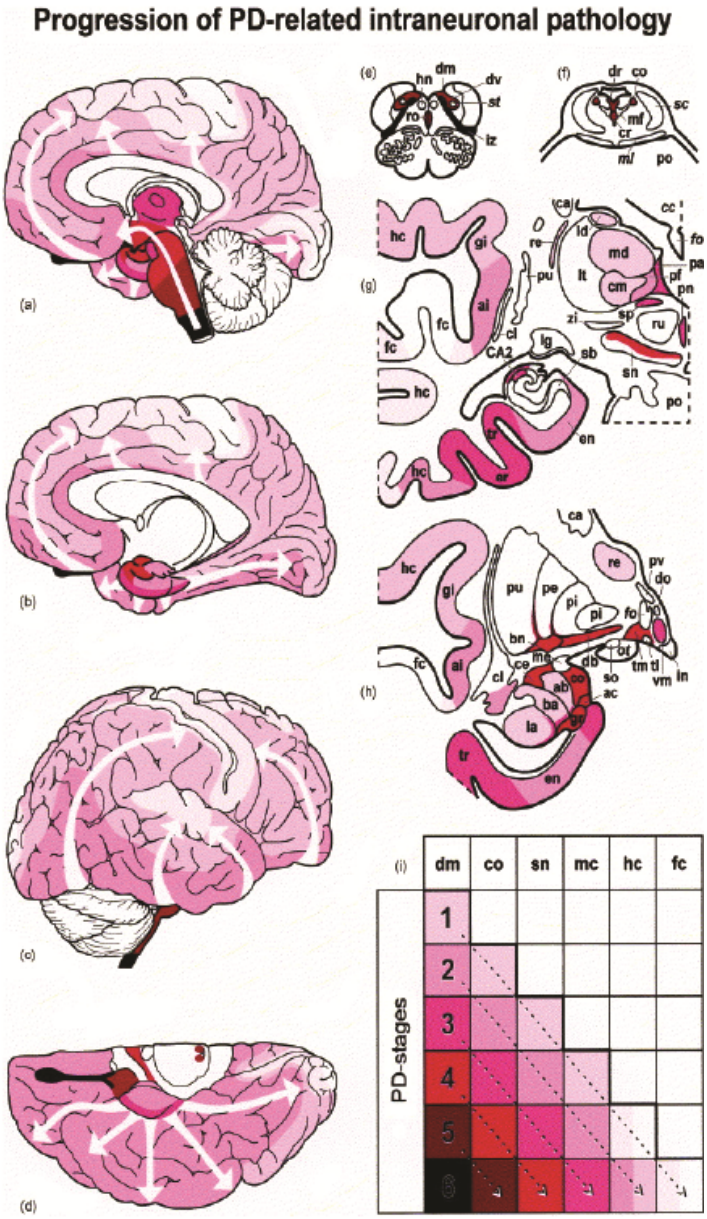

Figure 3: Braak staging for progression of Parkinson's disease neuropathology, extracted from Braak et al., 2003. Intraneuronal pathology is progressive, with lesions initially occuring in the dorsal IX/X motor nucleus (a and e) and anterior olfactory nucleus (a and d). The gradual involvement of less susceptible brain structures is represented as white arrows. Brain stem pathology extends upwards leading to cortical involvement (a-d, g-h). A simplified diagram shows the topographic expasion of the lesions (left to right) and simultaneous growth in severity of the overall pathology (top to bottoms with stages 1-6).

Neurodegeneration

When estimating cell loss in the SNpc, the use of tyrosine hydroxylase (TH) immune-markers is useful, but needs to be associated with neuromelanin staining, to differentiate catecholaminergic cells (neurons producing norepinephrine and epinephrine) containing TH and high concentration of neuromelanin, from TH+ DA neurons. Healthy ageing is associated with a mild neurodegeneration of both TH+ and

melanised cells in the SNpc, although the extent of this cell loss is not comparable to that of PD patients. Indeed, with disease progression, cell loss increases to 50-90% of TH+ cells of the SNpc at 4 years post PD diagnosis. Melanised neurons seem widely spared at the onset of pathology, but go through a variable amount of loss, with reduction by 33-80% of their number in the SNpc after a year of disease progression (Kordower et al., 2013) (Figure 4). Neurodegenerative TH+ cell loss is reverberated in the putamen with the loss of TH+ fibres, believed to represent projections of the SNpc DA cells to the striatum. The loss of dopaminergic innervation to the striatum is supported by the reduced activity of striatal L-dopa carboxylase compared to other regions such as thalamus and cortex, associated with PD (Lloyd and Hornykiewicz, 1970).

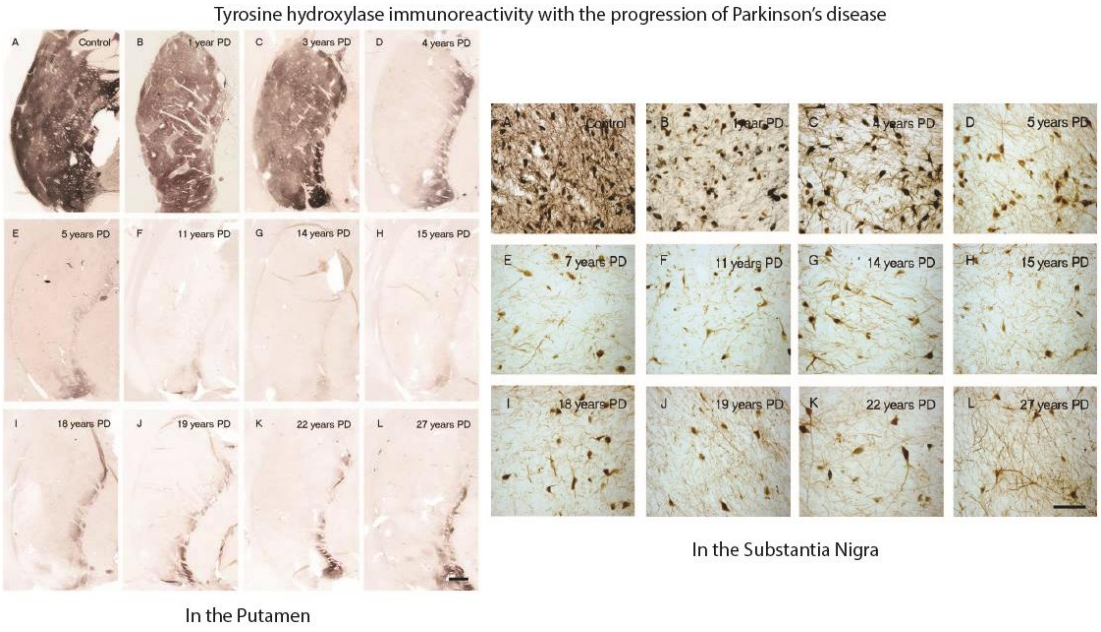

Figure 4: Tyrosine hydroxylase immunoreactivity in the putamen (left) and substantia nigra (right) in control subject and patients with PD with varying disease duration from time of diagnosis extracted from Kordower et al., 2013. Representative tyrosine hydroxyase-stained post-commisural putamen sections (left) and substantia nigra sections (right) from a control (A) and patients with PD with a disease duration since onset of 1 year (B), 4 years (C), 5 years (D), 7 years (E), 11 years (F); 14 years (G), 15 years (H), 18 years (I), 19 years (J), 22 years (K) and 27 years (L). Scale bar in L = 500um for the putamen slices and L = 100um for the substantia nigra slices.

The maintenance of some TH+ cell fibres after 4 years post-diagnosis may explain the maintained response to (high) doses of L-dopa for symptomatic relief in patients, thanks to the remaining L-dopa carboxylase activity in these cells (Kordower et al., 2013; Lloyd and Hornykiewicz, 1970). The loss of DA cells is more important in the ventrolateral tier of the SNpc, which projects in the putamen. The second most affected

tier is the ventromedial one, which itself projects to the caudate (Kordower et al., 2013).

Finally, the dorsal tier of the SNpc doesn't seem affected by DA neuron death before the latest stages of the disease. This repartition of the neuronal loss in PD is the opposite of the one found in healthy ageing, supporting the existence of risk factors increasing neuronal susceptibility to insults in this area (Fearnley and Lees, 1991). Cells of the ventral pars compacta of the SN project to the dorsal caudate, while cells of the dorsal pars compacta project to the ventral caudate. Associated in PD with greater loss of DA in the putamen vs caudate nucleus; and a greater loss in the dorsal striatum corresponding to a severe neuronal loss in the ventral SN (Gibb and Lees, 1991).

Imaging techniques can be used to estimate neurodegeneration in vivo and inform differential diagnosis of PD. Assessment of the integrity of the nigrostriatal structures can be achieved using dopamine transporter single photon emission computed tomography (DAT-SPECT) an imaging method relying on the use of pre-synaptic radioligands selectively targeted to the DAT as a biomarker of the nigrostriatal pathway. As a result, any anomaly, whether symmetric or not, of DAT uptake is suggestive of a degeneration of the DA neurons. DAT-SPECT is notably recommended in the differential diagnosis of degenerative parkinsonism from essential tremor (Benamer et al., 2000; Berardelli et al., 2013; Scherfler et al., 2007). Similarly, positron emission tomography (PET) scan can be used to detect striatal dopamine deficiency using fluoro-DOPA markers specifically reporting the activity of the dopa-decarboxylase (Dhawan et al., 2002). As such, it was suggested to be a useful in vivo estimate of disease progression (Morrish et al., 1998). Another useful imaging tool in differential diagnosis is conventional magnetic resonance imaging (MRI), used to differentiate PD from multiple system atrophy (MSA), an atypical parkinsonian syndrome. MSA presents with several specific structural abnormalities which are not found in PD and are observable via visual assessment of T1- and T2-weighted imaging (Mahlknecht et al., 2010).

It is worth to note that, although PD is mainly defined as the loss of the dopaminergic neurons of the substantia nigra pars compacta, there have been description of cell loss in other cerebral regions. For instance, computer modelling demonstrated a loss of about 63% of the neurons of the locus coeruleus in PD patients compared to age-matched controls, with little effect of the disease duration on the extent of cell loss (German et al., 1992). This observation was repeated by counting of nucleolated neurons in sections of the locus coeruleus of 19 PD patients compared to that of elderly healthy controls (Zarow et al., 2003). Similarly, PD is associated with the loss of nearly half the nerves of the adrenergic dorsal vagal nucleus, with cell loss correlating with patient's age, but no observable age-dependent cell loss in controls (Gai et al., 1995). Many other areas such as the serotonergic raphe nuclei, the cholinergic pedunculopontine tegmental nucleus projecting to the SN, Westphal-Edinger nucleus, the cholinergic nucleus basalis of Meynert, adrenergic neurons of the sympathetic ganglia and some peptidergic brainstem nuclei are affected by cell loss in PD (Agid, 1991; Jellinger, 1991). However, the majority of the motor features of PD are associated with the degeneration of the DA neurons of the SNc and this cell type has been at the centre of disease modelling and of research for cell-replacement therapy.

Lewy Bodies

Lewy bodies (LB) are neuronal inclusions classically staining with haematoxylin and eosin, strongly in the central core with a less intense surrounding and a peripheral halo of light or absent staining, in the SNpc of PD patients. However, many LBs do not have a core and are considerably variable in shape with some of this variability depending on their location, as they appear in all areas of neurodegeneration in PD (Gibb and Lees, 1994; Lewy, 1912). LBs are indeed mainly found in the cytoplasm of pigmented neurons of the substantia nigra and locus coeruleus, but also in the nucleus basalis, hypothalamus, cerebral cortex, cranial nerve motor nuclei, amygdala, and the autonomic nervous system within the CNS (Braak and Braak, 2000; Braak et al., 1994).

Post-mortem staging of PD pathology is achieved by the observation of the localisation pattern of LBs throughout the patient's brain. LBs follow a specific spatiotemporal sequence of deposition between cerebral structures which have been defined formally

as Braak staging (Braak et al., 2003). Of note, LB spread doesn't start in the substantia nigra in spite of the specific degeneration associated with PD in this region. As a result, it has been proposed that the absence of LBs in the substantia nigra is not an exclusion criteria for PD diagnosis, before other regions are checked. LB first appear in the intermediate reticular zone and/or the dorsal IX/X motor nucleus of the medulla oblongata (Braak stage 1), before spreading through this structure and reaching the pontine tegmentum (Braak stage 2). Only when these location are affected by LB accumulation do they appear in the midbrain and, in particular, the substantia nigra pars compacta (Braak stage 3). In Braak stages 4-6, LBs are found in the basal prosencephalon, mesocortex and, ultimately, spread through the neocortex (Braak et al., 2003) (Figure 3). It is mainly the spatiotemporal distribution of the LB which correlates with the progression of the pathology, rather than the severity of the LB pathology within given brain regions (Kingsbury et al., 2010). The distribution of LBs may underline the development of prodromes and the progression of symptoms in the patient's disease progression history (Braak et al., 2000).

The complete composition of LBs is yet to be resolved, as new molecules are discovered in these large intracytoplasmic protein aggregations. One major component is alpha-synuclein (α-syn), a 140 amino acid protein mainly produced in neurons and normally found in its soluble form in their axon terminals, the main location of LBs. α -syn is also found in Lewy fibrils, believed to be the building blocks of LBs (Baba et al., 1998; Jakes et al., 1994; Spillantini et al., 1997; Tu et al., 1998; Wakabayashi et al., 1992). In rat models, the pattern of expression of *SYN1*, a gene 95% similar to human SNCA, coincides with the distribution pattern of LBs in PD patients (Maroteaux and Scheller, 1991). Other components include both phosphorylated and unphosphorylated neurofilaments (Forno et al., 1986; Galloway et al., 1992; Goldman et al., 1983), paired helical filaments, ubiquitin, microtubule-associated proteins 2 (MAP2) (Galloway et al., 1992) and 5 (MAP5) (Gai et al., 1995), complement proteins (Yamada et al., 1992), protein kinase II (Iwatsubo et al., 1991), tyrosine hydroxylase (Nakashima and Ikuta, 1984), among others. Finally, parts of the composition of LBs may be disease-specific with proteins such as tropomyosin or tau being absent in LBs associated with PD, but a common finding in other forms of Lewy body disorders (LBDs) (Galloway et al., 1992). However, some (if not many) of the proteins identified

in LBs may have been trapped by the aggregation in a nonspecific manner, rather than being an essential component of LBs.

Peripheral nervous system involvement in PD

LBs are also found in various structures of the peripheral nervous system (PNS) in PD patients, such as the peripheral divisions of the autonomic nervous system: in the Auerbach's (or myenteric) plexus - located between the inner circular and outer longitudinal layers of the muscularis externa and responsible for peristalsis movements - and Meissner's plexus – nerves derived from the Auerbach's plexus found in the submucosa of the intestinal wall (Braak et al., 2006; Wakabayashi et al., 1988).

There is evidence for PD-associated neurodegeneration in the PNS, such as the loss of catecholamine innervation in the sympathetic nervous system of the heart (Goldstein et al., 2000). This denervation is associated with cardiac parasympathetic dysfunction thus very probably contributing with the development of orthostatic hypotension in subgroups of PD patients (Shibata et al., 2009). Orthostatic hypotension is a prodrome of PD and, accordingly, cardiac sympathetic denervation starts in the early stages of disease, and precedes the onset of motor symptoms (Goldstein et al., 2007, 2018; Orimo et al., 2007). Similarly, LB and α-syn neurites were identified in the hearts of PD patients, with LBs found in sympathetic nerve processes (Iwanaga et al., 1999).

3. Genetic aetiology

For next to 150 years after James Parkinson's Essay, PD was thought to have little or no genetic component and research focused on possible environmental factors associated with the pathology. This idea was so imbedded that having more than one relative affected by PD was an exclusion criteria in the most used PD clinical diagnosis guidelines (Hughes et al., 1992). Familial dominant transmission of PD gained support from large consecutive probands studies investigating the risk for PD associated with family history of the pathology (Lazzarini et al., 1994; Payami et al., 1994). Further, descriptions of large families with PD segregating in a manner highly suggestive of dominant inheritance, and their subsequent genetic analysis, allowed the advent of the genetic era of PD research (Golbe et al., 1990, 1996). Numerous genes have been

associated with autosomal dominant and recessive patterns of Mendelian inheritance of PD. These Mendelian loci account for about 5-10% of all PD cases and define the group of familial PD cases. Detailing the discovery and function of these genes is not the subject of this thesis, but some are worth mentioning.

The synuclein alpha gene *(SNCA)* is the gene encoding human α-syn, the major component of Lewy bodies. It is also the first gene in which mutations were definitely associated with the development of PD. Association of the 4q21-q23 locus with PD and the subsequent localisation of the *SNCA* gene in this locus (Polymeropoulos et al., 1996; Spillantini et al., 1995) lead to the description of the c.209G>A missense mutation leading to the p.A53T substitution. This mutation is found in complete segregation with the pathology, following an autonomous dominant inheritance pattern, in four large unrelated kindreds. p.A53T is likely to increase the propensity for the α-syn protein to aggregate, through deep structural changes to the αβ sheets succession of the native protein (Polymeropoulos et al., 1997). Another two mutations, namely p.A30P and p.E46K, have also been identified in German and Spanish families (Krüger et al., 1998; Zarranz et al., 2004). Duplications and triplications in that same gene are later associated with familial and sporadic cases of PD (Chartier-Harlin et al., 2004; Nishioka et al., 2006; Singleton et al., 2003). Moreover, mutations in *DJ1*, a protein chaperone normally involved in the correct folding of α-syn allowing for the reduction of α-syn aggregates, has been involved in autosomal recessive familial and sporadic forms of juvenile parkinsonism (Bonifati et al., 2003; van Duijn et al., 2001).

The leucine-rich repeat kinase 2 (*LRRK2*) gene variants are first associated to familial cases of PD as part of a candidate gene exploration within the *PARK8* locus on the 12q12 region (Paisán-Ruíz et al., 2004; Zimprich et al., 2004). Six autosomal dominant deleterious point mutations are then identified (Y1699C, R1441C, I1122V, I2020T, 3342A>G, R1441C) (Zimprich et al., 2004). *PARK8* has previously been associated to the segregation of the pathology in a Japanese family (Funayama et al., 2002). p.G2019S is first identified in 4 unrelated families with an autosomal dominant inheritance pattern (Di Fonzo et al., 2005). It is now known as the most common *LRRK2* mutation with frequencies of ~5% in familial PD cases (Goldwurm et al., 2005; Nichols et al., 2005). p.G2019S has an increasing penetrance with age, ranging from

28% at 59 years to 74% at 79 years (Healy et al., 2008). *LRRK2* has been involved in many fundamental cellular mechanisms commonly impaired in PD such as mitochondrial function, autophagy, vesicular trafficking and the promotion of cellular inclusions (Tsika and Moore, 2012).

Additional genes involved in the maintenance of mitochondrial health, Parkin and PTEN-induced putative kinase 1 (PINK1), are associated to autosomal recessive familial and sporadic forms of early-onset PD. The first described *Parkin* mutations consist in large deletions of exon 3 through to 7 in 14 families and exon 4 in additional 4 unrelated patients (Kitada et al., 1998; Matsumine et al., 1997, 1998). First PINK1 mutations are described in large consanguineous families as a truncating nonsense mutation and a missense mutation in a highly conserved amino acid, both in the kinase domain of the protein (Valente et al., 2001, 2004). *Parkin* is an E3 ubiquitin-protein ligase involved in the ubiquitin proteasome system (UPS) used to target proteins for degradation via ubiquitination (Shimura et al., 2000). The UPS enables the degradation and removal of aggregated and abnormal proteins through a non-lysosomal pathway. It is also involved in mitophagy when Parkin is recruited to the damaged mitochondria by the presence of outer-membrane-associated PINK1 on the cytosolic side of the mitochondria. The presence of a full-length PINK1 at the mitochondrial membrane is necessary for the recruitment of Parkin and the presence of both proteins is necessary for mitophagy of the damaged mitochondria. In the case of function-altering mutations in either protein, damaged mitochondria can accumulate in the neurons and prompt or facilitate their degeneration (Pickrell and Youle, 2015).

The subsequent use of large case-control cohorts and genome-wide association studies (GWAS) and their meta-analyses have allowed the identification of numerous rare high-risk loci and common low-risk loci associated with (mostly sporadic) PD (Chang et al., 2017; Nalls et al., 2014; Plagnol et al., 2011). This enables for the discovery of new genes involved in PD pathology, as well as the replication of previously defined Mendelian genes as risk factors for the development of sporadic PD (Bras and Singleton, 2009). One such risk factor is identified as variants in the GTP cyclohydrolase I gene (*GCH1;* 14q22.1-q22.2; OMIM 600225), associated with familial and sporadic PD, and the subject of my thesis.

4. Other risk factors

The primary risk factor for PD is ageing, with risk increasing from 1% over the age of 60 to 5% over the age of 85 in the general population (de Lau and Breteler, 2006). Healthy ageing is associated with extensive cell loss in the SN suggested to increase by 4.7% every decade (Fearnley and Lees, 1991; Rudow et al., 2008), which may be aggravated by PD risk factors and associated with earlier symptom onset in PD patients. A study of 273 healthy individual brains reveals the increased prevalence of LB with ageing, from 3.8% to 12.8% between the sixth and ninth decade, in which incidental LB cases may represent a group of pre-symptomatic PD brains as supported by the presence of additional PD-like features (Gibb and Lees, 1988). Another study of 744 brains from healthy non-parkinsonian subjects with a mean age of death at 88.5 years finds mild to severe SN neuronal loss in a third, 10% of which had concomitant LB pathology (Buchman et al., 2012).

Gender may also be a risk factor with PD traditionally considered a masculine disease supported by evidence for gender susceptibility with a slightly earlier age of onset in males, as well as an age standardised male:female ratio varying from 0.9 to 1.9 between studies (Twelves et al., 2003). Others suggest an increase of the male:female ratio with age, with an incidence similar between male and female under 50 years increasing to 1.6 at age 80 and over (Moisan et al., 2016). While hyposmia is a prodrome of PD, the organisation of the olfactory bulb, with regards to the number of TH positive dopaminergic cells found in them, varies between male and female controls and between female PD patients and controls (Huisman et al., 2008). Finally, hormones may have a role in PD risk with several studies demonstrating a protective effect of hormone-replacement therapies in post-menopausal risk for PD (Currie et al., 2004; Liu et al., 2014; Popat et al., 2005).

Many environmental factors are involved in the risk for development of sporadic PD, with evidence for the association of pesticide exposure (such as mitochondrial complex I inhibitor rotenone), in conjunction to rural living and agriculture, consumption of well water, heavy metal poisoning and head trauma with an increased risk of PD (Brown et al., 2006; Dick et al., 2007; Warner and Schapira, 2003). The

role of environmental factors is probably more prevalent in late-onset compared to early-onset PD, as supported by epidemiologic twin studies (Tanner et al., 1999).

5. Treatment

The most commonly prescribed treatment for managing the symptoms of PD is Levodopa, a pharmacological form of L-DOPA, the natural precursor of dopamine, which crosses the blood-brain-barrier, is transported into mDA neurons by the dopamine transporters (DAT), and used to produce dopamine and control movements (Hornykiewicz, 2010). However, the effects of the treatment wear off with time in about 70% of cases, and treatment-induced dyskinesias are observed in about 30% of PD patients treated with levodopa, requiring adjustments, the addition of other drugs such as amino acid decarboxylase (AADC)-inhibitors and monoamine oxidase B (MAO)-inhibitors to maintain levodopa dosage constant, complete removal of the treatment or the use of alternative therapeutic strategies such as deep-brain stimulation (Mizuno et al., 2018; Turcano et al., 2018). Some of these effects are probably due to the continuous loss of mDA neurons in the patients eventually leading to their brains incapacity to uptake and use the drug, or to mechanisms such as post-synaptic sensitization associated with long-term levodopa dosing (Bendi et al., 2018). To my knowledge, there is no evidence for a delaying effect of this drug on the progression of pathology in patients brains.

In the absence of neuroprotective strategies for the maintenance of the remaining pool of mDA neurons, cell replacement therapies may provide an alternative treatment. Research around this alternative provided us with proof-of-concept evidence for the use of this approach in humans, first with cells from foetal ventral midbrain, then with human embryonic stem-cell derived lines, to finally being developing trials using hiPSC-derived cells. These are reviewed in (Barker et al., 2017; Evans et al., 2012).

II. DOPA-responsive dystonia

1. Definition and symptoms

Dystonia are a heterogeneous group of movement disorders, characterised by intermittent or sustained muscle contraction leading to abnormal involuntary movements or postures, and represent the third most common movement disorder worldwide and 70,000 cases in the UK alone (Paudel et al., 2012). Among them, DOPA-responsive dystonia (DRD – DYT5; OMIM#128230) is a group of rare dystonia-plus syndromes, with dystonic symptoms being often associated with parkinsonism or extra-pyramidal symptoms. They are characterised by a dramatic and sustained improvement of symptoms in response to treatment with oral L-dopa (Balint et al., 2018; Kurian et al., 2011). DRD was first described as a progressive hereditary dystonia with marked diurnal fluctuation or Segawa's disease (Segawa et al., 1976). It classically presents with an early onset (before 20 years of age) of lower limb dystonia and gait disturbance, with a variable degree of generalisation associated with the progression of the disease. Diurnal fluctuation, that is the worsening of symptoms towards the evening and improvement after sleep, is often reported (Albanese et al., 2011; Nygaard et al., 1990). Symptoms presentation and responsiveness to treatment can vary greatly even within an affected family (Robinson et al., 1999). DRD is 2- to 4-fold more common in women than in men, with mutation penetrance 2.3 times higher in females than males but with no anticipation effect (Furukawa et al., 1998; Nygaard et al., 1988; Phukan et al., 2011).

DRD presentation can sometimes be quite different from its classical form, hence is often misdiagnosed. In consequence, diagnosis guidelines have included genetic screening of the relevant DYT loci (*see genetic aetiology below*) and a levodopa trial is warranted for the confirmation of the clinical assessment (Albanese et al., 2011; Nygaard et al., 1994; Robinson et al., 1999). Moreover, to differentiate DRD cases presenting with Parkinsonism from juvenile- and early-onset PD and secondary dystonia, single photon emission computerized tomography study with ligands for dopamine transporter (DAT), or positron emission tomography can be used. Indeed, DRD is generally accepted as a non-neurodegenerative disorder and patients with

DRD show normal uptake of the ligand by the DAT as opposed to the classical reduction of striatal ligand uptake classically observed in PD (Albanese et al., 2011; Marshall and Grosset, 2003; Nygaard et al., 1992). Abnormalities on imaging may be visible from the prodromal stage of PD, further supporting its use in the differential diagnosis of DRD (Noyce et al., 2018). The absence of neurodegeneration in DRD is supported by neuropathological examination of a limited number of cases which revealed a hypopigmentation of the SN associated to lower melanin levels in the absence of degeneration (Figure 5). Tyrosine hydroxylase activity is normal and there is no evidence for parkinsonian-like anomalies such as Lewy bodies (Furukawa et al., 1999, 2016; Grötzsch et al., 2002; Rajput et al., 1994; Segawa et al., 2013). Finally, as a GTP cyclohydrolase deficiency associated with reduced tetrahydrobiopterin levels, DRD diagnosis can be supported by low levels of pterins, dopamine and serotonin metabolites in the patient's cerebrospinal fluid (CSF) (Assmann et al., 2003) or by an abnormal phenylalanine-loading test (PLT) (Bandmann et al., 2003). Of note, these anomalies of the pterin pathway can be observed in mononuclear blood cells stimulated with phytohemagglutinin (Ichinose et al., 1995) and fibroblasts stimulated with cytokines (Bonafé et al., 2001a; Milstien et al., 1993).

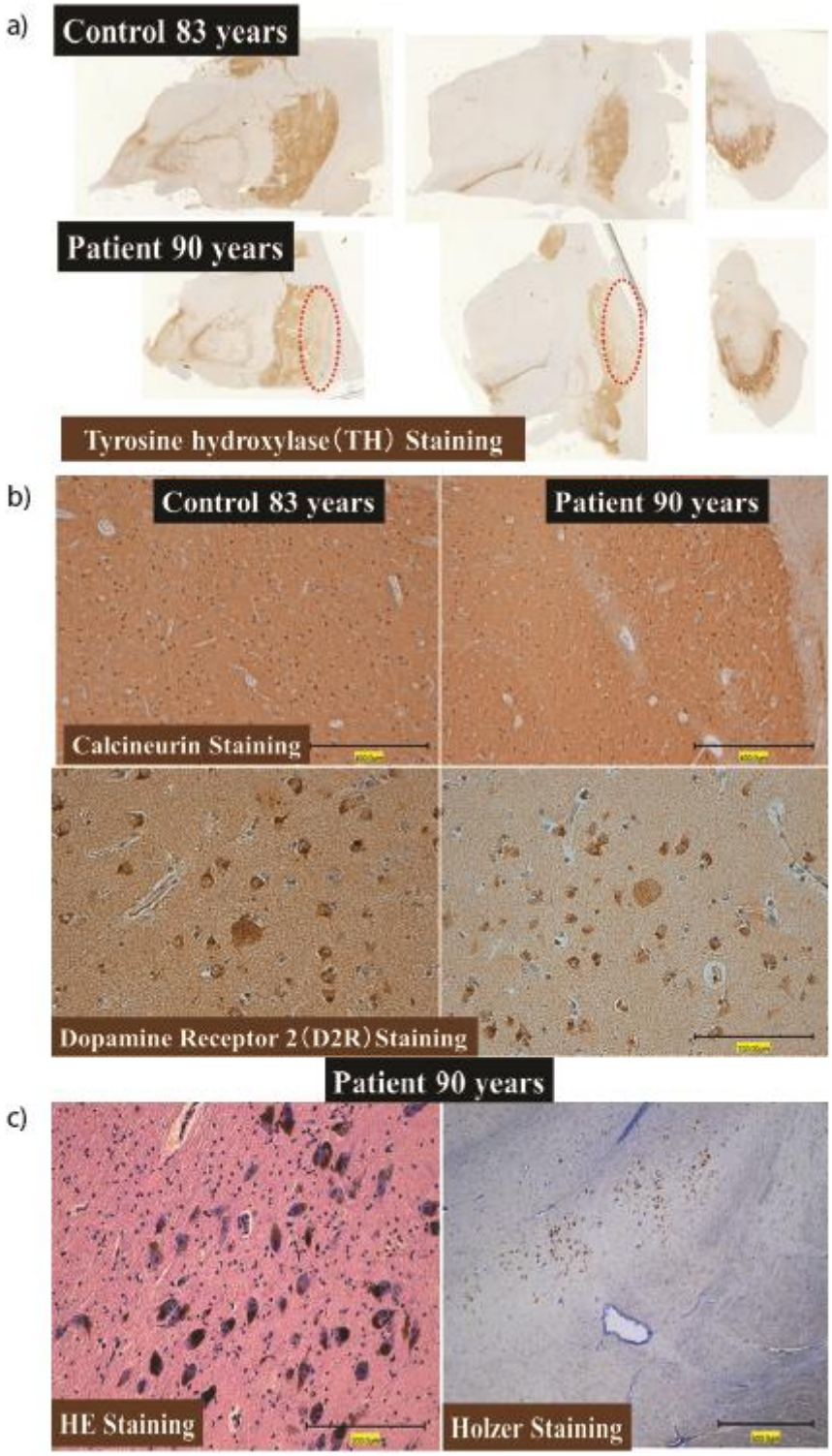

Figure 5: Post-mortem histopathophysiology of a 90 years old DRD brain from Segawa et al., 2013. (a) Immunohistochemistry for tyrosine hydroxylase (TH) in the 83-year-old control (first line) and the 90 year-old case (second line). TH immunoreactivity is reduced in the putamen of the case (red circle) compared to the control; but it is preserved in the substantia nigra. (b) Immunohistochemistry for calcineurin (upper images) and dopamine receptor 2 (lower images) in the putamen of control (left) and case (right). Immunoreactivity for both molecules is preserved in the case's putamen.(c) The substantia nigra of the DRD case does not show neuronal loss (HE staining) nor gliosis (Holzer staining).

In addition to the dystonic features, DRD has been associated with neuropsychiatric symptoms such as anxiety, depression, obsessive-compulsive disorder, as well as with sleep disturbances and restless-legs like syndromes (Van Hove et al., 2006). Depression seems quite prevalent in most of the patient studies recording this outcome, with 35% patients reporting severe mood-swings and 17% treatment-requiring depression in a 34 patient cohort (Trender-Gerhard et al., 2009) or 35% of all DRD patients reporting non-motor symptoms (70/354) presenting with depression in another cohort (Tadic et al., 2012). Sleep disturbances (characterised as day-time fatigue and difficulties sleeping at night in the absence of large systematic studies) are often resistant to the L-DOPA even when correcting the motor symptoms. Cognitive impairment has been observed in a small percentage of patients, more commonly among the ones which have not been treated with L-dopa since childhood in one study (López-Laso et al., 2011). Rodent models of tetrahydrobiopterin deficiency demonstrate signs associated with developmental delay, but these observations are not repeated in human patients (Ichinose et al., 2013). There is no support for alterations in the autonomic system or involvement of the cardiac function as opposed to PD (Antelmi et al., 2015). It is important to note these observations are generally limited to small cohorts of patients due to the rare nature of the pathology and these patients are mostly under L-Dopa treatment. Hence, large systematic studies in L-Dopa naïve patients using standardised symptom measuring scales are warranted to confirm these observations.

2. Genetic aetiology

GTP cyclohydrolase I (GCH1)

DRD is most commonly associated with mutations in the *GCH1* gene (OMIM #600225), found in 50-60% of all DRD cases (Hagenah et al., 2005). The majority follow an autosomal dominant inheritance pattern with incomplete penetrance (Ichinose et al., 1994; Nygaard et al., 1993). Autosomal dominant *GCH1* mutations are believed to result in a significant reduction of GTPCH activity through a dominant negative effect of the mutant protein on the normal enzyme (Hwu et al., 2000), and a few DRD cases have been associated with recessive *GCH1* mutations (Hwu et al., 1999; Opladen et al., 2011). GTPCH encoded by GCH1 catalyses the rate limiting step

of the production of BH4, the essential cofactor for the production of dopamine by tyrosine hydroxylase. The very large majority of *GCH1* mutations associated with DRD cases are found in the coding region of the gene, with a large number of point missense or nonsense mutations (40-60% cases).

Large exon deletions in the *GCH1* gene have been described: a heterozygous exons 1-4 deletion is detected in a sporadic DRD case and a complete heterozygous deletion of the gene (exons 1-6) is found in another patient from German and English descent in one cohort (Hagenah et al., 2005); another complete deletion of GCH1 exons 1-6 is found in an unrelated family with one individual with DRD and in her mother affected by PD (Eggers et al., 2012); Steinberger and colleagues identified heterozygous complete (exons 1-6) and partial (exons 2-6 and exons 4-6) deletions of the GCH1 gene is three separate German families affected by DRD (Steinberger et al., 2007); a heterozygous exon 1 deletion is identified in a DRD patient and his mildly affected mother in aTurkish family, while exons 1-3 de novo deletion is found in one other unrelated Turkish DRD case in a family issued from a consanguineous marriage (Klein et al., 2002); the same exons 1-3 deletion was reported in 3 unrelated families from a Han Chinese cohort of familial DRD (Wu-Chou et al., 2010); exons 3-6 are deleted in a Swiss family affected with DRD (Wider et al., 2008); exons 1-6 are deleted in 6 individuals from 4 different families and one exon 3-6 mutation found in a fifth family in one study using qPCR (Zirn et al., 2008); one 1.2kb long deletion including exon 3 is found in all six tested members of an English-Canadian family (Furukawa et al., 2000). Although all mutations in GCH1 have limited penetrance, large deletions such as the exons 1-3 may have a higher penetrance than point mutations (Wu-Chou et al., 2010). Of note, this mutation seems associated with a more important gender imbalance, with female carriers all presenting with a childhood onset, while all male had an adult onset (Wu-Chou et al., 2010).

Small insertions and deletions in *GCH1* are also associated with DRD, a few examples of which are mentioned here. For deletions: a single base deletion c.729delG in exon 5 of *GCH1*, leading to frameshift and early stop codon is associated with the pathology in monozygotic triplets sisters and fourth sister (Tachi et al., 2011); in familial cases, a paper finds a c.149delC in exon 1 and a c.212delT both leading to frameshift and

early termination in exon 1, a c.351delA leading to frameshift and early termination in exon 2, and an 18bp deletion (c.229delTCCATCCTGAGCTCGCTG) resulting in the loss of amino acids between Ser77 and Leu82 (Furukawa et al., 1998); c.631_632delAT leads to an early stop codon in exon 6 of GCH1 in five sporadic DRD cases (Clot et al., 2009; Furukawa et al., 1998; Hagenah et al., 2005). For insertions: c.316insTTC in exon 1, c.654insT in exon 6 and IVS5+3insT in intron 5 of GCH1 are identified in one cohort of mixed descent (Hagenah et al., 2005); a c.329insA results in early termination in exon 2 is found in a sporadic case (Furukawa et al., 1998).

Mutations affecting splice sites have been described, which include: IVS4+1G>A at the junction between exon 4 and intron 4 of GCH1 was identified in one individual with DRD, probably leading to the retention of intron 4 (Hagenah et al., 2005); c.510-2G>A in the 3' splice site of intron 3 leads to the skipping of exon 4 in a DRD family (Furukawa et al., 1998); c.344-2G>A at the 3' splice site of intron 1 leads to the skipping of exon 2 in two sporadic cases of DRD (Furukawa et al., 1998; Weber et al., 1997); c.626+1G>A is found in three sporadic DRD cases across two cohorts (Clot et al., 2009; Hirano et al., 1998); at the same location c.626+1G>C is found in two separate families and a sporadic DRD case (Clot et al., 2009; Garavaglia et al., 2004; Mencacci et al., 2014) and both potentially resulting in the skipping on exon 5 and the introduction of a premature stop codon; in a sporadic DRD cohort, c.453+1G>A, and c.509+1G>A are likely resulting in exon skipping (Clot et al., 2009); c.343+5G>C is identified in two DRD families, as a heterozygous mutation and as a compound heterozygous in association with K224R (Mencacci et al., 2014; Trender-Gerhard et al., 2009).

Additional mutations have been found in the 5' untranslated region of the *GCH1*gene, between the transcription start site and the translation start codon, in individuals with DRD in the absence of mutation in the coding region. The impact of these mutations on the expression levels of GCH1 are first investigated with a focus on the +142C>T mutation relative to the transcription start (+1), also known as -22C>T relative to the translation start codon. This transition is identified in segregation with DRD in multiple generations of a large family (Sharma et al., 2011), as well as in a two unrelated DRD patient (Clot et al., 2009; Tassin et al., 2000). The variant induces an

upstream open reading frame (uORF) which encodes a 73 amino acid peptide which localises in the nucleus, leading to cytotoxicity (Jones et al., 2017). As such, the mutation reduces the level of translation of the GTPCH protein without affecting its mRNA level nor stability (Armata et al., 2013). This discovery underlines the importance of increasing our knowledge and understanding of sequence variations outside of the coding region of our genome for a more complete understanding of genetic disorders.

Other genetic causes

Other genes downstream of GCH1 in the dopamine synthesis pathway have been involved in DRD. Autosomal recessive cases of DRD, for instance, are more commonly associated to mutations in tyrosine hydroxylase (*TH*) (OMIM #191290) or sepiapterin reductase (*SPR*) (OMIM #182125) than *GCH1*.

TH catalyses the synthesis of L-DOPA from tyrosine using BH4 as a cofactor, and first mutation in *TH* associated to DRD, Q381K, is found in homozygous state in two patients, in heterozygous state in unaffected sibling and parents and absent in 180 controls (Lüdecke et al., 1995). The next year, homozygous L205P *TH* mutation is described in a patient, carried in one allele by both its brother and parents, and absent in 130 healthy control chromosomes (Lüdecke et al., 1996). Numerous other point mutations have been involved in DRD since. Compound heterozygous *TH* mutations have also been described in DRD, for instance a 16month old Chinese DRD patient carries c.457C>T (R153X) and c.698G>A (R233H) alleles while both parents are healthy heterozygous carriers (Feng et al., 2018); or in two sporadic cases carrying c.1125C>G (p.Phe375Leu) and c.1399A>G (p.Ser467Gly), and c.956G>C (p.Arg319Pro) and c.1240G>A (p.Gly414Arg) respectively (Clot et al., 2009). Finally deletions in *TH* such as c.296delT or c.291delC which both encode for an inactive protein (Furukawa et al., 2001; Wevers et al., 1999).

SPR catalyses the synthesis of BH4 from PTP and is first associated with DRD in two families: one homozygous double base pairs transition c.354–355TC>CT leading to an early stop codon at position 119 (Q119X); and one compound heterozygote c.448A>G missense (R150G) and c.1397–1401delAGAAC leading to frameshift and

an early stop codon at position 152 (Bonafé et al., 2001b). Another DRD patient is found to carry a homozygous P163L mutation, with heterozygosity demonstrated in both unaffected parents (Abeling et al., 2006). Homozygous c.448A>G (p.Arg150Gly) point mutation and homozygous mutation putatively affecting a splicing site leading to the skipping of exon 3 of *SPR*, c.596-2A>G, are associated to two sporadic cases (Clot et al., 2009). One heterozygous mutation in the 5'UTR of *SPR*, c.-13G>A, is found in one of 95 DRD patients and absent from 100 controls and is associated with reduced enzyme activity (Steinberger et al., 2004). In an Egyptian family, DRD segregated with c.207C>G mutation in *SPR* associated with a common variant in dihydrofolate reductase (DHFR - rs70991108), another gene of the dopamine synthesis pathway. The latter increased penetrance of the first (Shalash et al., 2017).

Hence, all mutations identified in DRD affect genes of the dopamine synthesis pathway, and are ultimately believed to be associated with reduced L-dopa and dopamine synthesis, either through reduced TH expression or reduced TH activity through the limited availability of its obligatory cofactor BH4.Brain levels of biopterin and neopterin, proxies for the activity of GTPCH, and of dopamine are reduced by 80-90% in DRD compared to controls and this is accompanied by a reduction in TH activity in the patient's striatum (Furukawa et al., 1999; Warner and Bressman, 2007). Interestingly, a heterozygous *GCH1* mutation was able to affect these parameters in an asymptomatic DRD patient (Furukawa et al., 2002). It is likely that other genes putatively involved in DRD act similarly.

3. Treatment

Mutations in *TH* as well as in sepiapterin reductase (*SPR*), both enzymes involved in dopamine synthesis down-stream from GTPCH, have been identified in a small proportion of DRD cases (Clot et al., 2009), and would affect the BH4 pathway in a way which can be circumvented by the use of levodopa treatment. Accordingly, all forms of DRD may be caused by this reduced dopamine production and treated in the long-term by supplying the necessary dopamine precursor.

Treatment of DRD is based on Levodopa, with patients having a dramatic and sustained response to low doses (50-200mg/day) usually within days or weeks from

the start of treatment and in the absence of fluctuations, probably due to the intact dopamine storage capacity of these patients (Dressler et al., 2016; Phukan et al., 2011). The assumption that DRD patients are mainly immune to the levodopa-induced dyskinesia observed in PD has recently been under scrutiny, with the multiplication of reports supporting its relatively common occurrence, although these symptoms are mild (Dressler et al., 2016). Studies point at a higher risk for levodopa-induced dyskinesias in autosomal recessive forms of DRD compared to autosomal dominant ones, with 13.3% and 5.4% respectively in a literature meta-analysis (Kim et al., 2016). Other studies reported this treatment-related side-effect in 11% (3/27) or 20% (4/20) of their DRD patients (Hwang et al., 2001; Tassin et al., 2000). Importantly, these patients were receiving relatively higher doses of levodopa, and decreasing posology may be associated with reduced dyskinesias. Levodopa-induced dyskinesias may thus be associated with dopamine overdose or post-synaptic sensitization in DRD patients (Bendi et al., 2018). Interestingly, some dystonic symptoms such as writer's cramp, dysphonia and truncal dystonia, seem more resistant than others to the levodopa treatment (Trender-Gerhard et al., 2009). Moreover and similarly to PD patients, there is increasing evidence for non-motor symptoms such as depression, anxiety or obsessive-compulsive disorders with DRD, which are believed to be associated with an impairment of serotonergic metabolism due to the reduced availability of BH4 associated to GCH1 and SPR mutations, and may require additional non-dopaminergic treatment (Furukawa et al., 2016).

III. GCH1 in disease and putative cellular mechanisms

Mutations in *GCH1* are first identified in DRD cases, both sporadic and familial, with probands describing an significantly higher frequency of family history for PD than the general population (Ichinose et al., 1994; Nygaard et al., 1993). Several families including members affected by either one of the disorders are described and GCH1 mutations found to segregate with both disorders in these families (Eggers et al., 2012; Irie et al., 2011; Lewthwaite et al., 2015; Mencacci et al., 2014; Nygaard et al., 1990, 1992). *GCH1* variants are later associated to risk for sporadic PD through large exome sequencing cohorts and GWAS (Chang et al., 2017; Chen et al., 2016; Mencacci et al.,

2014; Nalls et al., 2014; Safaralizadeh et al., 2016; Zou et al., 2018). Genetic evidence for the role of *GCH1* in the risk for PD is further described in the Genetics chapter of this thesis.

GCH1 encodes the GTPCH protein, a homodecamer which catalyses the rate-limiting step for the production of tetrahydrobioptetin (BH4), itself an essential and natural cofactor of all three pterin-dependent aromatic amino acid hydroxylases: tyrosine-3-hydroxylase (TH, EC 1.14.16.3), phenylalanine 4-hydroxylase (PAH, EC 1.14.16.2), and tryptophan 5-hydroxylase (TPH, EC 1.14.16.4). The tyrosine-3-hydroxylase, encoded by the *TH* gene (11p15.5, OMIM 191290), is the enzyme that catalyzes the rate-limiting step for de novo synthesis of dopamine (Clot et al., 2009; Thöny et al., 2000), whilst PAH and TPH provide a role for BH4 in the de-novo synthesis of serotonin from phenylalanine and of tyrosine from tryptophan, respectively (Thöny et al., 2000). In addition, BH4 is a powerful antioxidant previously shown to scavenge superoxide in vitro (Nakamura et al., 2001), and to protect neurons against glutathione depletion in a BH4 up-regulated mouse model (Nakamura et al., 2000). During redox reactions, BH4 can be primarily oxidised to dihydrobiopterin (BH2) and subsequently to biopterin (B) (Ryan et al., 2014). Furthermore, BH4 is a coupler and an allosteric modulator necessary to the normal function of all three isoforms of nitric oxide synthase (NOS, EC 1.14.13.39), namely induced (iNOS), endothelial (eNOS), and neuronal (nNOS) (Nakamura et al., 2001; Thöny et al., 2000). Finally, it has been hypothesised that BH4 may help maintain the mitochondrial redox balance, with increased levels of BH4 reducing the production of mitochondria-derived ROS, and mainly superoxide. This effect could be through either direct interference of BH4 with ROS generation pathways in the mitochondria, and/or direct scavenging of ROS generated at the mitochondria (Bailey et al., 2017; Nakamura et al., 2001) (Figure 6). Lower BH4 content is observed in the CSF of PD patients compared to healthy controls using enzymatic activity assay (Lovenberg et al., 1979) and through the measurement of neopterin and biopterin by HPLC (Fujishiro et al., 1990). These are also reduced in the blood, brain and CSF of DRD patients (Furukawa et al., 1999; Wijemanne and Jankovic, 2015). Mutations in *GCH1* thus affect the level or activity of BH4, itself impacting on the maintenance of BH4-related functions. Understanding these

functions and their impairments in diseases may lead to the discovery of better treatments.

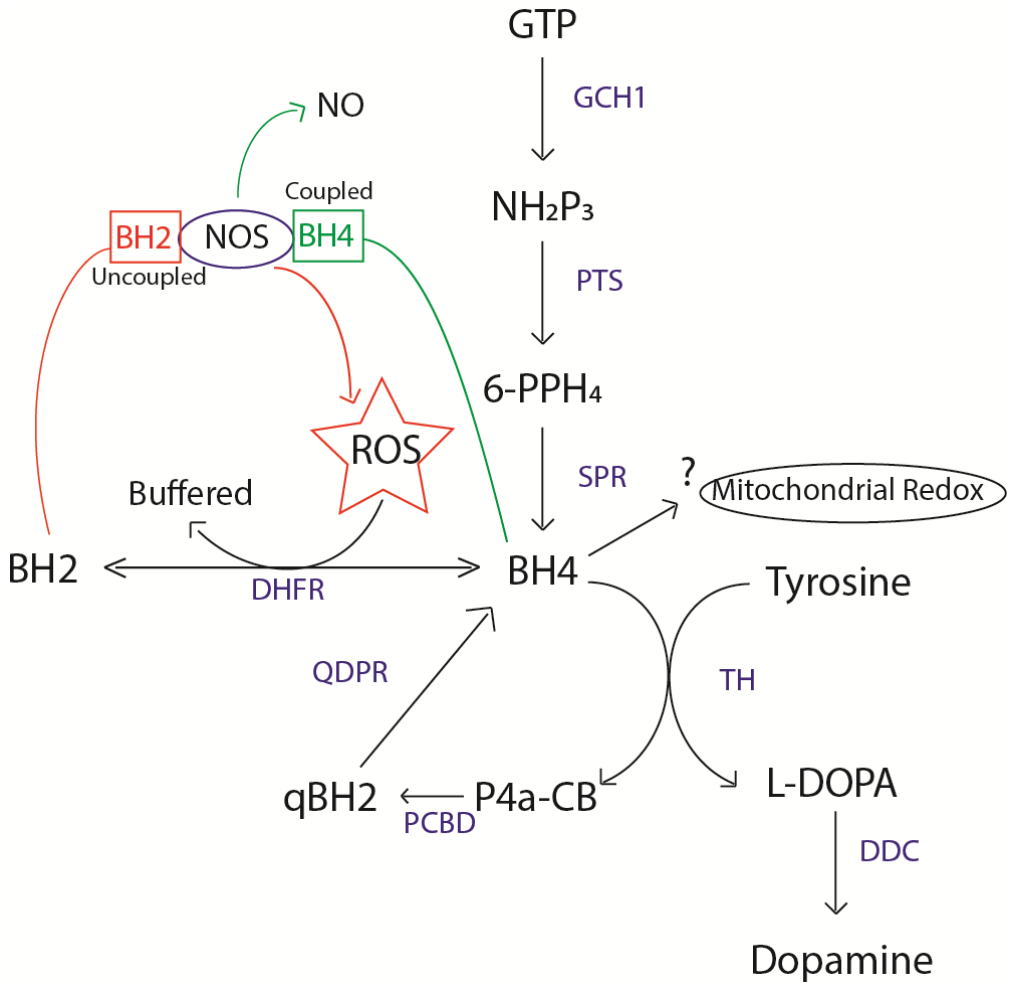

Figure 6: GCH1 and the downstream BH4 pathway - known and putative roles of BH4. Molecules transformed in the pathway are in black. Genes involved in the pathway are in blue: GCH1 = GTP cyclohydrolase I; PTS = pyruvoyltetrahydropterin synthase; SPR = sepiapterin reductase; TH = tyrosine hydroxylase; DDC = Dopa-decarboxylase; PCBD = pterin-4 alpha-carbinolamine dehydratase; QDPR = quinonoid dihydrobiopterin reductase; DHFR = dihydrofolate reductase.

SPR is necessary for the production of BH4 downstream of *GCH1* and mutations in this gene have been involved in DRD. There is some indication for the effect of *SPR* haplotype on PD age of onset (Sharma et al., 2006). Mutations in *SPR* impacting the production of BH4 may thus have similar downstream effect to *GCH1* mutations.

Some symptoms, such as sleep disturbances are observed in both PD and DRD, with rapid-eye movement (REM) sleep disturbances being a common prodrome of PD (Noyce et al., 2012) and a proportion of DRD patients reporting sleep disturbances

(Antelmi et al., 2015). In GCH1 mutant carriers, the reduced availability of BH4, leading to lower production of dopamine as well as serotonin and its derivative melatonin, all molecules which have been implicated in regulation of sleep cycles (Monti and Jantos, 2008), may be responsible for these disturbances.

1. Mitochondrial dysfunction

Mitochondria provide cells with the great majority of their energy in the form of ATP via oxidative phosphorylation, which makes use of O2 and the mitochondrial respiratory chain (Papa et al., 2012). Other functions of the mitochondria include - but are not limited to - the regulation of cellular calcium homeostasis, and of apoptosis, free radicals scavenging and acts as storage of the intermediates of Krebs cycle and pyruvate oxidation among others (reviewed in:(Giorgi et al., 2018; Spinelli and Haigis, 2018; Tilokani et al., 2018)). A multitude of these highly dynamic double-membrane bounded organelles are found in each cell, with each containing multiple copies of the mitochondrial DNA (mtDNA) in the form of discrete nucleoids within the mitochondrial matrix. mtDNA is a circular double-stranded DNA molecule, distinct from the cell nuclear DNA, and encoding only a portion of the proteins necessary for the production and maintenance of mitochondria; the rest being encoded by nuclear DNA, produced in the cytoplasm, and transported for assembly to the mitochondrion (Nunnari and Suomalainen, 2012).

The brain, which represents about 2% of the adult human body weight, uses 20% of all body oxygen consumption mainly for the production of ATP via oxidative phosphorylation. This is in part associated with the need for great amounts of energy to maintain ion homeostasis in the neurons in spite of action potentials and neurosecretion. Mitochondrial failure due to limited oxygen supply or energy production substrates thus causes rapid neuronal damage (Halliwell, 2006). Oxidative phosphorylation, the process of cell respiration which allows for the production of ATP, is based on the creation of an electrochemical gradient by protein complexes I, III and IV of the electron transport chain (ETC) on the internal mitochondrial membrane. Electrons are exchanged between these complexes allowing the shuttling of protons across the mitochondrial membrane, maintaining a mitochondrial

membrane potential (MMP) of -108 to -158mV in the cells (-139mV at rest in rat cortical neuron culture) (Gerencser et al., 2012) . The ATP synthase (complex V) is able to harness the energy of the MMP-directed release of protons across the inner mitochondrial membrane to produce ATP. This phenomenon of cell respiration, as well as other mitochondrial enzymes function in the TCA cycle, mono-amine oxidase of the outer mitochondrial membrane or cytochrome P450 of the inner membrane, leads to the production of large quantities of reactive oxygen species (ROS), mainly in the form of superoxide radicals. Superoxide has a life-span of ~1ns at the mitochondria before being transformed to H_2O_2 or reacting with other species to produce radicals such as peroynitrite can lead to oxidative damage of the mitochondria (described in (Angelova and Abramov, 2018)).

Ageing, the most important risk factor for the development of PD is associated with reduced quality and impaired function of the mitochondria. These may be associated with the accumulation of mtDNA mutations through oxidative stress or inaccurate replication and inefficient repair mechanisms as shown in human nigral neurons (Kraytsberg et al., 2006), or by affecting the activity of some of the mitochondrial respiratory chain complexes with a suggested decline of ATP producing capacity of the mitochondria of 8% per decade on average (Payne and Chinnery, 2015). PD brains demonstrate a higher proportion of mitochondrial deletions than age-matched healthy brains in the surviving mDA neurons of the substantia nigra, associated to lower ETC complexes activity and increased mitochondrial ROS production (Bender et al., 2006). About 25-30% of PD patients have mitochondrial complex I deficiencies, with reduced complex I activity identified in the SNpc of PD patients, probably resulting in increased ROS production and impairment of the MPP (Bose and Beal, 2019; Schapira et al., 1989). Mutations in PINK1 and Parkin (PARK2) genes, involved in mitophagy and mitochondrial function, are described in a proportion of PD cases and generally associated with early-onset autosomal recessive cases (Aboud et al., 2015; Abramov et al., 2011). Moreover, the neurotoxin 1-methyl-4-phenylpyridinium (MPP+), a complex I inhibitor used to model PD in animals, reduces BH4 production through depletion of GTP, the substrate of GTPCH (Ryan et al., 2014). Mitochondrial impairment in PD are reviewed in (Macdonald et al., 2018).

There is little known about mitochondrial involvement in DRD, but knocking down *GCH1* causes a striking increase of mitochondrial superoxide production through BH4 depletion, independently from NOS activity, supporting a direct role of BH4 in mitochondrial redox maintenance (Bailey et al., 2017).

2. Nitric oxide synthase uncoupling

Nitric oxide (NO) is produced by three cellular nitric oxide synthase (NOS) isoforms: neuronal NOS (nNOS) which is mainly expressed in the central nervous system and peripheral neurons, endothelial NOS (eNOS) mainly expressed at the endothelium, and inducible NOS (iNOS) which expression can be induced in many tissues using lipopolysaccharides or cytokines. All three isoforms catalyse the conversion of substrates L-arginine and molecular oxygen to NO and L-citrulline, and require the cofactors BH4, reduced nicotinamide-adenine-dinucleotide phosphate (NADPH), flavin adenine dinucleotide (FAD) and flavin mononucleotide (FMN). All NOS bind calmodulin and contain haem (Förstermann and Sessa, 2012). NO is a highly volatile molecule involved in cell-to-cell communication in the brain due to its ability to travel several cell lengths in its short life-span (~5seconds) (Bredt and Snyder, 1994; Jaeschke, 2010). When mutations in GCH1 affect the quantity of BH4 produced in the cell, NOS are uncoupled and produce both NO and superoxide in the cells (Bevers et al., 2006; Crabtree et al., 2009a). These species are highly reactive and can rapidly produce peroxynitrite which nitrates tyrosine residues in proteins, impairing their function (Kuzkaya et al., 2003). Similarly, an increase in BH4 availability through increased GCH1 expression using cytokines leads to increased eNOS activity in umbilical cord tissue (Rosenkranz-Weiss et al., 1994).

3. Oxidative stress

Oxidative stress is linked to a state of cellular imbalance between levels of ROS production and the capacity of the antioxidants to buffer these. When this balance is in favour of ROS production, oxidative damage accumulates until it impairs physiological cellular functions, themselves participating in the further production of

ROS or affecting the ability of cells to cope with damage. Eventually, this can lead to cell apoptosis.

Mutations in GCH1, through reduced BH4 content, are associated to increased ROS production by the mitochondria and around NOS, which uncoupling results in superoxide production. Meanwhile, BH4 is a powerful antioxidant, able to compensate for the knockdown of glutathione in nigrostriatal slice cultures (Gramsbergen et al., 2002), and its reduced concentration is associated with a diminished cell capacity to buffer ROS.

Additionally, oxidative damage to proteins, in the form of protein carbonyls, is increased throughout the brain by normal ageing, although to a lesser extent than in PD patients including areas typically affected by PD pathology such as substantia nigra and putamen (Alam et al., 1997; Smith et al., 1991).

4. Other phenotypes

It is worth noting that variants in GCH1 and variations in GCH1 expression and activity have been involved in other disorders, of which some non-neurological conditions.

In juvenile idiopathic arthritis (JIA), joints inflammation linked to pro-inflammatory cytokine production, is associated with an enhanced GCH1 enzymatic activity (as indirectly estimated by neopterin levels via ELISA measurement in 24 JIA patients' serum samples) and decreased BH4 activity (as indirectly estimated by the PHE/TYR ratio in the same samples via HPLC). Raises the hypothesis that inflammation increases *GCH1* activity but decreases the efficacy of the BH4 cofactor, which could lower the levels of brain neurotransmitters such as dopamine leading to the observed neurological symptoms of fatigue, depression, anxiety and affect cognition (Korte-Bouws et al., 2019).

There is a wide range of evidence for a role of GTPCH in pain modulation. Briefly, as this is not the focus of this thesis, *GCH1* polymorphisms associated with a lower GTPCH activity are often linked to lower pain perception and an increase in BH4 availability seems to lower pain thresholds in animal models and human patients (reviewed in (Hoofwijk et al., 2016; Nasser and Møller, 2014)). However, to my

knowledge, sensory functions have not been formally assessed in DRD or PD patients carrier of *GCH1* mutations.

A GCH1 haplotype associated with coronary artery disease, leading to reduced GCH1 activity in the blood of patients has also been found in linkage disequilibrium with the GCH1 variant associated to PD risk signal in a GWAS dataset (Antoniades et al., 2008; Mencacci et al., 2015; Ryan et al., 2015).

A wealth of papers have been published on the role of BH4 deficiency on eNOS activity (Bevers et al., 2006; Crabtree et al., 2009a; Vásquez-Vivar et al., 2003), cardiovascular disorders models (Hong et al., 2001; Landmesser et al., 2003; Laursen et al., 2001; Shinozaki et al., 1999) and endothelial function (Heitzer et al., 2000; Higashi et al., 2002; Stroes et al., 1997).

Although great advances have been achieved in the understanding of PD aetiology, treatments remain symptomatic and no cure has yet been discovered which limits the progression of the pathology. Using commonalities with other disorders, such as the genetic link between PD and DRD through GCH1 mutations, may allow to further define the specific mechanisms of disease.
My thesis aims at deciphering these differences to understand the role of the *GCH1* pathway in PD risk using a multi-disciplinary approach:

- Aim1 : to investigate the genetic risk for PD associated with genes of the *GCH1* and downstream BH4 pathway in a large exome cohort (Chapter 3)
- Aim 2: to determine the functional effect of a *GCH1* mutation in PD and DRD primary patient cells (chapter 4)
- Aim 3: to derive a PD-relevant CNS model of human midbrain dopaminergic neurons using small molecules to recapitulate neurodevelopmental cues (chapter 5)
- Aim 4: to investigate the functional effect of a *GCH1* mutation in the previously defined human patient-derived neuronal model (chapter 6)

Chapter 2: Materials and Methods

I. Molecular biology

1. Sanger sequencing

Sanger or dideoxynucleotide sequencing was developed by Frederick Sanger in 1977, and has widely been used ever-since due to its high reliability and accuracy for variants detection (Sanger et al., 1977). It is routinely used for the sequencing of targeted genetic regions and the validation of Next-Generation Sequencing (NGS) results for the exclusion of artefacts (Pittman and Hardy, 2013).

Sanger sequencing relies on the principle of random inhibition of the DNA polymerase by the inclusion of a small quantity of dideoxynucleotides (ddNTPs) in the DNA elongation mix among the deoxynucleotides (dNTPs). ddNTPs differ from dNTPs by the lack of hydroxyl group at the 2' and 3' carbon positions, preventing the formation of a phosphodiester bond with the following dNTP, hence stopping DNA chain elongation. Input DNA sample for Sanger sequencing is the result of a polymerase chain reaction (PCR) amplification of identical DNA molecules in each direction targeting a specific region of interest such as an exon or exon-intron boundary. During the sequencing reaction, multiple events of random inclusion of a ddNTP at any base during elongation of the target sequence is responsible for the creation of a large number of newly synthesised DNA fragments of every possible different lengths from the primer binding sequence until the last base of the DNA template (Sanger et al., 1977).

In the original method, Sanger made use of four separate sequencing reaction tubes each containing one ddNTP base added to the elongation mix. Fragments from each tube can be run separately in one column of an electrophoresis gel for the separation of these fragments according to their length. Sequence can then be re-transcribed manually base by base by attributing one base pair to each position according to their gel separation length (Sanger et al., 1977). Automation of the method uses

fluorophore-combined ddNTPs with each ddNTP associated with a fluorophore with a distinct emission fluorescence wavelength but similar excitation wavelength, allowing for the sequencing of all four ddNTP-terminated fragments in a single reaction tube. These are now separated using capillary gel electrophoresis and laser detection associated with automatic computerised sequence analysis for ease of readout using sequencers (Smith et al., 1986) (Figure 7).

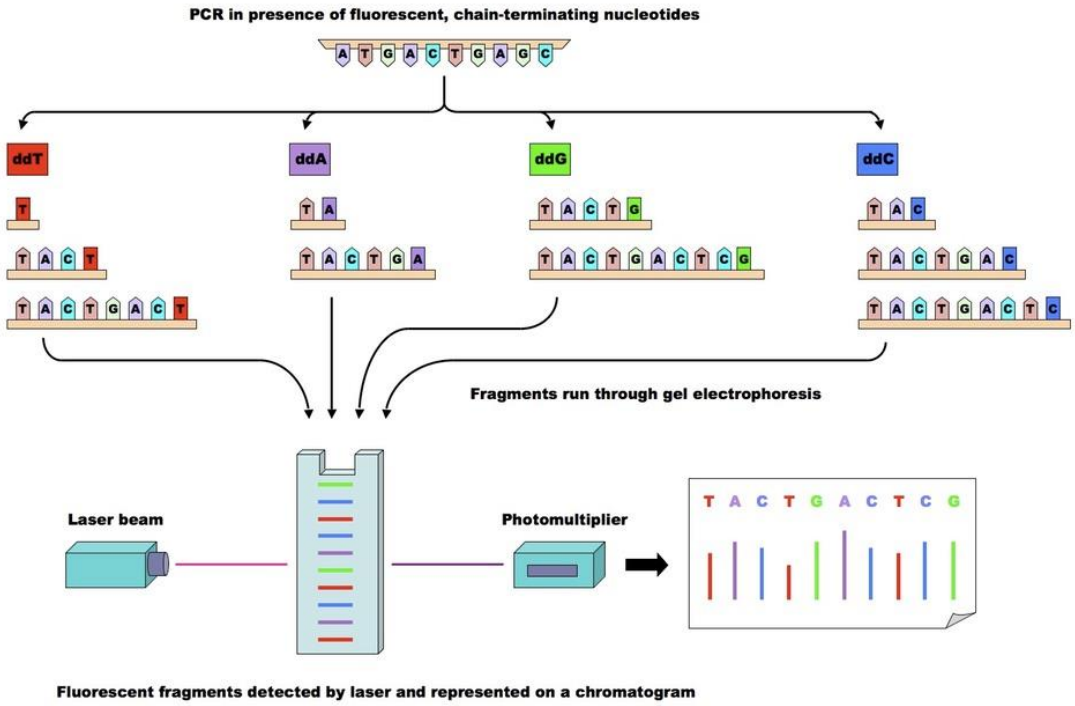

Figure 7: Principle of Sanger sequencing. The PCR in presence of fluorescent, chain-terminating nucleotide takes the product of a first PCR as input. Extracted from BioNinja website (http://www.vce.bioninja.com.au/aos-3-heredity/molecular-biology-technique/sequencing.html)

Experimental protocol:

In this project, Sanger sequencing is used to screen the complete set of exons and exon-intron boundaries of the *GCH1* gene in DNA extracted from iPSCs. Cells are grown to 80% confluence in a T25 flask and the Qiagen DNeasy mini kit (Qiagen) used to extract DNA. The FastStart PCR master mix (Roche) is used to amplify each exon with an additional few bases for its two exon-intron boundaries: each reaction is performed in a 15µL volume containing 7.5µL of FastStart PCR master mix (Roche), 0.5µL of each primer (5pmol/L), 30 ng of genomic DNA, and the appropriate quantity

of water to reach 15μL. Primers are designed in-house and include a custom-pair for the sequencing of 500bp on each side of the 343+5G>C mutation location (Table 2). Amplification of the fragments by PCR varies between exons and details of the PCR cycles are found in (Table 3, Table 4 and Table 5). The amplification product is run through a 1% Agarose gel along a 1Kb Ladder (New England Biolabs) and size of the fragments compared to their expected size. If PCR quality is thus validated, the amplicons are purified using ExoSAP-IT (Affymetrix Inc.), an enzymatic kit for the removal of primers and remaining ddNTP from the sample. The resulting purified amplicon is used as input for the sequencing reaction which is performed for in both forward and reverse directions for each fragment using the BigDye Terminator v3.1 sequencing chemistry (Applied Biosystems). Each reaction is performed in a 10μL volume containing 2μL Sequencing Buffer, 1μL of primer (10pmol/L), 0.5μL of BigDye Terminator v3.1 Ready Reaction Mix, 3μL of ExoSAP product and 3.5μL deionised water. Sequencing cycle: 96°C for 1 minute, {96°C for 10 seconds, 50°C for 5 second, 60°C for 4 minutes} for 25 cycles, hold at 4°C. Sequencing reaction is then filtered through a Sephadex G50 column (Sigma-Aldrich) on top of a Millipore plate (Millipore). The sequencing reaction is finally loaded on the ABI3730xl genetic analyser (Applied Biosystems) which allows for the simultaneous reading of a complete 96 well plate via the use of 96 capillaries. The analyser provides the sequencing results as an ".ab1" file which contains the computerised read sequence for each sample or well. These are compared to the RefSeq reference (NM_000161.3) using CodonCode Aligner v.6.0.2 (CodonCode Corporation) to ascertain the presence or absence of a mutation in the sequence.

GCH1	Forward Primer	Reverse Primer
Exon1	CCGGGCCATAAAAAGGAG	CGCCAAAAGTGAGGCAACTC
Overlapping 343+5 mutant	TGTGATCTAAGCAGGTTGCGT	CGATCCCCTGGCAAATCAGT
Overlapping 343+5 wild-type	CTTCCTGCGCCAAAAGTGAG	CGAGCTGAACCTCCCTAACC
Exon2	CTTTCCTCCCTCCGTTCTCC	ACCTGAGATATCAGCAATTGGCAGC
Exon3	AGATGTTTTCAAGGTAATACATTGTCG	TAGATTCTCAGCAGATGAGGGCAG
Exon4	GTCCTTTTTGTTTTATGAGGAAGGC	GGTGATGCACTCTTATAATCTCAGC
Exon5	CTCTGTGGCCCAGTCAGC	AGGCTCAGGGATGGAAATCT
Exon6	CATTTGTGTAAGAAGGGATATTTCG	AGTGACAAGGAATAAAGTTCACATC

Table 2: Sanger sequencing Primers for *GCH1* PCR and sequencing reactions

Step	Cycles	Temperature	Time
Denaturation	1	95°C	5 minutes
Denaturation Annealing Elongation	16	95°C 70°C 72°C	30 seconds 30 seconds 30 seconds
Touch-down annealing temperature	20	95°C 70-60°C 72°C	30 seconds 30 seconds 30 seconds
Denaturation Annealing Elongation	16	95°C 60°C 72°C	30 seconds 30 seconds 30 seconds
Final extension	1	72°C	7 minutes

Table 3: PCR cycle conditions for exons 2-6 of the *GCH1* gene. Cycle is a 70-touch-down-60 with a cycle by cycle reduction of temperature from 70°C to 60°C for annealing temperature during 20 cycles (0.5°C each cycle).

Step	Cycles	Temperature	Time
Denaturation	1	95°C	5 minutes
Denaturation Annealing Elongation	16	95°C 65°C 72°C	30 seconds 30 seconds 30 seconds
Touch-down annealing temperature	20	95°C 65-55°C 72°C	30 seconds 30 seconds 30 seconds
Denaturation Annealing Elongation	16	95°C 55°C 72°C	30 seconds 30 seconds 30 seconds
Final extension	1	72°C	7 minutes

Table 4: PCR cycle conditions for exon 1 of the *GCH1* gene. Cycle is a 65-touch-down-55 with a cycle by cycle reduction of temperature from 65°C to 55°C for annealing temperature during 20 cycles (0.5°C each cycle).

Step	Cycles	Temperature	Time
Denaturation	1	95°C	5 minutes
Denaturation Annealing Elongation	15	95°C 70°C 72°C	30 seconds 30 seconds 30 seconds
Touch-down annealing temperature	20	95°C 70-60°C 72°C	30 seconds 30 seconds 30 seconds
Denaturation Annealing Elongation	30	95°C 60°C 72°C	30 seconds 30 seconds 30 seconds
Final extension	1	72°C	7 minutes

Table 5: PCR cycle conditions for the 343_5 region of the *GCH1* gene. Cycle is an elongated 70-touch-down-60 with a cycle by cycle reduction of temperature from 70°C to 60°C for annealing temperature during 20 cycles (0.5°C each cycle), and a higher number of cycles than the regular 70-touch-down-60 cycle.

2. Exome sequencing – the Illumina method principles

The advent of next-generation sequencing (NGS), with the constant development of methods and chemistries with improved efficiency, allows for the query of largest parts of the genome in a timely and cost-effectively manner (Bras et al., 2012). Three main methods fall under the NGS umbrella: whole genome sequencing (sequencing of the complete genetic information in a sample, including both coding and non-coding regions); whole exome sequencing (WES – sequencing of the coding portion of the genome or exons) and targeted sequencing (sequencing of a specific and defined set of genes or genomic regions).

WES is currently preferred to other methods for the exploration of human genetic variations, as the method effectively focuses on the 1-2% of the genome containing protein-coding information, but in which 85% of all known mutations are found (Bamshad et al., 2011). Most methods focus on sequencing the 30 million bases of the consensus coding sequence (from the CCDS Project), although this varies between suppliers and chemistries (Pruitt et al., 2009). Focusing on the coding regions increases the capacity to analyse and interpret the effect of variants on proteins and considerably increases the cost-efficiency of sequencing, as well as of data storage and query servers (Bras et al., 2012; Lee et al., 2014).

The NGS methods rely on the massively parallel sequencing of DNA molecules using an automated system with spatial separation through a flow cell and enabling the time and cost-effective processing of millions of sequence reads amounting to gigabases of nucleotide sequence output. There are many different WES chemistries with variations in small technical details such as read length, accuracy or multiplexing capability. The main technical steps are common to most methods, and the steps used in most Illumina methods are described here (Figure 8). The DNA sample to sequence is first broken up into small fragments and sequence adaptors probes complimentary to all known exons of the genome are added to both ends of the fragments. These allow for fragments containing exons to be captured while the rest of the DNA fragments are washed away. The library of exon-containing fragments with their adaptors is then PCR amplified and gel purified. Clusters can be generated in the flowcell which can capture these adaptors-containing fragments on complementary surface-bound oligonucleotides. Bridge amplification is then used to amplify each fragment into

distinct clonal clusters. Sequencing relies on reversible terminator-based method which detects single bases while they are being incorporated to the DNA template strands, giving an accurate base-by-base sequencing. The sequence reads are aligned to a reference genome and can then be subjected to dataset quality control and further data analysis.

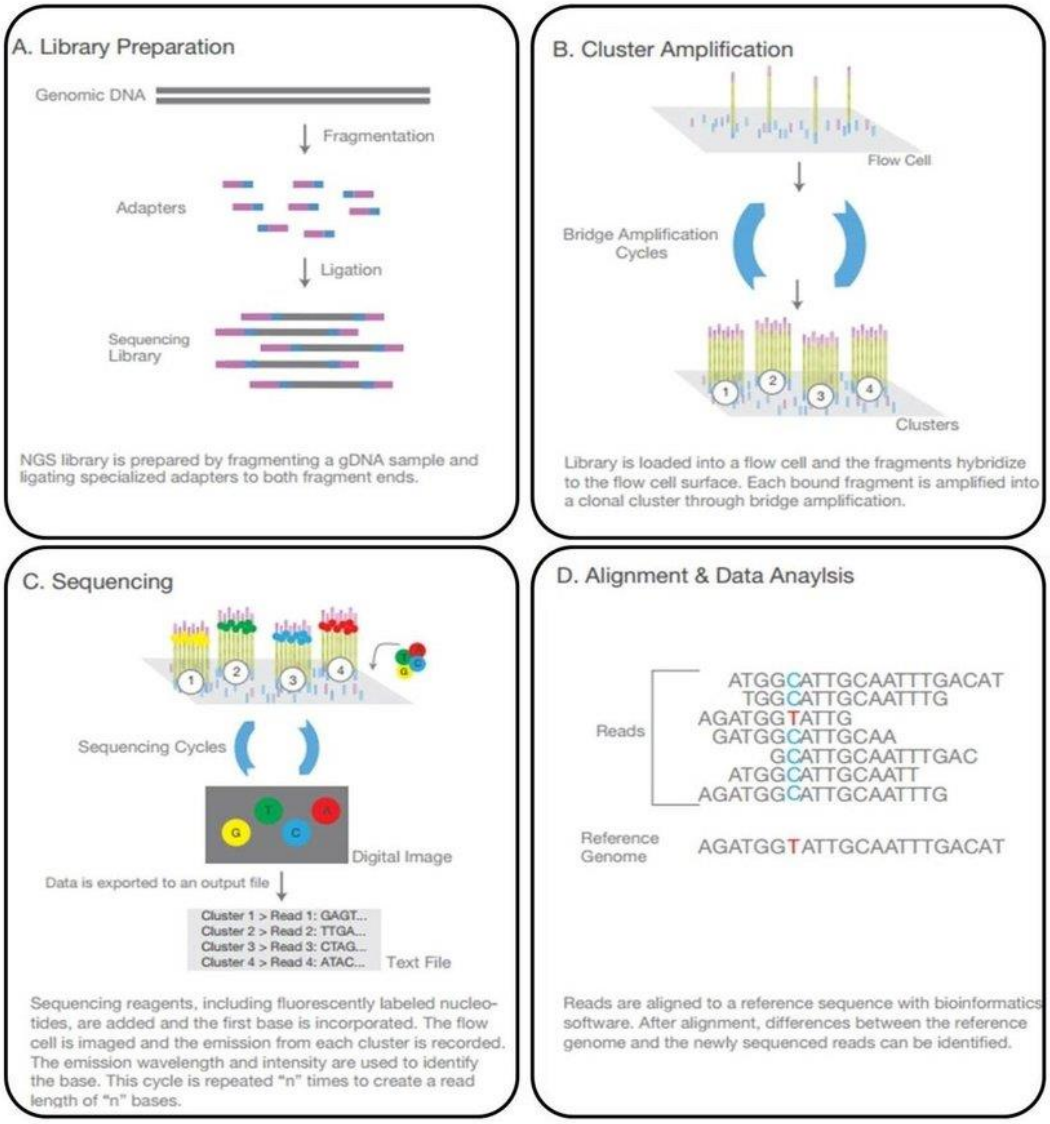

Figure 8: Overview of the whole-exome sequencing method by Illumina. Extracted from Illumina's "An introduction to Next-Generation Sequencing Technology"

3. Real-time polymerase chain reaction - qPCR

The real-time or quantitative PCR (qPCR) enables to quantitatively estimate the expression of genes of interest in comparison to housekeeping genes in a cell or tissue at the time of sampling (Mullis, 1990). These can be performed in one or two-steps,

with the latter being as follows: mRNA molecules are reverse-translated to cDNA (step 1) which can then be amplified and proportionally quantified to estimate the original number of specific mRNA molecules with great accuracy (step 2) (Figure 9) (Genetic Education Website, last accessed: 09 November 2019). Housekeeping genes expression is estimated in the same samples in order to normalise expression fluctuation of the mRNA of interest on this baseline. This allows for the correction of any discrepancies in the preparation of samples, hence sample-to-sample quantitative comparisons.

Experimental protocol:

Transcriptional levels of *GCH1* are determined in both fibroblasts and iPSCs using qPCR. Cells are grown to 80% confluency in T25 flasks and RNA is extracted, directly with lysis buffer in the flasks or from cell pellets after cells are harvested and spun, using the RNeasy Mini Kit (Qiagen). The obtained RNA concentrations are measured with a NanoDrop ND-1000 system (NanoDrop Technologies). 0.5μg of RNA from each extraction is reverse transcribed to complementary DNA (cDNA) using SuperScript III Reverse transcriptase (Invitrogen), dNTP Mix (Invitrogen) and Random Primers (Promega), according to manufacturer's instructions. The qPCR reaction is performed with TaqMan Fast Advanced Master Mix (AppliedBiosystems) on QuantStudio 7 Flex Real-Time PCR System (AppliedBiosystems) according to manufacturer's specifications. Primers used to amplify *GCH1* are pre-optimised and spanning the exons 4-5 boundary with a VIC marker (Hs00609198_m1). Endogenous control primers are targeted hypoxanthine phosphor-ribosyl-transferase 1 (HPRT1 - Hs02800695_m1) exons 2-3 boundary with a FAM marker. Both primers sets are used in the same well. All cDNA samples are run as triplicates. The qPCR reaction used the Fast program with 20 seconds 95ºC hold (polymerase activation) followed by 40 cycles of 1 second 95ºC denaturation and 20 seconds 60ºC annealation/extension. Results are read on QuantStudio software and analysed with Origin (OriginLab). Analysis is performed using the Livak method or the "Delta Delta CT" (ΔΔCT) method (Livak and Schmittgen, 2001). Each well ΔCt is calculated as $Ct(GCH1) - Ct(HPRT1)$ and $\Delta\Delta Ct = \Delta Ct\ (treated) - \Delta Ct\ (untreated)$ as normalised by the average of ΔCt for untreated controls of each line. 2^-ΔΔCt is calculated to estimate

the fold change in mRNA transcription as each of the previous calculation is in logarithm base two. These 2^-ΔΔCt are compared to each other and plotted.

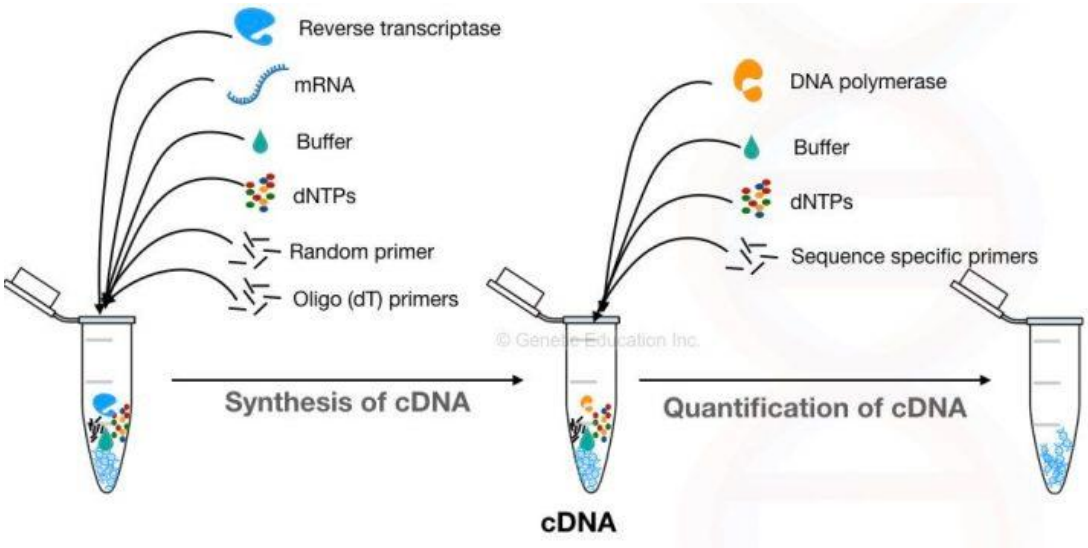

Figure 9: Principles of the two-step qPCR. Extracted from Genetic Education website (http://geneticeducation.co.in/reverse-transcription-pcr-principle-procedure-applications-advantages-and-disadvantages/)

4. Western Blot

Western blots are commonly used to determine the presence of a protein in a sample and to estimate the expression levels of this protein between samples. They rely on the size-based gel separation of a mixture of protein using the gel retardation method allowed by a density gradient gel. Proteins are then transferred to a membrane and the protein of interest is recognised by a specific antibody (Renart et al., 1979) (Figure 10). These are semi-quantitative as they can inform on the relative content in protein between samples ran in parallel but do not provide a direct quantitative measurement of the protein's concentration in a given sample.

Experimental protocol:

Cell are harvested, rinsed in PBS and pelleted before lysis or directly lysed in SDS-based lysis buffer (50mM Tris-HCl, pH 7.4, 100 mM NaCl, 1% Igepal CA-630 (Sigma I8896), 0.1% SDS, 0.5% sodium deoxycholate) added afresh with 1X complete

protease inhibitor cocktail (Roche). A small amount of sample is re-diluted in lysis buffer for the determination of general protein concentration using the DC Protein Assay kit (Bio-rad).

Equal quantities of protein between samples are mixed with 1X NuPAGE LDS Sample Buffer (Invitrogen) added with 50mM DTT. Proteins secondary and tertiary structures are broken by 5 minutes incubation at 95 ºC in the presence of DTT and reaction is stopped by placing samples on ice. Samples and SeeBlue Plus2 Pre-stained Standard ladder (Invitrogen) are loaded into pre-casted 4-12% gradient Bis-Tris gels (Invitrogen) and ran 45 minutes to 1 hour at 180V in 1X NuPAGE MOPS SDS Running Buffer (Novex).

To transfer the protein onto the nitrocellulose membrane (ThermoScientific), the membrane is first activated in ethanol for 2 minutes then rinsed in 1X NuPAGE Transfer buffer before being place onto the gel. Transfer apparatus is secured and transfer ran for 90 minutes at 25V. Success of protein transfer onto the membrane is assessed with Rouge Ponceau staining, which can then be rinsed off with TBS-T. For blotting, the membrane is first blocked with 5% milk in TBS-T at room temperature for 30 to 60 minutes. Proteins are marked with specific primary antibody at 1:500 in TBS-T 5% milk at 4°C overnight on rotator. Primary antibody is removed by three 5 minutes rinses in TBS-T. Secondary antibody specific to the specie of the primary is incubated 1 hour diluted at 1:5000 ratio in TBS-T 5% milk at room temperature. After rinsing of the secondary antibody three times 5min with TBS-T, 1:1 Pierce enhanced chemoluminescence (ECL) Plus Substrate mix (ThermoScientific) is poured onto membrane, left to react for 30-60 seconds, and excess removed by taping the membrane lightly with paper tissue. The blot is ready to be imaged using X-ray film in a dark room or Amersham 600 Imager (GE Healthcare).

To re-blot the membrane, ECL mix is rinsed three times 5 minutes in TBS-T and the membrane reactivated in 100% methanol then rinsed with water. The membrane can then be blocked again in TBS-T 5% milk and antibodies blotting repeated as previously.

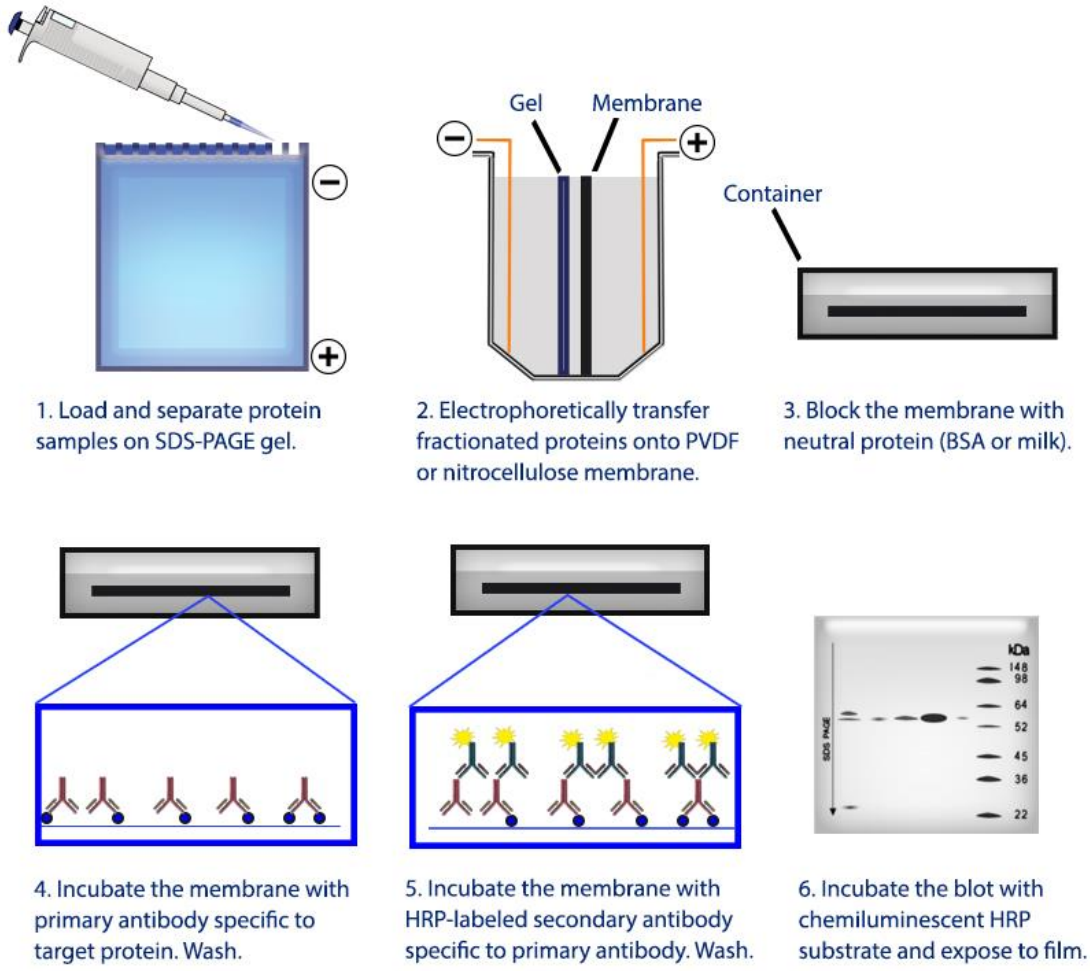

Figure 10: Principles of the Western blot. Extracted from the BioLegend website.(https://www.biolegend.com/en-us/western-blot).

II. Cell lines

1. Patients description

Skin biopsies were obtained by Dr. NE. Mencacci from three males of consecutive generations within one family: the proband (III-1) and his father (II-2) being affected with DRD, and the proband's grand-father (I-1) affected with PD (Figure 11).

The family was described by Mencacci and colleagues when investigating the burden of *GCH1* mutations as a risk factor for PD (Mencacci et al., 2014).

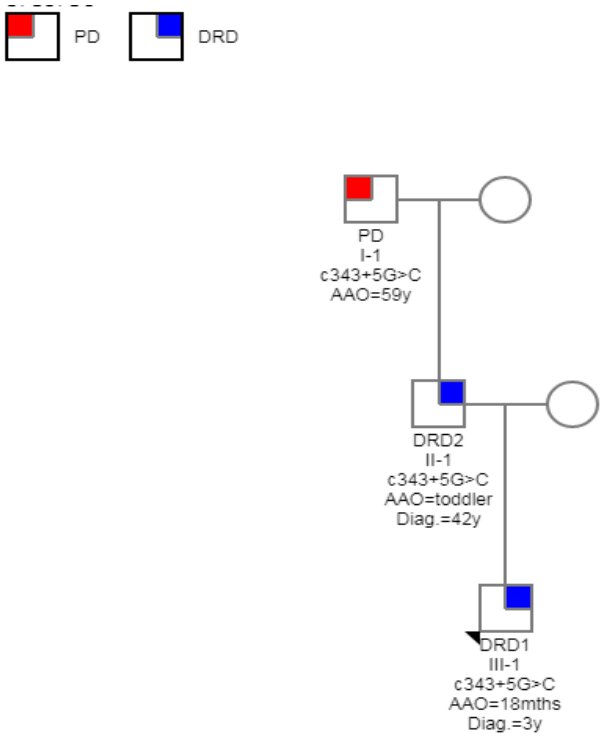

Figure 11: Family pedigree of fibroblasts donors. DRD are in blue, PD in red. The arrow points at proband (DRD1); both age at onset (AAO) and age at diagnostics (Diag.) are given when different. All males in pedigree are carriers of heterozygous c.343+5G>C mutation in *GCH1*.

The proband, an 18 years old British male (case III-1) developed turning of his feet with walking difficulties and falls at 18 months and was diagnosed with DRD at age 3. He was successfully treated with 300mg/day levodopa since diagnosis with no known development of treatment-induced secondary effects to date. His examination off-medicine confirmed the diagnosis and re-introduction of the treatment immediately improved his symptoms. The 123-Ioflupane FP-CIT single photon emission computed tomography (SPECT) or DaTSCAN, routinely used in PD diagnosis, was performed at age 17 and found normal (Figure 12 on the left).

The proband's father (case II-1) was at first misdiagnosed with cerebral palsy after a birth injury and subsequently diagnosed with DRD at age 42. He had bilateral asymmetric dystonia predominantly affecting his left side, with gait and trunk involvement. Trial of Levodopa treatment improved his symptoms immediately.

The proband's grand-father (case I-1) was examined at 65 years with a six-year history of parkinsonism, presenting initially with a resting tremor of his right arm and has had a slow progression since then. He showed no sign of dystonia. His DaTSCAN showed bilateral reduced tracer uptake more marked on the left (Figure 12 on the right), consistent with nigrostriatal dopaminergic innervation loss. He was diagnosed with PD and started on levodopa 300mg/day with a good response and no side effects (Mencacci et al., 2014).

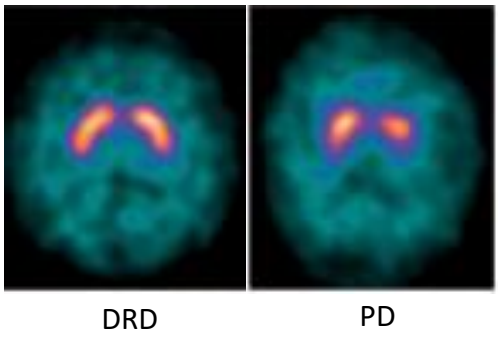

Figure 12: Comparison of a normal DaTSCAN image in the DRD proband (III-1) and PD patient (I-1). The PD one shows bilateral reduction of tracer uptake, more pronounced on the left (extracted from Mencacci et al., 2014

2. Mutation

All mutant lines are carrying the heterozygous 343+5G>C *GCH1* mutation, which is absent from all controls. Effects of the mutation are summarised in Figure 13: the mutation leads to the retention of intron 1 of the mRNA at splicing and the appearance of an early STOP codon. The premature stop codon arises 140bp after the end of exon 1, leading to a protein formed of the same first 114 amino acids (aa) as the wild-type protein followed by 47aa of intronic sequence. The final oligomer is 161aa long instead of the 233aa present in wildtype GTPCH (ExPASy translation tool). Native GTPCH has a molecular weight of 27.9kDa, whilst this mutant form is predicted to be reduced to 14.1 kDa (Stothard, 2000). This mutation was first identified in another family in which two siblings affected by DRD (one female and one male) were *GCH1* compound heterozygote: they both inherited c.343+5G>C from their unaffected mother and K224R mutation from their unaffected father (Bandmann et al., 1996a;

Robinson et al., 1999; Trender-Gerhard et al., 2009). The resulting mRNA may be degraded by nonsense mediated decay or transcribed into an inactive protein.

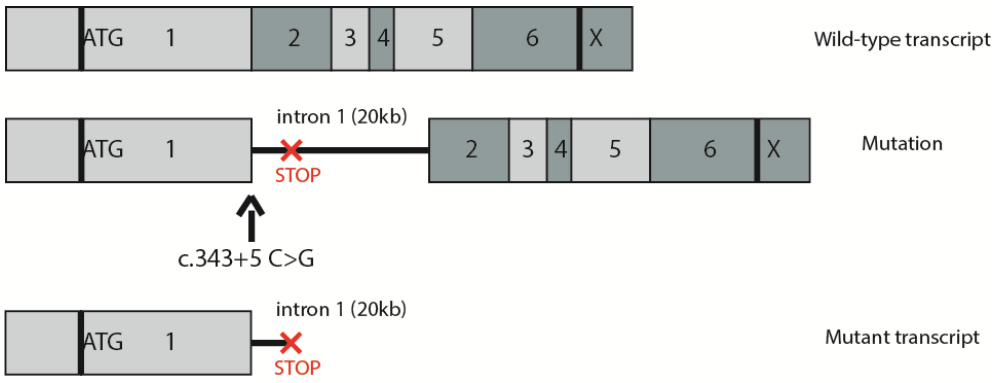

Figure 13: Schematics of the mutation carried by our patient cells. All patient cells carry a heterozygous 343+5G>C *GCH1* mutation which leads to retention of exon 1 of *GCH1* and the apparition of an early STOP codon, leading to a transcript likely to be degraded by the cell.

3. Fibroblasts

Skin biopsies are obtained from a family of *GCH1* mutation carriers presenting with PD (one donor) or DRD (two donors) by Dr. Niccolo Mencacci, healthy family members having declined participating in research. Biopsies are routinely processed by laboratory technicians in charge of the cell bank at the Institute of Neurology (UCL) and fibroblast cell lines established for research use. Frozen vials are obtained for all three lines as well as three independent healthy controls. Details about these lines can be found in Table 6. Briefly, control fibroblasts are age- and gender-matched to all three patient lines.

4. Human induced pluripotent stem cells

Patient fibroblasts are sent to the Censobio Company for iPSC reprogramming following an mRNA induced expression of POU5F1, SOX2, KLF4, MYC, NANOG and LIN28. Stringent quality control is performed on the expanded iPSC clones delivered by the company. Each line is tested for identity based on short tandem repeats (STR) profile compared to the original cell sample, for aneuploidy using a genotyping method kit (Karyolite BoBs), visually tested for viability for four passages, pluripotency tested for the line capacity to form all three germ layers (endoderm,

mesoderm and extoderm), for mycoplasma by qPCR and microbiological infection by inoculation for growth, finally pluripotency markers TRA-1-60, SSEA-4, SSEA-1 and POU5F1 are quantified via flow cytometry.

An additional four healthy control hiPSC lines routinely used in the lab are selected as controls. All details for the hiPSC lines can be found in Table 6.

Cell type	Line ID	Donor Phenotype	*GCH1* Mutation	Age of donor	Age at disease onset	Family history	Cell type of origin
Fibroblast	C1	Healthy	None	44	N/A	Brother FRDA – no signs	Skin Biopsy
Fibroblast	C2	Healthy	None	53	N/A	unknown	Skin Biopsy
Fibroblast	C3	Healthy	None	55	N/A	OPA1 non-carrier	Skin Biopsy
hiPSC	CTRL1	Healthy	None	73	N/A	unknown	Skin fibroblasts
hiPSC	CTRL2	Healthy	None	64	N/A	unknown	Skin fibroblasts
hiPSC	CTRL3	Healthy	None	0	N/A	unknown	CD34+ cord blood cell
hiPSC	CTRL4	Healthy	None	51	N/A	unknown	PBMCs
Fibroblasts and hiPSC	PD	Parkinson's disease	c.343+5G>C (heterozygous)	66	59	Son and grandson have DRD	Skin fibroblasts
Fibroblasts and hiPSCs	DRD1	DOPA-responsive dystonia	c.343+5G>C (heterozygous)	46	infancy	Father has PD, son has DRD	Skin fibroblasts
Fibroblasts and hiPSC	DRD2	DOPA-responsive dystonia	c.343+5G>C (heterozygous)	22	3	Grand-father has PD, father has DRD	Skin fibroblasts

Table 6: Cell lines used in this study. All cell line were Sanger sequenced for any mutations in *GCH1* gene. All donors are male

III. In vitro cell culture considerations

1. Infections, mycoplasma and STR checks

All lines used are routinely checked for mycoplasma infection using colorimetric (fibroblasts) or PCR-based (hiPSC) methods, and visually checked for any micro-

organism infection as cultures are performed in the absence of antibiotics. All infected cultures when discovered are discarded, and mycoplasma negative cells only are used in all experiments. The presence of the *GCH1* mutation c.343+5G>C in the heterozygous state is confirmed in the patients lines both at fibroblast and iPSC stages and the absence of any other *GCH1* mutation confirmed by Sanger sequencing. All control lines used do not carry any mutation in the *GCH1* gene. STR profiling is performed on fibroblasts at reception and on iPSC at completion of reprogramming by the Censobio company. Further STR checks are performed as a service by the Francis Crick Institute to estimate quality of iPSC and confirm lines identity.

2. Culture plates

All culture plates used in this project are flat plastic bottom plates treated for cell culture. These plates are routinely used as the plastic bottom promotes the attachment of mammalian adherent cells and their design allow for the distribution of gases between the wells and the outside environment, necessary for cell survival, while providing an efficient protection against micro-organisms.

The 8-wells ibidi chambers are flat micro-slides with 8-wells (Ibidi). It allows for short-term culture of cells and the use of confocal microscope directly in the wells for experimentation. Each of the ibidi chambers includes 8 square fields of 1.0 cm^2 each, with a bottom wall thickness of 180 μm, made of platic and covered with a polymer coverslip. Gas exchange between the medium and incubator's atmosphere partially occurs through the polymer coverslip. The ibidi chambers are used for plating of cells for functional experiments at both NPC and neuronal stages of the mDA induction protocol. This is of the outmost importance for the maintenance of cells in culture for prolonged periods of time after their last platting especially at the neuronal stage. They are also used for immunocytochemistry experiments and present the great advantage of reducing volumes and thus quantities of antibodies needed, as well as a clean separation of wells allowing for the use of several different antibodies across wells within a single chamber. The bottom of these plates is adapted to the use of confocal and other laser-based imaging systems allowing for both fixed (ICC) and functional (live-cell) imaging experiments using a wide range of systems.

3. Cell culture reagents

Product	Cat, Ref.	Company	Function	Usage
2-mercapto-ethanol	21985023	Gibco	Antioxidant by scavenging hydroxyl radicals	N2B27 media supplement
Accutase	A1110501	Gibco	proteolytic and collagenolytic enzymes mix	Splitting induction culture cells
B27 supplement	17504044	Gibco	Mammalian cell culture media	N2B27 media component
Dispase	D4818	Sigma-Aldrich	Protease	Splitting induction culture cells
DMEM	10566016	Gibco	Mammalian cell culture media	Fibroblasts media
DMEM/F12 media	31331028	Gibco	Mammalian cell culture media	N2B27 media component
DMSO	D2650	Sigma	Buffer	Additive for freezing media
E8 media	A1517001	Gibco	Mammalian cell culture media	iPSC media
EDTA	15575020	Invitrogen	Chelator of divalent cations	Splitting iPSC colonies and lifting them from geltrex
FBS	10082139	Gibco	Mammalian cell culture media	Fibroblasts media component
Geltrex	A1413302	Gibco	Basement membrane matrix	extracellular matrix for iPSC and induction cells
Glutamax	35050038	Gibco	L-glutamine with increased stability in vitro	N2B27 media supplement
Insulin	I9278	Sigma	Facilitate nutrient uptake by cells	N2B27 media supplement
Matrigel	356230	Corning	Basement membrane matrix	extracellular matrix for induction cells
N2 supplement	17502048	Gibco	Mammalian cell culture media	N2B27 media component
NEAA	11350912	Gibco	Increase cell growth and viability	N2B27 media supplement
Neurobasal media	21103049	Gibco	Mammalian cell culture media	N2B27 media component
Pen Strep	15140122	Gibco	Prevent culture contamination	N2B27 media supplement
Rock inhibitor	1254	Tocris	Selective ROCK-1 inhibitor	Thawing of iPSC and splits during inductions
Trypsin/EDTA	R001100	Gibco	Protease and chelator of divalent cations	splitting fibroblasts

Table 7: Cell culture media and reagents. Each line provides information on products origin, function and usage.

IV. Culture, maintenance and banking of fibroblasts

Experimental protocol:

All fibroblasts are cultured at 37ºC and 5% CO_2 in DMEM with GlutaMAX™ Supplement medium with 10% foetal bovine serum (FBS) (Gibco™, Thermo Fisher) in T175 flasks. Media is fully changed every other day or when it turns yellow. Fibroblasts are passaged with Trypsin-EDTA (0.05%) (ThermoFisher): cells are rinsed with PBS and covered with Trypsin/EDTA, then placed 3-5 minutes at 37°C 5% CO_2 or until cells are detaching. Cells are re-suspended in 5mL media and spun at 500g for 5 minutes. Supernatant is aspirated and cells resuspended 1:4-1:6 in DMEM/10% FBS. Cells can be frozen by following the same trypsin protocol for harvesting but re-suspended 1:6 in 90% FBS, 10% DMSO freezing media and frozen at -80°C or further banked in liquid nitrogen.

All cultures are mycoplasma negative as measured with MycoAlert® Mycoplasma Detection Kit (Lonza©). All experiments are made on low passages (P3-12).

V. Culture, maintenance and banking of hiPSC

1. iPSC maintenance media – Essential 8

Human iPSC (hiPSC) are cultured in feeder-free conditions using basement membrane matrix gel such as Geltrex to improve cell adhesion to the bottom of the plastic wells. Feeder-free culture is important for the maintenance of pluripotency and purity , the reduction of risk for mycoplasma infection of the hiPSCs, and the removal of non-human cells in culture (Young et al., 2010).

Experimental protocol:

hiPSC are maintained in culture on 6-well plates coated with Geltrex, in daily refreshed Essential 8 (E8) media (Gibco). Essential 8 supplement (50X – Gibco) is thawed at room temperature to ensure maintenance of bFGF activity and mixed 1X with E8 media in aseptic conditions. Reconstituted E8 media is kept at 4°C for a maximum of 2 weeks, a timespan during which all components should be stable and maintain their original concentrations, allowing optimal culture conditions. Complete E8 media

contains 8 ingredients: DMEM/F12, 64mg/mL L-ascorbic acid-2-phosphate magnesium, 14μg/mL sodium selenium, 100 μg/mL FGF2, 19.4mg/mL insulin, 543mg/mL NaHCO3, 10.7mg/mL transferrin and 2μg/mL TGFβ1 (Badenes et al., 2016).

2. Geltrex coating

Geltrex is a lactose dehydrogenase elevating virus (LDEV) free hESC-qualified reduced growth factor basement membrane matrix gel derived from murine Engelbreth-Holm-Swarm (EHS) tumor cells. Basement membranes are involved in tissue compartmentalisation as well as in cellular functions such as proliferation, migration, polarisation, adhesion and differentiation, and Geltrex is used to promote adhesion, growth and maintenance of pluripotency for hPSCs. Main Geltrex components include laminin, collagen IV, entactin, and heparin sulfate proteoglycan (Gibco).

Experimental protocol:
Geltrex stock is thawed overnight in an ice bucket in the cold room to maintain temperature below 4°C. Stock (12-18mg/mL) is then diluted 1:50 in cold DMEM to a final concentration of 240-360μg/mL. The diluted solution of Geltrex is quickly spread on wells in quantity sufficient to cover the entire growth surface area (in practice 1mL/well for 6-well plates). The coating is allowed to set for a minimum of 1 hour in 37°C in cell culture incubator for the solution to gel, forming an equivalent of basement membrane. It can be kept at 37°C for up to 5 days prior to use.

3. Splitting of iPSC

Human iPSC are split using EDTA, a chelator of divalent cations such as magnesium and calcium, both necessary in cell adhesion mechanisms. Added on adherent cells, EDTA actively removes these substrates leading to the inhibition of cation-dependent cell adhesion mechanisms and resulting in the abrogation of cellular adhesion and attachment. This results in the easy lifting of these cells from the bottom of the well, allowing for a minimally stringent splitting of the hiPSC.

Experimental protocol:

When the iPSC culture reach about 70-80% confluence, E8 media is removed and cells are rinsed with fresh sterile PBS to rid them of residual proteins, phenol red and divalent cations found in the media, before being covered with 0.5mM EDTA solution diluted in DPBS without calcium and magnesium. Cells are incubated with 0.5mM EDTA 4-5 minutes at 37°C or 5-8 minutes at room temperature, up until cells start to separate and round up, with holes appearing between the colonies. EDTA is gently aspirated and 2-3mL complete E8 media in a 5-10 mL stripette is used to gently detach and resuspend the cells into small colonies. Cells are re-plated on fresh Geltrex-coated 6-well plates at a dilution ratio of 1:6-1:10 depending on original confluence and growth speed of the line. Media is not refreshed the day after split to allow colonies to settle in culture at the bottom of the wells with the exception of high cell death and attachment being present on the day after splitting when media is changed to promote the survival of attached colonies. In cases where lines are difficult to grow and sensitive to splitting, 10μM ROCK inhibitor (RockI) can be added to the splitting complete E8 media. However, media needs to be changed with fresh complete E8 media on the next day to remove RockI.

4. Freezing and thawing iPSC

Experimental protocol:

Cells are detached following the EDTA cell-lifting protocol but are resuspended in 1mL E8 with 10% DMSO with a 5-10mL stripette, quickly placed into a freezing vial and stored in a isopropyl alcohol-filled Mr. Frosty -1°C freezing container box (Nalgene) in a -80°C freezer overnight or a minimum of 4 hours to reach desired temperature. The Mr. Frosty system allows for the controlled freezing of cryogenic vials at a rate of -1°C /minute, allowing for the maintenance of cells viability at later thawing. Cells can then be transferred to vial boxes and stored for a short period of time in the -80°C freezer or in liquid nitrogen tanks for longer storage such as cell banking.

Frozen vials are kept on dry ice from their banking location to the cell culture hood. Vials are gently thawed with minimum disruption of cell clumps in 3mL of fresh

complete E8 media using a 5-10mL stripette. Cells are then spun at 250g for 3 minutes to pellet and remove all DMSO, supernatant is aspired and discarded. Cell pellets are then gently re-suspended in fresh complete E8 media with 10μM RockI and plated on fresh geltrex coated 6-well plates. Cells are then incubated at 37°C and 5% CO_2 for 24 hours prior to RockI removal with media change with fresh complete E8 media. RockI is not used for routine feeding but allows to promote hiPSC survival and maintenance of pluripotency when thawed (Claassen et al., 2009).

5. Mycoplasma testing

The bacterial parasites known as mycoplasmas are prokaryotic organisms of various size and shape which widely contaminate cell cultures with 5-35% of tested cultures contaminated in various reports. Due to their small size and deformability, they easily pass through the filters used for culture medium sterilisation and, by lacking a rigid cell wall, are immune to antibiotics targeting cell-wall synthesis (Young et al., 2010). The most frequent species in tissue culture are *Mycoplasma hyorhinis, Mycoplasma orale, Mycoplasma arginine, Mycoplasma fermentas, Mycoplasma hominis, Mycoplasma salivarium, Mycoplasma pirum* and *Acholeplasma laidlawii* (Hay et al., 1989; Rottem and Naot, 1998). Infection can reach relatively high proportions with concentrations of mycoplasmas exceeding 10^8 cells per mL of media without causing cloudiness or cell growth (Young et al., 2010). Finally, mycoplasma infection affects most of the cell functions as they modulate the activity of host cells via both direct and cytokine-mediated indirect effects (Rottem and Naot, 1998).
By altering cell physiology, a mycoplasma infection would compromise all results and conclusions from cellular experiments. As a result, mycoplasma testing is performed routinely on all iPSC in culture in our laboratory using a highly sensitive PCR-based method.

Testing for mycoplasma contamination in culture uses the Universal Mycoplasma Detection Kit (ATCC® 30-1012K™), a proprietary formulated kit by ATCC using universal primers specific to the 16S rRNA coding region of the mycoplasma genome. By specific amplification of the mycoplasma genome, such an approach allows for the detection of over 60 species of mycoplasma, including the eight more common ones

mentioned above, as an easily detectable PCR band on gel. Assay is sensitive down to as little as 20 copies of mycoplasma in the tested sample (ATCC user manual). This assay is performed by the cell service platform of the Francis Crick Institute.

VI. mDA induction protocol methods for NPCs and neurons

1. mDA induction protocol

There are two major phases to the mDA induction protocol to direct the differentiation of hiPSC to mDA neurons: neurogenic and maturation. The first makes use of dual SMAD inhibition and SHH and Wnt signalling activation, the second uses neurotrophic factors and notch inhibition.

In the neurogenic phase, media is supplemented with dorsomorphin dihydrochloride, a potent BMP and PKA inhibitor, and SB-431542, a potent and selective inhibitor of TGF-β type I receptors, for dual SMAD inhibition (Chambers et al., 2009; Inman et al., 2002; Yu et al., 2008). SHH signalling is activated with the use of purmorphamine, a smoothened agonist, and Wnt signalling activated by CHIR-99021, a highly selective inhibitor of GSK-3 (α and β isoforms) (Huang et al., 2017b; Sinha and Chen, 2006). The success of this phase can be measured by the proportion of co-expression of FOXA2 and LMX1A in the nucleus of these cells, both markers of midbrain FP progenitors in the human brain (Nelander et al., 2009).

In the maturation phase, neural precursors committed to mDA differentiation are further matured into mDA neurons. Neurotrophins brain-derived neurotrophic factor (BDNF), glial cell-line derived neurotrophic factor (GDNF) and ascorbic acid (vitamin C) are used to support the maturation and survival of the cells. Media containing these three molecules is then further supplemented with cyclic adenosine monophosphate (cAMP), which activated PKA signalling at this later stage, and compound E which inhibits Notch signalling and promotes exit from cell cycle (Borghese et al., 2010; Xia et al., 2016). The success of this protocol is determined by ICC of mDA neuron markers: BIII-tubulin and tyrosine hydroxylase (TH).

Experimental protocol (Figure 14**):**

hiPSC are cultured to confluence in a geltrex-coated plate, when E8 media is removed, cells rinsed with PBS, placed in freshly reconstituted D0-6 media and media is changed daily. At D4, cells are split to clumps of 300-500 cells with dispase, and re-plated at a 1:2 ratio on Matrigel-coated plates in D0-6 media supplemented with 10μM RockI (for 24 hours). On D7, media is changed to D7-9 media after PBS rinse, with daily changes. On D10 of the protocol, and after PBS rinse, cells are placed in N2B27 media, prior to the D11 split: cells are trypsinised to clumps of 100-200 cells and seeded on matrigel-coated plates at a 1:3 ratio with N2B27 supplemented with 10μM RockI for 24 hours. Cells are now floor plate neural progenitors and should be expressing the corresponding markers (LMX1A/FOXA2). Cells can be fixed and expression of markers checked with ICC.

RockI is removed and cells placed in large quantity of D12-13 for 48 hours with no media change, before being rinsed with PBS and media replaced with D14+ media. Media is then changes every 2-3 days at first and up to every 4-5 days as maturation continues. Third split at around D20-25 can be performed with accutase and 1:2-1:3 split ratio onto matrigel-coated plates if cells are too confluent. Final split is performed on D35 with accutase at a proportion of 30-40.10^3 cells per ibidi chamber well for further maturation and functional/ICC analysis of the cells.

2. Media preparation

The neuronal maintenance medium (N2B27) is a 1:1 mixture of N2 and B27 media. N2 medium contains: DMEM/F12 GlutaMAX, 1X N2 supplement, 100μM non-essential amino acids, 100μM 2-mercaptoethanol, 5μg/mL insulin, 50 U/mL penicillin and 50mg/mL streptomycin. B27 medium contains: Neurobasal, 1X B27 supplement, 1X GlutaMAX supplement, 50 U/mL penicillin and 50mg/mL streptomycin. N2 and B27 media are kept in separate bottles at 4°C for a maximum of 28 days and are mixed 1:1 into N2B27 as needed.

All mDA induction protocol media are prepared freshly according to their recipe (Table 8) and kept at 4°C for a maximum of 4 days. Details for the origin and use of the different molecules can be found in Table 9.

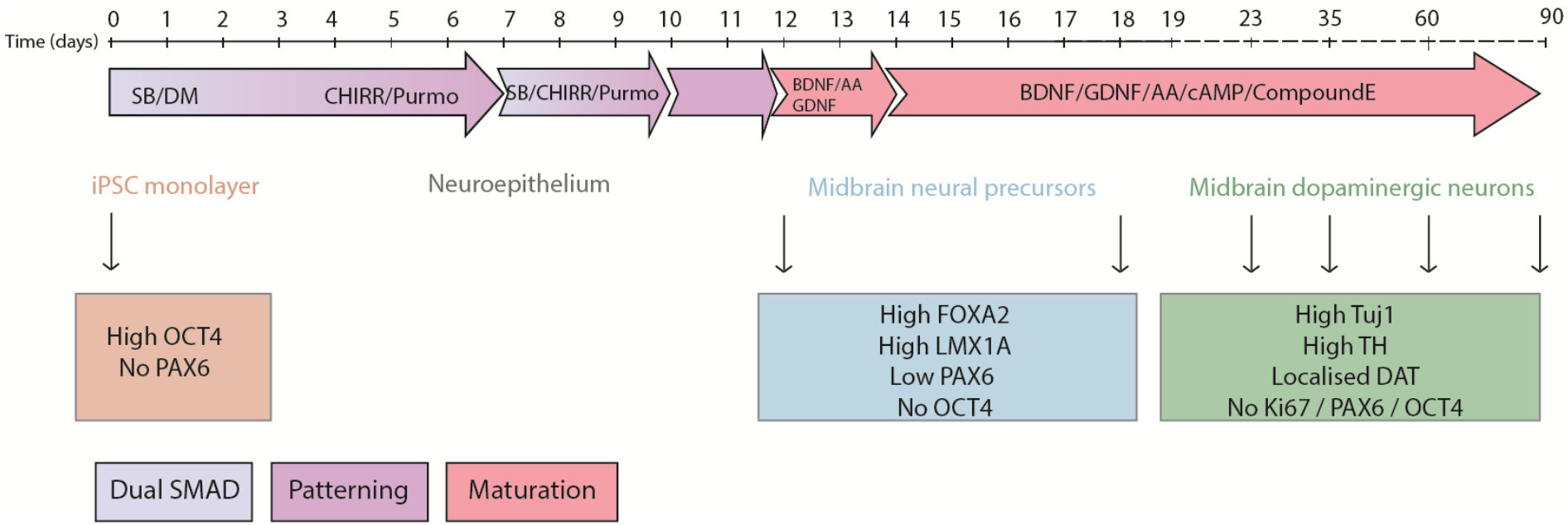
Time (days)
0 1 2 3 4 5 6 7 8 9 10 11 12 13 14 15 16 17 18 19 23 35 60 90
SB/DM
CHIRR/Purmo
SB/CHIRR/Purmo
BDNF/AA
GDNF
BDNF/GDNF/AA/cAMP/CompoundE
iPSC monolayer
Neuroepithelium
Midbrain neural precursors
Midbrain dopaminergic neurons
High OCT4
No PAX6
High FOXA2
High LMX1A
Low PAX6
No OCT4
High Tuj1
High TH
Localised DAT
No Ki67 / PAX6 / OCT4
Dual SMAD
Patterning
Maturation

Figure 14: In-house mDA neuron differentiation protocol. The principles and timeline of the protocol, as well as the small molecules used for the different steps are presented at the top. The different stages and expected staining associated with each are presented at the bottom. Each arrow marks a time point at which these markers were ascertained during the various protocol trials.

Media	SB	DM	CHIRR	Purmor-phamine	BDNF	GDNF	Ascorbic Acid	cAMP	Comp-ound E
D0-6	10mM	2mM	3mM	1mM	.	.	.	.	.
D7-9	.	2mM	3mM	1mM	.	.	.	.	.
D12-13	.	.	.	.	20ng/mL	20ng/mL	0.2M	.	.
D14+	.	.	.	.	20ng/mL	20ng/mL	0.2M	0.5mM	0.1mM

Table 8: Media composition for original mDA induction protocol. All reagents are diluted in N2B27 media (1:1 mixture of N2 and B27 media. N2 medium contains: DMEM/F12 GlutaMAX, 1X N2 supplement, 100μM non-essential amino acids, 100μM 2-mercaptoethanol, 5μg/mL insulin, 50 U/mL penicillin and 50mg/mL streptomycin; B27 medium contains: Neurobasal, 1X B27 supplement, 1X GlutaMAX supplement, 50 U/mL penicillin and 50mg/mL streptomycin.).

Product	Catalogue reference	Company	Function	Usage
Purmorphamine	SML0868	Sigma	Smo receptor agonist	SHH signalling activation
SB	SB431542	Tocris	TGF-βRI inhibitor	Dual SMAD (TGFb inhibition)
DM	3093/10	Tocris	AMPK and BMP-RI inibitor	Dual SMAD (BMP inhibition)
CHIR	4423/10	Tocris	GSK3 inhibitor	Wnt signalling activation
Ascorbic acid	A4544	Sigma	Antioxidant	Promotes mDA differentiation
Compound E	1949-250	Cambridge Bioscience	Notch inhibitor	stops cell cycle and promotes mDA differentiation
cAMP	D0627	Sigma	activates cAMP/PKA signalling	Promotes mDA differentiation
BDNF	248-BD-005	R&D	Neurotrophin	Supports neuralisation and neuron viability
GDNF	212-GD-010	R&D	Neurotrophin	Supports neuralisation and neuron viability
Retinoic Acid	R2625-100MG	Sigma	Caudalizing agent	Promotes caudalizing of neurons in differentiaiton
FGF	100-18b-100	Peprotech	Ventralizing agent	ventralises differentiating neurons

Table 9: Origin and usage of small molecules from the mDA induction protocol.

3. Matrigel coating

Matrigel (Corning) is a human ESC qualified solubilised basement membrane preparation extracted from EHS mouse sarcoma line cultures, a tumour rich in ECM proteins. Major components of Matrigel are laminin (56%), collagen IV (31%), heparan sulfate proteoglycans, and entactin (8%). It is used as a more robust replacement for Geltrex after 3 weeks in mDA induction culture as it has been demonstrated to provide a physiologically relevant environment for cell proliferation and differentiation (Ma et al., 2008).

Experimental protocol:

Matrigel is thawed on ice, mixed 1:50 with cold DMEM and immediately poured into the relevant plate format for cell culture. Plates are then left 1-3hours in the incubator at 37°C for matrigel to polymerise. Supernatant is aspirated and culture media placed on the matrigel-coated plated immediately before use. Cells can be plated directly onto it.

4. Dispase splitting

Dispase is a protease which cleaves fibronectin and collagen IV, both proteins necessary to the attachment of adherent cells to the basal membrane gel (geltrex or matrigel) in culture. Using dispase allows detaching the neuroepithelial sheet from the underlying basement membrane while maintaining the integrity of large cellular clumps during the mDA induction protocol.

Experimental protocol:

Media is aspirated in order to leave 1mL of media in each well and 200uL of dispase (10mg/mL stock concentration; 2mg/mL working concentration) is added in the media. The pipette tip is used to help cells detach from the border of the well. Cells are placed 7 minutes at 37°C in incubator until the neuroepithelial sheet lifts from the bottom of the well. Cells are then gently aspirated with a 5mL stripette and rinsed twice through a tube of PBS, by shaking the tube slightly and letting the cells reach the bottom by gravitation, before aspirating the surnatant of PBS and repeating the

process. The last pellet is re-suspended gently in 5 mL induction media supplemented with 10 uM RockI. Media is changed on the next day to remove RockI.

5. Accutase splitting

Accutase is a proprietary mixture of proteolytic and collagenolytic enzymes containing 0.5mM EDTA. It allows for the dissociation of the cells from the basement membrane as well, while keeping cells as clumps smaller than those obtained with dispase.

Experimental protocol:
Cells are washed with PBS, covered with Accutase (500uL/well) and placed 5-8 minutes at 37°C in incubator until cells lift. N2B27 media is used to re-suspend the last attaching cells and harvest the cells. Cell suspension is spun 3 minutes at 250g, supernatant is removed and discarded and cell pellet is re-suspended in the appropriate culture media supplemented with 10μM RockI.

6. Banking and thawing of midbrain FP neural progenitors

Prior to freezing, commitment to the midbrain dopaminergic lineage of the midbrain midbrain FP neuroprogenitors is confirmed as nuclear co-expression of LMX1A and FOXA2 by ICC. Midbrain FP neuroprogenitors from cultures with 85-100% co-expression of the LMX1A and FOXA2 markers are banked directly after staining is confirmed or after 2-5 days expansion in N2B27 supplemented with 0.1μM FGF2 refreshed daily, after a first split at 1:3 ratio onto plates freshly coated in matrigel.

Experimental protocol:
Cells are rinsed in PBS, harvested using dispase and re-suspended in freezing media composed of N2B27 with 10% DMSO and 0.1uM FGF2. Cells are placed in a Mr. Frosty and placed in -80°C freezer for 24 hours prior to being transferred to liquid nitrogen tanks for long-term storage.

For thawing, midbrain FP neuroprogenitors vials are kept on dry ice for transfer, then rapidly warmed by manual friction and re-suspended in excess amount of N2B27. Cell

suspension is spun down at 200 g for 3 minutes, the supernatant removed and pellets re-suspended in N2B27 with 10μM RockI. Cells are plated at a 1 vial to 2 wells ratio on matrigel-coated 6-well plates and placed in incubators for 24h before media change to either N2B27 for continuing differentiation protocol from D12 of protocol onwards; or N2B27 supplemented with 0.1μM FGF if kept at midbrain FP neuroprogenitor stage for further analyses at this stage of differentiation.

VII. Fluorescent reporters for functional imaging

1. Recording buffer

Recording buffer is a photo-stable, isotonic saline buffer made in the laboratory out of Hank's Balanced Salt Solution (HBSS), 10mM HEPES at physiologically-balanced pH 7.4. Composition: 156mM NaCl, 3mM KCl, 2mM MgSO4, 1.25mM KH2PO4, 2mM CaCl2, 10mM glucose and 10mM HEPES; pH adjusted to 7.4 with NaOH. The solution can be stably kept at room temperature, with pH monitoring and correction at regular intervals. Fresh falcons of the media are filtered through a 37μm syringe filter for removal of potential bacteria or debris prior to each use. The use of this recording buffer is compatible with most fluorescent dyes in cell functional analyses and appropriate for laser-based microscopy. The presence of HEPES allows to maintain the cells out of the incubator for prolonged period of time (1-2hours) without a CO2-controlled environment.

2. Hoeschst

Hoechst 33342 is a non-cytotoxic cell-permeant nucleic acid stain which emits blue florescence when bound to double-stranded DNA, with a maximum excitation/emission wavelength of 350/461 nm. As such, Hoechst is an appropriate alternative to DAPI for nuclear staining in live cells and can be associated with any cytoplasmic and non-competing nuclear dyes (such as Sytox Green) with a distinguishable excitation/emission spectrum. When its use is permitted by the experimental conditions, it is commonly used for easy and rapid localisation and focus of the cells by visualisation of their nuclei.

Experimental protocol:

Stock solution of 10mM Hoechst, kept at -20°C for long-term storage, is diluted in appropriate amount of recording buffer or cell culture media to a final concentration of 10μM for 15 minutes at room temperature and in the dark. On confocal microscope, the 405nm laser can be used to excite the fluorophore.

3. Monochlorobimane (mCB)

Monochlorobimane (mCB) is a cell permeable non-fluorescent molecule which readily reacts specifically with the principal intracellular low molecular-weight thiol reduced glutathione (GSH) and, when conjugated to GSH fluoresces with an absorption/emission maxima of ~ 394/490 nm. It has little affinity for binding to other thiols in the cells. Although the formation of mCB-GSH conjugate is dependent on the activity of the cytoplasmic enzyme glutathione S-transferase (GST), longer incubation periods permit a semi-quantitative measurement of GSH content of the cell independent of the enzyme's concentration (Chatterjee et al., 1999). In the following chapters, mCB is used to estimate the relative GSH content between cell lines, in all the cell types analysed: fibroblast, midbrain FP neuroprogenitor and neurons.

Experimental protocol:

Live cells are rinsed with PBS and incubated for 30 mins in the dark, at room temperature, with 50μM mCB diluted in recording buffer. mCB is kept in solution during recording. Images are acquired as z-stacks recovering the complete depth of the cells, using a Zeiss confocal microscope. mCB fluorescence is excited with the 405nm laser and the emitted fluorescence refined prior to image capture with the 410-530 nm filter, as the absorption/emission maximal wavelengths of the molecule are ~394/490 nm. 3-5 z-stacks are recorded per slide or well and results are analysed on the Fiji (ImageJ) software.

4. Tetramethylrhodamine methyl ester (TMRM)

Tetramethylrhodamine methyl ester (TMRM) is a cell-permeant cationic fluorescent dye used to measure the mitochondrial membrane potential (MMP) and indirectly estimate the mitochondrial function. TMRM fluoresces at maximal absorption/emission wavelengths of ~548/574 nm and readily penetrates the cells. In non-quenching concentrations (1-50nM), TMRM accumulates in the mitochondria in inverse proportion to the MMP according to the Nernst equation. As a result, when the MMP polarises (interior becomes more negative) the mitochondria accumulates more TMRM and TMRM fluorescence is more intense in the mitochondria; and when it depolarises (interior becomes less negative) the mitochondria accumulates less TMRM and TMRM fluorescence is less intense in the mitochondria. Accordingly, the use of specific inhibitors of different complexes of the mitochondrial respiratory chain, by affecting the capacity of the mitochondria to maintain its membrane potential, directly and relatively modifies TMRM fluorescence intensity. This provides a tool for qualitative assessment of the MMP and comparison of the MMP between cell lines relative to the controls. Finally, TMRM can only be removed from the mitochondria by a complete absolution of the MMP, which can be achieved with the use of ionophores such as FCCP (Nicholls, 2006; Perry et al., 2011).

Experimental protocol:

Live cells are incubated for 30 minutes, in the dark, at room temperature with 25nM TMRM diluted in recording buffer. TMRM is kept in solution during recording. Images are acquired using a Zeiss confocal microscope. TMRM fluorescence is excited with the 561nm laser and the emitted fluorescence refined prior to image capture with the 550-645 nm filter, and measured at 580nm as the maximal emission is ~574 nm. 3-5 z-stacks covering the complete depths of the cell bodies are recorded per slide or well and results are analysed on the Fiji (ImageJ) software.

5. MitoTracker red CM-H2XROS

The MitoTracker red CM-H2XROS (later referenced to as MitoROS) is a reduced non-fluorescent form of MitoTracker Red and as such is targeted to the mitochondria, where it accumulates dependent on the MMP. When oxidised by the mitochondria-

produced ROS, MitoROS red fluorescence is activated. This dye presents the great advantage of being specific for reporting the mitochondrial production of ROS mainly. However, the accumulation and thus fluorescence intensity of the dye is dependent on the MMP, which may be a potential confounder in experiments. Additionally, prior to the start of imaging, loading time has to include a sufficient delay in order for the dye to accumulate in the mitochondria and for the operator to focus the microscope on the organelles. Thus, the dynamics of this dye doesn't allow for reporting the complete behavioural change of the dye and through it the complete behaviour of the cell mitochondria. However, the linear mid-progression increase of the fluorescence intensity of the dye, accessible experimentally, is sufficient to compare the rate of mitochondrial ROS production between cell lines.

Experimental protocol:

Live cells are incubated for 15 minutes at room temperature and in the dark with 1 μM MitoTracker Red CM-H2XROS and 10nM Hoechst diluted in recording buffer. The dye is kept in solution during recording. Images are acquired as time-series using a Zeiss confocal microscope at the z-coordinate showing the bulk of the mitochondria visible across the depth of the cell. MitoTracker Red CM-H2XROS fluorescence is excited with the 561 nm laser and the emitted fluorescence refined prior to image capture with the 550-645 nm filter, as the absorption/emission maximal wavelengths of the molecule are ~ 579⁄599 nm. Hoechst fluorescence is excited with the 405 nm laser and image captured after fluorescence emission is focused with the 379-504 nm filter, as the absorption/emission maximal wavelengths of the Hoechst molecule are ~ 350⁄461 nm. Time-series is captured for 10 minutes with one image very 10-20 seconds (depending on acquisition time needed). Positive control uses the addition 50-100μM rotenone to inhibit complex I of the mitochondrial respiratory chain and observe a drastic increase in the ROS production associated with a significant increase in dye fluorescence intensity. In order to confirm the accumulation of the dye at the mitochondria, 1 μM FCCP, a mitochondrial respiratory chain uncoupler, is subsequently added to the well for the recording of the dye minimum fluorescence intensity signal after its release from the mitochondria through complete loss of MMP.

6. Bodipy 581/591 C11 (lipid peroxidation)

Lipid peroxidation is an oxidative reaction characterised by the removal of electron from lipids of cell membranes by free radicals. Cellular membrane lipid peroxidation, while happening in a low rate in basal conditions, is found greatly increased when cells are in a state of oxidative stress, and may be used as a proxy to estimate the deleterious effect of this state on the cells normal physiology. Bodipy 581/591 C11, a fluorescent lipid peroxidation indicator, is an undecanoic (straight chain line of 11 carbons) lipophilic acid, which acts like natural lipids and localises to the cell membranes, making these ideal membranes probes. In its reduced form, the dye fluorescence emission peak at 590 nm and the oxidation of the polyunsaturated butadienyl portion of the dye through the action of ROS oxidation at the membrane shifts peak emission fluorescence to 510 nm (Naguib, 1998). The ratio of dye fluorescence emission 510:590 nm wavelength is used to estimate the progression of lipid peroxidation at the membranes of live cells (Pap et al., 1999).

Experimental protocol:

Live cells are incubated 20 minutes with 5μM Bodipy C11 591:581 solution diluted in N2B27 media at 37°C 5% CO_2. For midbrain FP neuroprogenitors, loading is difficult and areas central to the well and containing a large proportion of cells uptaking the dye in its reduced form (green) are selected for imaging. For neuronal cells, areas containing a large proportion of neuronal-looking cells with both processes and nuclei visible are selected. Image acquisition is performed on a Zeiss Confocal Inverted microscope, with one image captured every 20 seconds at wavelengths of both 510nm and 590 nm for 10 minutes. Addition of 100μM hydrogen peroxide is used as a positive control for this experiment.

7. Dihydroethidium (DHE)

DHE is used as an intracellular superoxide production reporter dye. In its reduced form, DHE emits blue fluorescence (380nm excitation, 405-470nm emission) and is located in the cytoplasm. When oxidised by intracellular superoxide, the resulting molecule, 2-hydroethidium (EOH), shifts fluorescence to red (530nm excitation, 560

emission) and, as a derivate of ethidium, re-locates to the nucleus and intercalates with DNA. Of note, DHE can also intercalate with mtDNA, making the red fluorescence signal seemingly non-nuclear in highly compact and confluent cell cultures. The rate of increase of the red (530nm) fluorescence correlates with the rate of production of superoxide in the cells as EOH is stable in the cell, removing the risk for intra-conversion variability (Chen et al., 2013). The transformation of DHE to EOH is specific to the interaction of DHE with superoxide, with no other ROS or nitrogen species demonstrating this ability (Zhao et al., 2003). Image analysis is typically performed using nuclei selection, but overall red fluorescence dynamic change can also be used to determine the rate of superoxide production in the cells. Main caveat for the use of DHE is associated with the potential for the dye to be oxidised prior to its loading in the cells. Mainly: if the reporter is already fully oxidised, it loses its capacity to report superoxide production altogether; if the reporter is partially oxidised the red fluorescence will rapidly reach a plateau when dye capacity is saturated, leading to the rapid loss of dynamic range. Practically, oxidation of the dye can be limited by the use of freshly reconstituted DHE using reduced DMSO.

Experimental protocol:

Live cells are rinsed with PBS and loaded with 2μM freshly reconstituted DHE diluted in recording buffer for 3 minutes, in the dark at room temperature. Imaging records the changes in emission fluorescence of the dye and its re-localisation to the nucleus at 380nm excitation (reduced state) and 530nm excitation (oxidised state). Setup at the start of the first well maintains a difference between background and cells to a minimum of 2-3 fold in order to maintain ability to capture the full dynamic range of the dye. Images are acquired every 5 seconds for 8-10 minutes. An excess of hydrogen peroxide (100μM) is used at the end of recording as a positive control, associated with a drastic increase of 530nm fluorescence and quasi-loss at 380nm.

8. FURA-2 AM

FURA-2 AM is a sensitive, ratiometric fluorescent calcium indicator used to measure intracellular calcium in live cell experiments. The fluorescent dye is cell-permeant, has a high affinity for Ca2+ and the fluorescence excitation properties of the dye vary with

its binding to Ca2+, with the free form of FURA-2 being excitable at 380nm while the calcium-bound form is excited at 340nm wavelength. The dye emission fluorescence however is maintained at 510nm independently on its binding to Ca2+. Intracellular Ca2+ concentration is evaluated using the ratio of bound to unbound FURA-2 excitation fluorescence reads, thus correcting for uneven dye loading across cells, photo-bleaching, unequal cell thickness or dye leakage in live-cell experiments. This method has been used for decades and in various applications since the invention of this dye (Grynkiewicz et al., 1985).
The ratio of calcium-bound to free FURA-2, as calculated by dividing the fluorescence intensity of the cell soma at 510nm after excitation at 340nm and 380nm respectively, is used here to estimate transient intracellular Ca2+ bursts post-chemical stimuli. Different molecules are used to activate these reactions in our cells and characterise the cells in culture.

Glutamate, a pan-neuronal excitatory neurotransmitter, binds to post-synaptic receptors (NMDA-R, AMPA-R and kainite R), allowing a depolarising ion current into the cell or excitatory post-synaptic current which initiates neuronal action potential firing. 5μM glutamate is used here as a physiological concentration which would allow neurons to quickly depolarise while avoiding glutamate-associated excitotoxicity (Verkhratsky and Kirchhoff, 2007). Glutamate is also responsible for depolarisation of glial cells such as astrocytes and oligodendrocytes, limiting the specificity of the use of glutamate for neuronal cell characterisation in our cultures (Kettenmann et al., 1984a, 1984b). It does however provide a read-out for the presence of active glutamate receptors in the culture, supporting the functionality of the cells obtained by the end of the induction protocol.

Glutamate is substituted for KCl as neuronal excitation stimulus. An increase of K+ concentration in the extracellular media is associated with an influx of this positively charged ion through the membrane, according to Nersnt equation. This in turn results in the depolarisation of the neuron membrane potential, associated with the opening of voltage-dependent calcium channels (VDCC) associated with a transient burst of intracellular Ca2+ concentration picked up by FURA-2 ratio change (Hammond and Michel, 2015).

ATP is naturally released by glial cells such as astrocytes and by neurons in order to maintain glia-glia and bi-directional neuro-glial communication. ATP release extra-cytoplasmically allows the propagation of calcium waves among glial cells through activation of Ca2+ intracytoplasmic release (Guthrie et al., 1999), and not via intercellular connexions as previously believed (Cotrina et al., 1998). Glial-excreted ATP is directly associated with excitatory postsynaptic current increasing neuronal excitability in some neuron-glia systems such as in the hippocampus, or with inhibitory pre-synaptic effect on neurons, directly in its ATP form or as an adenosine donor, in other cases such as pain sensory system (Cotrina et al., 2000; Verderio and Matteoli, 2011). 100μM ATP is estimated to mimic the necessary concentration at the point of excretion from the astrocyte for an optimal glial calcium influx activation (Guthrie et al., 1999).

Experimental protocol:

Live cells are loaded for 30 minutes with 5 μM FURA-2 and 0.005% pluronic acid in recording buffer, at room temperature, in the dark. Cells are then washed twice with PBS and covered with fresh recording buffer for imaging. Image acquisition is performed using a Cairn xenon arc light source and Optoscan monochromator (Cairn), associated with an Optiscan II stage system and custom filter wheel (Prior Scientific), and an Andor sCMOS camera (Oxford instruments). Emission fluorescence at 510nm is measured after excitation of free FURA-2 (excitation maxima at 380nm) and calcium-bound FURA-2 (excitation maxima at 340nm) in sequential steps. The emission fluorescence in response to excitation variation or 340/380 excitation ratio is used to estimate intracellular calcium concentration fluctuations.

Baseline is recorded for 1.5-2 minutes before addition of stimulating molecules. At Timepoint1, neurons are excited with 5μM glutamate then allowed to recover for a couple of minutes prior to astrocytic cells excitation with 100μM ATP. At Timepoint2, KCl is substituted to glutamate for specific activation neuron calcium influx. However due to the reduced proportion of cells recovering from KCl compared to Glutamate, 100μM ATP is applied first to activate astrocytic cells, cells are allowed to recover prior to addition of 50mM KCl to activate neurons.

9. Diaminorhodamine-4M (DAR-4M)

Diaminorhodamine-4M (DAR-4M) AM is a fluorescent cell-permeable nitric oxide (NO) indicator with a lower detection limit of about 7 nM NO. DAR-4M AM is internalised through the action of esterases and reacts with NO, in the presence of O2, to form the corresponding fluorescent triazole compound in cell cytoplasm. This irreversible reaction leads to an increase by 840-fold of the fluorescence intensity of the dye. DAR-4M maximum wavelengths for excitation/emission fluorescence are ~560-575 nm. DAR-4M AM is reported to have greater NO specificity, better photo-stability, lower cytotoxicity and pH-sensitivity than earlier fluorescein-based NO probes (Kojima and Nagano, 2000; Kojima et al., 2001). DAR-4M AM excitation and emission fluorescence wavelengths are also higher than previously used compounds, allowing for the restriction of any confounding effects from cellular auto-fluorescence and the removal of the UV excitation-associated cytotoxicity.

Experimental protocol:

Live cells are loaded for 40 minutes with 10 μM of DAR-4M in recording buffer in the dark, at room temperature, after rinsing with PBS. The dye is removed and cells placed in fresh recording buffer for imaging. Fluorescence of the dye is excited with the 561 nm laser and dye fluorescence emission filtered with the 483-621 nm filter. Images are captured on a Zeiss inverted confocal with 3 z-stacks covering the complete depth of the cells recorded per well. Then time-series of one image every 5-10 seconds are captured. Baseline is recorded for about 3 minutes prior to the addition of 25mM L-Arginine to activate NO production as a necessary NOS substrate and cells are further imaged for 2-3 minutes in their activated form.

10. Sytox Green

Sytox Green is a low fluorescence, non-cell permeable dye, with a high infinity for nucleic acid. Upon loss of cell membrane integrity with cell death, the dye is able to enter dead cells and bind to the accessible nucleic acid, binding which increases its fluorescence intensity by 500-fold. Sytox Green fluorescence excitation/emission maxima are 504/523 nm when bound to DNA, making it possible to associate with Hoechst (350⁄461 excitation/emission maxima) to mark all the cell nuclei in

experimental sample. The dye excitation spectrum allows for the use of an Argon laser (488nm) in its imaging protocol.

Experimental protocol:

Live cells are incubated for 15 minutes with 250 nM Sytox Green and 10nM Hoechst diluted in N2B27 media at 37 degree 5%CO2 in incubator. Media and dyes are rinsed with PBS and cells are placed in recording buffer for imaging experiment. Image acquisition is performed on a Zeiss Confocal Inverted 880 with 20X lens. Acquisition consisted in 5 z-stacks for each well, two wells per line at the neuronal stage. Areas for imaging are selected at random at the centre of and all around the well using Hoeschst staining to locate cells nuclei.

VIII. Immunocytochemistry (ICC)

Immunocytochemistry (ICC) relies on the use of antibodies raised against a specific protein (or part of the protein) associated directly or indirectly with fluorescence markers allowing for the localisation of that protein within the different cell compartments. The antibodies used in this thesis are either monoclonal or polyclonal and the signal is amplified by the use of secondary antibodies conjugated to Alexa fluorophores. DAPI is used to stain the nuclei acids of cell nuclei for the easy localisation for imaging and counting of the cells for analysis.

Experimental protocol:

Cells destined for ICC are plated in either 8-wells ibidi chambers or over glass coverslips (13mm diameter, 0.1), both compatible with the use of confocal microscopes. Cells are first fixed using a solution of 4% paraformaldehyde (PFA) diluted in PBS for 20-30 minutes at room temperature. PFA is removed by several rinses with PBS and cells can be kept covered with PBS at 4°C in sealed plates until staining. Cells are first permeabilised in a solution of 0.2% Triton-X-100, 3% bovine serum albumin (BSA) in PBS for one hour at room temperature before being incubated with primary antibodies diluted to the appropriate concentration in PBS 3% BSA for 1 hour at room temperature or overnight at 4°C (Table 10). Primary antibodies are washed thrice for 5 minutes with PBS 3% BSA prior to incubation with fluorophore-

conjugated secondary antibodies, each diluted 1:500 in PBS 3% BSA, for an hour at room temperature in the dark. Secondary antibodies are rinsed thrice for 5 minutes in PBS with the last wash containing 10 μM DAPI for cell nuclei staining. Finally DAPI is rinsed off of all wells or coverslips and these are placed in PBS until mounting (coverslips) or directly for imaging (ibidi).

Name	**Species**	**Directed against**	**Company**	**Dilution ratio**	**Cat N#**
DAT	Rat	Anti-DAT	Sigma	1:200	142319121
FOXA2	Goat	Anti-HNF-3B	Bio-techne	1:100	AF2400
GCH1	Rabbit	Anti-*GCH1*-N-ter	Abcam	1:100	ab186633
GCH1	Rabbit	Anti-*GCH1*	Abcam	1:250	ab69962
GFAP	Chicken	Anti-GFAP	Abcam	1:500	ab4674
GIRK2	Goat	Anti-KCNJ6 / GIRK2	Sigma	1:250	ab65096
Ki67	Mouse	Anti-Ki-67	BD Bioscience	1:500	550609
LMX1A	Rabbit	Anti-LMX1A-C-terminal	Abcam	1:500	ab139726
OCT4	Goat	Anti-Oct3/4	R&D Biosystems	1:250	AF1759
PAX6	Goat	Anti-PAX6	Abcam	1:100	ab62803
TH	Chicken	Anti-Tyrosine-Hydroxylase	Abcam	1:250	ab76442
Tuj1	Rabbit	Anti-beta III Tubulin	Abcam	1:500	ab18207

Table 10: Origin and usage of primary antibodies for immunocytochemistry

Image acquisition is performed using an inverted confocal microscope (Zeiss). For each well or coverslip, 3-5 areas representative of cell density were selected randomly using DAPI 405nm channel. Snapshots were taken when cells are found in a single layer; z-stacks were used for capturing several layers of cells when necessary.

IX. Imaging machinery

1. Inverted confocal microscopes

Inverted confocal microscopes used in this project include several Zeiss models. Imaging with these microscopes relies on common principles of laser scanning confocal microscopy: lasers with specific wavelengths are used as excitation source; their rays are passed through excitation pinhole and filters and reflected on a dichromatic mirror through the objective and to the sample where it can excite the sample at specific focal planes. Excitation light wavelength is converted to emission light wavelength by wavelength-specific fluorophores present in the sample and reflected back through the lens and dichromatic mirror and to the camera or eyepiece through a pinhole (Sanderson et al., 2014, Zeiss Microscopy Online Campus website) (Figure 15). Focal planes images are obtained with the use of a pinhole which only allows light from an object in focus to pass through and reach the detector, in this application a photomultiplier, while light emitted from objects out of focus is defocused at the pinhole and barely passes to the detector. Images are obtained through the raster-scanning of the samples using all wavelengths befitting each application.

All experiments on fibroblasts were performed on the LSM 710 (Zeiss) without gas and temperature chamber. Experiments on iPSC-derived cell models made use of LSM 710, LSM 780 and LSM 880 with Airy Scan (Zeiss), in temperature-controlled environment set at 37°C.

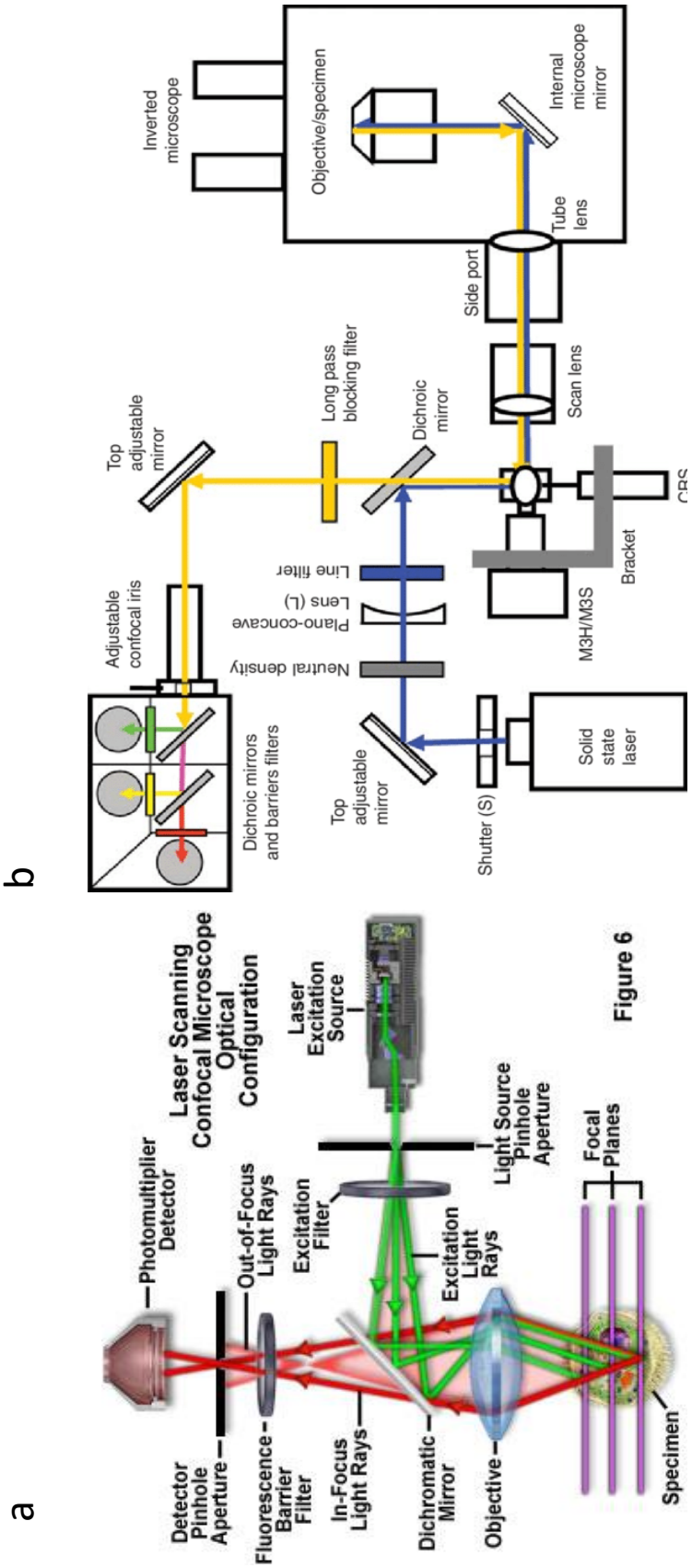

Figure 15: Principle of confocal microscopy. (a) general principle of laser-based confocal microscopy extracted from (http://zeiss-campus.magnet.fsu.edu/articles/livecellimaging/techniques.html); (b) inverted confocal setup allowing for live-imaging of cells in culture plates. Extracted from Sanderson et al., 2014.

2. Bespoke Andor camera fitted microscope

Live-cell imaging experiments for superoxide production and calcium-based imaging, using ratiometric dyes, make use of a bespoke Andor microscope composed of a Cairn xenon arc light source and Optoscan monochromator (Cairn), associated with an Optiscan II stage system and custom filter wheel (Prior Scientific), and an Andor sCMOS camera (Oxford instruments). The microscope relies on the use of a xenon arc lamp, which light is filtered through a monochromator to illuminate sample at a specific wavelength for excitation. The emission light from the specifically excited fluorophores passes through an emission filter to reach a cooled, sensitive camera allowing for the fast imaging of whole fields of cells while minimizing phototoxicity for the sample. Through the ability to rapidly change light excitation and emission filters with automated wheels, and the ability of the camera to acquire frames at an extremely rapid rate and of large fields of view, it is ideal for the measurement of ratiometric dyes in dynamic setups (Andor – Oxford instruments website).
As so, images are obtained much faster (~30 frames per second) than on a confocal microscope which often requires several seconds per acquisition frame, and suitable when confocal plane resolution and high spatial resolution of the sample are not required for analysis (Zeiss Microscopy Online Campus website).

X. Image analysis

Image analysis throughout this thesis makes use of commonly used image analysis softwares and scripts are written to automatize some analyses based on specific needs.

1. Data extraction from images

For all the images obtained on the bespoke Andor camera fitted microscope (Cairn), which is superoxide production (DHE) and calcium imaging (FURA2) experiments, image format necessitates the use of AndoriQ (Andor) for the extraction of data from the images. In DHE experiments, cell nuclei are manually selected and these regions of interest (ROIs) used for the extraction of localised 380nm and 530nm fluorescence in both fibroblasts and neuronal cells; overall 530nm emission fluorescence after background thresholding is obtained at the NPC stage as nuclei are not distinguishable.

In FURA-2 experiments, cell somas with a reaction to any stimulus are manually selected (ROIs) and total number of cells in the field recorded. In both cases data is then extracted from AndoriQ in a format compatible with Origin software (OriginLabs).

For all the other images obtained on Zeiss confocal microscopes (TMRM, mCB, MitoROS, Bodipy, DAR-4M, SytoxGreen and ICC), data extraction uses Fiji (ImageJ) with either manual or automatized methods.
For all z-stacks experiments (TMRM, mCB, and basal DAR-4M), an automatized script is used for the rapid analysis of the large number of files. The 'macro' on Fiji (ImageJ) goes as follows: each file is opened and checked against a determined path name, maximum intensity projection is performed, channels are split and only the fluorescence channels are kept. For each, thresholding is applied using the defined threshold option using values manually determined on control wells for each set of experiments.

For time-lapse experiments (DAR-4M continous, Bodipy and MitoROS) data extraction uses another automated script as follows: each file is opened and checked against a determined path name, channels are split for bodipy experiments only, and thresholding is applied using the defined threshold option using value manually determined on control wells for each set of experiments.

Analysis of the ICC images required manual counting due to the high confluency of cultures, forbidding the script-based imaging software such as Fiji or CellProfiler. At all stages, total number of nuclei in the field is determined with DAPI staining. Number of nuclei co-staining for other markers is noted. Cytoplasmic staining is assigned to a nucleus and the number of cells expressing a cytoplasmic protein of interest also noted.

2. Data analysis with Origin

Data analysis, plots and statistical comparisons between cell groups are obtained with Origin software (OriginLabs).

For all time-lapse experiments, results for the fluorescence intensity are plotted against time and a linear regression is ran to determine the rate of change in fluorescence which correlates to the corresponding biological function. Linear regressions in Origin make use of the weighted least-square method to fit a linear model function to the data. Extracted linear regression data is tabulated and the software used to normalise values and compare measurements statistically.

For DAR-4M experiments, the software is used to determine the average fluorescence prior to the L-Arginine stimulation and the difference between the peak of activation after stimulation and average baseline calculated. These as well as the complete-cell baseline values obtained by z-stacks are plotted separately.

For z-stacks and ICC experiments, data is entered, statistically tested and plotted using Origin (OriginLabs). All results correspond to the proportion of cells expressing each marker out of the complete number of cells in the field, these are compared between groups (with n = field).

Chapter 3: Genetic investigation of GCH1 and BH4 pathway in PD

I. Background

The role of genetic variants in the development of Parkinson's disease (PD) has been extensively investigated in the past decades, with the description of causative mutations inherited following a Mendelian pattern, as well as that of numerous variants increasing the risk for individuals to develop the pathology in their lifetime. One gene in which variants have recently been defined as a PD risk factor is GTP cyclohydrolase 1 (*GCH1;* 14q22.1-q22.2; OMIM 600225). *GCH1* encodes GTPCH, the enzyme controlling the first and rate-limiting step of the biosynthesis of tetrahydrobiopterin (BH4). BH4 is the essential cofactor for the activity of tyrosine hydroxylase (TH) in the rate-limiting step of production of dopamine in nigrostriatal cells (Kurian et al., 2011) (Figure 6). Mutations in *GCH1* were first described as the most common cause of dopa-responsive dystonia (DRD), a progressive hereditary form of dystonia that typically presents in childhood, marked by diurnal fluctuation, and having an excellent and sustained response to low doses of oral L-DOPA, generally free of side-effects (Ichinose et al., 1994; Segawa et al., 1976; Trender-Gerhard et al., 2009). The mapping of the DRD locus to chromosome 14q (Nygaard et al., 1993) and the subsequent signal association to the GTP cyclohydrolase gene (*GCH1* - 14q22.1-q22.2) (Ichinose et al., 1994), has since allowed the discovery of about 220 different mutations in that gene, listed in the Human Gene Mutation Database (HGMD) (Stenson et al., 2013).

1. Circumstantial genetic evidence and negative studies

The existence of a hereditary link between PD and DRD is hinted at through the informal description of a history of Parkinsonism in 14% of first degree relatives over 40years of age, in a series of 21 consecutive North-American DRD probands (Nygaard, 1993). This estimate is significantly higher than the prevalence of PD in the general North-American population and for a similar age band (0.6%, $p<0.05$). Moreover, these family members affected with PD mainly presented with a typical late-onset form of the pathology, mostly without history of childhood dystonia, and a mild response to levodopa treatment (Nygaard, 1993). This followed several

descriptions of PD cases in DRD proband's pedigrees: first in 1990, Nygaard and colleagues described a large North-American family pedigree with 96 family members, of which 10 were diagnosed with definite dystonia and 5 definite parkinsonian presentations; second in 1992, studying 29 relatives in another North American family from English descent revealed 3 parkinsonian subjects (AAO 50, 67 and 78) and 5 DRD subjects (AAO 5, 5, 6, 9 and 36y). Thus, these two studies give estimates of 15% and 10% for family history of PD in single DRD proband families (Nygaard et al., 1990, 1992). Estimates were even higher in a subsequent study where 35% (8/23) of unrelated DRD patients reported a positive family history for PD (Hagenah et al., 2005).

Furthermore, linkage analysis of *GCH1* variants in some 'DRD-PD' families found segregation of these mutations with both pathologies, of which: a PD patient (AAO 47y), whose sister is also affected by PD, had one neurologically normal niece and one niece who had been diagnosed with DRD around 13 years old. All affected family members were carriers of a heterozygous IVS3+1G>A mutation affecting the splice donor site of intron 3 leading to skipping of exon 3 and resulting in aberrant mRNA (Irie et al., 2011) (
Figure 16 - Family 1); a 65yo woman with PD (AAO 50years) and her daughter with DRD (AAO in teenage years) both had complete deletion of *GCH1* on one allele as determined by MLPA (Eggers et al., 2012) (
Figure 16 - Family 2); screening of 12 family members with phenotypes ranging from typical DRD to slow-progressing PD using Sanger and MLPA for several common PD genes and *GCH1* revealed the presence of a novel c.5A>G *GCH1* mutation in all affected individuals (both PD and DRD) which was absent in one 80 years old unaffected relative and one 75 years old relative with isolated rest tremor non-responsive to L-dopa treatment (Lewthwaite et al., 2015) (
Figure 16 - Family 3). Moreover, Mencacci and colleagues have previously described four 'DRD-PD' families in which 4 different mutations segregated with the phenotypes (Mencacci et al., 2014) (
Figure 16 - Families 4-7). The first proband presented with DRD onset at 18 months with their father being affected by DRD with no signs of PD at the age of 42. The proband's grandfather on his father's side was diagnosed with a successfully levodopa-

treated PD at age 59, with no sign of dystonia. All affected members of the family are heterozygous carriers of a c.343+5C>G mutation in *GCH1*, a mutation previously described in a couple of compound heterozygous advanced cases of DRD (Bandmann et al., 1996a; Trender-Gerhard et al., 2009) (
Figure 16 - Family 4). Another mutation previously described in DRD cases, c.626+1C>G, was found in two sisters from a second family, one with childhood onset DRD, the other with PD onset at 44 years. This mutation was previously associated with DRD cases (Garavaglia et al., 2004) (
Figure 16 - Family 5). Both c.343+5C>G and c.646+1C>G are believed to affect the splicing of *GCH1* mRNA. The remaining two families demonstrate segregation with compound heterozygous mutations in *GCH1*, associating a relatively common SNP to a more deleterious mutation. One proband presented with DRD onset at 11 years associated with a relatively common *GCH1* polymorphism P23L (carried by 1-2% population), her mother also carried this polymorphism as well as a DRD-associated mutation, F104L, and presented with an atypical parkinsonian syndrome with no tremor; this second variant was inherited from the proband's grandmother who presented with oromandibular dystonia at 66 years of age, classified as DRD although she refused a levodopa trial (
Figure 16 - Family 6). The other proband is a 41 years old woman who presented with DRD with bilateral foot inversion onset at 4 years of age. Her father has a one year history of typical parkinsonism at 67 years old. Both carry the R241Q *GCH1* mutation, a newly described variant predicted deleterious using in silico tools. The proband is a compound heterozygous carrier and inherited the V204I missense variant from an asymptomatic mother (Mencacci et al., 2014) (
Figure 16 - Family 7) . An overview of these studies can be found in Table 11&Table 12.

Due to the relatively common prevalence of PD in the general population (about 1% of individuals over the age of 50 in Europe), further evidence for the association of *GCH1* mutations with PD are necessary. In the first instance, investigations made use of small cohorts, and as a result failed to show a significant association between rare *GCH1* variants and sporadic PD. They are compiled in Supplementary Material Table 30. These negative studies had three major caveats: the small size of cohorts limiting

power, patient selection bias and selective sequencing of a limited number of variants. The first two caveats were reflected in several studies with either 29 familial PD with akinetic-rigid presentation (Bandmann et al., 1996b); 53 familial early-onset PD (Cobb et al., 2009); 87 early-onset PD (Hertz et al., 2006); and 97 sporadic late-onset PD, 28 early-onset PD and 9 familial PD from Southern Spain (Bandrés-Ciga et al., 2016). The last caveat generally applies to larger cohorts in which limited sequencing convey technical benefits: sequencing the 5 *GCH1* SNPs of the 'pain-protective' haplotype which is associated with lower *GCH1* expression in 233 dystonia cases, 1337 PD cases and 1090 relatively old controls found no significant association of these SNPs with the risk for PD ($p>0.05$) (Newman et al., 2014). Another study limited to the sequencing of a single *GCH1* SNP (rs11158026) in 589 sporadic PD and 634 controls from the Han Chinese population also failed to associate this SNP with PD in their cohort (Yang et al., 2017). Since a much larger number of *GCH1* variants have been associated with both DRD and PD phenotypes, this type of approach is reducing analysis power and increasing the likelihood of false-negative results.

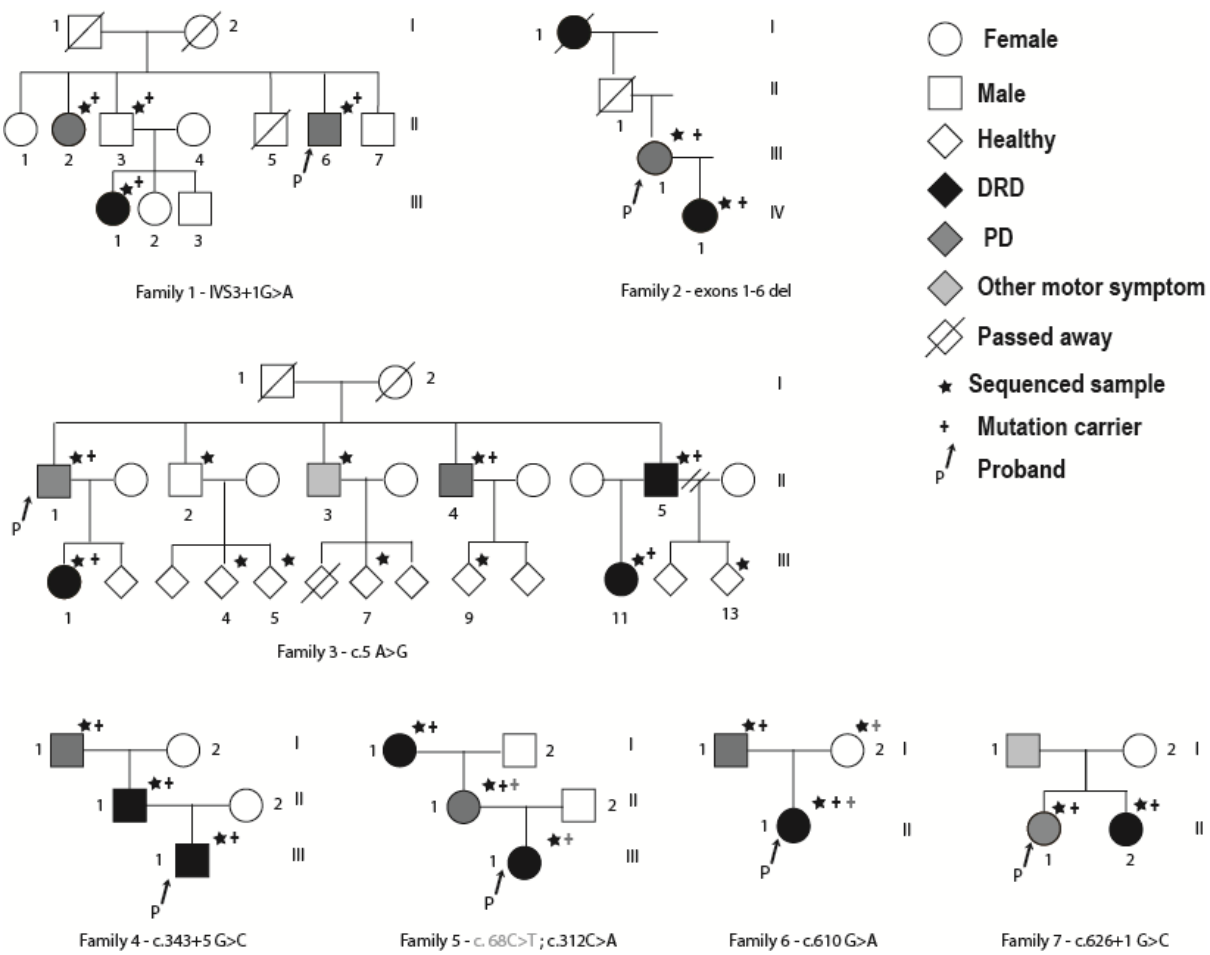

Figure 16: Pedigrees of DRD-PD families carrying *GCH1* mutations. DRD patients are in black, PD patients in dark grey and family members with motor symptom different from both pathologies in light grey. Probands are marked with a P, sequenced individuals by a star and carriers by a cross. Associated mutations are identified under each pedigree.

Reference	Study Type	N cases	N controls	Complete cohort	Conclusions	Comments
Nygaard et al., 1990	Large family pedigree	10 DRD 5 PD	81 family members	96 relatives from one family	10.5% DRD 5.2% PD	One family
Nygaard et al., 1992	Large family pedigree	5 DRD 3 PD	21 family members	29 relatives from one family	17.2% DRD 10.9% PD	One family
Nygaard, 1993	Self-report of PD family history in first degree relatives	21 unrelated DRD patients	-	21 consecutive North-American unrelated DRD patients	14% first degree relative ≥ 40y.o. with PD	Found to be typical PD phenotype subsequently

Hagenah et al., 2005	Self-report of PD family history	23 unrelated DRD patients	-	23 consecutive unrelated DRD patients of various descent	35% PD family history	*GCH1* mutation and its consequence identified in 87% of DRD patients

Table 11: Literature review circumstantial evidence: family history of PD in DRD patients

There always remains the possibility of the existence of population effects on the association of specific *GCH1* variants with risk for PD as possibly seen in large cohorts. In a Swedish/Norwegian cohort of 509 PD patients and 230 controls, no deleterious mutations but only putative benign variants (p.P23L and p.P69L) were identified in *GCH1* by deep targeted-sequencing (Rengmark et al., 2016). This may point at a population effect with a specifically low *GCH1* frequency in PD patients from Norway, limiting the power of even such a large cohort, or to a possible deleterious effect of these variants previously defined as 'benign' in this specific population. Finally, the authors report coverage gaps which may me masking mutations in their cohort.

Family	Reference	Pedigree description	Conclusions	Comments
1	Irie et al., 2011	PD proband and DRD affected niece	All affected family members carry c.IVS3+1G>A *GCH1* mutation	Predicted exon 3 skipping
2	Eggers et al., 2012	PD proband and DRD affected daughter	Complete heterozygous deletion of *GCH1*	Detected by MLPA
3	Lewthwaite et al., 2015	12 family members: 2 EOPD, 1 PD, 3 DRD (see pedigree for details)	Segregation of heterozygous c.5A>G *GCH1* mutation in all affected members	Absence of mutation in unaffected relative
4	Mencacci et al., 2014	DRD proband, his DRD	Segregation of heterozygous	Mutation previously

		affected father and PD affected grand-father	c.343+5C>G *GCH1* mutation	described in compound heterozygous DRD cases
5		PD proband with a DRD affected sister	Both carry the c.646+1C>G *GCH1* mutation	Mutation previously described in DRD cases
6		DRD proband, her PD affected mother and DRD affected grand-mother	Proband carries p.P23L *GCH1* mutation, mother is compound heterozygote p.F104L/p.P23L *GCH1* carrier and grand-mother p.F104L *GCH1* heterozygous carrier	p.P23L is a common polymorphism carried by 1-2% of the population
7		DRD proband with PD affected father and asymptomatic mother	Proband is compound heterozygous for p.R241Q/p.V204I; father heterozygous p.R241Q carrier and asymptomatic mother heterozygous p.V204I carrier	p.R241Q was newly described here and predicted deleterious in silico

Table 12: Literature review circumstantial evidence: *GCH1* mutation linkage analysis in PD-DRD families. Family number corresponds to pedigree numbers in

Figure **16**.

2. Strong support for a genetic association

These caveats were circumvented in the first place by the use of larger sporadic PD cohorts and by the advent of next-generation sequencing techniques (NGS) allowing for easier detection of point mutations in these large patients cohorts. An overview of these studies can be found in Table 13.

Separate studies using NGS methods have supported an association of deleterious *GCH1* variants with higher risk of developing neurodegenerative PD. First, in a whole-exome sequencing cohort of 1318 unrelated PD cases and 5935 controls, where the frequency of *GCH1* variants was found significantly higher in PD cases (0.75%) than in controls (0.1%; OR = 7.5; 95% CI 2.4-25.3) (Mencacci et al., 2014). Secondly this association was supported by a meta-analysis of GWAS data using a common set of 7,893,274 variants across 13,708 cases and 95,282 controls with the characterisation of *GCH1* as a low-risk susceptibility locus for PD (OR = 0.889, $p = 7.13x10^{-11}$). The

result replicated in a separate cohort of 5,353 cases and 5,551 controls (OR = 0.948, p = 0.039) and the overall OR of 0.9 ($p = 5.85x10^{-11}$) was eventually associated with one SNP (rs11158026; MAF=0.335) (Nalls et al., 2014). Further validation of *GCH1* mutants association with risk of PD was through another GWAS including 6,476 PD cases and 302,042 controls (OR=0.90, $p=2.65x10^{-7}$), where risk was associated with the same SNP (rs11158026) (Chang et al., 2017). The importance of this single SNP within *GCH1* in risk of PD was further investigated in a Taiwanese population of 598 PD patients and 553 control subjects. In this non-European cohort, the minor allele frequency for rs11158026 is significantly higher in PD patients compared to controls (OR = 1.29, 95% confidence interval (CI) = 1.09- 1.52, p = 0.003) (Chen et al., 2016). Further, the association of rs11158026 with PD was validated in another non-European cohort of 600 sporadic late-onset PD and 1200 unrelated healthy controls from Iran (p=0.025, OR = 1.17, 95%CI = 1.02–1.34) (Safaralizadeh et al., 2016). Finally, a follow-up meta-analysis of 5 studies screening East-Asian population, with a total of 5588 PD cases and 5876 controls suggested an association of the rs11158026 *GCH1* variant with PD in these populations (p = 0.04, OR 1.08, 95% CI 1.00e1.16) (Zou et al., 2018).

Reference	**Study Type**	**Cohort**	**Results**	**Conclusions**
Mencacci et al., 2014	Whole exome cohort	1,318 unrelated PD 5,935 controls (European cohort)	0.75% *GCH1* in PD, 0.1% mutants in controls. p = 0.003 OR = 7.5. 95%CI = 2.4-25.3	Significantly higher *GCH1* mutation frequency in cases than controls
Nalls et al., 2014	GWAS meta-analysis	13,708 PD 95,282 controls	$p = 7.13x10^{-11}$ OR = 0.889	*GCH1* is a low-PD susceptibility locus
	GWAS replication cohort	5,353 PD 5,551 controls	p = 0.039 OR = 0.948	Validation in replication cohort

	Complete GWAS cohort	19,061 PD 100,833 controls	$p = 5.85x10^{-11}$ OR = 0.9 MAF=0.335	Overall association with rs11158026
Guella et al., 2015	Genet-targeted sequencing	526 PD 290 controls	*GCH1* variants frequency of 0.57% in PD and 0.3% in controls (benign only)	Similar to Mencacci et al., 2014 frequencies
Chen et al., 2016	Targeted SNPs sequencing cohort	598 PD cases 553 controls (Taiwanese cohort)	RS11158026 SNP (*GCH1*) P = 0.003 OR = 1.29 95% CI = 1.09-1.52	*GCH1* Rs11158026 association with PD in non-European cohort
Safaralizadeh et al., 2016	Targeted SNPs sequencing cohort	600 sporadic late-onset PD & 1,200 controls (Iranian cohort)	RS 11158026 *GCH1* SNP P = 0.025 OR = 1.17 95% CI = 1.02-1.34	*GCH1* Rs11158026 association with PD in non-European cohort
Chang et al., 2017	GWAS meta-analysis	6,476 PD 302,042 controls (European cohort)	Rs 11158026 *GCH1* SNP $P = 2.65x10^{-7}$ OR = 0.90 95% CI = 0.89-0.93	Validation of *GCH1* Rs11158026 association with PD in European cohort
Xu et al., 2017	*GCH1* exons sequencing using inverted molecular probes for high-throughput	1,758 PD 1,565 controls (Chinese cohort)	0.46% in PD and 0.06% in controls p = 0.04 OR = 7.15 95% CI = 0.94-58.64	Significantly higher *GCH1* mutation frequency in cases than controls
Zou et al., 2018	Sequencing studies meta-analysis	5,588 PD 5,876 control (Various East-Asian)	Rs11158026 *GCH1* SNP P = 0.04 OR = 1.08 95% CI = 1.00-1.16	*GCH1* Rs11158026 association with PD in non-European cohort

Table 13: Literature review definite genetic proof for *GCH1* association with risk for PD in large sporadic cohorts.

Using gene-targeted sequencing in relatively large cohorts, *GCH1* mutation frequencies were first found relatively consistent to that of the first Mencacci exome study in a cohort of 528 patients and 290 controls, with frequencies of 0.57% (3/528) and 0.3% (2/290) respectively (Guella et al., 2015). It is worth to note that the authors reported an absence of mutations in their controls as both variants found in this group are known benign *GCH1* polymorphisms (Guella et al., 2015). Additionally, using molecular inverted probes for high-throughput sequencing, Xu and colleagues were able to screen all exonic regions of *GCH1* in 1758 PD patients and 1565 healthy controls finding significantly different variant frequencies of 0.46% and 0.06% , respectively (OR=7.15, 95%CI=0.94-58.64; p=0.04). Of note, the single variant identified in one control sample was predicted to be benign (Xu et al., 2017). Using a similar approach for the sequencing of 1082 PD patients and 1110 controls, a separate team found overall higher *GCH1* variant frequencies of 1.02% and 1.44% respectively. Although variant frequency was higher in controls, all variants previously reported pathogenic were carried by cases and burden analysis of the presumed pathogenic variants using sequence kernel association test (SKAT) was significant, whilst similar analysis of all rare *GCH1* variants, defined as MAF < 0.01, was not statistically significant using the optimised SKAT (SKAT-O) package (Rudakou et al., 2018). In these studies, removing known benign variants from the analysis allowed a correction to the false-negative results, pointing at the potential necessity of such variant selection for calculating appropriate risk scores for *GCH1* variants. Following a similar method for all genes with rare deleterious but common benign polymorphism frequencies is warranted to increase the power of genetic analyses in relatively large cohorts.

3. Mechanisms of *GCH1* mutations

In dopaminergic neurons, *GCH1* is catalysing the rate-limiting step for the production of BH4, the essential cofactor of *TH* for the synthesis of dopamine. BH4 is also a coupler for the isoforms of nitric oxide synthase (Crabtree et al., 2009b; Kuzkaya et al., 2003), a strong antioxidant (Nakamura et al., 2000, 2001), and has a role in the maintenance of mitochondrial redox balance (Bailey et al., 2017). A handful of enzymes are directly involved in the 'dopamine-BH4 pathway', through their role in the production or maintenance of the BH4 pool, as well as in the production of

dopamine (Figure 6). Mutations in *TH* and sepiapterin reductase (*SPR*), two genes downstream from *GCH1*on the BH4 pathway, have been identified in a small proportion of DRD cases (Bartholomé and Lüdecke, 1997; Blau et al., 2001; Bonafé et al., 2001b; Bräutigam et al., 1998; Clot et al., 2009; Lüdecke et al., 1995, 1996). There is also some evidence for the involvement of *TH* in the risk for PD, probably through its direct role in dopamine synthesis. Mutations in *TH* are as frequent as *GCH1* mutations in sporadic PD cohorts (0.69%) (Rengmark et al., 2016). They have more commonly been described in cases of infant- or juvenile-PD (Bademci et al., 2010; Lüdecke et al., 1996; Swaans et al., 2000), although these may possibly be clinically misdiagnosed DRD cases.

I hypothesized that genes of the BH4-pathway, in addition to *GCH1*, may have a role in the risk for sporadic PD. Others have shown the involvement of BH4-pathway genes in DRD, resulting in the screening of a similar set of genes in a cohort of 64 DRD patients (Clot et al., 2009). Using targeted sequencing and MLPA, 47 (73.5%) of them were found to carry a heterozygous point mutation (n = 40 = 62.5%, of which 2 compound heterozygous mutations) or a large deletion (n=7 = 11%) in *GCH1*. Of the 17 patients not carrying a *GCH1* mutation, 14 were screened for *TH* and *SPR* mutations, with 4 patients (28.5% screened cohort; 4.7% overall cohort) carrying a point mutation in *TH* and 2 (14% screened cohort; 3% overall cohort) a mutation in *SPR* gene (Clot et al., 2009). This hints at a role for variants in other genes of the dopamine-BH4 pathway in DRD risk which may be translatable to PD as well. It is also important to note that the small cohort size of this study might be limiting its power and that the frequency of mutations in these genes may be underestimated in the DRD population.

4. The need and the difficulties of using a large exome dataset

Literature describing the role of *GCH1* variants in the risk for PD underlines the need for using large cohorts in an attempt to capture the effect of rare variants. Whole exome sequencing cohorts present the great advantage to capture genetic variations within the realm of the coding regions of our genome, unravelling mutations we are able to associate with potential deleterious changes in the corresponding protein. As opposed

to targeted gene or variant sequencing, this more comprehensive genetic sequence supports both the discovery of new variants and the consolidation of previously described genetic associations with strong confidence. They also provide a great advantage for a high-quality and precise analysis of the association of gene groups with specific phenotypes. However, while a good tool for genetic association research, building such sequencing cohorts can be extremely complex and time-consuming, from recruiting enough participants for both disease and control groups to analysing relevant variants after proceeding to the quality control of the data.

This chapter proposes to investigate the role of *GCH1* and associated genes of the dopamine-BH4 metabolic pathway in the genetic risk of PD through the use of a large exome cohort. This investigation makes use of a uniquely large whole-exome cohort of PD patients and controls obtained through the Parkinson's Disease Genetics Sequencing Consortium (PDGSC). I present the frequencies and types of mutations identified in the cohort, before detailing the quality control used to build a high quality sequencing dataset. I then make the case of the necessity to perform a pathway-driven quality control for more accurate analysis of the limited number of genes that constitute my pathway of interest and present the results of such a quality-control prior to discussing the role of these genes in the risk for PD in the cohort using burden and sequence kernel association tests. This final analysis is ran on the complete set of variants across all 8 genes found in the cohort, as well as all the variants found in the three genes most commonly associated with DRD and responsible for the de novo production of BH4 from GTP, namely *GCH1*, PTS and SPR. Variants are then separated into three groups on the base of their annotation.

II. Methods

1. Participants

The study includes 9588 samples, of which 3442 PD patients and 6146 controls. All cases and 763 controls were recruited by members of the Parkinson's Disease Genetics Sequencing Consortium (PDGSC), an international collaboration of investigators from academia, non-profit organizations and industry, aiming at unravelling genetic variants associated with PD risk. PD patients are clinically diagnosed according to the UK

Parkinson disease Society Brain Bank criteria (Hughes et al., 1992). Controls have no diagnosis of PD or any other movement disorder at the time of their sequencing. An additional 5383 control samples are obtained from the Alzheimer Disease Sequencing Project (ADSP) control cohort (dbGaP accession phs000572.v1.p1). Additional phenotypic information including sex, age at onset (cases) or last assessment (controls) and sequencing centre is collected for each participant. Recorded ethnicity for the ADSP control cohort is American (probably of European descent). Recorded ethnicity for the PDGSC cohort is variable between centres although mainly European (with German, Finnish, Norwegian, British, mixed European and American of European descent sub-groups).

2. Sequencing

Samples were obtained, processed and sequenced in each participating PDGSC recruiting centre using various Illumina chemistries (details per centre unavailable). ADSP control samples were sequenced by using a HiSeq 2000 platform (Illumina). All sequencing data are centralised at the NIH and first processed by Mike Nalls (Data Tecnica). FASTQ files are obtained from each PDGSC centre sample set and ADSP control samples are downloaded in the short read archive in the SRA's proprietary format, decrypted and then reformatted to FASTQ. Sequences are called following the Genome Analysis ToolKit (GATK v3.4) and Best Practices guidelines (Broad Institute). Briefly: PDGSC data are merged and aligned by chromosome at the GVCF stage in batches of 200 samples. They are then run through the HaplotypeCaller phase of the pipeline to generate a joint called VCF (Variant Called Format file). Variant calls and read-depths are calculated with GATK. The complete PDGSC exome dataset including all 9588 samples in a pre-quality control VCF, is uploaded to the GoogleCloud data storage for shared access for all PDGSC members.

3. PDGSC exome dataset quality control organisation

The quality control of the PDGSC dataset was carried out in collaboration between the NIH (Mike Nalls) and UCL (Demis Kia and myself). Collaboration with Merck industries provided an extra dataset which was analysed by John Eicher to inform the

selection of threshold for the different QC parameters of the PDGSC dataset. Author's contribution to the quality control consisted in active participation in the troubleshooting and decision making along the different step, and minor changes to the quality control script.

4. PDGSC exome dataset quality control

Sample pruning and principal component calculation and analysis (PCA) using the Hapmap dataset

The HapMap3 dataset is filtered to retain SNPs with MAF < 0.01 with Plink2 (Purcell et al., 2007; The International HapMap Consortium, 2005). In parallel the original PDGSC VCF is first annotated using VEP (variant effect predictor – Ensembl), and then filtered to remove all samples with missing genotype > 15%, and all samples with MAF > 0.01, call-rates < 90% and variants in Hardy-Weinberg disequilibrium ($p<0.001$ for Hardy-Weinberg equilibrium test). All SNPs found in the HapMap3 dataset are extracted from the filtered PDGSC SNP list and both datasets are merged using Plink2 resulting in the HapMap/PDGSC file. Palindromic SNPs are removed from the HapMap/PDGSC dataset using R. Linkage Disequilibrium Adjusted Kinships (LDAK) is used to thin these SNPs with threshold set as r2 > 0.2 in every 1000 kb window (Speed et al., 2012). Merged data is then pruned following an independent pairwise approach with window size of 200 base-pairs (bp), step size of 10 bp and pairwise r2 threshold > 0.2. Sex check and heterozygosity levels are run on these pruned variants and output analysed to establish threshold for ambiguous sex and heterozygosity level in these samples. Samples are excluded based on ambiguous sex ($0.35<F<0.65$) and unusual proportion of heterozygosity in the sample (<-0.07 and >0.125). Relatedness is calculated between each pair of samples and one sample for each pair with relatedness > 0.125 is removed (corresponding to second degree relatedness). The Plinkseq package is used to run i-stats and variants are excluded based on: number of non-reference genotypes (excluding NALT > 35,000 and NALT < 15,000), number of genotypes with minor allele per individual (excluding NMIN < 10,000), number of heterozygous genotypes for an individual (NHET < 5,000 and NHET > 25,000), total number of called variants for an individual (NVAR < 500,000), genotyping rate for an individual (RATE < 0.9), number of singleton per individual

(SING == 0 and SING > 500), mean quality for variants that have a non-reference phenotype in an individual as expressed by the QUAL variable in the original VCF (QUAL < 6,000,000), number of PASS'ing for which an individual has a non-reference genotype (PASS < 5,000) and mean Ti/Tv ratio for variants for which an individual has a non-reference genotype (TITV < 3.1) after viewing density plots. PCs are finally calculated for all remaining samples of the merged HapMap/PDGSC dataset using FlashPCA (Abraham and Inouye, 2014; Abraham et al., 2017). PCA plots are used to identify all samples from PDGSC dataset whose ancestry is not European to be removed as population outliers, with European ancestry being defined as PC ± 3SD from the HapMap European population group (CEU TSI) mean after visual inspection of PC1-2 plot.

Sample QC for the PDGSC dataset only

Using the original PDGSC VCF, all variants with MAF > 0.01, call-rates < 90%, Hardy-Weinberg disequilibrium ($p<0.001$) and variants with missing ids are removed. Remaining variants are pruned following an independent pairwise approach with window size of 50 bp, step size of 10 bp and pairwise r2 threshold > 0.2. Pruned variants are run through PlinkSeq and identical thresholds are used for exclusion: NALT > 35,000 and NALT < 15,000; NMIN < 10,000; NHET < 5,000 and NHET > 25,000; NVAR < 500,000; RATE < 0.9; SING == 0 and SING > 500; QUAL < 6,000,000; PASS < 5,000; TITV < 3.1. The remaining variants are used for sample QC.

X-chromosomes are split and sex-check run with Plink. Samples are removed based on sex-check 0.35 < F < 0.65. Heterozygosity check on Plink is used to remove outliers (<-0.07 and >0.125). Samples previously identified with a non-European ancestry using the HapMap/PDGSC PCA are removed. All samples with recorded age < 18 are removed as well. All remaining PDGSC data are run through Plink relatedness calculation and all samples with relatedness > 0.125 are excluded. A second estimation of relatedness using identity by descent (ibd) is used to ensure removal of all related or contaminated samples. Finally all sample removal lists are merged, duplicates removed and the list used to filter the original PDGSC VCF.

Variant QC for the PDGSC dataset only

The sample-QCed dataset is used for additional removal of poor quality variants, defined as: variants with MAF > 0.01; call-rate < 90%, hwe p < 0.001; missing id; call-rate < 85% in either cases or controls; mean depth < 15 in either cases or controls; monomorphic and multiallelic variants, star alleles (corresponding to incorrectly called insertion/deletion variants), as well as variants with extreme MAF (< 1% or > 99%) in one group and absent from the other. Differential missingness, characterised as the comparison of missing rate for each variants between cases and controls compared by Fisher exact test, with a threshold at p < 10e-25 can be added.

Final sample checks for coherence

Extra samples are excluded based on: contamination or lane-sweep using the freemix metric calculated with VerifyBAMId in GATK, Ti/Tv ratio which represents aggregate transition to transversion ratio to control for false positives (threshold of +/- 3SD) (that is outside of the 3.19-3.62 range), as well as cohorts containing too small number of samples and cohorts with abnormally high mean depth compared to all other cohorts as visualised on box-plots.

5. Investigating the BH4 pathway

Mutation frequency analysis in BH4 pathway

Frequency of BH4 pathway gene variants is first estimated in minimally QCed exome data. The gene intervals for *GCH1*, *TH*, *DDC*, *PTS*, *SPR*, *PCBD1*, *QDPR* and *DHFR* are extracted from the original PDGSC dataset VCF, prior to quality control. Insertions and deletions called mistakenly as multiple consecutive single base-pair variants or 'star alleles' are corrected. These arise when an intrinsic calling error had increased the number of variants by calling every base within insertions and deletions as a multitude of single variants. These occurrences are reduced to a single call per insertion/deletion by keeping the reference allele as the first upstream affected base. The remaining variants are extracted from the VEP annotated VCF files and run through SnpSift v4.1, a component of the SnpEff package (Cingolani et al., 2012a, 2012b). SnpSift calculates the number of heterozygous and homozygous variants as well as total number of alternative alleles in case and control groups separately. Fisher

exact tests for significant association of variants with disease phenotype are then calculated based on these values, using different genetic models: dominant, recessive, and allelic (based on allele counts). Co-dominant model uses Chi-Square distribution with two degrees of freedom giving a strict p-value; trend p-value is calculated following the same model with a Cochran-Armitage test (weighted method) (Cingolani et al., 2012b). Variants with a MAF > 0.01 in either cases or controls are removed. P-values are corrected for multiple comparison with the false discovery rate (FDR) correction using the p.adjust function in R (R Core Team, 2014) All variants identified in cases only are first analysed, followed by all other variants, with their in-silico predicted effect and previous association with either DRD or PD discussed based on a literature search. For all variants, complete dataset Annovar annotated files and Ensembl website are queried to complete all missing information.

BH4-pathway based QC

The original PDGSC VCF is used to proceed to a pathway-based QC. Multi-allelic variants are removed as they are over-represented in this sample, probably due to the multi-site nature of the sequencing step of the dataset. 'Star alleles' calling insertions and deletions as a multitude of point mutations due to an intrinsic error of the base calling process are corrected. Together, these represent 126,183 variants across the whole exome set.

After these first exclusions, mean depth and number of genotyped sites are calculated for each sample across our variant set using depth matrices established on the entire sequencing dataset. Both mean depth and number of genotyped sites are plotted against study centre of origin for each sample and samples from outlier centres removed. In the remaining sample, participants for which less than 75% of the BH4-pathway sites are covered by sequencing (call-rate < 0.75) or for which mean depth across genotyped sites was inferior to 15 are removed. The distribution of mean-depth and number of sequenced sites across the genes of interest pre- and post-sample quality control steps are compared visually.

After removal of unsuitable samples, sequencing information for remaining samples at the sites of interest is extracted from the original VCF, and used to calculate Hardy-

Weinberg disequilibrium, and MAF and mean-depth at each position cases and controls groups separately. Welch t-test for unequal variances and Wilcoxon rank t-test are used to evaluate the statistical significance of differential depth between phenotype groups calculated based on mean-depth values. Variants are removed as: MAF = 0 in cases or controls and MAF ≥ 0.01 in the other group; MAF = 1 in one group and MAF <= 0.99 in the other; monomorphic variants for which frequency counts in the cohort are equal to 0 for either reference or alternative allele. Finally, differential missingness between case and control groups is calculated based on number of genotyped sites for the remaining variants, and all variants with p < 5e-25 as estimated with either Welch or Wilcoxon corrected t-tests are excluded from further analysis.

Burden analyses – defining covariates

PCs are calculated for each sample based on a high-quality set of variants after the removal of variants and samples based on: differential missingness and/or differential depth between cases and controls t-test p-values > 10.e-25; MAF < 0.05, missing call rates > 0.05, hardy-weinberg equilibrium exact test p-value < 1e-5; star alleles. These 'high quality' variants are then pruned using standard thresholds (50bp windows, increments of 5bp and pairwise r2 threshold < 0.5) after ranges of human genome containing large LD blocks, as defined in the flashpca package, are removed from the dataset. Flashpca is then implemented with recommended settings as per package developer instructions to calculate the first 5 principal components (PC) of the cohort (Abraham and Inouye, 2014; Abraham et al., 2017). Other covariates include information recorded at inclusion of samples in the PDGSC cohort such as age, sex and study-group; as well as values for mean-depth and n-sites calculated during the pathway-based QC steps.

Pathway-based burden analysis

Samples and variants remaining from the pathway-based QC step are extracted from the original VCF and annotated with ANNOVAR (Wang et al., 2010). Annotation-based grouping defines three variants groups: loss-of-function, non-synonymous, and cadd. The loss of function group includes variants annotated as: "stopgain", "stoploss",

“frameshift insertion”, “frameshift deletion” and “splicing”. The non-synonymous group includes variants annotated as: “nonsynonymous SNV”, “stopgain”, “stoploss”, “frameshift insertion”, “frameshift deletion”, “nonframeshift insertion” and “nonframeshift deletion”. The CADD group only includes variants with a CADD13_PHRED score ≥ 12.37, which are estimated to represent the 2-3% of the most damaging variants in the genome (Kircher et al., 2014).

These variants groups, as well as the complete set of variants of the BH4-Dopamine pathway post pathway-based QC and the three genes in which variants are involved in DRD risk group (BH4_synthesis group - including *GCH1*, *PTS* and *SPR*), are used to run burden and association tests using the rvtest package. Burden tests include the combined multivariate and collapsing (CMC) method, Zeggini test and Madsen-Browning (MB) test. Association tests include the variable threshold (VT) Price method and the optimal unified sequence kernel association test (SKAT-O). All these tests are run on all variants with MAF ≤ 0.01. Burden and kernel tests are run with the use of covariates to reduce bias inherent to the structure of the dataset: 5 first PCs, sex, age, number of genotyped sites for each sample, mean depth for each variant and study centre. As to date, rvtest has not implemented the use of covariates for the VT Price test.

Three separate research questions are evaluated with rvtest: do all variants in the BH4-dopamine pathway have an effect on the risk for PD in the cohort with no regard to the direction of their effect? Do the genes in which variants have previously been involved in risk for DRD have an effect on this risk? And does a specific annotation-based sub-group of variants have an influence on this risk? Tests p-values associated to each of these research questions are corrected using the false discovery rate (FDR) approach with adjusted p-values calculated with the p.adjust command on R (R Core Team, 2014).

III. Results

1. PDGSC QC full dataset

The original pre-QC PDGSC dataset includes 1,812,821 variants across 9588 samples (3410 PD patients and 6144 controls) (Table 14). This comprises of roughly equal proportions between sexes (4783 males and 4771 females). To mitigate the effect of population stratification associated to ancestry in the cohort, we first visualise the distribution of the PDGSC samples across the different population subsets of the HapMap project (The International HapMap Consortium, 2005) using the plotting of the two first principal components (PCs) calculated based on common variants of the PDGSC/HapMap datasets (Figure 17&Figure 18). As can be observed in Figure 18a,b,e, the majority of the PDGSC samples co-localise with European ancestry samples from the HapMap populations based on PC plotting. A few samples from the PDGSC dataset rather align with PC plots for African and Asian ancestry (Figure 18c-d) and are excluded from the sample list in order to control for population stratification. Chosen cut-off is for PCA ±3SD from CEU TSI mean which leads to the removal of 317 samples (3.3%).

Variant-level QC reduces the PDGSC dataset from 1,812,821 in the original VCF to 938,385 variants in the post-QC PDGSC dataset (52% of all variants remaining). QC exclusion lists are as follows n (% total variants in original dataset): mean depth in controls < 15 removes 59,192 (3%) variants; mean depth in cases < 15 removes 54,774 (3%) variants; call-rate in controls < 0.85 removes 288,892 (16%) variants; call-rate in cases < 0.85 removes 284,859 (16%) variants; multiallelic sites represent 126,183 (7%) variants; monomorphic variants remove another 430,265 (24%) variants and alleles corresponding to an error in variant call leading to variant being called by a star 81,165 (4%) variants. Once variants flagged by two or more of these thresholds are reduced to one occurrence, 874,436 variants are removed as part of the QC (i.e. 48% of original total number of variants) (Table 15).

Study	N controls	N PD cases	Total n Samples
ADSP	5382	0	5382
Baylor	0	105	105
Cambridge	0	28	28
DZNE	36	121	157
IPDGC	416	907	1323
Luebeck	0	40	40
Majamaa	0	235	235
Mayoclinic	0	24	24
Munichneuro	0	71	71
Oslo	0	55	55
Oxford	1	228	229
PPMI	178	395	573
Tuebingen	1	92	93
Ucl	0	515	515
UCL	24	373	397
Umiami	106	84	190
Vienna	0	137	137
All	**6144**	**3410**	**8614**

Table 14: Original PDGSC dataset structure pre-QC. Numbers of controls, cases and total number are defined by cohort of the PDGSC dataset.

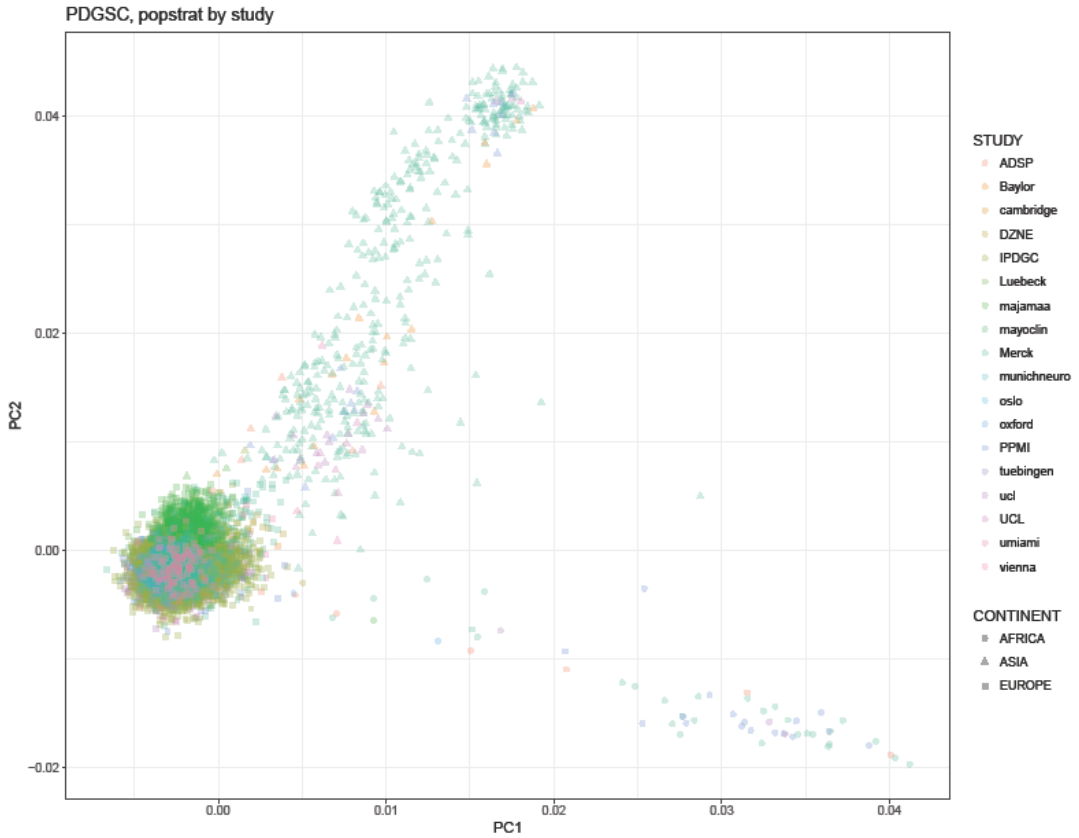

Figure 17: Principal components analysis of the pre-QC PDGSC dataset. Most of the cohort overlaps with the European population markers for first two PCs. Colours represent the different cohorts within PDGSC. Shapes represent samples ancestry continents (Africa = square; Asia = triangle; Europe = circles). Plot courtesy of Demis Kia.

Variant QC	**QC Threshold**	**Exclusion n (%)**
Mean depth	< 15 in controls < 15 in cases	59,192 (3%) 54,774 (3%)
Call-rate	< 0.85 in controls < 0.85 in cases	288,892 (16%) 284,859 (16%)
Multiallelic sites		126,183 (7%)
Monomorphic variants		430,265 (24%)
Star alleles	Error call indel	81,165 (4%)
TOTAL	Single variants removed	**874,436 (48%)**
Post-QC	**Remaining**	**938,385 (52%)**

Table 15: PDGSC full-dataset variant QC metrics. Parameters, thresholds and resulting exclusion numbers and percentage from pre-QC dataset for the different steps of the variant-level QC are presented.

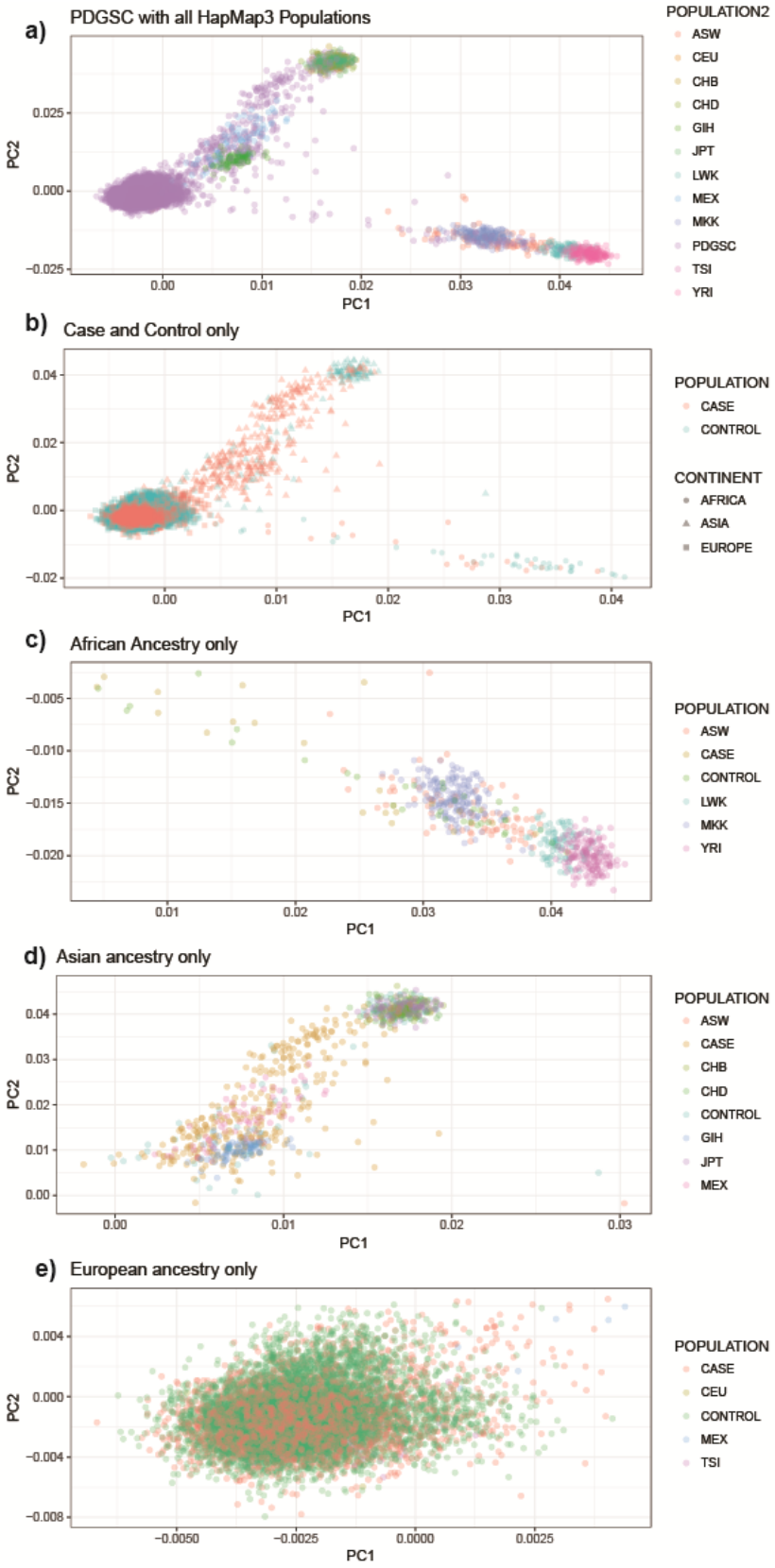

Figure 18: Principal components analysis of the pre-QC dataset. The first two principal components are plotted as: all PDGSC samples as a population alongside other populations from HapMap (a); PDGSC samples coloured by case/control status with shapes representing continents (Africa = square; Asia = triangle; Europe = circles) (b); samples with African ancestry for PDGSC and HapMap (c); samples with Asian ancestry for PDGSC and HapMap (d); and samples with African ancestry for PDGSC and HapMap (e). Plots courtesy of Demis Kia.

Sample-level QC reduces the PDGSC dataset from 9588 samples (3442 PD cases and 6146 controls) to 8729 samples (2871 PD cases and 5858 healthy controls). Sample exclusions, after removal of 317 for non-European ancestry on PCA (±3SD from CEU TSI mean cut-off), are as follows: 22 samples for sex mismatch ($0.35 < F < 0.65$); 145 samples for relatedness (> 0.125 or second-degree relative); 41 istats (various thresholds); 75 samples for heterozygosity (het < - 0.07 and het > 0.125); 38 under-aged samples (with recorded age < 18); and 2 for identity by descent. Further sample-level QC leads to the removal of 12 samples from the ADSP controls are removed due to freemix > 0.05 (verifyBAMId) and 1 sample for Ti/Tv ratio ± 3 SD. Finally, whole studies were removed from the cohort due to considerably higher than average mean-depth, and all samples from control groups are removed when they represent 1-3 samples per study; representing an additional 214 samples removed.
Altogether, the remaining samples represent 8729 participants, with 2871 PD cases and 5858 healthy controls (i.e. 8.9% of the original number of samples are removed) (Table 16). The breakdown of the remaining samples by study centre can be found in Table 17.

Sample QC leads to the removal of less than 10% of the original number of samples, whilst variant QC is associated to the removal of 48% of the variants in the original sequence files. When adding the commonly used criterion of differential missingness with a threshold at $p < 10e\text{-}25$ to the QC to correct for multiple comparison, another 24.5% of the post-QC variants are removed, leaving 39% of the original set of variants in the post-QC dataset.

Sample QC	**QC Threshold**	**Exclusion n (%)**
Sex mismatch	0.35 < F < 0.65	22 (0.2%)
Relatedness	> 0.125	145 (1.5%)
I-stats	15,000 < NALT < 35,000 10,000<NMIN<27,500 5,000<NHET<25,000 NVAR < 500,000 RATE < 0.85 SING ==0 OR > 500 QUAL < 6,000,000 PASS < 5,000 Ti/Tv < 3.1	33 (0.3%)
Heterozygosity	Het < -0.07 & Het > 0.125	75 (0.8%)
PCA	Mean CEU TSI + - 3 SD	317 (3.3%)
Underage samples	Age < 18	38 (0.4%)
IBD	Ibd > 0.125	2 (< 0.02%)
Freemix	> 0.05	12 (0.1%)
Ti/Tv ratio	< 3.19 & > 3.62	1 (< 0.01%)
Study removal	High mean-depth Low control numbers	214 (2.3%)
TOTAL	Samples flagged for single parameter	**859 (8.9%)**
Post-QC	**Remaining**	**8729 (91%)**

Table 16: PDGSC full-dataset sample QC metrics. Parameters, thresholds and resulting exclusion numbers and percentage from pre-QC dataset for the different steps of the sample-level QC are presented.

a)	Case	Control
ADSP	0	5171
Baylor	73	0
Cambridge	28	0
DZNE	80	22
IPDGC	877	408
Luebeck	36	0
majamaa	216	0
Oslo	36	0
Oxford	215	0
PPMI	365	161
Tuebingen	92	0
ucl	784	0
umiami	69	96
Total	2871	5858

b)	Male	Female
ADSP	2205	2966
Baylor	38	35
Cambridge	19	9
DZNE	50	52
IPDGC	767	518
Luebeck	21	15
majamaa	120	96
Oslo	25	11
Oxford	123	92
PPMI	342	184
Tuebingen	57	35
ucl	496	288
umiami	77	88
Total controls	2612	1864
Total cases	1864	1209
Total	4340	4389

Table 17: Breakdown of number of participants in each study centre separated as case/control (a) and by gender (b).

2. BH4-pathway genes frequencies in minimally QCed dataset:

Overall frequencies of *GCH1*-BH4 pathway genes were first analysed in the cohort, using a minimalist QC to include a maximum of the sequenced variants and samples for these genes. After extracting the intervals of the BH4-pathway genes from the original VEP-annotated file, variant calling is corrected when inclusion/deletions are called as multiple variants (star alleles). The remaining 300 variants are run through SnpSift to estimate the association of each variant with the disease, following dominant, recessive, co-dominant and allelic models. Of note, some variants are annotated as part of the insulin gene (*INS*) due to the extremely close genomic location of this gene to the *TH* one (O'Malley and Rotwein, 1988). Likewise, some variants of the *DHFR* gene are annotated as part of the MutS Homolog 3 (*MSH3*) gene. These are manually corrected after confirmation of their location as falling within the appropriate gene range, leading to the removal of 8 variants. Finally, all 23 variants with a detected MAF > 1% in either controls or both cases and controls are removed, leaving 269 variants found in the cohort across all genes of the BH4-dopamine pathway, distributed as 92 in TH, 41 in DDC, 32 in SPR, 27 in DHFR, 26 in *GCH1*, 25 in QDPR, 16 in PTS and 10 in PCBD1.

Uncorrected p-values obtained with SnpSift are first used with a threshold of $p < 0.05$ to identify top variants. The p-values are then corrected using the FDR method, leading to the loss of significant association of any of these variants with phenotype in the cohort. Of the 269 variants, 12 with MAF ≤ 0.01 have an uncorrected p-value ≤ 0.05 for at least one inheritance model (Table 18). None of these significant results are obtained under the recessive inheritance model, perhaps unsurprisingly as autosomal recessive forms of PD are often early onset or familial, which would have precluded their inclusion in the present study.

All but two of the variants are more frequently found in PD cases than healthy controls, underlying their possible role as protective variants reducing risk of PD in these individuals. The first one, p.Met239Ile (c.717G>T) in exon7 of the *DDC* gene is found in relatively high frequencies in both control and cases in the cohort, of 0.15% and 0.45% respectively. These are in alignment with the variant's frequency in general European population cohorts with frequencies ranging from 0.13%-0.75%. This variant is annotated as splice region variant, possibly leading to the splicing of one of the 14 known alternative transcript of the DDC protein. It is predicted to be benign in silico (Table 18). The second one, p.Arg15His (c.44G>A), is in the first exon of *TH,* is found in 6 controls but no cases in the heterozygous state in the cohort and has previously been associated with one case of homozygous TH deficiency-linked Segawa syndrome (unpublished but submitted to ClinVar). Although pathogenicity of this variant still remains to be established, these controls might be healthy carriers of the variant, which otherwise seem to not affect their risk of developing PD. In silico estimates of the variant's effect are variable.

All other four variants in TH are missense variants uniquely found in cases, all heterozygous carriers, probably due to the strong likelihood for homozygous carriers of TH mutations to present with extreme PD phenotypes or with early onset DRD-like syndromes such as TH deficiency and thus be excluded from this PD cohort. The c.772G>A mutation in exon 7 of *TH* (rs536382000) has previously been associated with a case of dominant tyrosine hydroxylase deficiency (van de Warrenburg et al., 2016) and is found with a much higher frequency of 0.146% in our cases than in the general population (0.01-0.03%; Chi-squared = 11.958, 1df, p = 0.0005). In silico

simulation predicts the variant to be damaging or disease causing (Table 18). TH variant c.545T>C carried by three heterozygous cases has previously been associated with autosomal recessive DRD (ClinVar) and found at a much higher frequency in the cohort (0.088%) than in European population samples (0.007-0.03%). With a SIFT score of 0.05 it is predicted deleterious but other in silico estimations are variable and the damaging effect of the variant at the heterozygous state remains to be determined in the context of PD. The last two TH variants, c.67G>A in exon 1 and c.1411C>A in exon 13, rs201081519 and rs374465917 respectively, are identified in three heterozygous PD carriers (0.088%), a markedly higher frequency than in the general population (0.01-0.03%). Neither have been previously described in DRD or PD and c.1411C>A is predicted likely disease causing while c.67G>A is likely benign (Table 18).

In the SPR gene, c.209T>C mutation is identified in two cases, one homozygous and the other heterozygous, but not in controls. This mutation has not been identified previously described in relation to SPR deficiency, DRD or PD or within the commonly used general population datasets. It is however predicted deleterious (SIFT score 0) or probably damaging (PolyPhen score 1) in silico and validation of the mutation by direct sequencing of these patients is warranted.

Finally, in the PTS gene, c.91C>T gives rise to a synonymous codon change which is likely to be tolerated in the three heterozygous carriers. All three variants identified in the *QDPR* gene are carried by both cases and controls in much higher frequency than the variants found in the other genes of the BH4-dopamine pathway as well as compared to the general population datasets frequency. These may be associated with sequencing artefacts and need to be confirmed for further analysis.

None of the 26 *GCH1* variants found in the cohort are associated with an uncorrected p-value < 0.05; 11 of these variants are found in cases only and 10 in controls only; only one variant is found in the homozygous state in a single case with no other carrier in the cohort. One *GCH1* variant, c.542-2A>G, presents with similarities to the mutation further studied in the functional part of this thesis, as a splice acceptor variant in exon 5 of the *GCH1* gene, affecting splicing at the exon 4-5 junction. This mutation

may have a similar effect to the one studied in our family and is found in two heterozygous carrier PD cases but not in controls.

	Gene	CHR	POS	ID	REF	ALT	Cases	Controls	CC_DOM	CC_REC	CC_ALL	CC_TREND
1	SPR	2	73114770	.	T	C	1_1_3	0_0_0	0.1072	0.3275	0.0351	0.05448
2	QDPR	4	17513661	rs762480653	G	GCCT	1_12_14	0_9_9	0.05369	0.399	0.03402	0.04846
3	QDPR	4	17513660	rs940829956	AGCC	A	1_13_15	0_8_8	0.02082	0.3991	0.01245	0.01725
4	QDPR	4	17492326	rs112209600	C	G	0_6_6	0_3_3	0.03198	1	0.03204	0.02291
5	DDC	7	50571755	rs11575377	C	A	0_5_5	0_27_27	0.00568	1	0.00574	0.009497
6	PTS	11	112099324	rs780189909	C	T	0_3_3	0_0_0	0.05668	1	0.05671	0.02829
7	TH	11	2192973	rs199648386	C	T,A	0_0_0	0_6_6	0.05329	1	0.05333	0.0518
8	TH	11	2192950	rs201081519	C	T	0_3_3	0_0_0	0.05762	1	0.05764	0.029
9	TH	11	2189756	rs147569564	A	G	0_3_3	0_0_0	0.06734	1	0.06736	0.03648
10	TH	11	2188681	rs536382000	C	T	0_5_5	0_0_0	0.008605	1	0.00862	0.004829
11	TH	11	2186478	rs374465917	C	A	0_3_3	0_0_0	0.02962	1	0.02964	0.009664

	Consequence	Genetic alteration	Proteic change	Exon number	ExAC European	gnomAD _ Exomes_Europ	gnomAD_Genomes_Europea	TopMed	ClinVar
1	missense_variant	c.209T>C	p.Leu70Pro	exon1	_	_	_	_	_
2	inframe_insertion	c.16_17insAGG	p.Ala5_Ala6ins	exon1	_	_	_	_	_
3	inframe_deletion	c.15_17delGGC	p.Ala7del	exon1	2.00E-04	_	_	2.00E-04	_
4	missense_variant	c.588G>C	p.Glu196Asp	exon6	1.08E-03	7.80E-04	6.00E-04	5.50E-04	BH4-deficient hyperphenylalanemia ;
5	missense_variant&splice_region_varia	c.717G>T	p.Met239Ile	exon7	7.26E-03	2.23E-03	7.00E-03	1.32E-03	_
6	synonymous_variant	c.91C>T	p.Leu31Leu	exon2	3.00E-04	_	2.00E-04	_	_
7	missense_variant&NMD_transcript_v	c.44G>A	p.Arg15His	exon1	1.07E-04	4.00E-05	1.00E-04	9.00E-05	AR DRD ; TH deficiency ; uncertain significance
8	missense_variant&NMD_transcript_v	c.67G>A	p.Ala23Thr	exon1	2.44E-04	2.60E-04	3.00E-04	3.60E-04	_
9	missense_variant&NMD_transcript_v	c.545T>C	p.Thr182Ala	exon4	1.00E-04	1.20E-04	3.00E-04	7.00E-05	AR DRD ; uncertain significance
10	missense_variant&NMD_transcript_v	c.772G>A	p.Glu258Lys	exon7	2.18E-04	3.00E-04	3.00E-04	1.10E-04	AD DRD ; uncertain significance
11	missense_variant	c. 1411C>A	p.Ala471Ser	exon13	1.52E-05	1.20E-04	1.00E-04	6.00E-05	_

	SIFT	PolyPhen	CADD	REVEL	MetaLR	Mutation Assessor
1	deleterious (0)	probably_damaging (1)				
2						
3						
4	tolerated (1)	benign (0)	likely_benign (10)	likely_benign (0.29)	tolerated (0.218)	neutral (0)
5	deleterious (0.01)	benign (0.001)	likely_benign (20)	likely_benign (0.14)	tolerated (0.021)	neutral (0.008)
6	tolerated (0.08)	possibly damaging	likely_benign (21)			
7	deleterious_low_confidence(0)	probably_damaging(0.988)	likely_benign (27)	likely_disease_causing	damaging (0.98)	low (0.399)
8	tolerated_low_confidence(0.25)	benign (0.001)	likely_benign (19)	likely_benign (0.27)	damaging (0.892)	low (0.202)
9	deleterious (0.05)	benign (0.313)	likely_benign (21)	likely_benign (0.486)	damaging (0.922)	medium (0.694)
10	deleterious (0.02)	possibly_damaging (0.704)	likely_benign (24)	likely_disease_causing	damaging (0.514)	medium (0.909)
11	deleterious(0.01)	probably_damaging (0.962)	likely_benign (26)	likely_disease_causing	damaging (0.987)	medium (0.914)

Table 18: Variants of the PDGSC dataset with significant variant frequency association with phenotypic group based on SnpSift analysis and uncorrected p-values ($p < 0.05$). Missing information from the SnpSift annotation was filled with Annovar annotations and Ensembl dataset search.

3. BH4-pathway based PDGSC exomes QC

In order to prevent the loss of relevant variants through the stringent QC based on the complete sequences of the PDGSC cohort, a pathway-specific and less stringent QC is performed. First, sequencing data is extracted for all eight genes of the BH4 pathway (*GCH1*, *TH*, *DDC*, *PTS*, *SPR*, *PCBD1*, *QDPR* and *DHFR*) from the raw ANNOVAR annotated files (Wang et al., 2010).

Data extracted for all 7 chromosomes harbouring the 8 genes of interest across the cohort represents 603,083 variants in 9,554 samples (6,144 cases and 3,410 controls), after exclusion of samples with missing information for covariates (34 samples missing age or phenotype information). After reduction of ranges from chromosomes

to the BH4-genes ranges and the removal of multiallelic variants and correction of abnormally called insertions/deletions, 455 variants are left within the BH4-pathway gene-set. Number of genotyped sites per sample and mean-depth along these 455 variants are calculated for each participant and plotted against their study of origin (Figure 19). Two study centres representing 208 participants are removed from analysis due to their abnormally high mean depth and number of genotyped sites (munichneuro and Vienna cohorts on Figure 19). Applying thresholds for minimum proportion of sequenced sites (>75% or 341 out of 455) and mean depth (> 15 read coverage on any site) (Figure 20: pre-threshold with blue line representing cut-off), there remains 8,614 samples, of which 5,484 controls and 3,130 cases (Figure 21: post-qc) (Table 19a). These include an equal proportion of male and female samples (with 4327 males and 4287 females). Details of the distribution of cases and controls across studies centres after sample level quality-control step can be found in Table 20.

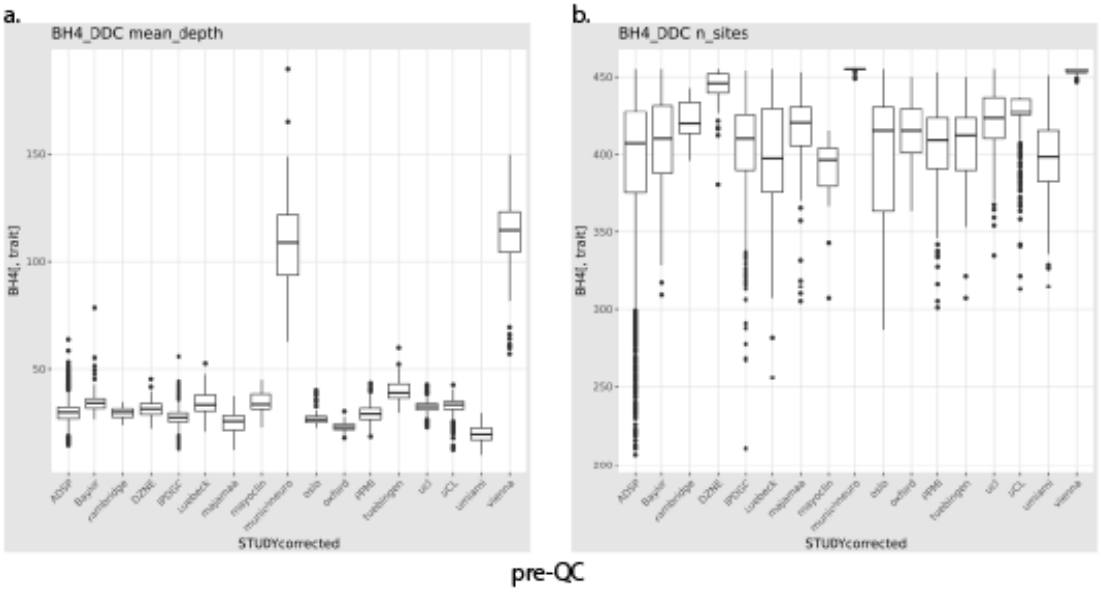

Figure 19: BH4-pathway quality control metrics prior to sample quality control. a. Mean depth per sample plotted against study groups. b. Number of genotyped BH4-pathway sites per sample plotted against study groups.

Variant-level quality control starts after sample-level quality control step removed 170 variants from the original set of 455 variants, as these variants are only found in samples which have been removed during that first quality-control step. Using variant-related threshold parameters, an extra 28 variant are removed as follows: MAF = 0 in either cases or controls and MAF > 0.01 in the other phenotype group (6 variants removed); mean-depth < 15 in either cases or controls (5 removed variants);

missingness in cases or in controls > 0.15 (10 variants removed); monomorphic variants (7 variants removed) out of 455 variants. Of the remaining 234 variants, 53 more are removed using p < 5e-25 as cut-off for differential missingness between case and control groups, leaving a total of 204 variants post-quality control (Table 19b).

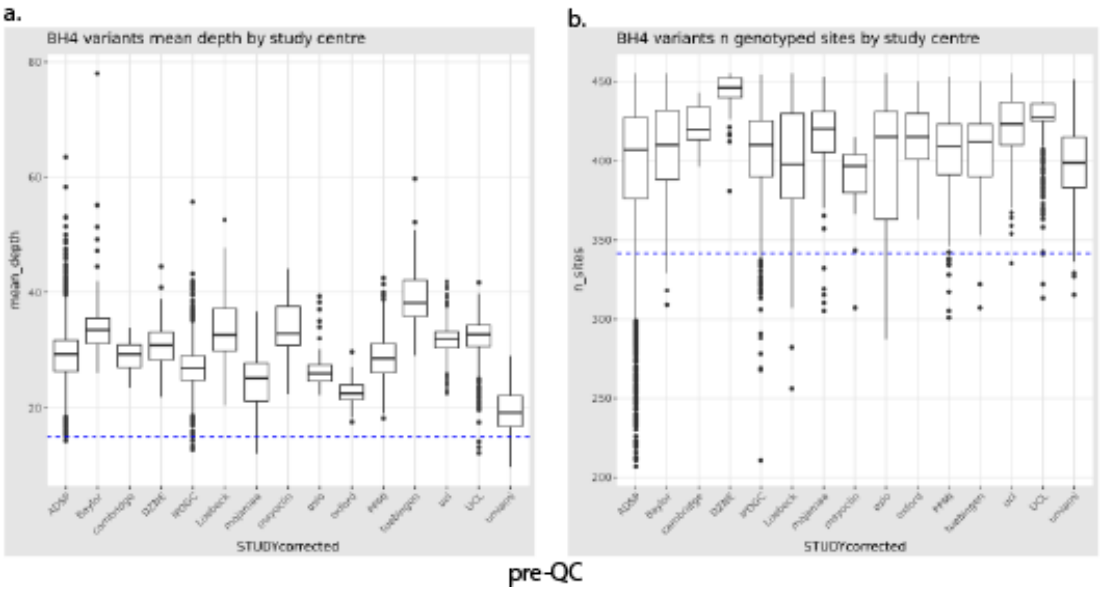

Figure 20: BH4-pathway quality control metrics after removal of two study cohorts with quality control thresholds a. Mean depth per sample plotted against study groups, blue line represent quality control threshold for mean-depth = 15. b. Number of genotyped BH4_pathway sites per sample plotted against study groups, blue line represents quality control threshold for 75% of all BH4-pathway sites.

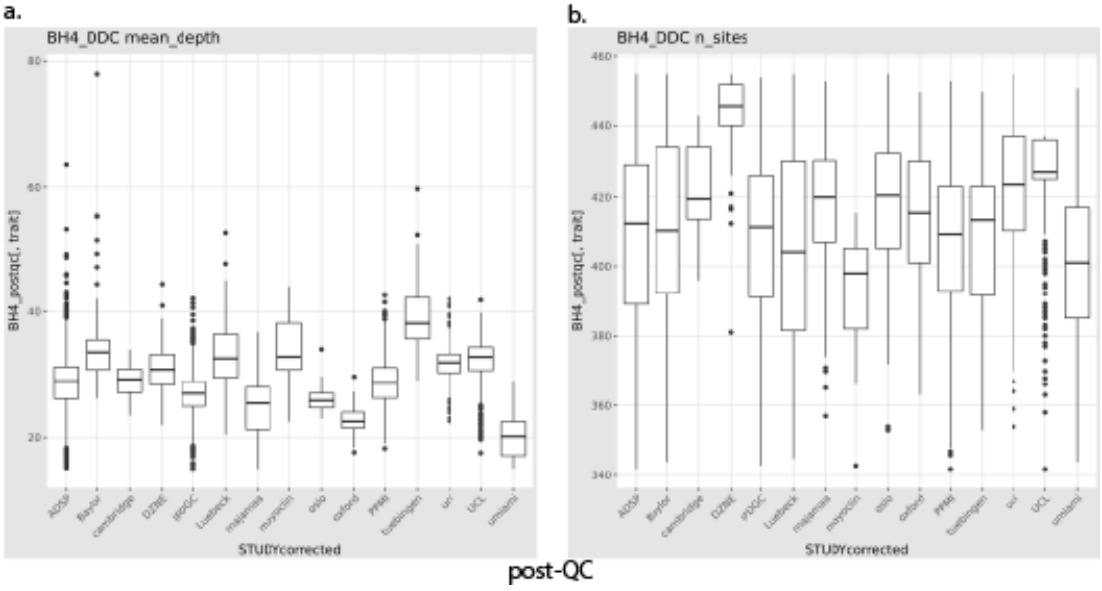

Figure 21: BH4-pathway quality control metrics after sample quality control thresholds a. Mean depth per sample plotted against study groups; b. Number of genotyped BH4_pathway sites per sample plotted against study groups.

a)

Sample QC	Threshold	Exclusion n(%)
Missing information	Age or phenotype	34 (0.3%)
Cohort issues	High mean-depth and n-sites	208 (2%)
Mean depth	< 15	732 (7.5%)
N-sites	> 0.75	
TOTAL	Single flag	974 (10%)
Post-QC	Remaining	8,614 (90%)

b)

Variant QC	Threshold	Exclusion n(%)
Absent post sample-QC	-	170 (37%)
Extreme MAF	MAF = 0 in one group & MAF > 0.01 in other	6 (1.3%)
Mean-depth	< 15	5 (1.1%)
Missingness	> 15	10 (2.2%)
Monomorphic	-	7 (1.5%)
Differential missingness	P < 5e-25	53 (11.6%)
TOTAL removal	Single flag	251 (55%)
Post-QC	Remaining	204 (45%)

Table 19: PDGSC pathway-based QC metrics. Parameters, thresholds and resulting exclusion numbers and percentage from pre-QC dataset are presented for both sample-level QC (a) and variant-level QC (b)

The classically included criterion of differential depth is not used in this quality control due to the structure of the data. Indeed, these samples are coming from different studies which may have used different sequencing chemistries resulting in high variation in sequencing depth between cohorts. Additionally, there is a high variation in the proportion of cases and controls between the included studies, with some cohorts including case samples only, while the ADSP cohort only includes controls (Table 20). Variation is less important between sexes (Table 21). This inter-cohort structure would confound calculations for differential depths, supporting the exclusion of that criterion in the pathway-based quality control. Using a threshold at $p < 5e\text{-}25$ for Wilcoxon test for differential depth between cases and controls, only 78 variants would remain. It was thus decided to omit this criterion from this pathway-based QC, as it was decided in the complete exome one.

Study	N controls	N PD cases	Total n Samples
ADSP	4771	0	4771
Baylor	0	101	101
Cambridge	0	28	28
DZNE	36	121	157
IPDGC	387	890	1277
Luebeck	0	35	35
Majamaa	0	224	224
Mayoclinic	0	23	23
Oslo	0	44	44
Oxford	1	228	229
PPMI	174	388	562
Tuebingen	1	90	91
Ucl	0	514	514
UCL	19	372	391
Umiami	95	72	167
All	**5484**	**3130**	**8614**

Table 20: Distribution of cases, controls and total number of samples across the different PDGSC cohorts post pathway-based QC.

Study	N Males	N Females	Total n Samples
ADSP	2057	2714	4771
Baylor	53	48	101
Cambridge	19	9	28
DZNE	71	86	157
IPDGC	757	520	1277
Luebeck	22	13	35
Majamaa	124	100	224
Mayoclinic	13	10	23
Oslo	31	13	44
Oxford	130	99	229
PPMI	358	204	562
Tuebingen	58	33	91
Ucl	315	199	514
UCL	239	152	391
Umiami	80	87	167
Total controls	2457	3027	5484
Total cases	1870	1260	3130
All	**4327**	**4287**	**8614**

Table 21: Distribution of sexes in the different study groups post-pathway QC. Number of males and females are given for each study group, independently from their disease phenotype. Bottom rows provide the total numbers for each sex in cases and controls separately and together across the complete post-pathway QC cohort.

4. Burden tests

Sequencing data for all post-QC 8,614 samples and 204 variants is extracted from the original VCF, 159 of these variants have a MAF ≤ 0.01 and these are grouped for the burden tests as: all_variants group for all variants across the 8 genes of the pathway; BH4_synthesis group for all variants in the *GCH1*, PTS and SPR genes; and annotation groups LoF, non_syn and CADD for loss-of-function, non-synonymous variants and variants with CADD score ≥ 12.37 respectively, based on variants' ANNOVAR annotation. Burden tests are run using rvtest with a focus on rare variants with MAF ≤ 0.01 and consist in burden tests (CMC, Zeggini, MB and VT-Price) and kernel test (SKAT-O). All but VT-Price make use of covariates to increase test accuracy through reducing the potential effect of data-structure associated confounders; VT-Price cannot use covariates and is run with MAF ≤ 0.01 as its upper threshold. These covariates are: 5 first PCs, age, sex, study centre, number of genotyped sites and mean depth for each sample. Uncorrected p-values obtained with rvtest as well as FDR corrected p-values for multiple comparison correction are presented for each test group in Table 22 a-c.

Looking at the burden associated with all variants from the BH4-dopamine pathway with a MAF ≤ 0.01, only the VT-price burden test p-value is significant with a cut-off of p ≤0.05 with FDR-corrected p-value = 0.026 associated to an optimal frequency of 0.001336 (Table 22a). This is supportive of a role for extremely rare variants with a frequency around 0.1% in the risk for PD associated with the BH4-dopamine pathway. Of note, this result should be confirmed in a separate dataset as there remains to possibility that, as the only test not correcting data structure with the association of covariates, this positive signal may be the result of data stratification in the sample.
When limiting the variants selection to all 27 variants found in the BH4_synthesis group with a MAF ≤ 0.01, all tests but the VT Price result in a statistically significant p-value after correction and on the base of a p ≤ 0.05 threshold (Table 22b). This is supportive for the role of rare variants in these three genes in the risk for PD in the cohort.

a)	All variants (159 variants)	
Test	**uncorrected p-value**	**FDR adjusted p-value**
Zeggini	0.847843	0.847843
SKAT-O	0.358685	
Madson-Browning	0.649351	
CMC	0.690894	
VT_Price	0.0052	**0.026**

b)	BH4_synthesis group (27 variants)	
Test	**uncorrected p-value**	**FDR adjusted p-value**
Zeggini	0.0111624	**0.027906**
SKAT-O	0.018694	**0.031156667**
Madson-Browning	0.0338	**0.04225**
CMC	0.0111624	**0.027906**
VT_Price	0.16469	0.16469

c)	Annovar-based annotation groups		
	Test	**uncorrected p-value**	**FDR adjusted p-value**
CADD (81 variants)	**CMC**	0.241306	0.872134
	Madson-Browning	0.561167	
	SKAT-O	0.707923	
	VT_Price	0.0666	
	Zeggini	0.337842	
LoF (6 variants)	**CMC**	0.684405	
	Madson-Browning	0.814996	
	SKAT-O	0.864151	
	VT_Price	0.872134	
	Zeggini	0.684405	
Non_syn (102 variants)	**CMC**	0.678721	
	Madson-Browning	0.761035	
	SKAT-O	0.789526	
	VT_Price		
	Zeggini	0.738536	

Table 22: Burden test results in the different variant groups with (a) all 204 variants across the *GCH1*-BH4 pathway genes; (b) variants of the BH4 synthesis subgroup of genes containing *GCH1*, PTS and SPR, regardless of their annotation; (c) variants in all genes of the cohort separated by their annotation with loss-of-function (LoF), non-synonymous (non_syn) and CADD >= 12.37 (CADD) groups. Results are presented for each test as uncorrected p-value obtained with rvtest and FDR adjusted p-value for correction of multiple comparison obtained with R p.adjust function.

Finally, it is common to separate variants based on their annotation to evaluate the burden of some sub-types of mutations on phenotype risk in exome-resequencing

studies. Here, none of the groups separated as non_syn, LoF and CADD from the complete BH4-dopamine pathway genes list seem to be specifically associated with risk for PD in the cohort (Table 22c). This is unsurprising as this limits the number of variants in each group, down to only 6 variants in the LoF group, which may be limiting the ability of these tests to identify an existing signal. Moreover, the complete set of genes did not show significant association with the risk for PD in the first place, and applying a similar separation of variant effect groups on the BH4_synthesis genes only limits the number of variants too drastically to keep statistical power.

IV. Discussion

This chapter analyses the role of variants in *GCH1* and related genes of the BH4-dopamine pathway on the risk for PD using the PDGSC dataset, the largest known PD exome dataset to date, including 9588 samples (3410 PD patients and 6144 controls) across 16 PDGSC centres and one ADSP control dataset. A few interesting variants are found in the non-QC version of the dataset and merit further analysis in other datasets or in vitro. Burden analysis following the pathway-based QC of the PDGSC dataset highlights a role for extremely rare variants of the BH4-pathway in the risk for PD, with these variants likely to be found in the BH4 synthesis subgroup of genes including *GCH1*, PTS and SPR. The role of these three genes in the risk for PD should be further investigated to confirm these results.

Such a large cohort significantly increases the likelihood to identify rare genetic risk factors. Moreover, due to the much higher number of variants sequenced than on microarray, exomes increase the chances to capture rare variants yet unidentified in PD (Manolio, 2010; Singleton et al., 2010). The efforts necessary to complete the quality-control of the complete PDGSC exome dataset are described in this chapter and the results available to the IPDGC and associates for the query of genes and pathways. From an original 1,812,821 variants across 3410 cases and 6144 controls, the QC reduces the dataset to 938,385 variants (52% of original) across 8729 samples (2871 cases and 5858 controls). This is obtained with high stringency on most aspects of the exome-wide quality control to palliate for the atypical structure of the data

associated with the use of various sequencing chemistries and the variation in proportion of cases and controls between the multiple participating centres. These characteristics of the dataset also limit the QC by preventing the use of differential depth as a variant QC filtering parameter which is highly biased by sequencing chemistry and base calling algorithms. These together increase the likelihood of type I error by removing samples with informative sequence in the queried genes due to inconsistencies along their genotyping or to discard variants with a particularly low sequencing quality in one cohort but with informative values in the other. That is why, when focusing on the effect of rare variants in the 8 genes of the *GCH1*-BH4 pathway, it becomes necessary to proceed to a pathway-based quality control which allows for the removal of a maximum of sequencing artefacts while maintaining the capacity of this dataset to capture real variants in these genes.

Analysing the rare variants found in the *GCH1*-BH4 pathway genes after minimal QC provides first insights into the distribution of mutations in the cohort. Of the 269 variants remaining, 92 are found in TH, 41 in DDC, 32 in SPR, 27 in DHFR, 26 in *GCH1*, 25 in QDPR, 16 in PTS and 10 in PCBD1. Of these, 12 variants are significantly associated with the disease phenotype with a cut-off for uncorrected p-values < 0.05 and their putative and known effects have been further discussed. Unsurprisingly, none of the variants maintains a significant association with phenotype once p-values are corrected following the FDR approach, as the high number of tests associated with this handful of variants in the cohort size limits the power of these tests. These results warrant the repetition of such an explorative analysis of BH4-dopamine pathway-associated gene mutations in larger PD cohorts, either through exome sequencing or targeted sequencing of these regions.

The pathway-focused QC allows for the retention of samples with high quality variants along the BH4-dopamine genes specifically, overcoming the possibility that real variants captured by the exomes in this area could be removed due to low-quality sequence in other parts of the exomes or type II error. It also limits the likelihood of type I error in these loci by removing all samples and variants for which sequencing quality is not adequate in these genes. The cohort is reduced to 3130 cases and 5884 controls and an overall 204 variants following the pathway-based QC. Of these, 159

are rare variants (MAF ≤ 0.01) and their burden in PD risk estimated in the PDGSC cohort.

Burden tests, which collapse rare variants into genetic scores and test the association between these scores and the observed trait, are performed using rvtests in our case-control setup (Zhan et al., 2016). This package is implemented for the following tests:

- Combined Multivariate and Collapsing (CMC) method, which applies a multivariate test (Hotelling's T^2 test) to evaluate the joint effect of common and rare variants collapsed in different MAF categories (Li and Leal, 2008);
- Zeggini, similar in model to CMC, uses a multivariate test but aggregates counts of rare variants and uses a linear regression of phenotype in function of the proportion of rare variants at which the individual carries a minor allele (Morris and Zeggini, 2010);
- Madsen-Browning which uses a comparison of the weighted sum of variants between cases and controls in order to identify an excess of mutations in cases compared to controls, with weights calculated as the estimated standard deviation of the total number of mutations in the complete cohort. Madsen-Browning uses a Wilcoxon rank-sum test and obtains p values by permutation (Madsen and Browning, 2009).

These tests are run on all variants with a MAF ≤ 0.01 to increase the likelihood to capture rare deleterious variants, with the 5 first PCs, sex, age, number of genotyped sites in the sample, mean depth and study centre as tests covariates to reduce bias inherent to the dataset.

However, burden methods are based on strong assumptions that the great majority of rare variants from the analysed set are causal and associated with the phenotype with the same direction and magnitude of effect (after adjustment for the weights). When these assumptions are not respected, these tests can suffer a substantial loss of power (Neale et al., 2011).

The variable threshold Price (VT) algorithm is thus used as it allows for data-adaptive thresholds in order to increase robustness of burden calculations. The original approach is based on regression of phenotype on individuals' genotype using a variable threshold for allele frequency while incorporating computational predictions of

variants functional effects. Statistical significance is assessed by permutation testing with variable thresholds (Price et al., 2010). This implementation by rvtest uses variable threshold for MAF and a two-sided significance test. However it doesn't allow for the use of covariates, and is thus run on all variants of the BH4 pathway with a MAF $\leq$ 0.01. However, as with burden tests, it assumes the presence of a large proportion of causal variants with same directionality of effects (Lee et al., 2014).

To overcome the directionality assumption of the above-mentioned tests, sequence kernel association test (SKAT), a score-based variance-component tests using a regression method to analyse the variance of genetic effects in order to test for association of rare variants with a phenotype; or its optimal unified version (SKAT-O) optimised for use on smaller whole-exome datasets, can be used (Lee et al., 2012; Wu et al., 2011). SKAT and SKAT-O are able to handle scenarios where variants in the same unit (gene or pathway) affect the phenotype in opposite directions, or when the region of interest contains a large proportion of non-causal variants, and can easily adjust to covariates. SKAT-O includes the added value of using the data to maximize the power of the test by adaptively selecting the best linear combination of burden test and SKAT. However if the assumptions underlying either burden or SKAT are largely true, SKAT-O can be found less powerful than this test (Lee et al., 2012, 2014). SKAT presents with advantages over burden tests, especially in the cases where the majority of the analysed variants (~90%) are non-causal, by dramatically increasing the power of the test; however this advantage is lost when a higher proportion of variants ($\geq$ 50%) are causal (Lee et al., 2012). The optimal unified test SKAT-O outperforms both types of tests in all causal variant proportions scenarios as well as in scenarios where causal variants have opposite directions up to 50%/50% protective/deleterious variants. SKAT-O thus outperforms both burden tests and SKAT (Lee et al., 2012). These characteristics of SKAT-O make it more appropriate for the analysis of risk and protective variants mixes belonging to the same unit (here pathway). Results obtained from these algorithms are thus more robust in our dataset, although the use of the other burden analysis algorithms has its advantages. A summary of the characteristics of each test is found in Table 23.

	Test	**Method**	**Assumptions**	**Disadvantages**	**covariates rvtest**
Burden tests	CMC	Collapses variants by MAF categories	powerful when large proportion of variants are causal and their effects in the same direction	dependent on causality and effect direction	Yes
	Zeggini	linear regression of phenotype on proportion of rare variants carried by each individual			
	Madsen Browning	compares weighted sum of variants between cases and controls			
Adaptive burden test	VT Price	uses permutation testing with variable threshold for MAF - computational prediction of variant effect to regress phenotype on individual's genotype			No
Kernel	SKAT-O	score-based variance-component test which maximizes test power by adaptively selecting the best linear combination of burden test and SKAT	distribution normality for continuous traits	loses power v/s burden tests when burden test assumptions are respected	Yes

Table 23: Recapitulation of the characteristics of each test used in the analysis of the role of GCH1-BH4 pathway variants on the risk for PD

As for most genetic testing in large exome cohorts, the nature of the analysed set of variants is largely unknown and assumptions for the selection of a single test at risk of increasing the risk for type I (false positives) and type II errors (false negatives). There is thus no unifying theory for the selection of the ideal test and I have applied several

tests, thus inflating the possibility for type II errors through multiple testing. Multiple testing correction is thus applied on all resulting p-values using the Benjamin and Hochberg method, which controls for false-discovery rate (FDR); a less conservative correction method than Bonferroni, thus more appropriate in the context of genomics data analysis (Benjamini and Hochberg, 1995; Goeman and Solari, 2014; Goldman).

Additionally, in the context of rare variants analysis by exome re-sequencing, population stratification, which is defined as allele frequency differences between cases and controls due to systematic ancestry differences, can have a dramatic effect on increasing the risk of type I error (Price et al., 2010). This is accentuated here by the multi-centre and multi-chemistry structure of the PDGSC dataset, supporting the use of PCs for correction of population stratification. Importantly, top PCs may not always reflect population structure and both quality controls and PC calculation for use as covariate in burden tests presented here follow the recommendation to use high-quality variants for their calculation, by proceeding to the removal of long-range LDs, assay artefacts identified as low-quality variants and samples with family relatedness prior to PC calculation (Lee et al., 2011; Price et al., 2006, 2010).

Furthermore, other covariates used to increase testing accuracy by reducing the effect of potential confounding factors include: 5 first PCs, age, sex, number of genotyped sites and mean depth for each sample. The effect of population genetics is smoothened using PCs. Age is associated with higher risk for PD, with prevalence in Europe increasing steadily from 0.6% to 2.6% between the ages of 65 and 85 years (De Rijk et al., 2000). Sex is a much discussed risk factor, with PD being originally defined as a male-specific disorder although with variable support in more recent studies (De Rijk et al., 2000; Parkinson, 1817). The effect of sex on risk for PD could be dependent on age, as although there seems to be a slightly higher proportion of males affected by the disease through earlier age groups, this difference is not always significant (Hirsch et al., 2016). Due to this uncertainty, as well as to the significant difference in sex proportion between the case and control groups in our study (Pearson's Chi-squared test for sex and phenotype association: $X2 = 177.35$; $df = 1$; p-value < 2.2e-16), it is included here as a covariate for burden calculations (Table 21). Finally, samples within the PDGSC originate from different centres which have proceeded to their sequencing

and original QC and base-calling according to different Illumina sequencing chemistries and in-house protocols. As a result, number of genotyped sites and mean depths are added as covariates in addition to study centre to limit the effect of the study design of the PDGSC cohort on these burden calculations.

The observations with regards to the association of mutations in the BH4-dopamine pathway genes with risk for PD need to be further validated in larger sequencing datasets. The absence of a significant signal in the single-variant analysis is unsurprising due to the limited power of the study: assuming a similar frequency in mutations to *GCH1* in the other genes of the pathway (0.75%), a prevalence of PD of about 1% (corresponding to European individuals above 60 years), and a genotype relative risk of 1.25 (common to most complex disorders), the cohort has an expected power of 0.135 for $\alpha = 0.05$ (Johnson, 2017; Pawitan et al., 2009; Skol et al., 2006). Single variant analysis for the same parameters would reach a power of 0.8 at significance level of $\alpha = 0.05$ with a cohort size of about 35,000 participants with the current case to control ratio of 0.555. The use of burden and sequence kernel association tests for this analysis is motivated by the lack of power of this exome dataset.

Of note, PD cases samples included in the PDGSC dataset are limited to idiopathic participants for which no causal mutation has been identified. This of course leads to the removal of several samples and variants previously described in IPDGC papers and may bias this analysis towards a false-negative signal. This is exemplified by the loss of all variants described by Mencacci and colleagues in a previous IPDGC dataset which was in parts incorporated in the current PDGSC cohort (Mencacci et al., 2014).

Finally, the variant-calling approaches used may not be capturing the complete burden of *GCH1* and BH4-dopamine pathway genes on risk of PD due to the technical difficulty to capture indels in exome sequencing. Indeed, when SNVs are captured with an accuracy varying from 95-99% with exome sequencing, dependent on calling platform, the accuracy of capture of indels can be as low as 75% (Laurie et al., 2016). It is especially low for medium to large indels, between 20 and 200 base pairs, and for heterozygous samples due to the short read aggregation nature of the exome

sequencing method (Zook et al., 2014). Deletions could represent more than 10% of the deleterious *GCH1* mutation in DRD patients (Hagenah et al., 2005), and could also play an important role in PD. By following the recommendation of the GATK best practice for variant calling and read alignment, there is an increased chance these variants have been captured in the PDGSC cohort. Moreover methods are being developed for a more performant investigation of indels through exome sequencing, such as IMSindel which focuses on intermediate sized indel detection from exome and genome sequencing data (Shigemizu et al., 2018), and these could be applied to similar datasets in the future should the raw sequencing reads be available for analysis.

Analysing the largest known PD exome dataset to date thus demonstrates a cumulative effect for mutations in the genes involved in the *GCH1*-BH4 pathway on the risk for PD, beyond *GCH1* variants only.

Chapter 4: Investigating the effect of the *GCH1* 343+5G>C mutation in patient fibroblast models.

I. Introduction

GTP cyclohydrolase I (*GCH1*, 14q22.2; OMIM#600225) mutations have been associated to DOPA-responsive dystonia (DRD) and later with risk for familial and sporadic Parkinson's disease (PD) (Irie et al., 2011; Mencacci et al., 2014; Nalls et al., 2014; Nygaard et al., 1993). Both movement disorders present with very different phenotypes and the co-existence of this genetic risk factor between two phenotypes suggests a divergence between the deleterious mechanisms involved in the pathogenesis downstream from the mutation. Understanding the differences between these mechanisms is fundamental for the better understanding of these pathologies and the development of efficient and progression-limiting treatments.

GCH1 encodes GTPCH, which catalyses the rate-limiting step for the production of tetrahydrobiopterin (BH4). BH4 is an obligatory cofactor for all three prerin-dependent aromatic amino acid hydroxylases: tyrosine hydroxylase (TH) which catalyses the rate-limiting step for the production of dopamine from tyrosine, phenylalanine hydroxylase and tryptophan hydroxylase (Thöny et al., 2000). It also has functions as a very powerful antioxidant, a coupler for all three isoforms of nitric oxide synthase (NOS) and has an undefined role in the maintenance of mitochondrial redox (Bailey et al., 2017; Nakamura et al., 2000, 2001; Thöny et al., 2000) (Figure 6).

Fibroblasts can be easily obtained from skin biopsies of patients and healthy controls alike and used for the study of the effect of mutations on live cellular functions. They are robust and present all the age-relevant characteristics of the patient. Fibroblasts have previously been used in the study of PD and the diagnosis of DRD. In the study of the mechanisms of PD, primary fibroblasts are found helpful as they recapitulate key aspects of the pathology. Indeed, alterations of the respiratory chain activity are visible in fibroblasts of 15 PD patients compared to 32 healthy controls (Wiedemann

et al., 1999) as well as impaired oxidative decarboxylation of pyruvate in 6 patients compared to 4 controls (Mytilineou et al., 1994).
Another team demonstrated a decrease in complex V activity in the mitochondria of 20 sporadic PD patients compared to 19 age-matched controls (del Hoyo et al., 2010). And the activity of another enzyme glucocerebrosidase, the most common genetic risk factor for PD, can be estimated in fibroblasts and successfully compared between PD patients carrying a GBA mutation and healthy controls (Collins et al., 2018). For the diagnosis of DRD however, as fibroblasts have a very low constitutive *GCH1* expression, differences in GTPCH activity, which relies on the estimation of the production of BH4 and its metabolites, between DRD and healthy controls can only be observed when *GCH1* expression is activated by a cytokine treatment (Bonafé et al., 2001a; Milstien et al., 1993). This method is powerful enough to allow to discriminate between DRD and other GTPCH deficiencies (Opladen et al., 2011).

Although this model is not specifically relevant to a dopamine-synthesis disorder, fibroblasts are extremely versatile and can be modified or reprogrammed towards better model. For instance, a team has demonstrated that the double transduction of *GCH1* and TH into fibroblasts is sufficient for the production of BH4 and dopamine by these cells (Bencsics et al., 1996). Another application is the differentiation of these cells into dopaminergic neurons, using either directed differentiation (Caiazzo et al., 2011; Jiang et al., 2015; Pfisterer et al., 2011), or via reprogramming to induced pluripotent stem cells (iPSC) and further differentiation to midbrain dopaminergic neurons (mDA neurons) (Kirkeby et al., 2012; Kriks et al., 2011). The latter approach was elected for further investigations into the effect of the *GCH1* mutation in the studied family. First investigations into the effect of the c.343+5G>C using fibroblasts and fluorescent dye reporters for the cell functions putatively associated to the *GCH1*-BH4 pathway as a model are presented in this chapter. Here skin cells are obtained from family members affected by either PD or DRD, all carrying a heterozygous c.343+5G>C mutation (Figure 11). This mutation is predicted to cause the retention of the first intron and an early stop codon (Figure 13) (Mencacci et al., 2014).

II. Materials and methods

1. Fibroblasts

Skin biopsies are obtained by Dr. NE. Mencacci from three males of consecutive generation in a previously described family (Mencacci et al., 2014). All three affected members of the family carry a heterozygous c.343+5G>C mutation in *GCH1*. Fibroblasts cultures are derived from the biopsies by the technicians in charge of the Institute of Neurology (UCL) cell bank. Controls are obtained from the same cell bank (C1-3), from skin biopsies of healthy donors (often relatives or spouses of patients attending the clinic) and are sex matched. Additional age matching is approximated for all three mutant lines: the proband (DRD2) to C1 within 22 years, his father (DRD1) with C2 within 7 years, and the grandfather (PDmut) with C3 within 14 years. Characteristics of the fibroblasts lines can be found in Table 24.

Identifier	**Phenotype**	***GCH1* Mutation**	**Family history**	**Age at biopsy**
C1	Healthy	-	Brother FRDA – no signs	44
C2	Healthy	-	-	53
C3	Healthy	-	2 sisters and mother OPA1 non-carrier	55
DRD2	DRD	343+5G>C	Father DRD Grand-father PD	22
DRD1	DRD	343+5G>C	Father PD Son DRD	46
PDmut	PD	343+5G>C	Son and Grand-son DRD	69

Table 24: Characteristics of the fibroblasts. All donors are male. All controls are healthy and not known to be affected by a neurological pathology or to carry a *GCH1* mutation. FRDA, Friedreich ataxia. OPA1, gene associated with optic atrophy pathologies and blindness. Age at biopsy is in years.

2. Fibroblasts culture and maintenance

All fibroblasts are cultured at 37ºC and 5% CO2 in DMEM with GlutaMAX™ Supplement medium with 10% foetal bovine serum (FBS). Fibroblasts are passaged with Trypsin-EDTA (0.05%). Cells are banked in liquid nitrogen in culture media supplemented with 10% dimethyl sulfoxide (DMSO). All cultures are mycoplasma negative as measured with MycoAlert Mycoplasma Detection Kit (Lonza). All experiments are made on low passages (P3-12).

3. Induction of *GCH1* expression

Cells are seeded onto 25mm coverslips in 6-well plates and cultured to complete confluence to prevent effect of cytokine treatment on cell proliferation. Fibroblasts are treated with recombinant human interferon-gamma (IFN-γ and tumor necrosis factor alpha (TNF-α at concentrations of 250 and 100 kilounits/L, respectively, for 24 hours prior to experiments, in fresh medium. Untreated cells are placed in cytokine-free fresh medium for 24h to be used as experimental controls.

4. Testing *GCH1* RNA expression after cytokine stimulation

Fibroblasts treated 24h with 250 kU/L IFN-γ and 100 kU/L TNF-α and untreated controls are harvested by trypsinisation and washed in PBS. Dry pellets are kept at -80ºC until use. Estimation of transcriptional levels of *GCH1* is performed using real-time polymerase chain reaction (qPCR). Total RNA is extracted from cell pellets individually using the RNeasy Mini Kit (QiAgen) and RNA concentrations measured with NanoDrop ND-1000 system (NanoDrop Technologies). 0.5μg of RNA from each extraction is reverse transcribed to complementary DNA (cDNA) using SuperScript III Reverse transcriptase (Invitrogen), dNTP mix and Random Primers. Reactions are kept at -20ºC overnight. qPCR is performed with TaqMan Fast Advanced Master Mix on QuantStudio 7 Flex Real-Time PCR System (AppliedBiosystems) according to manufacturer's specifications. Primers used to amplify *GCH1* are pre-optimised primers spanning the exons 4-5 boundary with a VIC marker (Hs00609198_m1). Endogenous control primers are targeted to hypoxanthine phosphoribosyltransferase 1

(HPRT1 - Hs02800695_m1) exons 2-3 boundary with a FAM marker. Both primers are used in the same well. All cDNA samples are run as triplicates. The qPCR reaction used the Fast program with 20 seconds 95ºC hold (polymerase activation) followed by 40 cycles of 1 second 95ºC denaturation and 20 seconds 60ºC annealation/extension. Results are read on QuantStudio software and analysed with Origin (OriginLab). Analysis is performed using the Livak method or the "Delta Delta CT" (ΔΔCT) method (Livak and Schmittgen, 2001). Each well ΔCt is calculated as $Ct(GCH1) - Ct(HPRT1)$ and $\Delta\Delta Ct = \Delta Ct\ (treated) - \Delta Ct\ (untreated)$ as normalised by the average of ΔCt for untreated controls of each line.

5. Estimations of mitochondrial membrane potential (MMP)

Cells onto 25mm coverslips in recording chambers are loaded with 25nM tetramethyl-rhodamine methyl ester (TMRM) in a HEPES-buffered salt solution (HBSS) for 30 to 45 minutes at room temperature. Dye is present during imaging. TMRM is excited by laser at 560nm wavelength and fluorescence measured at 580nm emission wavelength on a LSM710 VIS (Zeiss) equipped with a META detection system and a X40 oil immersion objective (adapted from (Bartolome et al., 2013)). Basal MMP is recorded with 3-10 Z-stacks for each coverslip and analysed using Fiji (ImageJ). All z-stacks maximum fluorescence projection over mitochondrial areas values are averaged across each coverslip to get a representative value for each experiment and comparisons between conditions are estimated using Origin (OriginLab).

6. Measurement of cellular superoxide production

Cells onto 25mm coverslips in recording chambers are loaded with dihydroethidium (DHE) in HBSS for 5 to 7 minutes at room temperature in the dark. Ratiometric DHE fluorescence is recorded with an excitation length at 380nm and 530nm for 10 minutes with a Cairn xenon arc light source and Optoscan monochromator (Cairn), associated with an Optiscan II stage system and custom filter wheel (Prior Scientific), and an Andor sCMOS camera (Oxford instruments); and analysed on Andor iQ 2.9.1 software (Andor) by hand-selection of all nuclei in the field. Fluorescence intensity at 605:518 emission fluorescence are recorded for each nucleus at each timepoint and exported to

Origin 2017 (OriginLab). Ratio values for each cells are normalised by their own minimum, and average, standard deviation and standard error from the mean (SEM) across all cells within a field are calculated for each time-point. The average and SEM are plotted and the slope of the best linear fit is recorded to estimate the rate of ROS production for each experimental condition.

7. Measurement of cellular reduced glutathione (GSH)

Cells on 25mm coverslips in recording chambers are loaded with 50mM monochlorobimane (mCB) in HBSS for 30 minutes at room temperature. mCB only fluoresce when conjugated with GSH and dye is kept present during imaging. mCB is excited with 400nm laser line and fluorescence is measured at 430nm on a LSM710 VIS (Zeiss). 5-10 Z-stacks are recorded for each coverslip and analysed with Fiji (ImageJ). All z-stacks maximum fluorescence projection values are averaged across each coverslip for further calculations.

8. Statistical analysis

Average values from all three untreated controls is calculated for each experiment and used to normalise all other experimental values. Normalised values are used to analyse trends in combined experimental sets. Data is pooled as: controls (all three control lines), mutants (all three patient lines), DRD (DRD1 and DRD2 cells), PD (PDmut cells).

Kolmogorov-Smirnov normality test is performed on each data set for each of the defined groups and all tests are unable to reject normality ($p<0.05$). Comparisons between mutants and controls in basal conditions use two-sample t-tests. Comparisons between three or more groups use one-way ANOVA. Significant results are then identified by their Tukey corrected multiple t-testing values (Tukey, 1949). For each ANOVA, assumption of homogeneity of variances is tested and confirmed with Levene's test. For all statistical tests, level of significance is set at $\alpha= 0.05$.

III. Results

1. In untreated fibroblasts

Basal MMP

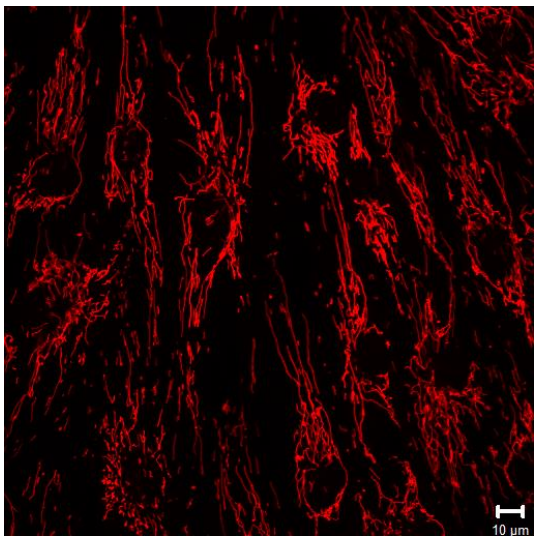

Figure 22: Example of TMRM loading into the fibroblasts mitochondria

As a cell-permeant cationic dye, TMRM is incorporated and sequestered by the active mitochondria in a manner reflecting the degree of polarisation of the MMP. Hence variations in fluorescence intensity reflect changes in the MMP polarisation. Basal MMP is first estimated in unstimulated fibroblasts as a proxy to mitochondrial health between cell lines using complete z-stacks of cells (Figure 22). Maximum intensity fluorescence values are compared across experiments (6 replicates per cell line) after normalisation using average intensity across all three control lines. Mutants show a significantly depolarised MMP compared to controls (T-test $p = 0.01929$), which is consistent with a depolarised MMP in both disease groups separately (Figure 23).

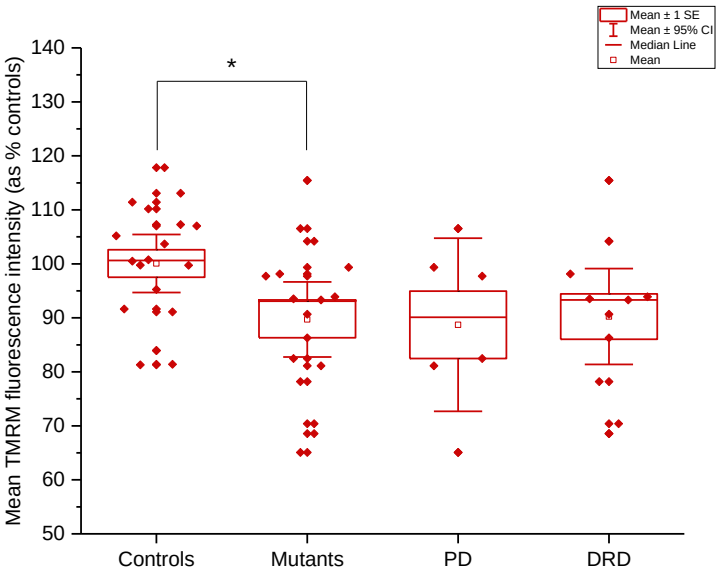

Figure 23: Basal MMP polarisation estimated with TMRM intensity normalised as percentage of the average of controls. Results from all control lines are pooled as 'Controls' (3 lines); results from all cases are pooled as 'Mutants' (3 lines) and further presented in separate box plots separated by phenotype with 'PD' (1 line from PD patient) and 'DRD' (2 lines from DRD patients). Each point represents a z-stack maximum intensity projection value normalised to the average of controls on the day of experiment. Box plot represents: mean (circle), median (line) median ± 1SE (standard error - box) and mean ± 95% CI (confidence interval – whiskers). Stars indicate statistically significant difference with $\alpha < 0.05$ between groups.

Basal superoxide production

Superoxide production is assessed using dihydroethidium (DHE) dye, a cell-permeant free radical sensor which exhibits blue fluorescence in its basal form hydroethidium (□excitation = 380nm, □emission = 518nm) until oxidized to ethidium (□excitation = 530nm, □emission = 605nm)by superoxide where it intercalates within the cell's DNA, staining its nucleus a bright fluorescent red. The reduced:oxidised ratio is used as a proxy to determine the rate of produced superoxide in live cells. Ratios (7 replicates per cell line) normalised by average of all three control values are compared between mutants and controls and across phenotypic groups (PD, DRD and controls) with no significant difference observed (all $p>0.05$) (Figure 24).

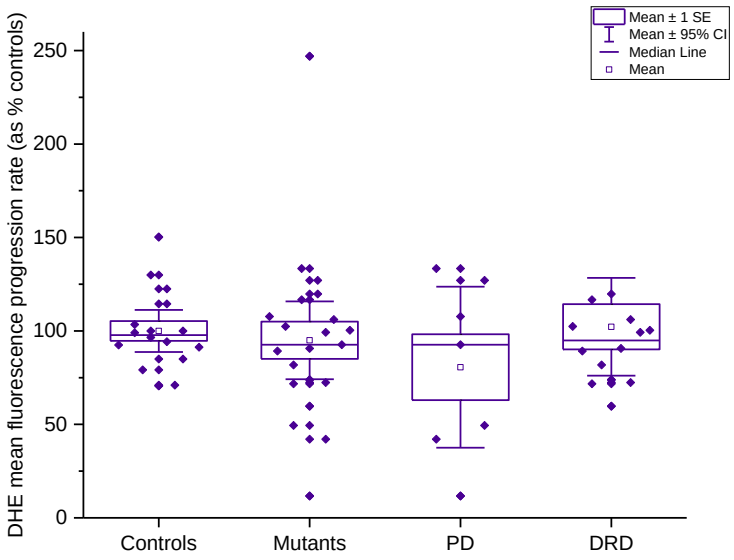

Figure 24: Basal rate of production of superoxide estimated by slope of oxidised:reduced DHE ratio normalised to average of controls. Results from all control lines are pooled as 'Controls' (3 lines); results from all cases are pooled as 'Mutants' (3 lines) and further presented in separate box plots separated by phenotype with 'PD' (1 line from PD patient) and 'DRD' (2 lines from DRD patients). Each point represents a well slope value normalised to the average of controls on the day of experiment. Box plot represents: mean (circle), median (line) median ± 1SE (standard error - box) and mean ± 95% CI (confidence interval – whiskers).

Basal content in reduced glutathione (GSH)

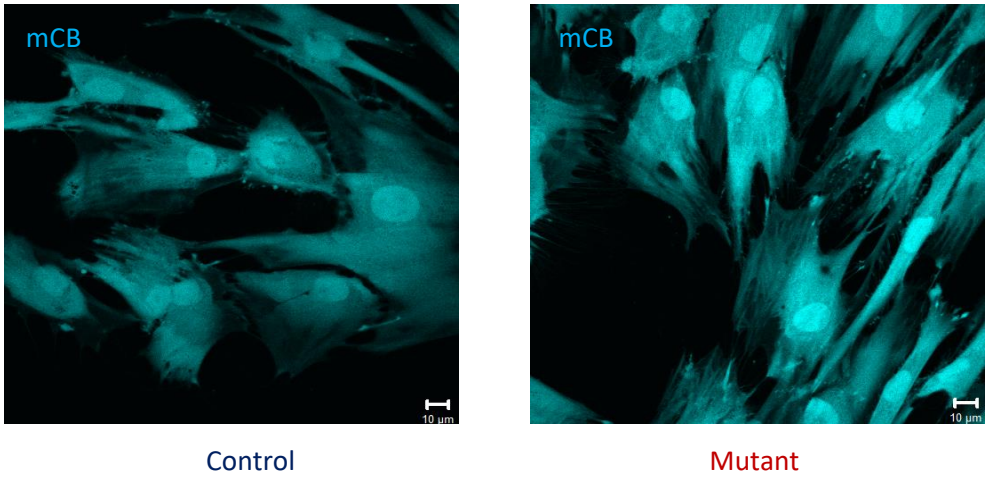

Figure 25: mCB loaded in fibroblasts. Examples in control line (left) and mutant line (right).

Monochlorobimane (mCB) is a non-fluorescent cell-permeant molecule, which quickly reacts with thiols, the majority of which GSH, forming a fluorescent compound (□excitation = 400nm, □emission = 430nm). Fluorescence intensity thus

directly reflects cellular content in GSH (Figure 25). There is a significantly higher content in GSH in mutants compared to controls cells (T-test p = 0.0164) which is driven by the DRD subgroup (one-way ANOVA p = 0.04975; Tukey-corrected p = 0.04325) (Figure 26). There may also be higher GSH content in the PD subgroup compared to controls (although non-significant).

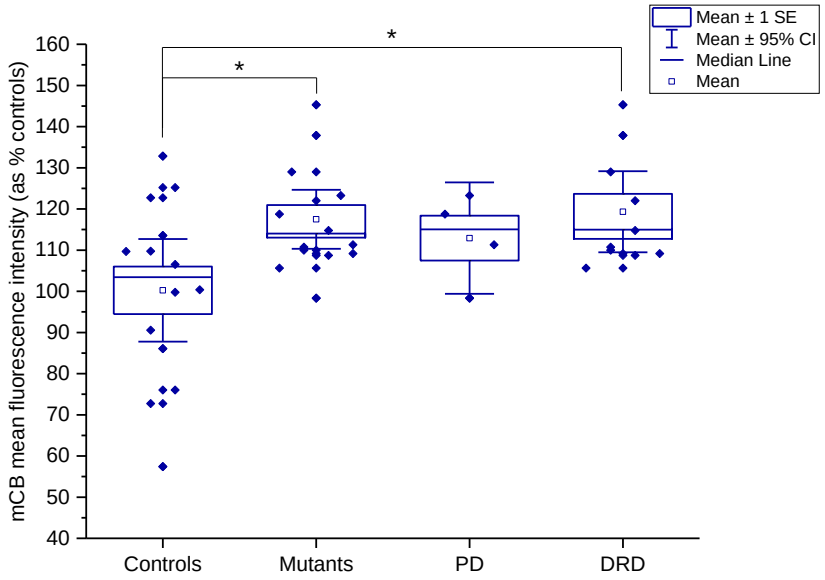

Figure 26: Basal cellular GSH content estimated by mean mCB fluorescence intensity normalised to control. Results from all control lines are pooled as 'Controls' (3 lines); results from all cases are pooled as 'Mutants' (3 lines) and further presented in separate box plots separated by phenotype with 'PD' (1 line from PD patient) and 'DRD' (2 lines from DRD patients). Each point represents a z-stack maximum intensity projection value normalised to the average of controls on the day of experiment. Box plot represents: mean (circle), median (line) median ± 1SE (standard error - box) and mean ± 95% CI (confidence interval – whiskers). Stars indicate statistically significant difference with $\alpha < 0.05$ between groups.

2. Induction of *GCH1* expression in the fibroblast model

Fibroblasts are known to express *GCH1* at low basal levels, which may be too low to measure an effect of the mutation between cell lines using this model (Uhlén et al., 2015). To stimulate *GCH1* expression in the fibroblasts, a previously described cytokine treatment (250kU/L IFN-γ and 100kU/L TNF-α) can be applied to the cells for 24h prior to experiments (Milstien et al., 1993). This treatment has successfully been used by an independent team to observe differential levels of biopterin metabolites between DRD and control cells (Bonafé et al., 2001a). Treatment-induced increased *GCH1* transcription is confirmed in 3 independent biological samples by

qPCR in all 6 lines tested. This increase is not significantly different between pooled controls and mutants with an average increase in controls of 23.8±7.4 fold and of 12.7 ±2.7 fold increase in mutants (p = 0.17) (Figure 27).

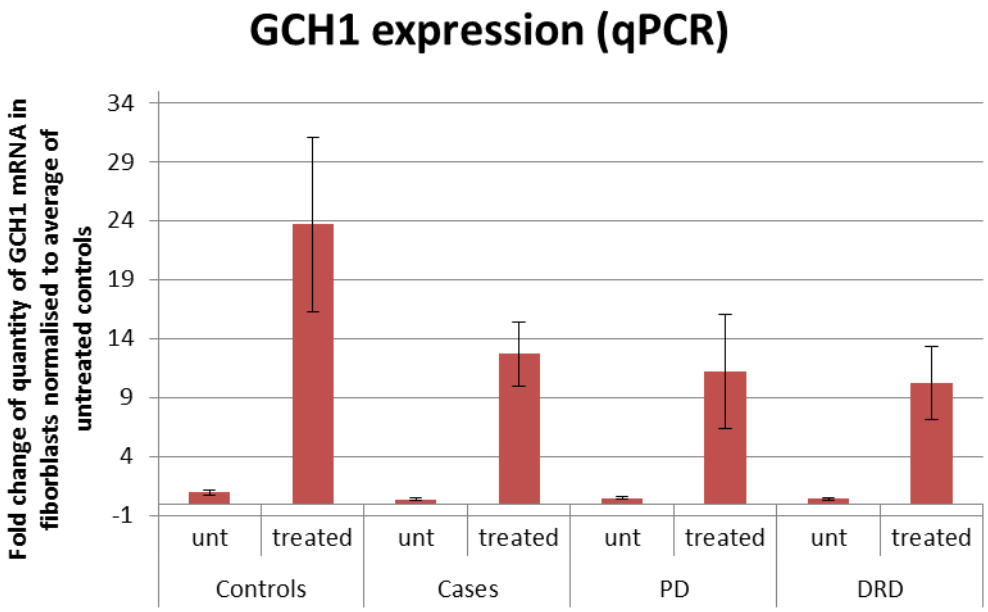

Figure 27: *GCH1* transcription in fibroblasts as measured by qPCR. Transcription levels are compared between untreated (unt) and cytokine-treated cells (treated) in controls (3 lines), cases (all 3 cases lines pooled), with the results separated by phenotype with PD (1 line) and DRD (2 lines pooled).

3. Effect of *GCH1* expression stimulation by cytokines in fibroblasts

GCH1 induction and MMP

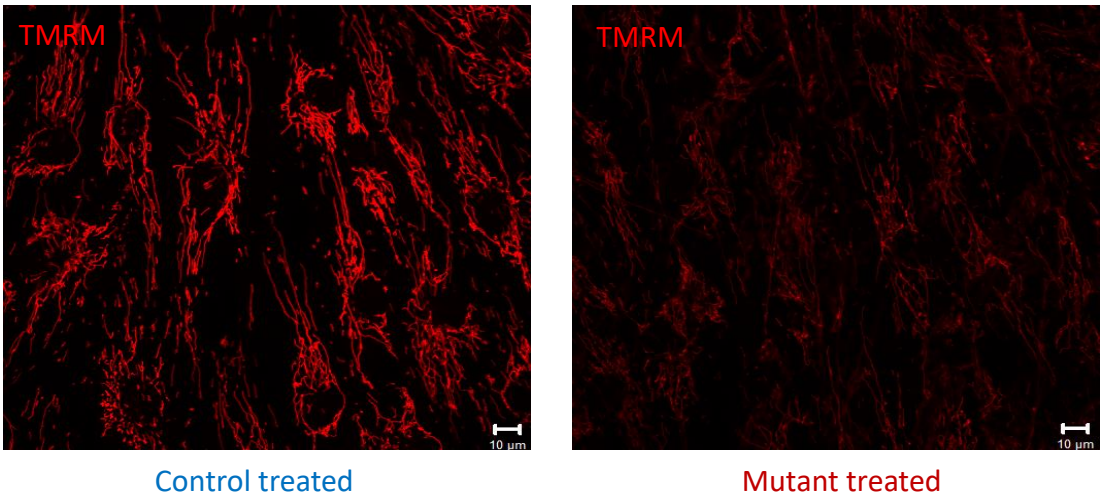

Figure 28: Example of TMRM intensity differences between lines after 24 hours cytokine treatment. Representative images showing lower TMRM intensity in cases compared to controls.

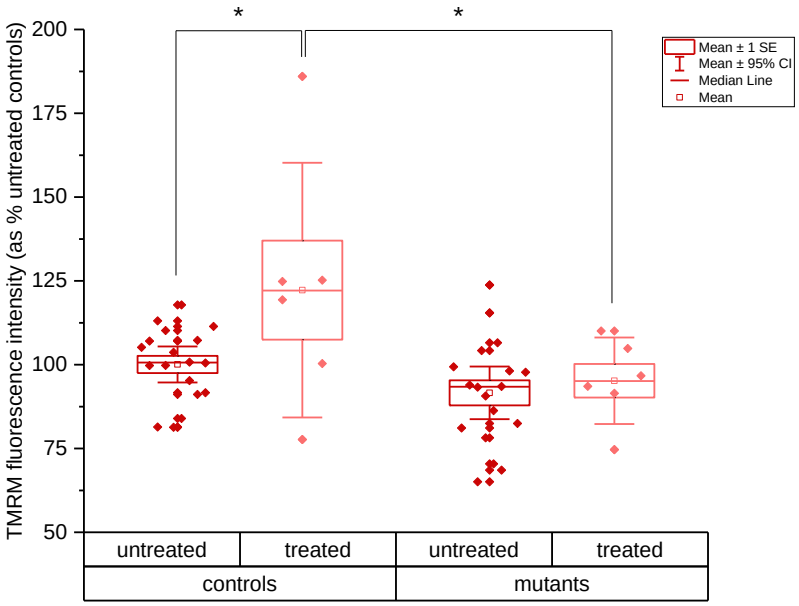

Figure 29: MMP polarisation estimated by TMRM fluorescence intensity normalised to the average of untreated controls. Untreated groups are in dark red, treated groups are in pink. Results from all control lines are pulled as 'Controls' (3 lines); results from all cases are pulled as 'Mutants' (3 lines). Each point represents a z-stack maximum intensity projection value normalised to the average of controls on the day of experiment. Box plot represents: mean (circle), median (line) median ± 1SE (standard error - box) and mean ± 95% CI (confidence interval – whiskers). Stars indicate statistically significant difference with $\alpha < 0.05$ between groups.

TMRM fluorescence is compared between treatment groups across cell lines (Figure 28). Data are obtained for 5 coverslips per cell line for the untreated group and 2 coverslips per cell line for the treated group. For each experiment, average TMRM intensity of the pooled untreated controls is used to normalise all other measurements. Induction of *GCH1*expression leads to significant differences between groups (ANOVA p = 0.00263), with significant increase of TMRM intensity, or polarisation of the MMP to 122.2 % ±14.7 that of untreated controls (Tukey –corrected p = 0.04). Although there was a significant difference between mutants and controls before treatment (Figure 23), the statistical significance is lost due to the Tukey multiple testing correction when comparing all groups for the effect of treatment. Additionally, the treatment unveils a significantly depolarised MMP in mutants compared to controls (Tukey corrected p = 0.04126) (Figure 29). There are no significant change between treated and untreated mutants. These results suggest that increasing *GCH1* expression leads to increased MMP polarisation associated with wild-type but not mutant forms of *GCH1*. Further analysis of the phenotypic subgroups shows that induction of *GCH1*

expression is associated with polarisation of MMP in controls and PD cells, but not in DRD cells (Supplemental Material Figure 82). These differences could point to specific differences in disease mechanisms between the pathologies. However, these results could not be analysed statistically due to low numbers (n=2 experimental replicates for treated PDmut line).

GCH1 induction and superoxide production

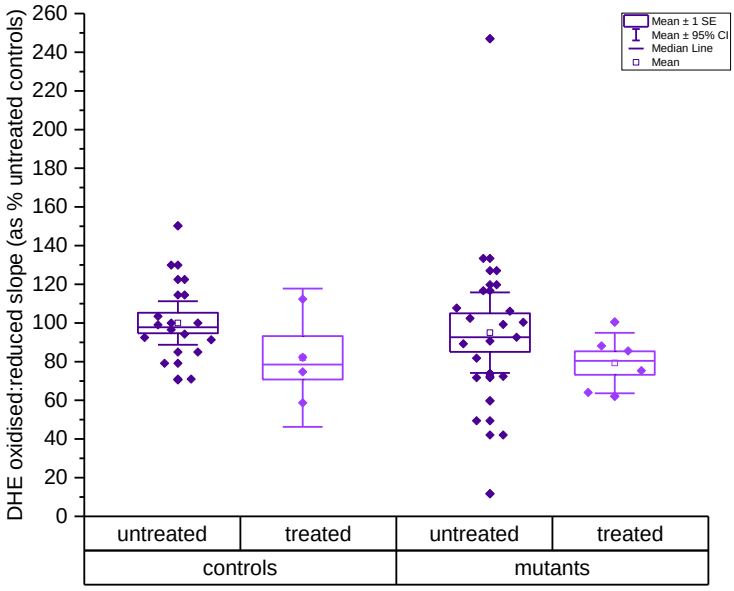

Figure 30: Rate of production of superoxide estimated by slope of DHE oxidised:reduced ratio, normalised to the average of untreated controls. Untreated groups are in dark purple, treated groups in light purple. Results from all control lines are pulled as 'Controls' (3 lines); results from all cases are pulled as 'Mutants' (3 lines). Each point represents a well slope value normalised to the average of controls on the day of experiment. Box plot represents: mean (circle), median (line) median ± 1SE (standard error - box) and mean ± 95% CI (confidence interval – whiskers).

The rate of superoxide production, as approximated by the slope of progression of the oxidised:reduced DHE with time, is compared between untreated (7 coverslips per cell line) and treated (2 coverslips per cell line) fibroblasts. Rates are normalised by the average of untreated control values within each experiment before being pooled and compared. There are no significant differences between untreated groups (Figure 24). There is a non-significant tendency to lower superoxide production in treated compared to untreated groups when comparing controls to mutants (Figure 30), as well as across the phenotypic subgroups (Supplemental Material Figure 83). However, numbers of observations are low and this would need repetition.

GCH1 induction and cellular GSH levels

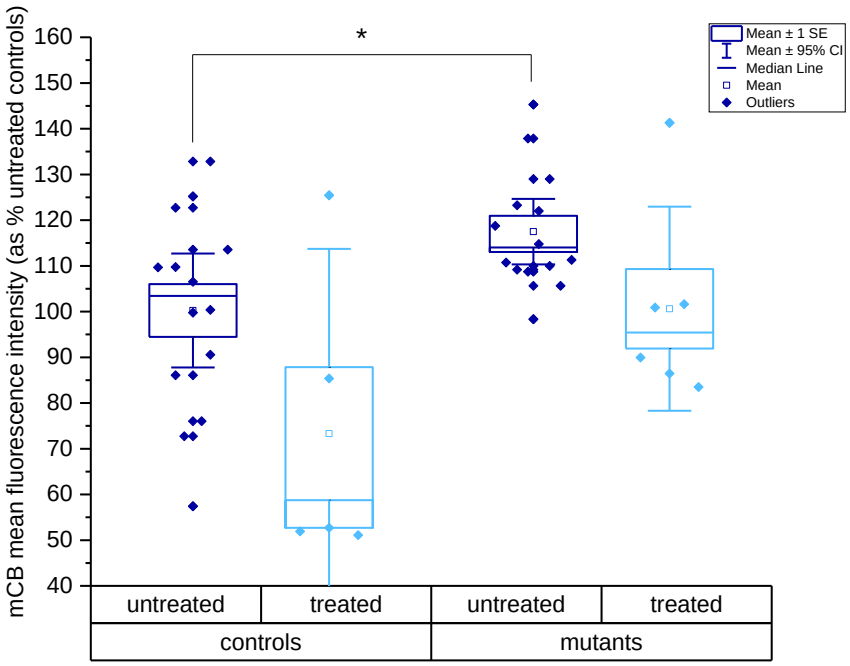

Figure 31: Cellular GSH content estimated by mean mCB fluorescence intensity normalised to control. Untreated are in dark blue, treated are in light blue. Results from all control lines are pulled as 'Controls' (3 lines); results from all cases are pulled as 'Mutants' (3 lines). Each point represents a z-stack maximum intensity projection value normalised to the average of controls on the day of experiment. Box plot represents: mean (circle), median (line) median ± 1SE (standard error - box) and mean ± 95% CI (confidence interval – whiskers). Stars indicate statistically significant difference with $\alpha < 0.05$ between groups.

Cellular levels of GSH are compared across untreated (5 coverslips per cell line) and treated (2 coverslips per cell line) fibroblasts. Each experiment is normalised by the average of untreated control measurements. *GCH1* induction treatment leads to significantly decreased mCB fluorescence intensity in mutant cells compared to their untreated counterpart (ANOVA $p = 0.00221$), however it could not be traced to another comparison than untreated controls to untreated mutants (Figure 31). Similar trends are observed in separate phenotypic groups (Supplemental Material Figure 84). There may be a lower GSH content in treated cells compared to untreated cells and higher GSH content for mutant cells compared to controls (non significant). This suggests that increasing the level of expression of *GCH1* is able to reduce GSH within all cells and that mutant cells have higher basal GSH content than controls which is not corrected by *GCH1* expression induction.

IV. Discussion

Investigating the effect of a putative loss-of-function *GCH1* mutation on *GCH1*-BH4 pathway associated functions first makes use of patient-derived fibroblasts using fluorescent dyes. In untreated fibroblasts, basal MMP is depolarised while GSH content is increased in mutants compared to controls. There is no difference in superoxide production between these groups. Expression of *GCH1* is stimulated with a 24 hours cytokine treatment and found to increase the levels of wild-type *GCH1* mRNA in the cells. The *GCH1* induction treatment leads to an increased polarisation of the MMP in control cells, while the depolarisation of the mutants compared to controls is still visible between treated groups. All treated groups show decreased GSH cellular content associated to the increase *GCH1* expression, and GSH is still increased in mutants compared to controls in the treated condition. The treatment has no effect on superoxide production.

The cytokine method to induce *GCH1* expression is first developed as an efficient way of discriminating between subtypes of BH4 deficiencies in children with similar phenotypes, where relative concentration of different pterins in the cells correlated with CSF measurements in the same patients (Milstien et al., 1993). The method is replicated and similar observations made in two subsequent independent studies where it is used to differentially diagnose DRD from other BH4 deficiencies (Bonafé et al., 2001a) and to differentiate DRD from other GTPCH deficiencies (Opladen et al., 2011). The increase of expression of *GCH1* with 24hours cytokine treatment is confirmed by qPCR in all fibroblasts lines, with the quantity of wild-type *GCH1* mRNA reduced by half in mutant compared to control lines. To further confirm the induction of *GCH1* on a protein level, several attempts at the use of two commercially available polyclonal antibodies raised against human GTPCH for Western blot application detection lead to the visualisation of several bands, none of which at the expected molecular weight of 28kDa (data not shown). It remains possible that GTPCH would be alternatively spliced between cell types, so the experiment will be repeated in iPSC and neuronal cells.

MMP polarisation, estimated with TMRM, is used as a proxy for mitochondrial health variation between cell lines. Both before and after treatment, mutant lines show a

significantly depolarised MMP compared to controls which may underline a less healthy mitochondria in mutation carriers. The *GCH1*-inducing treatment is associated to an increased MMP in controls but not mutant cells, which may be indicative of a lower adaptability of the mutants' mitochondria to changes in energy requirements due to cytokine treatment. These results support a potential role for wild-type *GCH1* in maintaining mitochondrial health and normal function, probably through increased BH4 production. This effect may be due to the putative role of BH4 in mitochondrial redox maintenance.

Further investigations are necessary to determine the mitochondrial phenotype associated with the *GCH1* mutation.

Fibroblast in culture rely mainly on glycolysis for their ATP production and culture media, which contains glucose, can be replaced with a low-glucose high-galactose media in order to increase their use of oxidative phosphorylation for the production of ATP (Hayashi et al., 1991; Robinson et al., 1992). By thus increasing the reliance of the cells on ETC function for energy production, this method is commonly used to increase the visibility of subtle mitochondrial impairments in fibroblasts models, and in particular their effect on the MMP (Allen et al., 2014; Mortiboys et al., 2008). Comparison of MMP polarisation between lines using TMRM can be repeated after 24-72 hours culture of the fibroblasts in galactose media. Dynamic investigations of the mitochondrial respiratory chain using complex-specific toxins (e.g. oligomycin as complex V inhibitor, rotenone as complex I inhibitor and FCCP as mitochondrial decoupling agent) may be added to further describe the effect of the mutation.

NADH/FAD autofluorescence measurements (Bartolomé and Abramov, 2015) can be used to compare the reliance of lines on oxidative phosphorylation in glucose as well as in galactose culture media.

Oxygen consumption as well as the absolute amount of ATP in the cells and the capacity of the mitochondria to produce ATP can be measured with probes, reporter assays for ATP or HPLC for the exact quantification of ATP, ADP and AMP in cultures (Bell et al., 2018; Esteras et al., 2017; Manfredi et al., 2002).

With regards to the role of BH4 as an antioxidant, investigating the effect of the mutation on both antioxidant content (GSH) and superoxide production is based on the hypothesis that the mutation would lead to a decrease by half of available GTPCH

in the cells, which would be associated with lower BH4 production, limiting the antioxidant pool in the cells, leading to increased superoxide production and lower GSH availability.

First, there is no effect of the mutation, with and without treatment, on the superoxide production rate in fibroblasts. It is possible to be associated with a rapid reaction of superoxide with other molecules abundant in fibroblasts, limiting its ability to be observed with DHE, associated either with nitric oxide (NO) and similarly reactive species which presence and product could be measured with the use of fluorescent dyes (Beckman and Koppenol, 1996), or with the presence of a strong GTPCH-independent antioxidant system which instantaneously buffers superoxide at its point of production. This could be confirmed by measuring the production of NO by NO synthases using dyes such as DAF-FM and DAR-4M (Kojima and Nagano, 2000), measuring the production of superoxide by the mitochondria using MitoSOX Red dye or directly measure ROS species using high-performance liquid chromatography (HPLC).

Second, the cellular content in GSH, a very powerful antioxidant, is significantly increased in mutants compared to controls, while *GCH1*-inducing treatment leads to GSH content decrease. Changes in GSH content can either be associated with changes in its expression to palliate to the cellular need for antioxidant protection or through its oxidation to GSSG. The higher GSH content in mutants compared to controls may be associated with the reduced availability of GTPCH, which is interchangeable with GSH in a dopaminergic neuronal cell model (Nakamura et al., 2000), even in low expression conditions such as in fibroblasts. When GTPCH expression is increased in the fibroblasts, increasing the antioxidant defence of the cells, GSH expression may be lowered to conserve energy. This is more likely in this model than a treatment-induced increased oxidation as there is no effect of treatment on superoxide production by the fibroblasts. Moreover, treatment does not equalise GSH content between mutants and controls, probably due to the 'loss-of-function' nature of the mutation studied. This would need to be repeated in fibroblasts from patients with alternative mutations in *GCH1*.

Finally, investigations of the effect of this *GCH1* mutation on dopaminergic metabolism and NOS function are limited. First by the relatively low expression of

tyrosine hydroxylase (TH), the rate-limiting enzyme necessary for the production of dopamine from tyrosine, in fibroblasts: TH, which uses BH4 as an essential enzymatic cofactor, is detectable at very low levels via RNAseq and undetectable at the protein level in skin fibroblasts by the Human Atlas Project (Uhlén et al., 2015). Thus the cytokine treatment is able to increase GTPCH, BH4 and their metabolites in fibroblasts but not boost their ability to produce dopamine. Second, fibroblasts are not known to produce basal NO levels, but there may be a role for increased expression of inducible NOS (iNOS) in human fibroblasts in the context of wound healing (Witte and Barbul, 2002). One possible hypothesis is that inflammation-dependent expression of cytokines by the macrophages is associated with GTPCH and downstream BH4 expression in both macrophages and fibroblasts which induce iNOS activity and production of NO, thus promoting wound healing. This would also explain the ability to use cytokine treatment to induce GTPCH in fibroblast.

Effects of the c.343+5G>C mutation in *GCH1* can be measured in patient-derived primary fibroblasts cultures and suggest an impairment of mitochondrial function and of GSH levels in the cells. Further models more relevant to the dopamine-related phenotypes observed, in PD through the specific degeneration of the midbrain dopaminergic neurons and in DRD through the important response of symptoms to levodopa treatment, are developed and used in the following chapters.

Chapter 5: Generating human midbrain dopaminergic neurons

I. Background

Understanding the role of GTP cyclohydrolase 1 (*GCH1*) variants in the risk for Parkinson's disease (PD) necessitates the investigation of molecular and cell functional impairments. The definition of these impairments becomes more important when comparing the development of PD to that of dopa-responsive dystonia (DRD) in patients affected by either disease carrying the same mutation in *GCH1* (in this thesis c.343+5G>C *GCH1*). Describing the differential consequences of this mutation on downstream pathways thus requires the development of an appropriate disease model.

PD is primarily a movement disorder associated with the specific degeneration of the midbrain dopaminergic (mDA) neurons of the substantia nigra pars compacta (SNpc), the neurons responsible for the control of movements in mammals (Hodge and Butcher, 1980). The good and sustained response of DRD patients to low doses of L-dopa (Tassin et al., 2000), associated with the absence of evidence for neurodegeneration in both in-vivo imaging and post-mortem pathology reports (Albanese et al., 2011; Furukawa et al., 1999; Marshall and Grosset, 2003), are suggestive of the association of a functional impairment of mDA neuronal capacity to produce adequate amounts of dopamine with DRD. However, while the dopamine synthesis function seems involved in DRD, patient response to treatment suggests an intact uptake and usage of L-dopa in their mDA neurons (Clot et al., 2009).

Accordingly, this project uses cells derived from patients affected by either DRD or PD, obtained from the same family, and carrying a single heterozygous loss-of-function *GCH1* mutation, to compare the mechanisms involved in both disease phenotypes to healthy function based on the use of an *in vitro* human mDA neuronal model.

The method described in this chapter aims at differentiating patient induced pluripotent stem cells (iPSC) to mDA neurons. This chapter first explores current knowledge of mDA neuronal development and then describe the existing methods and their

limitations. The rationale behind the proposed protocol, its results, and the potential for future improvements of mDA modelling are discussed.

1. The need for an appropriate disease model

Designing an appropriate model at the crossroads between PD and DRD is essential to the understanding of *GCH1*-associated impairments in both disorders as well as providing a good framework for the testing of new therapies prior to clinical trials. The SNpc, a central structure of the brain whose function or integrity is impaired in both pathologies, is inaccessible in living humans. Access is limited to post-mortem tissue from donated brains, which are both rare (even more so for DRD patients due to low incidence) and largely limited to the end-stage pathology. Indeed, PD patients' brains are often accessed years after the onset of the pathology and decades after the putative start of disease-related dysregulations; in DRD these tissues are extremely rare, often from individuals who passed away years after the onset of symptoms in their childhood and possibly after years of dopaminergic treatments of unknown consequence on histo-pathophysiology (Kordower et al., 2013; Mencacci et al., 2015). In both instances, these caveats greatly limit our capacity to observe the mechanisms underlying disease progression in human tissues.

Alternative models for the observation of disease progression are based on animals, offering access to larger quantities of samples at various stages of the disease, the ability to modify and select specific genetic sequences, with significantly shorter gestational period and lifespan than humans, and the possibility for the operator to completely control their environment (The Jackson Laboratory, 2019). The capacity to modify their genetic sequence in a stable way while controlling their environment allows the study of both the function of the gene in itself as well as the effect of defined environmental variables on the risk for development of pathologies. Animal models of PD are made to recapitulate pathogenesis in one of two ways: neurotoxin-induced and genetically engineered.

Neurotoxin animal models replicate the pathological and behavioural changes of the human PD in mammals using pharmaceutical agents able to induce the specific

degeneration of nigrostriatal neurons. Most are based on the use of systemic injection of Methyl-phenyl-tetrahydropiridine (MPTP), a substance with specific dopaminergic toxicity first described in sudden parkinsonism cases in a subgroup of drug abusers (Langston et al., 1983). MPTP is able to pass the blood-brain-barrier (BBB) where glial monoamine oxidase B and oxidation then convert it to its active form (MPP+) which can then be carried by dopamine transporter (DAT) to enter the SNpc mDA neurons. In mDA neurons, MPP+ blocks the activity of complex I of the mitochondrial respiratory chain leading to rapid cell degeneration through ATP depletion, and increased nitric oxide and reactive oxygen species (ROS) production (Chiba et al., 1985). MPTP has since been used in a variety of mammalian animal models. However, one important limitation for MPTP models is their constant failure to demonstrate Lewy-body (LB) pathology, an important hallmark of PD in humans while they can recapitulate specific cell loss and cardinal symptoms of the pathology in animals (Shimoji et al., 2005).

Another complex I inhibitor, rotenone, is able to reproduce the selective loss of nigrostriatal dopaminergic neurons when injected systemically by crossing the BBB and entering mDA cells independently of DAT activity. As well as complex I inhibition, rotenone inhibits proteasome activity leading to proteolytic stress (Sherer et al., 2003). More importantly, rotenone is able to reproduce LB-like pathology with the observation of ubiquitin-positive and α-synuclein containing cell inclusions in rat models (Betarbet et al., 2000). Finally, rotenone used as a pesticide has previously been associated with increased risk for PD in humans (Brown et al., 2006). But rotenone models lack reproducibility due to high variation in animal lesion in response to the toxin, are non-specific with evidence for the degeneration of other types of neurons and are linked to high mortality due to rotenone's toxicity for other tissues such as the heart, liver or kidneys (Lapointe et al., 2004).

One important caveat for the use of these neurotoxin models is the dramatically rapid loss of neurons after pharmacological treatment which highly differs from the typical slow progression of neurodegeneration in human patients (Huang et al., 2017a). It also drastically limits the window of opportunity to observe the fundamental mechanisms underlying cell death in these models. Another neurotoxin model uses intra-striatal injection or infusion of 6-hydroxydopamine (6-OHDA) (Ungerstedt et al., 1974). This

model recapitulates common phenotypes and metabolic changes of PD animal models and is associated with a rapid loss of striatal projections followed by the progressive loss of nigral cells over several weeks, offering a longer window to observe fundamental cellular changes in PD development (Blandini et al., 2007). 6-OHDA, as a hydroxylated analogue of DA, is uptaken by mDA cells via DAT activity, making it a DA neuron-specific toxin. 6-OHDA accumulates in the cytosol where it auto-oxidizes producing hydrogen peroxide, and in the mitochondria where it induces oxidative stress via increased ROS production through mitochondrial complex I and IV inhibition (Rodriguez-Pallares et al., 2007).

Genetic animal models, carrying known PD gene mutations, address some of the drawbacks of neurotoxin models, such as the absence of an age-dependent progression of lesions and LB pathology, offering a larger window for the observation of underlying disease progression mechanisms. While increasing the maintenance time required for these animals to provide results, speed of ageing is relatively short in small mammals, with animals reaching a full maturation age at 3 months and an equivalent age as to typical PD onset in humans (around 60 years) at 18-24 months (Flurkey et al., 2007). Genetic animal modelling of PD is achieved by alterations of either the animal's genomic sequence or its gene expression profile. Genetic engineering mainly allows alterations in human genes homologues or by the inclusion of the human gene under the control of a relevant endogenous promoter. Additionally, use of genetic constructs or exogenous approaches such as micro RNAs (miRNA) allow for the temporally-controlled alteration of gene expression in such models.

Transgenic and neurotoxin non-mammalian models are developed as a cheaper, higher-throughput alternative due to their reduced genomic complexity, easier and cheaper maintenance and their shorter lifespan. They also present with consequent advantages over mammalian models such as transparency of zebrafish embryos allowing use of fluorescent reporters to directly observe neurodevelopmental consequences of mutations; or the conserved metabolic dopamine synthesis pathway between Drosophila melanogaster and human, with many genes involved in PD having at least one fly homolog. For instance, drosophila melanogaster age-related protein

changes show by 44 days of life and this model is relatively easy to maintain in laboratories (Fleming et al., 1986).

One major caveat in the use of non-human models is due to inter-species variations which have the potential to impair the translational aspects of studies. This is important in pharmacology with differences in drug metabolic capabilities and capacity for molecule binding to receptor as a result of their varying distribution and activation properties (Creese et al., 1979; Martignoni et al., 2006). Overcoming the obstacle of inter-species differences, *in vitro* models using human pluripotent stem cell (hPSC)-derived mDA neurons provide an alternative model for understanding disease mechanisms; identify therapeutic targets and trial relevant compounds; and for the development of cell-replacement therapies. Human embryonic stem cells (hESC) were first used to develop methods recapitulating mDA neurodevelopment in a dish. However, legitimate ethical concerns limit the access to hESCs for fundamental research and their use in therapeutic applications. Furthermore, hESCs as opposed to patient cells are not necessarily carrying the appropriate genetic background on which to study the fundamental disease mechanisms underlying the development of these pathologies; although genetic engineering or external stressors are used to approximate the disease in this model. Finally, using hESCs in cell replacement therapies comes with the risk of immune-rejection and are associated with the additional immune-suppression treatments which may have a deleterious effect on patients.

As a result, PD modelling strives to move beyond the use of animal models for the study of human pathology by accurately producing large amount of mDA neurons carrying the entire genetic background of the patient *in vitro*. The iPSC technology provides a virtually unlimited cellular source recapitulating two main features of hESCs: pluripotency and ability to propagate in culture indefinitely, while conserving the complete genetic background of the individual (Takahashi and Yamanaka, 2006; Takahashi et al., 2007). Human iPSCs can also undergo directed differentiation which necessitates bespoke programmes of appropriate neurodevelopmental cues in a time-specific manner. As such, the development of mDA neuron induction protocols is at the centre of a large body of publications since 2004. However, of 74 papers describing new or substantially modified protocols identified within 13 years since this first

publication, only 26 methods (19%) have been reused in subsequent publications not sharing authors with the original one (Marton and Ioannidis, 2018). This may be indicative of the difficulty to reproduce these methods in external laboratories or the need for better, more reproducible protocols. Many challenges in the development of these methods may be associated with the difficulty to recapitulate the appropriate neurodevelopmental cues in vitro, in the absence of the cell-to-cell spatiotemporal communication of a complete organism. It is necessary to note that iPSC-derived mDA neurons are not a perfect model, as prolonged cultures of iPSC are prone to the accumulation of genetic and epigenetic changes which result in culture heterogeneity with the risk of selecting cells with mutations promoting their survival in culture which can affect their capacity to differentiate, or render them inappropriate for cell therapy use due to increased mutagenic risk and affect their reliability as a stable model for fundamental research (Bock et al., 2011; Hu et al., 2010; Liang and Zhang, 2013). These are also accentuated by the difference in expression of genes from several differentiation pathways in different lines associated with a variable ability to differentiate into selected cell types, a limitation to in vitro studies and clinical translation (Carcamo-Orive et al., 2017). Additionally, the use of iPSC for the study of late-onset disorders is limited by the loss of senescence and age-related markers i.e. elongation of telomeres in reprogrammed cells compared to parent cells (Marion et al., 2009), mitochondrial metabolism similar to that observed in development (Suhr et al., 2010), and that these are all observed even in reprogrammed senescent and centenarian cells (Lapasset et al., 2011). Finally hiPSC-derived models of mDA neurons demonstrate a genome-wide gene and exon expression level more similar to foetal than post-mortem tissue patterns (Patani et al., 2012a). One proposed method to age cells is the use of progerin-induced ageing, successfully used in iPSC-derived genetic PD models with observation of PD-specific phenotype such as progressive loss of TH expression, enlarged mitochondria, LB-precursor inclusions, dendrite degeneration and neuromelanin accumulation (Miller et al., 2013). Finally some aspects of the ageing process such as the re-establishment of adult mitochondrial metabolism is observed in induced differentiation models from iPSC (Suhr et al., 2010).

2. Midbrain dopaminergic neuron development in the human brain

The midbrain dopaminergic neurons encompass a small population of an estimated 400,000-600,000 cells, representing 0.0005% of all neurons in the human brain (Pakkenberg et al., 1991). They are involved in movement, motivation, learning, decision-making, attention and value-encoding. mDA neurons thus make the essential link between salience, associated with learning and memory, and its expression through animal behaviour as translated by movements. The mDA neurons found in the SNpc are mainly involved in voluntary movement control and are preferentially degenerated in PD. SNpc mDA neurons are thus at the cellular basis of PD neuro-pathogenesis, making them an ideal model for the study of this pathology. Their origin and the directed differentiation protocols used to produce mDA neuronal models *in vitro* are discussed here.

The mDA neuronal subtypes

The midbrain dopaminergic neurons (mDA) are separated into three areas in the murine and primate brain, namely A8, A9 and A10 (Felten and Sladek, 1983; Olson et al., 1972). These three areas differ by their point of origin and the target region they innervate (Figure 32). The dopaminergic neurons of the A9 and A10 groups are mainly distinguished by the location of their soma and projections, their morphology and their calcium binding protein expression, as well as by their susceptibility to neurodegeneration in PD. The A9 mDA neuronal bodies are found in the SNpc, project predominantly to the dorsolateral striatum or putamen and dorsal caudate nucleus in humans, and participate in the control of movement. A9 cells are large and angular and express the potassium channel subunit G protein activated inward rectifier potassium channel (GIRK2). They also constitute the subgroup of neurons selectively vulnerable to neurodegeneration in PD. The A10 neuronal cells are found in the ventral tegmental area (VTA) and project to the ventral striatum and various limbic structures such as the nucleus accumbens, cingulate and prefrontal cortex (Felten and Sladek, 1983; Grealish et al., 2010; Smits et al., 2006). As such, it has a role in the fine tuning of movement, the control of emotion and reward mechanisms (Cohen et al., 2012; Lammel et al., 2012). Impairments of the VTA are associated with addictive and affective disorders but its mDA neurons are largely spared in PD (Braak and Braak,

2000). VTA cells are rather small and round compared to A9 cells, they mainly express calbindin and are relatively spared in PD. The differences in calcium-binding protein expression between A9 and A10 cells are similar in rats and humans, although humans have comparatively more dopaminergic cells than rats in these areas (McRitchie et al., 1996). Finally, the retrorubral field or A8 cells group is found in the lateral reticular formation dorso-lateral to the substantia nigra, they have a similar shape but smaller size than nigral neurons (Felten and Sladek, 1983). Together, the VTA and retrorubral field form the mesolimbocortical system known to regulate emotional behaviour, reward mechanisms, natural motivation, signalling aversive outcomes, and are involved in a range of psychiatric disorders (Bromberg-Martin et al., 2010; Dahlstrom and Fuxe, 1964; Felten and Sladek, 1983; Smits et al., 2006).

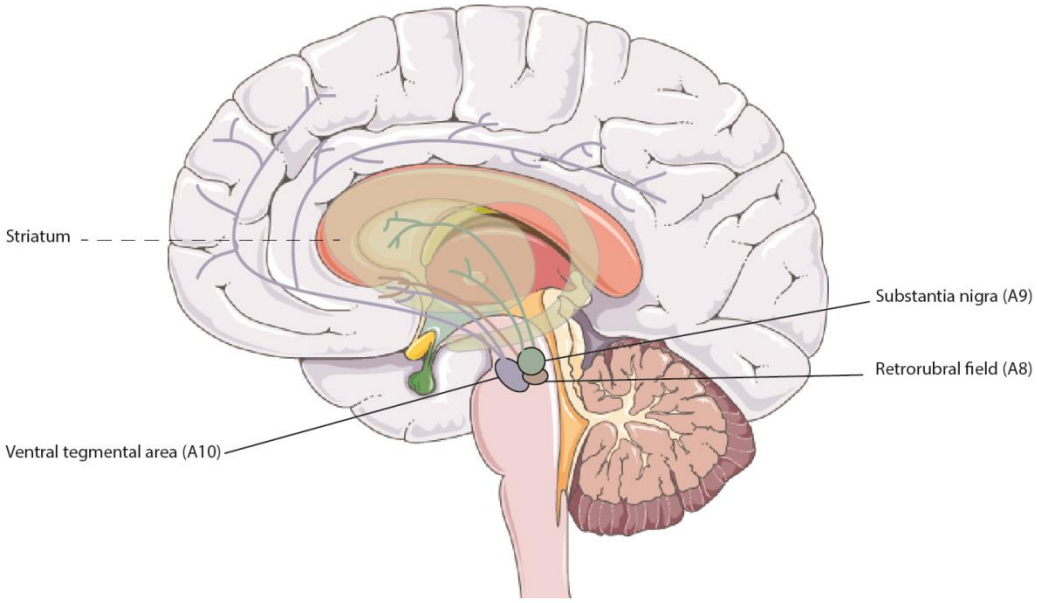

Figure 32: Dopaminergic neuron groups (A8-A10) with their point of origin and projections in the human brain.

These distinctions between A9 and A10 neuronal areas are important for the success of engraftment therapies in PD models. Successful replacement of mDA neurons targeted to the striatum is demonstrated in rats (Grealish et al., 2010). Using a transgenic murine model expressing GFP under the control of the tyrosine hydroxylase (*TH*) promoter, another team demonstrate that A9-type precursors expressing Girk2 could target striatal structures and mature in the adult brain, while calbindin-expressing A10-type neurons targets the frontal cortex and other forebrain areas (Thompson et al., 2005). Molecular patterning at a neural precursor stage may thus determine the identity

but also the migration and capacity to develop connections of these neuronal cell types. Axon guidance, allowed by a combination of attractive and repulsive signals to which neurons originating from different areas are more or less sensitive, all in order to reach the appropriate target region are reviewed elsewhere (Bissonette and Roesch, 2016).

Finally, in human PD patients, neurodegeneration starts in the ventral part of the SNpc before spreading laterally and, as PD progresses beyond its first decade, the number of residual TH-positive and melanin containing neurons remains relatively stable, suggesting the co-existence of two subpopulations of nigral neurons with substantially different vulnerabilities to PD neurodegeneration and anatomical locations (Fearnley and Lees, 1991; Kordower et al., 2013). This comes in support of the existence of different groups of mDA in the midbrain with consequences in disease vulnerability beyond neurodevelopment and normal adult function.

In the case of DRD, there has been no observation of degeneration in post-mortem tissue and via dopamine transporter-based imaging, suggesting the mutations do not lead to mDA degeneration (Nygaard et al., 1992; Segawa et al., 2013). However, DRD is associated with lower TH immunolabelling, in spite of the maintenance of pre-synaptic dopaminergic molecules, in the striatum and in the absence of cell loss in the substantia nigra (Segawa et al., 2013). DRD may thus be associated with the dysfunction of the same A9 cells as in PD, although through a distinct, non-degenerative pathway. More research is warranted to determine whether the other mDA cell groups are affected in DRD.

Developmental basis of midbrain neuron specification (Figure 33)

During development, ESCs are slowly differentiated by the progressive restriction of their pluripotency with stem cells able to differentiate into any cell type of the organism; leading first to neural progenitors able to differentiate to many different neural cell types, then midbrain floor plate (FP) neural progenitors, co-expressing Forkhead Box A2 (FOXA2) and LIM Homeobox Transcription Factor 1 Alpha (LMX1A), able to differentiate into mDA neurons as well as midbrain cells. Finally the cells are fully differentiated and matured into their neuronal subtype. These are

often associated with migration and development of targeted connections for neuronal cells.

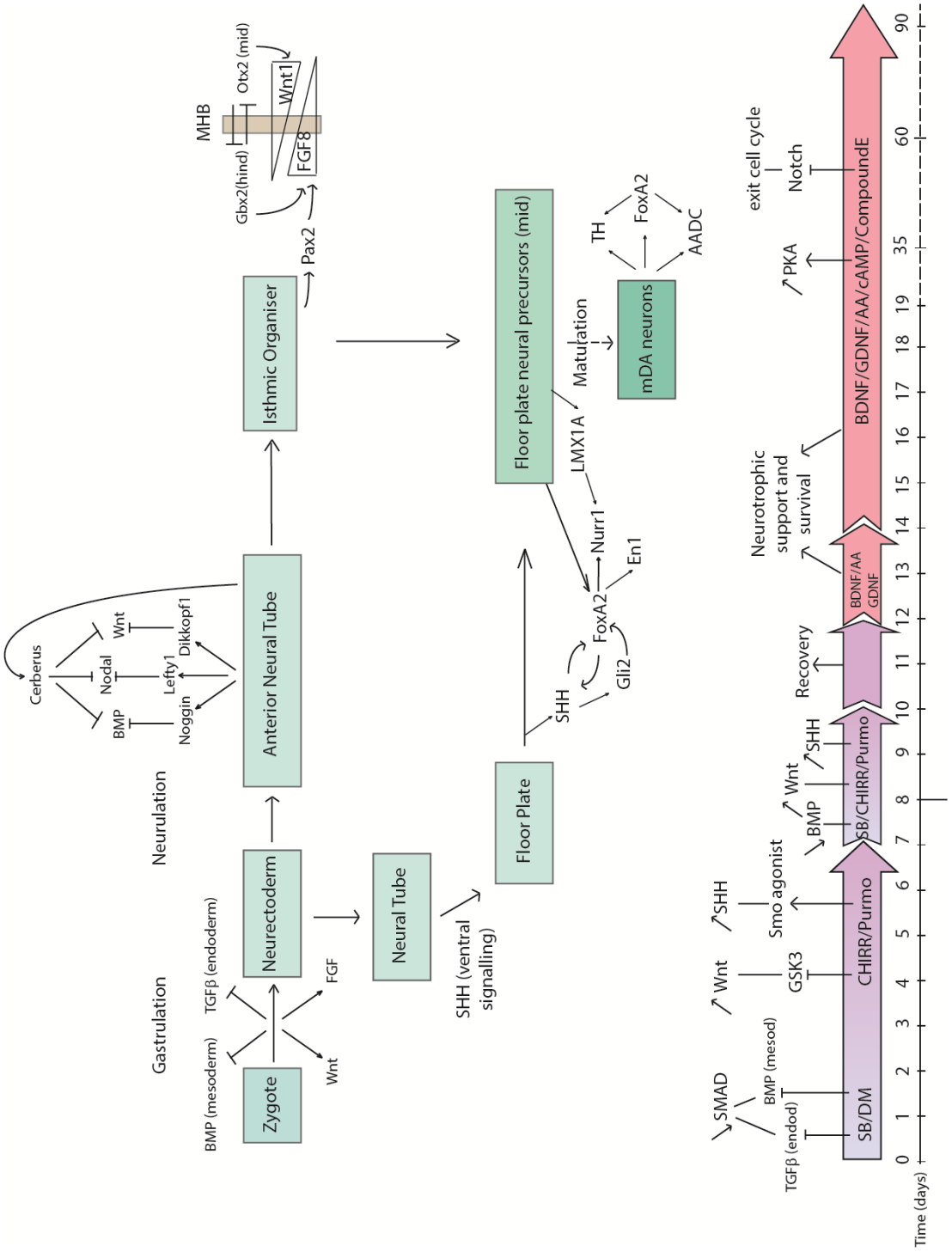

Figure 33: Developmental basis of mDA neuron specification. The top diagram reprensents the main events of the specification of mDA neurons *in vivo*; the bottom diagram reprensts how the inhouse induction protocol mimics these milestones *in vitro*. Names of the molecular signalling pathways involved in black. Small arrows represent secretion and activation, blunt ended arrows represent inhibition.

Midbrain development has been extensively researched in smaller mammals such as the mouse, and comparative studies in embryos have shown that human midbrain development occurs through a similar sequence of events as in mice, although along a longer time-period (Freeman et al., 1991; Nelander et al., 2009). The most commonly accepted model of cell migration pattern for the development of the midbrain was described in 1971: mDA neurons are generated at the midline of the ventricular zone of the midbrain neuroepithelium with precursors migrating radially to the ventral midbrain (Hanaway et al., 1971). A further perpendicular migration from the lateral neuroepithelial patches forms the SNpc, while cells from the medial part of the neuroepithelium migrate to the VTA (Smidt et al., 2004a). Cells acquire their mature mDA phenotype while migrating and, when in the ventral field, the cells have matured to display a full dopaminergic phenotype (Hanaway et al., 1971) and express markers such as Th or paired-like homeodomain transcription factor 3 (Pitx3).

A complex series of events allows for the molecular patterning necessary for this migration and differentiation. During gastrulation, the neurectoderm is specified along the antero-posterior axis by the activation of fibroblast growth factors (FGF) and wingless-type MMTV integration site family members (Wnt) and the inhibition of the mesodermal differentiation factors (bone morphogenic proteins – BMPs) and endodermal differentiation factors (transforming growth factor beta – TGFβ). Following the gastrulation with its definition of the three germline tissue layers, expression of a set of posterior signal inhibitors at the rostral end of the embryo allows for the molecular definition of the anterior neural tube. These signals include a Wnt inhibitor (dickkopf 1), a Nodal inhibitor (left-right determination factor 1), a BMP inhibitor (noggin) and a multifunctional inhibitor of all three signals (Cerberus) and are detected as early as E4.5 in the developing mouse brain (Takaoka et al., 2007).
Subsequently, an early and crucial event in the development of the midbrain is the determination of the isthmic organiser (IsO) defining the midbrain-hindbrain boundary (MHB) from E7.5 in the developing mouse anterior neural tube. The patterning of the MHB is dependent on the mutual repression of two transcription factors: the midbrain-expressed orthodendicle homolog 2 (*Otx2*) and the gastrulation brain homeobox 2 (*Gbx2*) expressed in the hindbrain (Broccoli et al., 1999; Millet et al., 1999; Wassarman et al., 1997). At the MHB, the IsO secretes the morphogen fibroblast

growth factor 8 (Fgf8) under the induction of the paired homeobox2 (*Pax2*) transcription factor. Fgf8 expression is maintained by Gbx2 and thus found at higher concentration in the hindbrain than the midbrain. The gradient of FGF8 drives hindbrain cell fate in high concentration areas and pushes cells to take a midbrain identity in the tissues anterior to the IsO where Fgf8 concentrations are lower, as Fgf8 is necessary in low concentrations to induce midbrain fates (Basson et al., 2008; Crossley et al., 1996). Concurrently, *Otx2* found in the midbrain activates the expression of the Wnt1 morphogen which controls the development of a posterior midbrain region and an anterior hindbrain region on both sides of the MHB due to its gradient of expression. In the absence of Wnt1, midbrain and cerebellar structures disappear as early as E9 in the mouse, supporting the early and fundamental function of this morphogen in the development of these structures (McMahon and Bradley, 1990; McMahon et al., 1992; Thomas and Capecchi, 1990).

Another major event of midbrain development is the formation of the FP, the origin of which has been widely discussed due to discrepancies in experimental results (reviewed in (Placzek and Briscoe, 2005)). One theory reconciles most results by suggesting the existence of a time and location-specific set of developmental cues from the notochord, prechordal mesoderm and potentially from other yet undefined neighbouring structures, giving rise to this falsely homogeneous-looking structure.

Indeed, the formation of cells defined as the FP presents with a high variation in cellular composition and molecular signature along the embryonic antero-posterior (A-P) axis. The FP is thus likely to be an anatomical structure composed of various cell types with separate developmental origins and variable functions along the A-P embryonal axis (Placzek and Briscoe, 2005). The FP, a glial-rich structure which acts as a signalling centre, arises at the ventral midline of the neural tube, prior to its closing. The signalling pathways associated to the development of the FP have been extensively studied in amniotes. Sonic hedgehog (*SHH*), a general ventralizing signal for the CNS, and its downstream obligate Shh signalling molecule smoothened (Smo) are necessary for FP formation in mouse and chick studies (Incardona et al., 1998; Wang et al., 1995; Wijgerde et al., 2002). Indeed, downstream Shh signalling induction through the inactivation of an endogeneous Smo inhibitor, *Patched*, is sufficient for

the ectopic formation of FP-patterned cells in mice (Goodrich et al., 1997). There is evidence of a role for TGFβ in enabling cells to respond to Shh signal in early midbrain specification as well as later mDA neuronal survival (Farkas et al., 2003; Roussa and Krieglstein, 2004). Further downstream in the Shh signalling cascade, GLI-family transcription factors are controlling Shh target gene expression, with Gli2 being responsible for the activation of several genes associated with spinal cord and FP induction, including *Foxa2* (also known as Hnf3β) (Ding et al., 1998; Matise et al., 1998; Sasaki et al., 1997). The activation of *Foxa2* expression in the midline of the neural tube via Gli2 associated to the secretion of the morphogen SHH by the subjacent notochord or prechordal mesoderm is measurable in mice from E8 (Ang and Rossant, 1994; Sasaki et al., 1997). A short window of opportunity for Shh signalling to induce FP determination is demonstrated by the unique competency of cells of the open neural plate to form the FP in response to this signal. Shh signalling components are then rapidly downregulated in the FP (Placzek and Briscoe, 2018). By E8.5, the FP is able to secrete Shh itself via activation by *Foxa2* expression hence becoming a secondary ventral organiser of the neural tube (Bai et al., 2004). Subsequently, the FP is responsible for influencing cellular identities and directing axonal trajectories (Placzek and Briscoe, 2005). Foxa1 and Foxa2 are continually required for mDA neuron development and maintenance, with first a positive effect on Ngn2 expression and neurogenesis at the neural precursor stage, followed by a requirement for Foxa1/2 for the expression of Nurr1 and En1 in immature mDA cells and for the expression of *TH* and L-amino-acid decarboxylase (*AADC*) in mature mDA neurons. These developmental functions require a time- and dosage-dependent regulation of Foxa1/2 expression (Ferri et al., 2007).

In the rostral FP, at the level of the midbrain, expression of *Otx2* provides the ventral mesencephalic midline progenitors with a neurogenic activity and specifies their mDA fate. Otx2 is necessary and sufficient for the specification of mDA neurons at the FP, as demonstrated by ectopic expression in a mouse model, at least partially through the induction of Lmx1a expression (Ono et al., 2007). Lmx1a was indeed demonstrated to regulate proneural gene expression such as Msx1 in murine and avian models, as well as to promote neural progenitor proliferation during neurodevelopment (Andersson et al., 2006; Ono et al., 2007). Lmx1a may also function as a specific

activator of downstream genes such as *Nurr1*. Msx1 suppresses alternative cell fates and induces exit from cell cycle as well as pan-neuronal differentiation of the glial-like ventral midline FP cells, and is believed to set the timing of DA neuron generation probably through Ngn2 expression (Andersson et al., 2006; Placzek and Briscoe, 2005). In vitro, Lmx1a is able to induce mDA neuron differentiation from mesencephalic neural progenitors but not from any unspecified ESC, suggesting the need for pre-existing ventralisation of these progenitors, probably via Shh signalling, for an efficient effect of Lmx1a (Andersson et al., 2006). Lmx1a has been identified as a mDA neuron specified factor downstream from Otx2 in the rostral FP (Ono et al., 2007). These neurodevelopmental events are summarized in Figure 33.

A few studies offer an insight into the mDA neuron development within the human embryo, mainly through immunocytochemistry (ICC) at different stages post-conception (PC). mDA neurons in humans as well as in murine model arise from the radial glia-like cells of the mesencephalic FP under the control of Wnt signalling (Bonilla et al., 2008; Ono et al., 2007). mDA neurogenesis is predicted to start around 5.3 weeks PC, then followed by the appearance of TH+ cells around 6 weeks PC and a subsequent important increase of the TH+ cell population at weeks 6-8 PC, before terminating at about week 10-11 (Freeman et al., 1991; Nelander et al., 2009). 8 weeks PC marks the start of visible axonal extension and nigrostriatal bundles, with these TH positive cell extensions visible in the early putamen structures at 9 weeks PC and in the caudate nucleus and nucleus accumbens at around weeks 10.5 PC (Freeman et al., 1991; Olson et al., 1973; Pickel et al., 1980). The majority of the mDA neurons are showing dendritic extensions by weeks 11.2 PC (Freeman et al., 1991). A separate study shows dendritic extension to continue at least until weeks 11.7 PC (Olson et al., 1973). Cells of the human mesencephalic FP co-express brain lipid-binding protein (BLBP) and LMX1A between weeks 5-8 PC, while FOXA2 is expressed in both the FP and the basal plate at similar stages (Nelander et al., 2009). However, only a very few BLBP-positive cells do differentiate to mDA neuron, and BLBP expression may be a remnant of the neuroepithelial origin of the FP in humans as well as in mice (Hebsgaard et al., 2009). FOXA2 in conjunction with LMX1A can thus be used as rather neuronal specific markers to identify human midbrain FP neural precursors.

It is thus commonly accepted that FGF8 produced by both the IsO and the rostral forebrain, SHH and TGF-β signals from the ventral neural tube, and Wnt1 expression (under the control of Otx2) in the midbrain are necessary and sufficient for the development of mDA neurons (Prakash et al., 2006; Ye et al., 1998). Consequently, these molecules have been widely used in attempts to differentiate mDA neurons from pluripotent cells *in vitro*.

Specification and maintenance of mDA neurons

A few other transcription factors play an important role in both the specification and the maintenance of mDA neurons. First, in mDA FP neural progenitors, the expression of both Lmx1a and Lmx1b, in collaboration with Foxa2, as well as of Nurr1 and Pitx3 are paramount for the optimal differentiation of these cells.

Nurr1 is expressed from E10.5, preceding Th expression in the midbrain, and null Nurr1 mouse models show expression of Pitx3 but not Th at early embryonic neural precursor stage, with Pitx3 expressing cells not surviving long after birth of the animal (Saucedo-Cardenas et al., 1998; Zetterström et al., 1997). Additionally, DAT and vesicular monoamine transporter-2 (Vmat2) expression depend on Nurr1 activity but not Pitx3, making Nurr1 necessary for late neurotransmitter expression in mDA cells but not their early development (Smits et al., 2003). Lmx1b is expressed by mDA neurons in both SNpc and VTA from E7.5 and is maintained through life. Lmx1b is necessary to the activation of expression of Pitx3 and, in the absence of Lmx1b and thus Pitx3, TH-positive neurons are lost during their development (Smidt et al., 2000). Lmx1b is thus necessary for the proper specification of mDA neurons during the early mDA development program, independently of their neurotransmitter phenotype, itself controlled by Nurr1. The terminal differentiation of mDA neurons thus requires two separate pathways converging to provide all functional features to mDA neurons.

Pitx3 (OMIM 602669) is expressed in the midbrain, eye lens and skeletal muscle during murine development but only maintains expression in the midbrain of the adult mouse (Smidt et al., 1997). Using *Pitx3*-null model Aphakia (Ak), Smidt and colleagues show that Pitx3 expression is activated one day after Nurr1 (Law et al., 1992), and two days after Aadc (Teitelman et al., 1983) in a manner similar to Th.

Additionally, Pitx3 and Th expression fully overlap in the murine brain, although its expression is around six times higher in the VTA than SNpc (Korotkova et al., 2005; Zhao et al., 2004). Unlike Th, Pitx3 brain expression is restricted to the mDA neurons in both developing and adult mouse brain (Smidt et al., 1997) and has not been found in other dopaminergic cells outside of the midbrain. In the Ak mouse, TH is expressed in the midbrain at E11.5 in an indistinguishable manner to controls. Yet from E12.5 onwards, the TH-positive cells from the rostro-lateral midbrain, normally forming the SNpc, are absent in the Ak mouse (Smidt et al., 2004b). The absence of Pitx3 is thus lethal to SNpc mDA cells, making SNpc but not VTA cells developmentally dependent on Pitx3. However Th expression is not dependent on Pitx3, as demonstrated in the Lmx1b null model (Smidt et al., 2000). In humans, Pitx3 mutations are associated with eye-development pathologies (Semina et al., 1998) suggesting a potential similarity to mice in its function.

Altogether, Pitx3 expression is required for the specification and survival of the mDA of the SNpc in a region-specific manner. Both Th and Pitx3 are expressed in the ventral midbrain after the initial migration of midbrain FP neural progenitors from the neuroepithelium, suggesting these genes have no direct function in proliferation nor migration of these cells. Pitx3 may have a role in 'vitalizing' DA progenitors arriving at the primordial SNpc, and it may influence proliferation and migration indirectly (Smidt et al., 2004a). Interestingly, one consequence of Lmx1b ablation is the lost co-expression of Th and Pitx3 (Smidt et al., 2000). Further, Pitx3 may be a marker for a subtype of mDA neurons and promote their survival in pathologies such as PD, where Pitx3 is normally expressed in the surviving SNpc mDA cells (Smidt et al., 1997).

Mature mammalian mDA neurons are co-expressing markers such as LMX1A, TH, DAT, PITX3, AADC or DDC and *GCH1*, are post-mitotic and able to produce dopamine. They can also secrete dopamine as a neurotransmitter and re-uptake it at their synapses.

3. mDA neuron published protocols and yields (other labs)

Reference	Cells	Method	NPC results	mDA results	Comments
Chamber et al., 2009	hESCs & hiPSCs	Dual SMAD inhibition & SHH activation	82% neural induction by Noggin and SB dual SMAD inhibition	Some TH+/BIII+ cells with morphology dependent on density	No proper quantification of ICC at neuronal stage
Swistowski et al., 2010	hESCs & hiPSCs	EB with FGF8 and SHH & Wnt and SHH activation	Produces NSCs with high expression Sox1, Nestin, Musashi D10	30% TH+, all of which co-express GIRK2	DA neurons survive graft in rats and improve their function
Cooper et al., 2010	hESCs & hiPSCs	Serum replacement medium & activation Wnt + RA regionalisation & SHH activation	15% FOXA2+ at D19 + some OTX2 and abundant 3CB2 (radial glia) co-expression	10% FOXA2+; 3% FOXA2+/BII+ and <1% FOXA2+/BIII+/TH+ cells at D49	Low final yield and radial glia marker at FP progebitor stage
Kriks et al., 2011	hESCs & hiPSCs	Dual SMAD inhibition & activation Wnt and SHH signalling	59% FOXA2+/LMX1A+ cells at D11 & up to 98% FOXA2+/LMX1A+ cells at D25 when TH expression starts	75% TH+, 80% FOXA2+, 60% LMX1A+ and 55% NURR1+ cells at D50	Good grafting in mouse, rat and monkey models
Xi et al., 2012	hESCs & hiPSCs	Dual SMAD inhibition & activation Wnt and SHH signalling	~ 90% FOXA2+ cells of which 95% co-LMX1A+ and co-EN1+ at D18	60% FOXA2+/TH+ cells among the Tuj1+ cells at D35	These cells electrophysiologically resemble mDA neurons
Kirkeby et al ., 2012	hESCs	Dual SMAD inhibition & activation Wnt and SHH signalling (with EB formation)	81% FOXA2+/LMX1A+ cells & abundant EN1+ ; transplantable NPCs D10	TH+/FOXA2+/MAP2+ cells at D35	No proper quantification of ICC at neuronal stage but maintenance of identity after grafting in rats
Nolbrant et al., 2017	hESCs	Dual SMAD inhibition & activation Wnt and SHH signalling	80-95% FOXA2+/LMX1A+ cells at D11	around 10% TH+ cells, of which 87% co-express FOXA2/LMX1A at D44	Good grafting of D16 cells in rats

Table 25: Overview of relevant references for mDA induction from hPSCs. Table presents type of cells and general method used, and available information on cell characterisation at midbdrain FP progenitor and mDA neuronal stages based on immunocytochemistry.

Based on the knowledge of the neurodevelopmental cues associated with the differentiation and maturation of the mDA neurons, many labs have attempted to develop in vitro models from human and animal ESCs or iPSCs, in order to understand the mechanisms associated with PD or to treat PD via cell therapy. The next paragraphs give an overview of the main methods developed using human cells. Main results for these studies are grouped in Table 25. Figure 34 presents the general principles and molecules used for each of the studies described in Table 25.

Basis for the mDA induction protocol

The two main protocols on which the mDA induction methods presented here are based were published sequentially by the Studer and Parmar laboratories. Kriks and colleagues succeeded in the derivation of mDA neurons from both hESCs and hiPSCs using a dual SMAD inhibition in the presence of SHH signalling activators (purmorphamine and SHH) for ventralisation, FGF8 and chemical GSK3β inhibition (CHIR) for the activation of canonical Wnt signalling (Kriks et al., 2011). Early neural precursors were patterned to midbrain with coexpression of LMX1A and FOXA2 in 59% of the cells at D11 in culture. At D25 cells show an intermediate phenotype, with 98% of cells co-expressin FOXA2 and LMX1A but only 20% TH+/FOXA2+ cells. These later gave rise to cultures with about 75% TH+, 80% FOXA2+, 60% LMX1A+ and 55% NURR1+ cells at D50, which were electrophysiologically active with a behaviour similar to mDA neurons, and which successfully grafted in mouse, rat and non-human primate models (Kriks et al., 2011).

Similar results are obtained using a variation in timing and concentration of the GSK3 inhibitor (Kirkeby et al., 2012). They demonstrated the capacity for Wnt activation to specify different rostro-caudal identities dependent on the concentration of GSK3 inhibitor. This optimisation allowed them to obtain FP progenitor cultures with 81% co-expression of FOXA2 and LMX1A, with a majority of them also expressing EN1 (non-quantified) and which are then able to differentiate into mDA neurons (paper did not provide a quantification of the neuronal cultures) (Kirkeby et al., 2012). The detailed protocol associated with this paper, with information on troubleshooting was published soon after (Kirkeby et al., 2013). A later variation of this protocol, with removal of purmorphamine from SHH activation at the start, delayed FGF8 and slow

adaption of cells to maturation media with incomplete media (BDNF, AA and FGF8 only) for 5 days prior to use of full maturation media as described in preceding protocol, is published by Kirkeby and colleagues (Nolbrant et al., 2017). These gave rise to 80-95% LMX1A+/FOXA2+ cultures at D11, followed by only 10% TH+ cells, of which 87% co-express LMX1A and FOXA2 by D44 (Nolbrant et al., 2017). All information is available in Table 25 and Figure 34.

Other relevant previously published protocol

Chambers and colleagues use Noggin and SB to inhibit SMAD signalisation to push neuralisation prior to the use of patterning molecule activating SHH signalling and neurotrophic support for maturation (Chambers et al., 2009). SHH signalling using SHH-N recombinant protein was at first warranted (Hynes et al., 1995) and applied to numerous protocols, before the advent of Smoothened agonists for the stable activation of SHH signalling *in vitro.*

Similarly, the necessity to activate Wnt for the specification of the cells to the midbrain and not FP only was hindered by the lack of a small molecule capable of activating Wnt without genetic modification of the cells. This came around in the form of CHIR99021, a GSK3β inhibitor allowing the activation of the canonical Wnt signalling pathway. Xi and colleagues then demonstrated that, in addition to dual SMAD inhibition, SHH activation alone leads to a FP destiny but that the addition of an appropriate quantity of Wnt activation concomitantly was necessary for the development of mDA neurons (Xi et al., 2012).

One group points at the lack of appropriate regionalisation of the dopaminergic neurons they had produced using Noggin (Sonntag et al., 2007), with an important co-expression of PAX6 and ISLET1 two transcription factors associated with the dorsal diencephalon but not the midbrain (Cooper et al., 2010). They proceed by describing the use of RA for regionalisation to the midbrain and SHH for the ventralisation of the obtained cells, with low final yield of < 1% cells co-expressing FOXA2/BIII/TH by the end of the cells differentiation and maturation (Cooper et al., 2010).

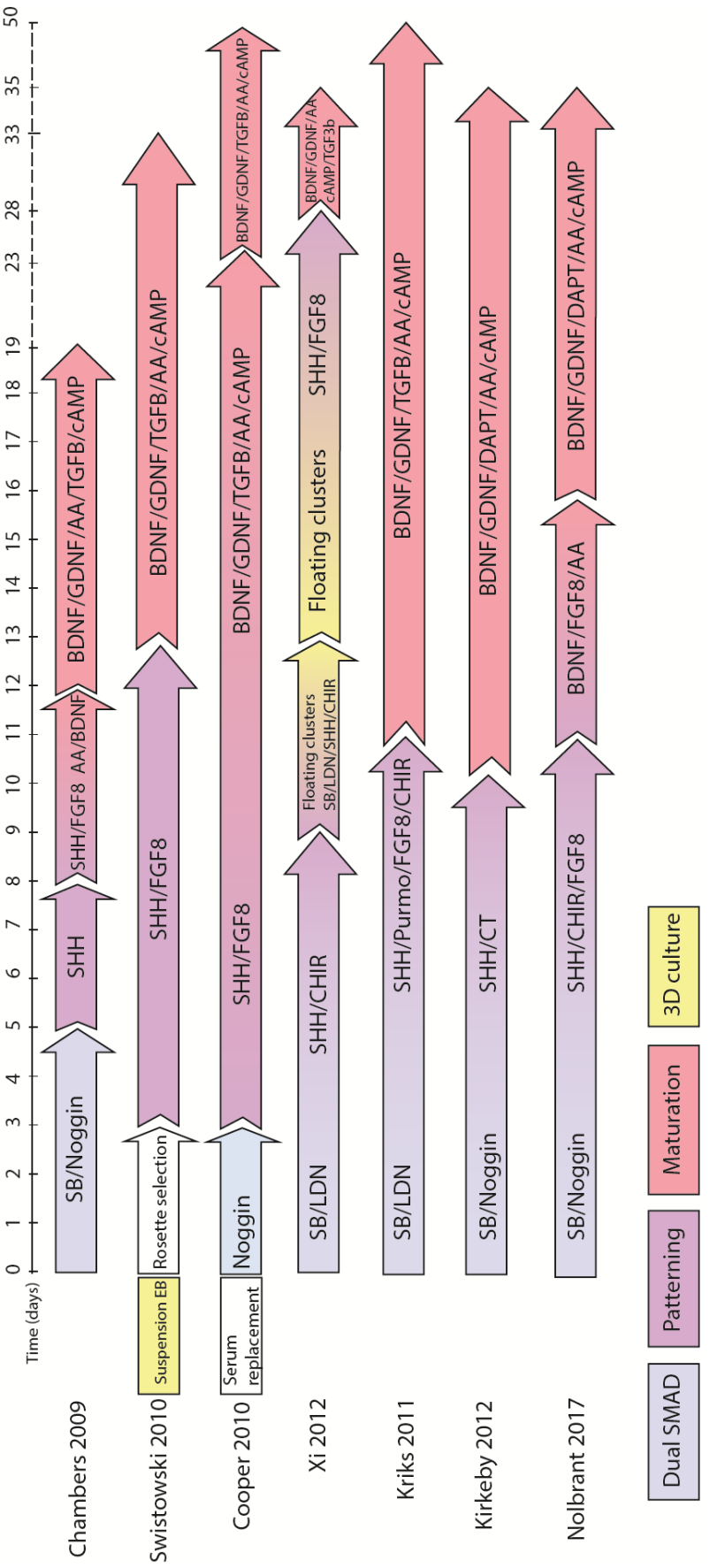

Figure 34: Graphic representation of the most general aspects of the protocols referenced in Table 25.

The same year, another group applied their mDA hESCs-differentiation method to two hiPSC lines, using embryoid bodies followed by SHH and FGF treatment, further replaced by neurotrophic factors. Final cultures contain a large majority of BIII+ cells, with about 30% TH+ cells all co-expressing GIRK2 (Swistowski et al., 2010).

This chapter presents the rationale of our in-house method for mDA neuron induction, as well of efforts to improve the method's yield. It will discuss the caveats and advantages of such a protocol, as well as the possible future applications for this much needed model. Cells issued from this protocol are then used for functional analysis of the differential effect of a *GCH1* mutation between PD and DRD phenotypes in the next chapter.

II. Methods

1. iPSC lines:

Fibroblasts from three patient from a family carrying a heterozygous *GCH1* loss-of-function mutation (c.343+5G>C) and presenting with either PD or DRD were obtained by Dr Niccolo Mencacci. Reprogramming of these fibroblasts to iPSC lines was performed by Censobio, an external company which reprograms cells for research. Stringent quality control of each line is performed by the company before delivering the cell lines: genotyping for aneuploidy, short tandem repeats (STR) profiling in comparison to the original cell sample, pluripotency test with the formation of all three germ-layers (endoderm, mesoderm, ectoderm), mycoplasma and microbiological tests, viability test and pluripotency marker expression via flow cytometry.

Four hiPSC lines from healthy donors routinely used in our lab are selected to complete our case-control set. All iPSC lines are checked for mutations in all 6 exons and exon-intron junctions using Sanger sequencing. Table 26 summarizes the characteristics of the hiPSC lines used for mDA induction.

iPSC line	Donor Phenotype	*GCH1* Mutation	Age of donor	Age at disease onset	Sex of donor	Cell type of origin
CTRL1	Healthy	None	73	N/A	Male	Skin fibroblasts
CTRL2	Healthy	None	64	N/A	Male	Skin fibroblasts
CTRL3	Healthy	None	0	N/A	Female	CD34+ blood cell
CTRL4	Healthy	None	51	N/A	Male	PBMCs
PD	Parkinson's disease	c.343+5G>C (heterozygous)	66	59	Male	Skin fibroblasts
DRD1	DOPA-responsive dystonia	c.343+5G>C (heterozygous)	46	infancy	Male	Skin fibroblasts
DRD2	DOPA-responsive dystonia	c.343+5G>C (heterozygous)	22	3	Male	Skin fibroblasts

Table 26: iPSC lines used in this study. All cell line were Sanger sequenced for any mutations in *GCH1* gene. All lines are from male participants.

2. mDA induction protocol

iPSC are grown in E8 media on geltrex-coated wells and passaged with 0.5mM EDTA. The mDA induction protocol can be started when cells have reached complete confluence (D0): E8 media is removed, cells rinsed with PBS, and placed in freshly reconstituted D0-D6 media. Media is then replaced daily and in excess with D0-D6 media until D6 of the protocol. At D4, cells are split with dispase and plated at a 1:2 ratio as clumps of 300-500 cells onto matrigel coated plates in D0-D6 media supplemented with 10μM RockI (for 24 hours). On D7, media is changed to D7-D9 media after rinsing of cells with PBS, followed by daily changes with D7-D9 media until D10 when cells were rinsed in PBS and placed in N2B27 only. Second split is performed on D11 using dispase, and cells are plated at a 1:3 ratio as clumps of 100-

200 cells onto matrigel-coated 6-well plates in N2B27 supplemented with 10μM RockI for 24 hours. At D12, cells are rinsed with PBS and placed in D12-D13 media for 48 hours with no media change. Cells are rinsed with PBS and placed in D14+ media from protocol D14 onwards. Media can then be changed every 2-3 days at first and up to every 4-5 days as maturation continues. An intermediate accutase splitting of the cells can be performed at D20-25 with cells plated on matrigel-coated 6-well plates at a 1:2-1:3 ratio. Final splitting is performed around D35 using accutase, with cells plated at a final proportion of 30,000-40,000 cells/well in matrigel-coated 8-wells ibidi chambers for further maturation and functional and ICC experiments.

3. Media composition

The neuronal maintenance medium (N2B27) is a 1:1 mixture of N2 and B27 media. N2 medium contains: DMEM/F12 GlutaMAX, 1X N2 supplement, 100μM non-essential amino acids, 100μM 2-mercaptoethanol, 5μg/mL insulin, 50 U/mL penicillin and 50mg/mL streptomycin. B27 medium contains: Neurobasal, 1X B27 supplement, 1X GlutaMAX supplement, 50 U/mL penicillin and 50mg/mL streptomycin. N2 and B27 media are kept in separate bottles at 4 degrees for a maximum of 28 days and are mixed 1:1 into N2B27 as needed.

Media	SB	DM	CHIRR	Purmor-phamine	BDNF	GDNF	Ascorbic Acid	cAMP	Comp-ound E
D0-6	10mM	2mM	3mM	1mM	.	.	.	.	.
D7-9	.	2mM	3mM	1mM	.	.	.	.	.
D12-13	.	.	.	.	20ng/mL	20ng/mL	0.2M	.	.
D14+	.	.	.	.	20ng/mL	20ng/mL	0.2M	0.5mM	0.1mM

Table 27: Media composition for original mDA induction protocol. All reagents are diluted in N2B27 media (1:1 mixture of N2 and B27 media. N2 medium contains: DMEM/F12 GlutaMAX, 1X N2 supplement, 100μM non-essential amino acids, 100μM 2-mercaptoethanol, 5μg/mL insulin, 50 U/mL penicillin and 50mg/mL streptomycin; B27 medium contains: Neurobasal, 1X B27 supplement, 1X GlutaMAX supplement, 50 U/mL penicillin and 50mg/mL streptomycin.).

All differentiation media consist of mixtures of molecules diluted in N2B27: medium for D0-D6 of protocol is composed of 10μM SB, 2μM DM, 3μM CHIRR and 1μM purmorphamine; D7-D9 medium contains 2μM DM, 3μM CHIRR and 1μM purmorphamine; D12-D13 medium contains 20ng/mL BDNF, 20ng/mL GDNF and 0.2mM ascorbic acid; D14+ adds 0.5mM cAMP and 0.1μM compound E to D12-D13

medium. Recapitulation of these media composition can be found in Table 27. All mDA protocol media are prepared freshly and kept at 4 degrees for a maximum of 4 days. Additionally, the time-point appropriate media is supplemented with 10μM RockI for 24 hours at each splitting step of the mDA protocol. All media are kept at 4 degrees and required amounts are warmed up to room temperature on benchtop prior to each media change. All reagents necessary for the preparation of mDA protocol media are kept at -20°C after being reconstituted and adequate small quantities are thawed on bench as necessary for each media preparation. Detailed protocols for iPSC maintenance, dispase and accutase splitting, well coating with geltrex and matrigel and media preparation can be found in the Materials and Methods chapter.

4. mDA induction protocol variation trials

Different variations of the mDA induction protocol presented here were trialled in an attempt to improve the survival of mutant cell lines through the protocol and to increase the final yield of mDA neurons of our method.

Trialled changes for the definition of a more efficient mDA induction protocol are:

- Purmorphamine variation: purmorphamine is withheld from the media composition for the first 48 hours of the original mDA induction protocol in order to increase the effectiveness of neural conversion in our cultures;
- Retinoic acid variations: 0.1uM of retinoic acid (RA) is added to the induction media after the time-point defined as midbrain FP neural progenitor to increase the posterior patterning of the maturing cells, as well as improve the effectiveness of neural conversion and differentiation. As the appropriate condition and timing for the addition of RA is undefined, trials are as:
    - RA1 – addition of RA one day prior to compound E
    - RA2 – addition of RA at the same time as compound E
    - RA3 – addition of RA at the same time as compound E and with the addition of 10μM RockI in the first 24 hours.

To increase survival, timing and ratio for splits are adjusted from the original protocol as follows: cells are split 24 hours earlier than described in the protocol when cells

start lifting off the bottom of the well, and second split at the neural precursor stage is increased from 1:3 to 1:4 when cells are overly confluent.

5. Cell type characterisation

At pre-defined time-points, cells plated on either 8-wells ibidi chambers or glass coverslips (diameter 13mm) in 24-well plates, are fixed using 4% PFA in PBS solution. Briefly, the media is removed; cells are rinsed in PBS and treated 20-30 minutes with 4% PFA at room temperature. PFA is removed and cells rinsed twice with PBS and kept covered in PBS in sealed plates at 4°C prior to ICC experiments.

ICC experiments on fixed cells follow a few simple steps: fixed cells are first permeabilised in a solution of 0.2% Triton-X-100, 3% bovine serum albumin (BSA) in PBS for one hour at room temperature before being incubated with primary antibodies diluted to their appropriate concentration (see below) in PBS 3% BSA for 1 hour at room temperature or overnight at 4°C. Primary antibodies are washed thrice 5 minutes with PBS 3% BSA prior to incubation with fluorophore-conjugated secondary antibodies for an hour at room temperature in the dark. Secondary antibodies are rinsed thrice 5 minutes in PBS 3% BSA with the last wash containing DAPI for cell nuclei labelling. Finally DAPI is rinsed off of all wells or coverslips and these are placed in PBS until mounting (coverslips) or directly for imaging (ibidi).

Image acquisition is performed using an inverted confocal microscope (Zeiss). For each well or coverslip, 3-5 areas representative of cell density were selected randomly using DAPI 405nm channel. Snapshots were taken when cells are found in a single layer; z-stacks were used for capturing several layers of cells when necessary.

Images are analysed on Fiji (ImageJ) using Cell counter, a manual counting tool and manual selection of regions of interest (ROIs) when appropriate. Areas where nuclei are not clearly delineated are removed from all channels prior to counting. Cell counter and ROIs manager sets files were saved for future reference. Expression of each marker is expressed as the proportion of cells positive for the marker out of all DAPI-stained nuclei in the field.

III. Results

1. Rationale of the mDA induction method

The method for induction of mDA neurons from hiPSC developed in our laboratory can be separated in two major phases: neurogenic phase associating neural FP induction signals to inhibition of pluripotency via dual SMAD inhibition; and maturation phase with the use of neurotrophic factors and Notch inhibition to arrest the cell cycle Figure 14.

In the first (neurogenic) phase, iPSC are placed in a mix of small molecules to achieve dual SMAD inhibition and activation of both SHH and Wnt signalling. The dual SMAD inhibition method, first described by Chambers and colleagues, induces neuralisation through the blockade of endodermal (TGFβ) and mesodermal (BMP) signals (Chambers et al., 2009). TGFβ inhibition is achieved through the use of SB-431542 (SB), a potent and selective inhibitor of TGF-β type I receptors ALK5, ALK4 and ALK7 (Inman et al., 2002); and BMP signal is inhibited through the use of dorsomorphin dihydrochloride (DM), a potent inhibitor of BMP type I receptors ALK2, ALK3 and ALK6 and of protein kinase A (PKA) (Yu et al., 2008). Use of PKA inhibition is further supported by the PKA-sensitivity of DA differentiation in vitro (Hynes et al., 1995). SHH signalling is activated with purmorphamine, a Smoothened agonist which directly binds to Smoothened receptor to promote the expression of Hh target genes via Gli transcription factors expression (Sinha and Chen, 2006). The activation of SHH signalling concomitant to dual SMAD inhibition is found necessary to upregulate FOXA2 expression, via Gli, allowing for a patterning of the pre-neuroepithelial cells obtained by dual SMAD alone to the FP and not the PAX6 expressing neuroepithelium fate (Denham et al., 2012). Finally, activation of Wnt signalling is permitted by the addition of CHIR-99021 (CHIR), a highly selective inhibitor of GSK-3 (both α and β isoforms). GSK3β is an enzyme involved in β-catenin phosphorylation, leading to its degradation. In its unphosphorylated form, β-catenin first accumulates in the cytoplasm and then eventually localizes in the nucleus to modulate gene transcription allowing signal transduction through the canonical Wnt/β-cat pathway (Huang et al., 2017b). Downstream targets of Wnt signalling

include LMX1A, PITX3 and NURR1, all essential for mDA patterning and/or survival (Xi et al., 2012).

The success of the first phase in patterning iPSC to the mDA neuronal fate can be estimated with ICC experiments based on the nuclear co-expression of FOXA2 and LMX1A around D12 of the induction protocol (Andersson et al., 2006). LMX1A expression is present in human mDA neural progenitors in the ventricular zone of the FP as early as PC week 6 and is maintained throughout the mDA neuron life (Hebsgaard et al., 2009). Expression of both LMX1A and FOXA2 is observed in the midbrain FP progenitors in the developing human brain (Nelander et al., 2009).

In the second (maturation) phase, neural precursors which have been committed to mDA differentiation path are placed in neurogenic conditions to further support their maturation to mDA neurons. During this maturation phase, cells are first placed in the presence of ascorbic acid and neurotrophins: brain-derived neurotrophic factor (BDNF) and glial cell-line derived neurotrophic factor (GDNF). These neurotrophins are required for the differentiation and survival of mDA neurons at different stages in the developing human brain. Ascorbic acid (or vitamin C) is a naturally occurring antioxidant known to protect cells against ROS-associated oxidative stress and to stimulate mDA differentiation from neural precursors *in vitro* and *in vivo* grafts (Bagga et al., 2008; Kalir and Mytilineou, 1991; Yan et al., 2001). Importantly in the case of dopaminergic neurons, BH4 gets oxidised to BH3 by buffering the ROS produced during dopamine synthesis and ascorbate is necessary for the reduction of BH3 to BH4 (Kuzkaya et al., 2003). All three molecules are also able to protect mDA neurons against toxin-induced injuries both *in vitro* and *in vivo* (Sautter et al., 1998; Sun et al., 2005; Wagner et al., 1985). Co-culture of mDA neurons with BDNF and GDNF improve the quality of mDA neuron cultures prior to grafting (Sautter et al., 1998).

Media containing all three molecules is subsequently supplemented with cyclic adenosine monophosphate (cAMP) and compound E. cAMP is used to activate cAMP/PKA signalling pathway by enhancing PKA enzymatic activity and is known to promote mDA neuron differentiation from hPSCs (Xia et al., 2016). Moreover, later introduction of compound E in the media in addition to the neurogenic factors inhibits Notch signalling through γ-secretase inhibition, effectively delaying the cell cycle

transition from G1 to S phase long enough for the neurons to terminally differentiate. Notch is required for the maintenance of neural precursors in an undifferentiated self-renewing state, effectively preventing neurogenesis *in vivo*, and allowing fast-cycling precursors to overcome any post-mitotic differentiated cell in the culture dish. Notch inhibition with compound E is thus used to promote neuronal differentiation, leading to a more mature cell phenotype *in vitro* (Borghese et al., 2010). Compound E was successfully used in previously published protocols for the derivation of various neuronal subtypes from hiPSCs (Hall et al., 2017; Xie et al., 2018).

The success of this protocol at inducing differentiation of mDA neurons from iPSC is determined by the proportion of cytoplasmic expression of BIII-tubulin and TH. Other markers such as DAT and GIRK2 are also associated with mDA neuron maturation and their expression can be assessed using ICC.

2. Attempts at the mDA induction protocol

A total of 13 inductions are performed using *GCH1* and control lines, of which:

- Subsets of the cell cohort, each pairing mutant and control lines, are used for trialling the original mDA induction method (4 separate attempts);
- Due to high variability in cell survival and protocol yield between these first attempts, a control line was used for further protocol optimisation (4 separate attempts);
- Final induction protocol is chosen and run on complete sets of cell lines (all 3 *GCH1* mutant lines and 3-4 control lines) (5 separate attempts)

Of these 13 inductions, five did not provide any results due to: infections (2) or spontaneous cell death and detachment in the absence of infection prior to analysis time point (2), or due to media composition trial associated with cells detachment (1). For the remaining 8 inductions, ICC is used to determine phenotype at various time-points and results are discussed here. Cells from 4 inductions are used for functional imaging and results presented in the next chapter. A breakdown of the cell lines used, protocols attempted and characterisation results available is given in Table 28.

	Lines	Protocol	NPC staining (D12)	mDA staining	Functional imaging	Comments
1	CTRL1 PD	Original mDA induction	FOXA2 LMX1A PAX6 OCT4 (CTRL1 only)	TH BIII	No	Testing the original protocol
2	CTRL2 DRD1	Original mDA induction	LMX1A PAX6 OCT4	TH BIII PAX6 OCT4	No	Testing the original protocol
3	CTRL1	mDA induction variations trials	FOXA2 LMX1A PAX6 OCT4	BIII GFAP Ki67 TH GIRK2 DAT	No	Comparing conditions to determine best protocol Intermediate D21 ICC
4	CTRL1	mDA induction variations trials	FOXA2 LMX1A PAX6 OCT4	BIII GFAP Ki67 TH GIRK2 DAT	No	Comparing conditions to determine best protocol
5	CTRL1 CTRL2 CTRL4 PD DRD1 DRD2	Original mDA induction and purmorphamine variation	FOXA2 LMX1A BIII GFAP Ki67 NFIA OCT4		Yes at NPC and mDA stages	Ameliorated frequency and ratio of splitting, two inductions ran simultaneously

6	CTRL1 CTRL2 CTRL4 PD DRD1 DRD2	Original mDA induction	LMX1A FOXA2	-	No	Aborted at D14 as NPC ICC results were not optimum
7	CTRL1 CTRL2 CTRL3 CTRL4 PD DRD1 DRD2	Original mDA induction	LMX1A FOXA2	-	Yes at NPC stage	Aborted at D28 of protocol as neuronal cell overgrown by cells of unknown nature in culture
8	CTRL1 CTRL2 CTRL3 CTRL4 PD DRD1 DRD2	Original mDA induction	LMX1A FOXA2	-	Yes at NPC stage	Used for confirmation of functional imaging in NPCs from previous sets of induction

Table 28: Breakdown of the different inductions which have provided characterisation results

3. Characterising cells at the iPSC stage using ICC

ICC is performed prior to the start of the mDA induction protocol (D0) as quality control for the maintained pluripotency of the lines (OCT4) and the absence of spontaneous neuronal differentiation (PAX6, a neuroepithelial marker). Both markers are transcription factors and are thus located in the nuclei. At D0, 99.42% of all cell nuclei stained with DAPI show nuclear expression of OCT4 (94.11-100%, n = 5605 positive cells out of 5638 cells analysed across 12 fields in all our lines). Moreover not a single one of these cells is found positive for PAX6 (

Figure 35). This supports the maintenance of pluripotency and the absence of spontaneous neuronal differentiation in our iPSC cultures, making these cultures appropriate for undergoing the mDA induction protocol.

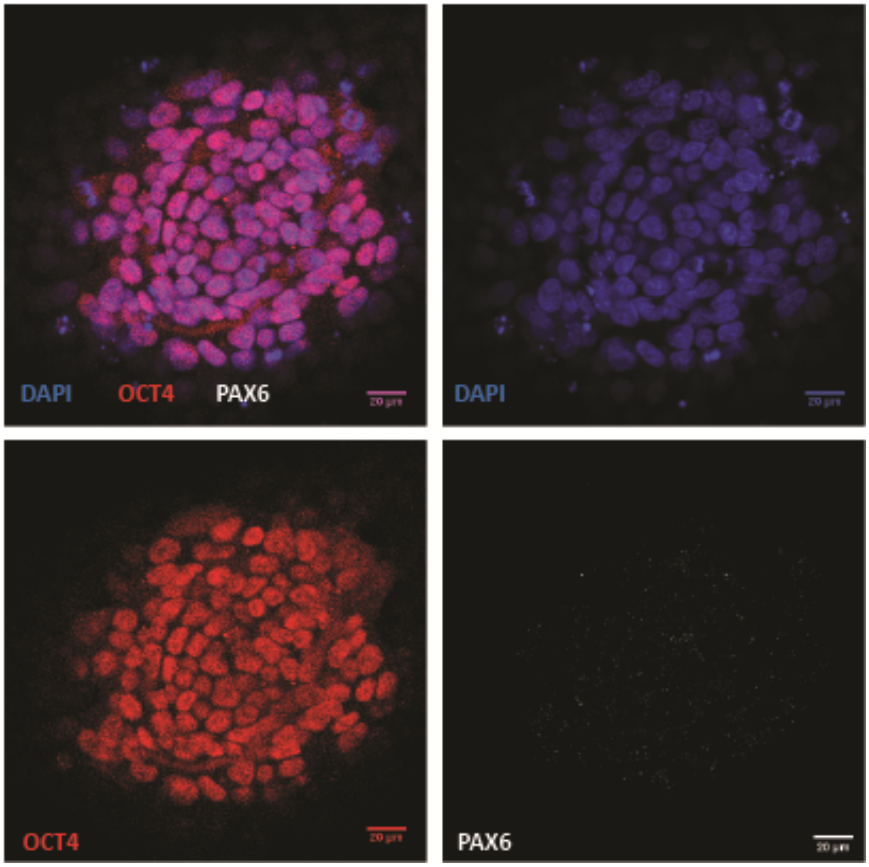

Figure 35: OCT4-PAX6 staining example in iPSCs PD line at D0, prior to start of induction protocol. OCT4 expression can be observed in all DAPI-stained nuclei, while there is no visible PAX6 staining in these cells.

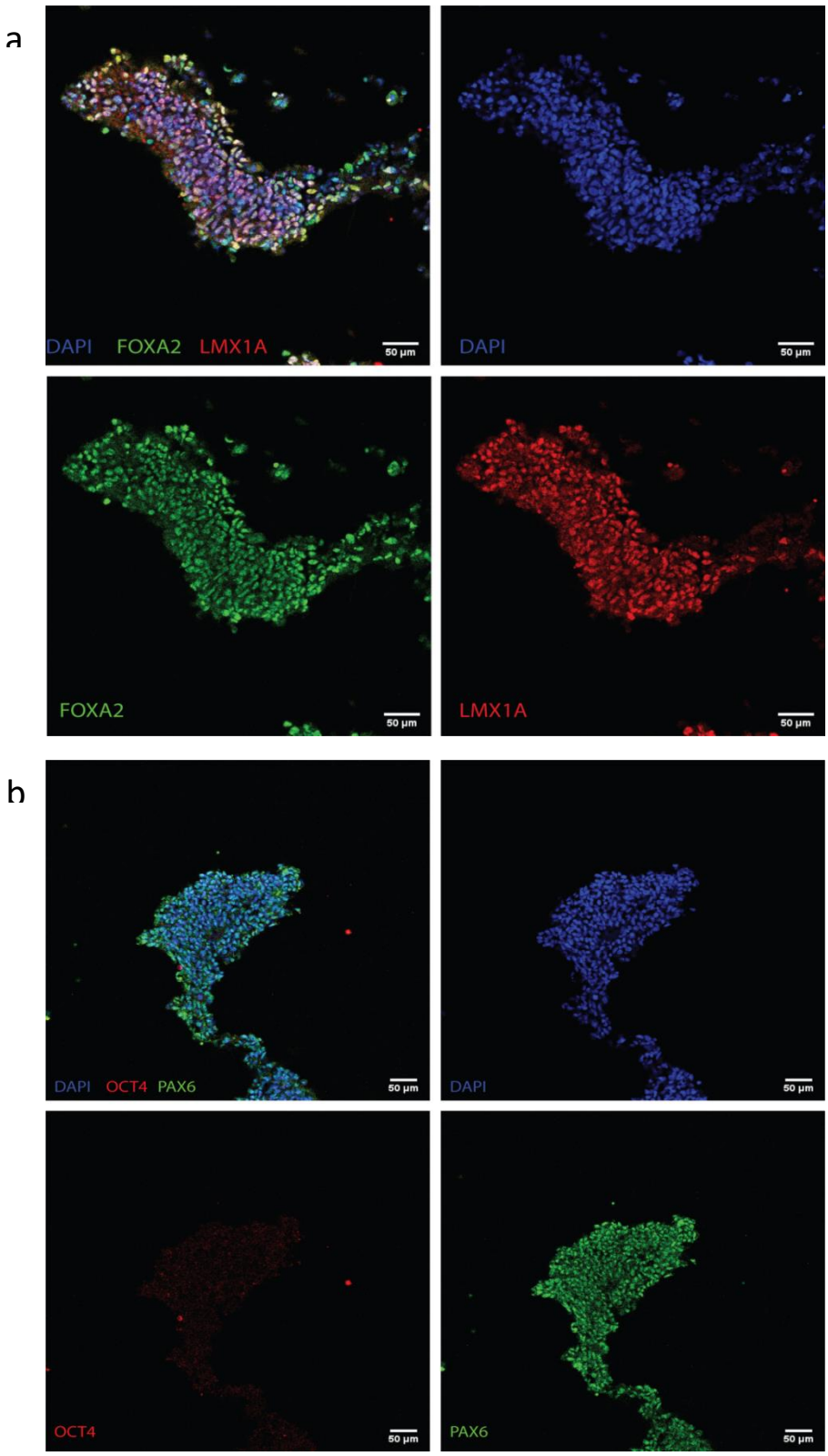

Figure 36: Example of ICC for mDA FP neuroprecursor cells at D12 of the mDA induction protocol. Figure shows the strong co-expression of LMX1A and FOXA2 (a), as well as PAX6 (b); associated to the loss of expression of OCT4, a pluripotency marker (b) in control cells.

4. First attempt results and rationale for improving method

During the mDA induction protocol, cells are subjected to external cues aiming to reproduce their normal differentiation conditions in the developing brain. Accordingly, at D12 of the mDA induction protocol which corresponds to a time-point between the neurogenic and maturation phases of the protocol, cells should have reached the intermediate stage of mDA FP neural progenitors, when cells are developmentally patterned to becoming mDA neurons but do not yet express mature mDA neuron markers. To confirm this, cells are tested for the co-expression of markers of the FP (FOXA2) and roof plate (LMX1A) typical of the midbrain using ICC (Figure 36a). Expression of the pluripotency marker OCT4 and the early neuroepithelial marker PAX6 are also ascertained to establish the identity of the cells in culture and the success of the protocol at neuralizing our cells at this stage (Figure 36b). Between my first two inductions, each performed on a case-control pair (CTRL1 and PD for the first set and CTRL2 and DRD1 for the second set) ICC was performed on both controls and the DRD1 line (after the early death of all PD cells prior to protocol D4 first split). All cells have lost their pluripotency marker OCT4 by D12 of the mDA induction protocol (n = 5283 cells across 6 fields) in both first sets of induction. However, cell fate markers differ between inductions. High proportions of cells express each marker in the first induction set with: 97.9% LMX1A+ (96.73-99.57%, n = 2503 cells across 3 fields); 94% FOXA2+ (87.75-98.27%, n = 2503 cells across 3 fields); and 94.7% PAX6+ (88.84-98.28% n = 2445 cells across 4 fields) (Figure 37a). In the second induction set, there is a slightly lower expression of LMX1A (75% cells LMX1A+ in n = 994 cells across 2 fields) and a drastically decreased proportion of PAX6+ cells (10.9% PAX6+ cells in n = 2838 cells across 2 fields) (Figure 37a). Altogether these results suggest an important variation in differentiation behaviour between lines and/or inductions with this method, from an early stage. However the method is efficient at supporting midbrain markers expression from this first stage of differentiation (Figure 37b).

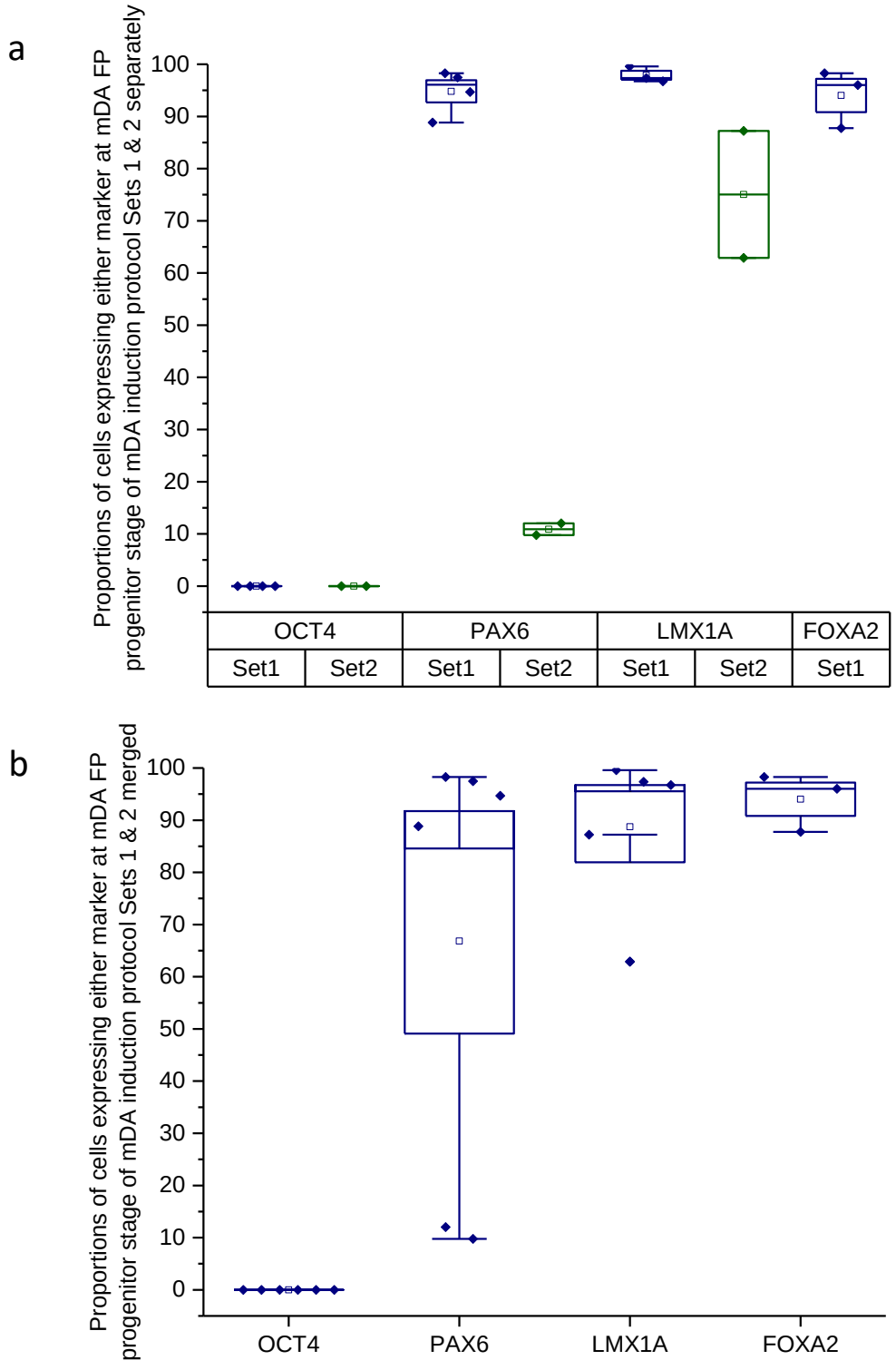

Figure 37: Characterisation of cells undergoing the mDA induction protocol at D12 for the first two induction sets. Results are presented for these two sets (a) separately and (b) pooled together. Cells marked by ICC as expressing each of the four markers are counted and proportion is calculated as number of cells expressing each marker / total number of cells estimated using DAPI staining.

The mDA induction protocol was primarily designed to yield a high proportion of mDA neurons within a month in culture. Markers for mDA neural differentiation are immuno-labelled at this time-point to determine protocol feasibility in the *GCH1* lines. Results are pooled for both sets as they are very similar. Neural differentiation efficiency is first assessed using anti-Tuj1 antibody which recognises epitopes of BIII-tubulin in our cells, expressed in all neurons; and TH for the mDA subtype (Figure 38&Figure 39). The cultures comprise of only 8.9% Tuj1+ cells (2.38-19.51%, n = 4457 cells analysed across 9 fields) (Figure 40). Additionally, 5.3% of all cells are TH+ (0.72-9.59%, n= 3163 cells analysed across 8 fields), a marker of dopaminergic differentiation in neurons, as TH is a necessary enzyme for the production of dopamine. Finally, no OCT4+ or PAX6+ cells are visible in these cultures (n = 1267 cells analysed across 2 fields). PAX6 is an early pan-neuronal marker which is found restricted to the forebrain in later developmental stages (Mastick and Andrews, 2001), supporting the non-forebrain commitment of the visible neurons in our cultures. Similarly, there was no GIRK2 labelling in any cells (n = 3595 cells across 8 fields), a specific marker of the midbrain. There remains the possibility that the GIRK2 primary antibody was defectuous as other members of the laboratory failed to observe any positive cells in different types of cultures. And a small proportion of cells of ~2.5% Ki67+ cells are still dividing (Figure 40). These suggest that the further maturation of our mDA-patterned midbrain FP neural progenitors does not yield a high proportion of mDA neurons by D30. Moreover, with regards to these first results, it is necessary to modify our protocol to increase mDA neuron differentiation yields in our cultures through to the second stage of differentiation.

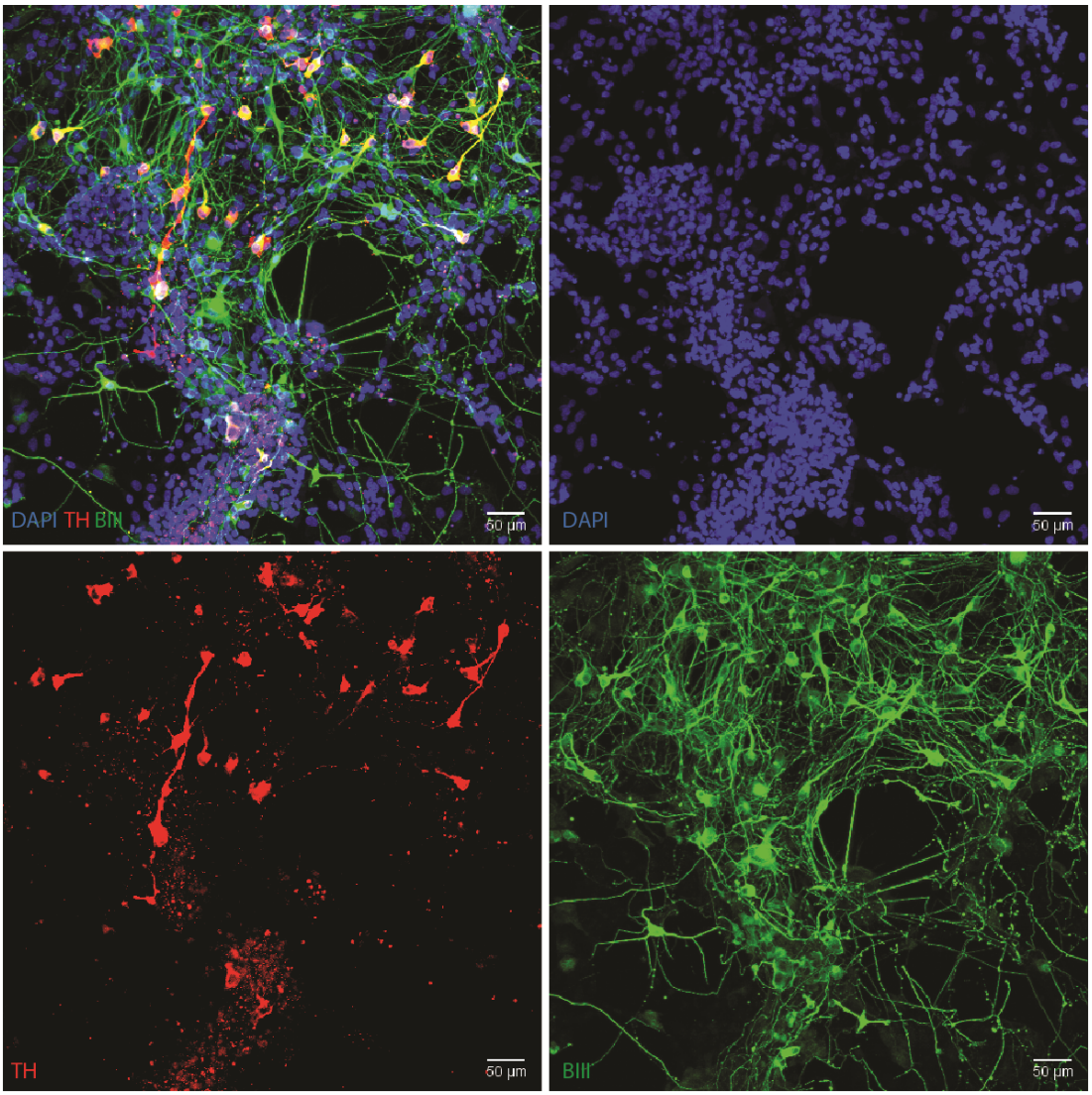

Figure 38: Example of staining at D65 of the mDA induction protocol. Figure shows the co-expression of BIII, TH and DAPI, as well as each staining separately on control cells in a complete field of view.

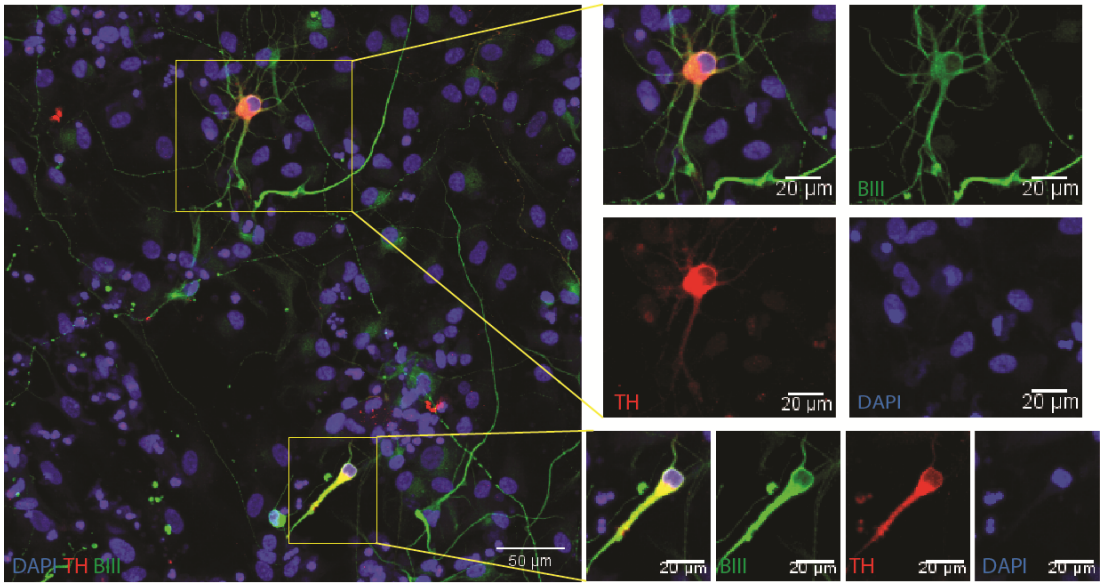

Figure 39: Example of staining at D65 of the mDA induction protocol, with detail from a field of view. Figure shows the co-expression of BIII, TH and DAPI, as well as each staining separately on control cells.

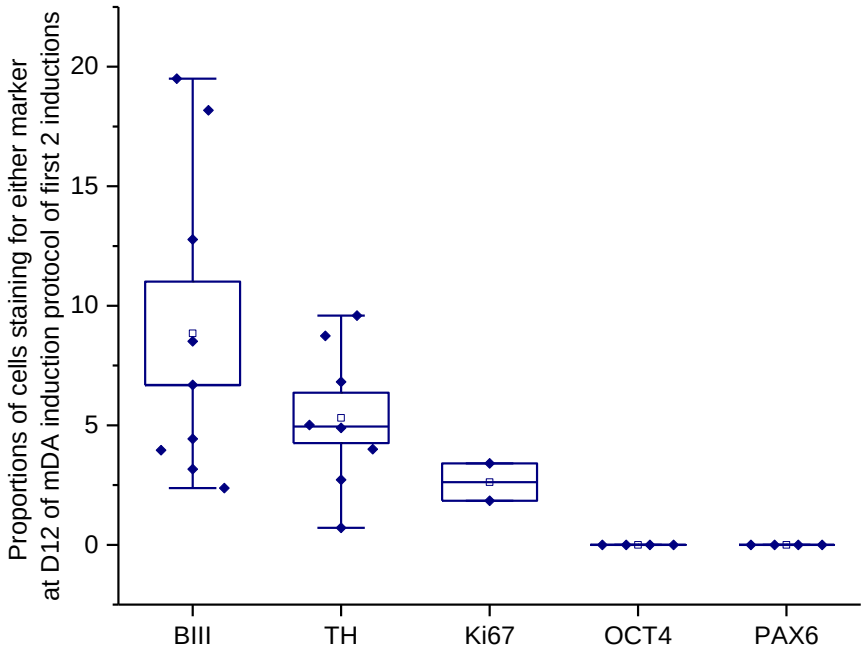

Figure 40: Characterisation of cells undergoing the mDA induction protocol around D30 for the first two induction sets pooled together. Cells marked by ICC as expressing each of the five markers are counted and proportion is calculated as number of cells expressing each marker / total number of cells estimated using DAPI staining.

5. Defining the right conditions

Using these first two inductions as baseline, and the control used in the first induction attempt which yielded relatively pure mDA patterned cultures at D12 with low yield by around D30 as model, protocol modifications were attempted.

The first attempted modification aimed at delaying the activation of SHH signalling in our cultures, similarly to its expression starting post-gastrulation and after the loss of complete pluripotency of the PSCs during development, by withdrawing purmorphamine for the first 48hours of the mDA induction protocol. There is no significant effect of the delaying of SHH signalling activation on the patterning of the midbrain FP progenitors obtained at D12 of the mDA induction protocol. While the original protocol yielded 56% LMX1A+ cells (15.4-92.4% in n= 3014 cells across 5 wells), 58% of the cells are LMX1A+ in the purmorphamine delay condition cultures (35.5-80.5% in n = 3301 cells across 7 wells) at D12. Proportion of PAX6+ cells in

these cultures are 7.9% (5.8-10.7% in n = 1892 cells across 5 wells) and 17.1% (15.2-19.5% in n = 2845 cells across 3 wells) for the regular and delayed SHH conditions respectively (Figure 41). There are differences in proportions of LMX1A+ and PAX6+ cells between the two sets of inductions for these trials on the same control line, but numbers of fields are too low in each set to compare these statistically (data not shown). However this suggests a role for variability between inductions, independent from the used cell line.

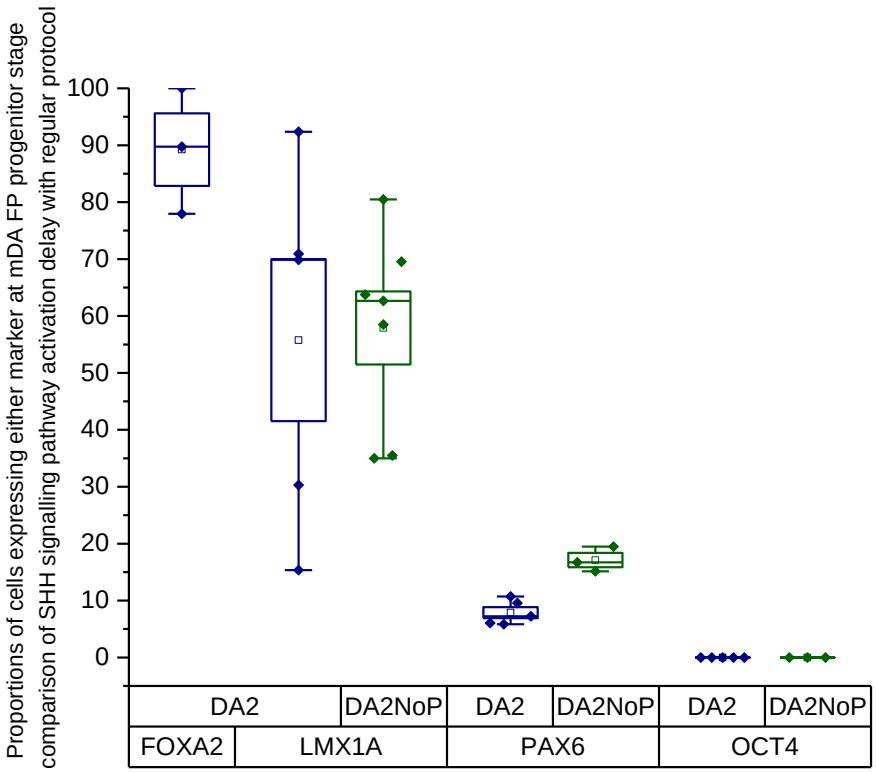

Figure 41: Protocol variation with SHH delaying. Represents the ICC characterisation of D12 cells, for regular mDA induction protocol (DA2) and SHH delaying trial (DA2NoP). Cells marked by ICC as expressing each of the five markers are counted and proportion is calculated as number of cells expressing each marker / total number of cells estimated using DAPI staining

The effects of delaying activation of SHH signalling for 48 hours are assessed as the final proportion of cells expressing either TH or BIII-tubulin or both, as well as by the absence of Ki67 immunolabelling consistent with a post-mitotic neuronal state at D40. Proportions of cells expressing BIII-tubulin are 56.5% cells in the regular protocol (52.5-66.6% in n = 880 cells across 4 fields) and 51.4% in the SHH delay condition (24.3-80% in n = 348 cells across 3 fields) (Figure 42). Similarly, the number of TH+ cells are 17.4% (9.5-23.6% in n = 901 cells across 4 fields) and 9.9% (7.9-11.9% in n

= 694 cells across 2 fields) in these two conditions respectively (Figure 42). Ki67 expression in these cultures is estimated alongside BIII-tubulin, with cultures showing 21.3% Ki67+ cells using the initial method (11.4-27.5% in n = 880 cells across 4 fields) and 30.1%(22-46.1% in 348 cells across 3 fields) using the SHH delay condition (Figure 42). None of the Ki67+ nuclei are found in cells expressing cytoplasmic BIII, supporting a successful differentiation to post-mitotic neuronal cells. The cultures show no PAX6, OCT4, DAT or GFAP expression in either condition at this stage.

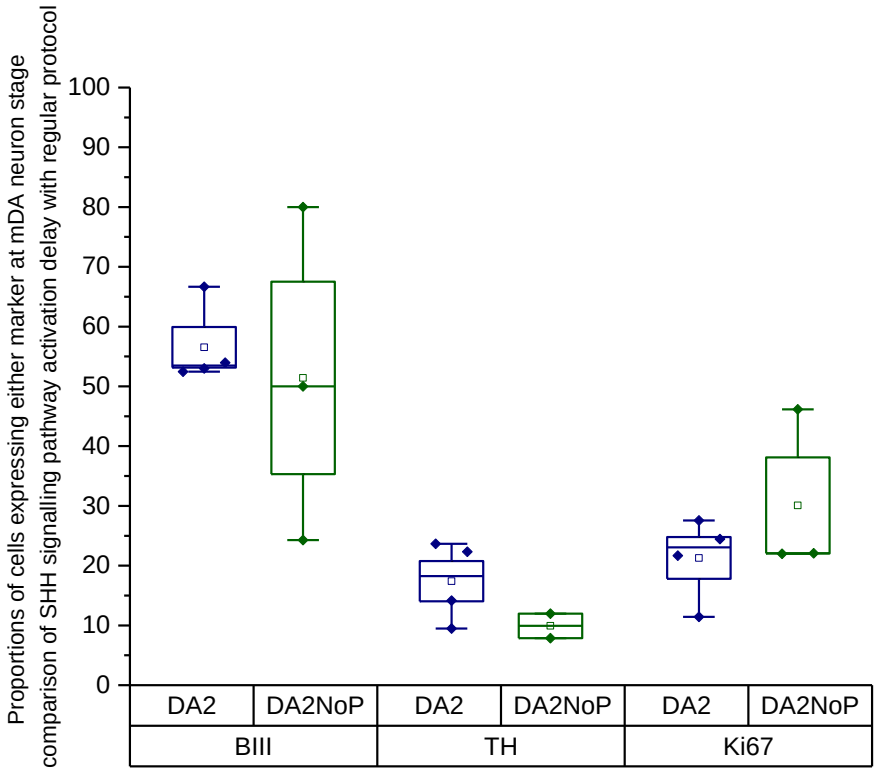

Figure 42: Protocol variation with SHH delaying. Represents the ICC characterisation of D40 cells, for regular mDA induction protocol (DA2) and SHH delaying trial (DA2NoP). Cells marked by ICC as expressing each of the five markers are counted and proportion is calculated as number of cells expressing each marker / total number of cells estimated using DAPI staining.

PAX6 is an early marker of the neuroepithelium (~D4), which is later only found in the forebrain. The significance of PAX6 expression at the stage described here as midbrain FP progenitor may be associated with either delayed inhibition of its expression in culture or a more rostral identity of the cells than warranted. In order to improve the rostro-caudal patterning another modification of the protocol consists in the addition of 0.1uM of the caudalizing agent retinoic acid to the cultures using three

different experimental paradigms, namely R1, R2 and R3. These are tested in parallel to the SHH delay condition trial. As these are implemented later than D12, their efficiency at promoting the induction of mDA neurons is estimated using dopaminergic neuronal markers BIII, TH and DAT, as well as Ki67 as a marker for mitotic cells and GFAP for glial cells. At D40, that is 4 weeks after addition of RA to the cultures, proportion of cells expressing BIII, TH and Ki67 are roughly similar between conditions. Proportion of BIII+ cells vary from 15.8% to 80% between wells and across the different conditions, with the highest yield stably achieved by the regular mDA induction protocol with 56.5% BIII+ cells on average (52.4-66.6% in n = 880 cells across 4 fields) (Figure 43). Proportion of TH+ cells vary from 5.9-23.7% between wells and across the different conditions, with the highest yield stably achieved by the regular mDA induction protocol with 17.4% TH+ cells on average (9.5-23.6% in n = 880 cells across 4 fields) (Figure 43). Finally, the proportion of Ki67+ cells vary from 7.6-53.8% between wells and across the different conditions, with the lowest yield stably achieved with the RA2 condition on the base of delayed SHH activation with 11.05% Ki67+ cells on average (7.66-14.45% in n = 1399 cells across 2 fields) (Figure 43). None of the cultures show expression of either GFAP nor DAT. The first supports the absence of mature astrocytes in our cultures. The second, as DAT is a marker for mature DA neurons, may be suggesting that the cultures will require a longer maturation stretch to obtain fully mature mDA neurons. However, DAT is present in pre-synaptic neurons at the synaptic cleft, and as such its absence from the culture may be associated with the lack of dopaminergic synapses (Horn, 1990).

There is thus no statistically significant effect of the delay of SHH signalling activation or the addition of RA, following any of the three defined experimental paradigms, on the proportion of cells expressing any of these three mDA markers. Moreover, the original protocol seems to achieve more advantageous yields overall, with a somewhat higher proportion of BIII+, TH+ and lower Ki67+ cells, all supportive of an overall higher experimental yield. An optimised version of the original protocol is thus used, including minor changes to plating density and frequency of media changes from empirical experience, to produce the cultures used for functional imaging.

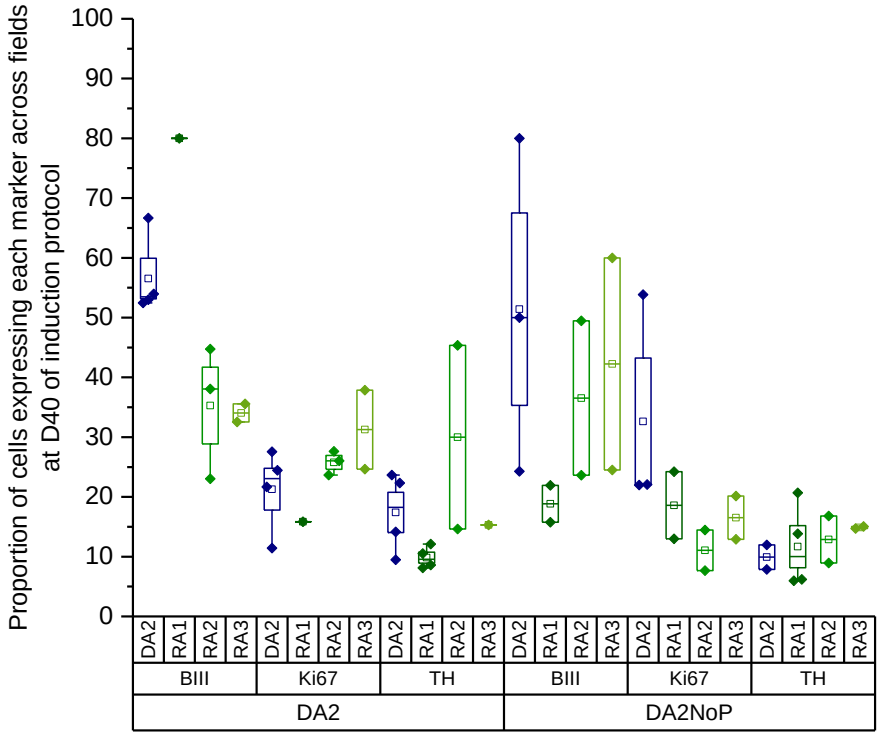

Figure 43: Proportion of cells expressing each marker at D40 of induction protocol. Cells are stained for BIII expression, Ki67 expression and TH expression. Conditions for the induction are defined as regular (DA2) or delayed SHH activation (DA2NoP) with the addition of RA 0.1uM according to the different protocol paradigms (RA1-3) or without (DA2).

6. Line to line variability

Induction efficiency varied between the lines used, with most differences found between controls and *GCH1* mutant lines. While there was no identifiable difference between the cell groups defined as cell-donor phenotype in OCT4 expression as a marker for pluripotency prior to the start of the mDA induction protocol (Figure 44), differences are observed for all final markers by the end of the protocol (Figure 45). Indeed, control lines overall yielded higher proportions of neurons (BIII labelling), of which more were dopaminergic (TH labelling). However, this was in the presence of a more important proportion of mitotic cells in control and DRD group than PD group (Ki67 labelling) and with more background glial differentiation in controls than mutant groups (GFAP labelling) (Figure 45). These observations are not statistically significant, probably due to the low number of observations and further validation will be necessary to validate this finding.

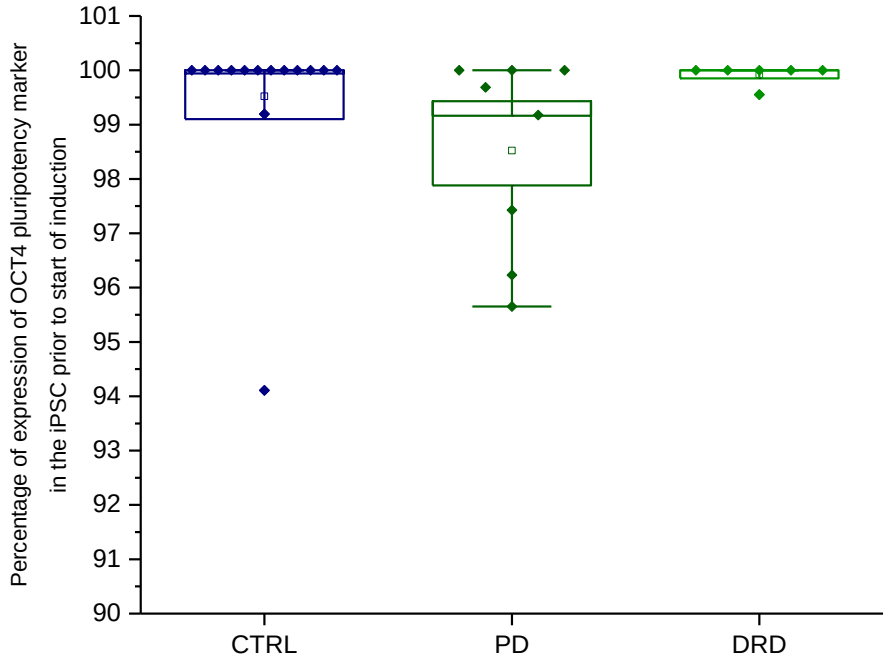

Figure 44: OCT4 expression at the start of induction protocols. Oct4 is used as a marker for pluripotency in cell groups defined by donor phenotype

Nevertheless, this supports the role for an inter-line variation in the mDA neuron yield of the proposed protocol, which may be associated with adverse effect of the mutation on the capacity of the *GCH1* mutant cells (PD and DRD groups) to efficiently differentiate into mDA neurons. This is supported by previous observations of a rescue of mDA differentiation capacity by BH4 and sepiapterin treatments in iPSC-derived model of BH4-insufficiency (Ishikawa et al., 2016). Additionally, one reason for the limited number of observations by the end of the protocol is the loss of lines by detachment or well-wide cell death, especially in the PD and DRD groups, supporting this hypothesis.

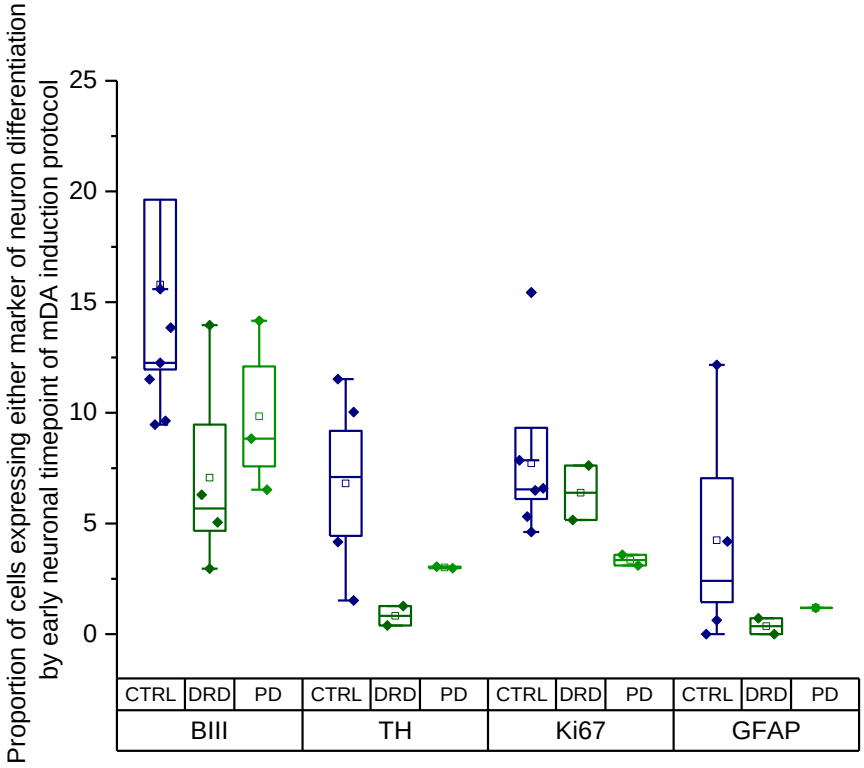

Figure 45: Expression of neuronal differentiation markers at the end of the mDA induction protocol. Groups are defined by cell donor phenotype

IV. Discussion

Many protocols making use of small molecules to replicate natural neurodevelopmental cues, have failed to produce high purity mDA neuron cultures from hPSCs in a timely manner. This chapter presents the protocol developed by the Patani laboratory to achieve this goal, as well as my attempts at improving this method using delayed SHH signalling activation and stronger rostro-caudal specification. These attempts were unsuccessful to significantly increase method's yield and the protocol chosen to produce the cells used in the functional analysis chapter of this thesis consists in the original method, while including minor changes in length, frequency of splits and splitting ratios.

Results from the several attempts at the protocol varied greatly between inductions but also between lines. Both may be at least in part associated with hiPSC presenting a high variability of gene expression, with line-specific enrichment of developmental pathway gene expression, affecting their differentiation tendencies (Carcamo-Orive et al., 2017; Liang and Zhang, 2013). Hence, case-control pairs are originally used to trial the protocol in both wild type and mutant cells and confirm the ability of the iPSC lines to undergo neural differentiation, and a single control is used for trialling protocol changes in an attempt to limit observed variations to the effect of these controlled changes in culture conditions. The last sets of induction are performed on either 3 or 4 controls and 3 patient lines for further functional analyses. This is in the absence of a strict consensus on the number of lines, both cases and controls, necessary for the development and replication of a differentiation protocol. Additionally, the used iPSC lines are passaged more than 15 times as an extended number of passages helps to reduce the risk for high proportion of CNVs in iPSC lines (Hussein et al., 2011; Laurent et al., 2011). Importantly lower differentiation efficiencies and higher variability have been observed in iPSC lines compared to ESC lines, making the application of protocols developed in ESCs more complex to adapt to iPSC-based research projects (Hu et al., 2010).

The yields achieved with our method are quite comparable to those reported in the literature using similar methods (Cooper et al., 2010; Nolbrant et al., 2017; Swistowski et al., 2010), with the exception of Kirks and colleagues who obtained 75% TH+, 80%

FOXA2+, 60% LMX1A+ and 55% NURR1+ cells at D50 (Kriks et al., 2011), although these could not be replicated in our lab using their method. Finally some articles did not provide precise counts of their final yields, nor reasons for these omissions (Chambers et al., 2009; Kirkeby et al., 2012). Survival and differentiation yields are quite different between and within inductions, pointing at a possible effect of proliferation, gene expression or genetic background on the induction ability of the cell lines used in this project. The highest degree of discrepancy between lines is generally found between cases and controls, with observations such as the recurrent loss of mutant cell lines at various stages of differentiation, with no predicted effect of the mutation on the neurodevelopment of mDA neurons. In order to maintain observation of variation to the differences existing between control and mutant lines, other sources of variation are tested for. Due to the high number of failed attempts at inducing mDA differentiation, the operator and effect of the mutation on differentiation capacity are tested as potential sources of technical discrepancy. Dr Minee Choi trialled the method in parallel on different mutant lines but with the same controls, and observed similarly high variation in differentiation yield and cell survival both between lines and between inductions. These difficulties may be underlying the lack of improvement of the time-efficiency of protocols in 13 years, one of the main aim of these trials, pointing at a possible "minimum" period of time needed for human dopaminergic neuron maturation *in vitro* (Marton and Ioannidis, 2018).

1. hiPSC model advantages and issues

hiPSC-derived neurons from patient cells have many advantages associated with their origin. hiPSC provide researchers with the complete genetic background which gives rise to a disorder, increasing the chances to observe similar phenotypes in vitro as in vivo, and the possibility to study the mechanisms associated with this phenotype or to test new drugs. The ability to stably produce large quantities of high purity mDA neurons in culture, from the self-renewing hiPSC source, will greatly improve the access to disease-relevant human tissue for the study of PD and other mDA neuron-associated disorders such as DRD. It would also facilitate their use in cell replacement therapy approaches with an important reduction of the risk for graft rejections when the iPSC are derived from the grafted patient. However, iPSC-derived models are

imperfect due the nature of both iPSC reprogramming and induction methods, such as cell age marker 'reset'. An alternative method would be direct differentiation of mDA neurons from fibroblasts, which can allow the maintenance of epigenetic markers associated with the age and the effects of environmental cues on the patient (Caiazzo et al., 2011), both important factors in complex late-onset disorders such as PD. These protocols may also be able to remove the teratogenic risk associated with iPSC-derived grafts due to the possible presence of progenitor cells in the culture, while maintaining their safety for cell replacement therapies by removing the donor-host rejection risks. Direct induction of skin fibroblasts to neuronal cells was demonstrated in 2010 using three transcription factors in a lentiviral expression vector (Vierbuchen et al., 2010). It was closely followed by the use of transcription factors with crucial roles in dopaminergic neuron specification and maturation to allow direct conversion of fibroblasts to DA or mDA neurons (Caiazzo et al., 2011; Kim et al., 2011; Pfisterer et al., 2011) or induced midbrain dopaminergic neural progenitors (Kim et al., 2014), in some cases with the addition of small molecules to increase yields. However these methods are using lentiviral vectors which convey some risks for cells integrity and limit conversion ability. These caveats are being overcome with the development of methods involving the use of a combination of small molecules and microRNA (Jiang et al., 2015).

Finally, most methods aim at the production of quasi-pure cultures containing a single cell type (here mDA neurons). This removes all observations of the effect of cell type interactions in the disease mechanisms, cell survival and fine-tuned neurodevelopmental cues. Co-culture of mDA with astrocytes increased mDA neuron survival while protecting mDA neurogenesis and attenuating mitochondrial dysfunction in an iPSC-derived mDA model (Du et al., 2018), suggesting the potential presence of high stress in pure mDA cultures and along the differentiation of this cell subtype, supporting a strong potential for cell death *in vitro*.

2. Technical difficulties for yield determination with ICC

Induction protocols require very high confluency at early stages for the definition of a neuroepithelial-like cell layer necessary to the derivation of midbrain FP progenitors;

as well as in later stages where high confluency is necessary to the survival of the cells. However, at this later stage, there remains the possibility that such a high confluency may hinder the ability for the neurons to mature due to contact-mediated inhibitions (Šestan et al., 1999) or simple lack of space to extend neurites. Additionally, replating cells once mDA neurons are post-mitotic and present with long and complex networks of neurites is a technical challenge often resulting in massive cell death, while replating them earlier at a lower ratio impacts cells viability. From the minor inconvenience of having to dissociate nuclei visually for the study of nuclear labelling in highly confluent settings, the difficulty to associate cytoplasmic labelling with a defined nucleus with little doubt, even more so with long and intersecting projections, becomes highly challenging and cannot yet be automatized. Selecting areas of low cell density to overcome these difficulties may be tempting but will bias all results as they are not representative of the cultures. Due to the highly subjective nature of such counts, and in order to remove a part of the operator-associated bias, all images for each labelling experiment are analysed on the same day, allowing less biased comparisons within inductions for the trial of separate conditions.

3. Future improvements

One possible approach to increase the yield of induction of mDA neurons from hiPSC is the use of FACS sorting using specific external markers. This can be performed at the NPC stage selecting for CD184+/CD271-/CD44-/CD24+ cells which are co-expressing PAX6, Sox1 and Sox2 as per a previous report (Yuan et al., 2011). Although these selected cells have a high survival rate they are multipotent and can further differentiate into both neurons and glial cells (Yuan et al., 2011), which may not improve the yields achieved with cultures co-expressing LMX1A and FOXA2 obtained with the mDA induction protocol. Sorting at a later stage than the one defined as NPC in this protocol could yield better results. The same paper proposes a later sorting of CD184-/CD44-/CD15low/CD24+ cells yielding post-mitotic neurons (98% BIII+ 2% Nestin+ and 0.6% ki67+ cultures) which are able to fire action potentials (Yuan et al., 2011). One additional external protein, Corin, has been extensively used for the separation of neural progenitors of the ventral midline with a mDA fate, as it is co-expressed with FP4, an intracellular protein itself co-expressed with LMX1A (Ono

et al., 2007). Corin is also expressed in other cells of the caudal FP and its sole expression does not guarantee mDA fate, necessitating its combination with another undefined marker to separate rostral and caudal mDA FP cells. Finally, Schondorf and colleagues have used a combination of CD24high/CD29-/CD184-/CD44-/CD15- to increase by 6.1 fold the expression of DA markers in their iPSC-derived mDA model by sorting a population of cells containing 15-20% TH+ cells co-expressing FOXA2, NURR1, GIRK2 and VMAT2 as well as showing punctate synapsin 1 labelling (supporting a mature neuronal phenotype in these cultures) (Schöndorf et al., 2014).

Another possible improvement is associated with the stricter mimicking of neurodevelopmental cues such as the transient activation of Wnt necessary for the development of the midbrain, which is then inhibited in this anterior neural tube structure as a caudalizing and dorsalising factor in the development of the neural tube (Nordström et al., 2002; Ulloa and Martí, 2010). At a stage similar to advanced midbrain FP progenitor in vitro, the use of a Wnt antagonist, such as XAV939 or WNT-C59 (Motono et al., 2016), may increase efficiencies of mDA neuron induction protocols.

Transplantation efficiency studies have found that mDA yield following engraftment of cells in rat models do not correlate significantly with the expression of genes which are commonly used to identify mDA progenitors and neurons in most in vitro differentiation protocols, namely Foxa2, Lmx1a, Corin, TH, Nurr1 and DDC. Other markers, specific of the caudal ventral mesencephalon (VM) and the midbrain-hindbrain boundary including Pax5, FGF8, SPRY1, EX1/2, SP5, ETV4/5, CNPY1, TLE4 and Wnt1 correlate better with yields *in vivo* (Kirkeby et al., 2017). Single cell sequencing of LMX1A positive mouse VM demonstrated that progenitor cells expressing caudal VM markers En1/2, Wnt1 and Cnpy1 are significantly more likely to produce mDA neurons than cells expressing Lmx1a/b, Foxa1/a2, Otx2, Msx1, and Nurr1 that ultimately produce glutamatergic subthalamic neurons (Kee et al., 2017). Replacing the previously used markers with markers for a caudal VM could thus improve the comparison of dopaminergic neuron differentiation protocols for the purpose of transplantation (Marton and Ioannidis, 2018). However this does not preclude the possibility that these commonly used markers are also valid *in vitro* for

the identification of an appropriate subtype of neural progenitor able to mature to mDA neuron in culture. These may however be of importance for protocols aiming at cell-therapy translation.

Fidelity and relevance of the models has to be ascertained by comparison of the in vitro iPSC-derived neuronal cell models and their counterparts in vivo-derived embryonic, foetal, adult and aged cells (Patterson et al., 2012). Transcriptome studies find iPSC-derived cortical neuron models to resemble an embryonic state, although length of culture advances their molecular maturation to some extent. However, despite several months in culture, cell maturity doesn't seem to get beyond that of foetal human cells in their transcriptional signature (Stein et al., 2014). Similar observations were made in comparison of whole-genome gene expression and transcript splicing between hESC-derived multipotent neural precursor cells and differentiated mDA neurons and post-mortem foetal and adult human counterparts from brain samples (Patani et al., 2012b). Yet undefined molecules could be added to cell cultures for improving maturation. It remains possible that intrinsic properties of iPSCs-derievd cell types, as iPSC undergo forced development both artificially induced and significantly shortened, may prevent them from acquiring an adequate transcriptional maturation.

This chapter thus describes the methods used to derive midbrain dopaminergic neuronal cells from patient-derived iPSC, a model relevant for the study of *GCH1*-related disorders *in vitro*. Cells derived from the most successful attempts to this protocol have been used to investigate the effect of the 343+5G>C *GCH1* mutation on cell functions putatively associated with *GCH1* and its downstream product BH4. These results are developed and analysed in the next chapter.

Chapter 6: Functional investigations of GCH1 mutation-associated Parkinson's disease and DOPA-responsive dystonia phenotypes in an iPSC-derived dopaminergic neuron cell model

I. Introduction

The development of an appropriate patient-derived model of midbrain dopaminergic (mDA) neurons allows for the comparison of cellular functions between Parkinson's disease (PD) and DOPA-responsive dystonia (DRD). This model could hold the key to understanding the development of such different disorders in patients carrying the same GTP cyclohydrolase 1 (*GCH1*) mutation. Variants in *GCH1* are found in 87% of DRD cases but less than 1% of the PD cases, however more than 35% of DRD patients report first degree family history of PD (Clot et al., 2009; Hagenah et al., 2005; Mencacci et al., 2014). Single *GCH1* mutations segregate with both pathologies in large families demonstrating the dual phenotypic effect of these mutations in humans (Irie et al., 2011; Lewthwaite et al., 2015; Nygaard, 1993). This points at possible mechanistic differences, possibly at the cellular level, between patients carrying the same *GCH1* mutation but exhibiting different pathological phenotypes. These differences found between molecular and organism level may be replicated in a patient-derived cell model such as the one used in this chapter.

The association of a single *GCH1* mutation with two different phenotypes could be explained by variations in the impact of the reduction of BH4 levels on the BH4-associated mechanisms in the patient's mDA neurons. In DRD, which presents with a midbrain dopamine depletion phenotype which can be corrected by the supplementation of a dopamine precursor downstream of BH4-associated TH activity, the phenotype is probably associated with an impairment of the dopamine synthesis aspect of BH4 function, while other BH4-associated functions may be preserved. DRD patients show no signs of neurodegeneration as suggested by rare brain histopathology reports (Furukawa et al., 1999; Rajput et al., 1994; Segawa et al., 2013). In contrast to *GCH1*-related PD associated to neurodegeneration as evidenced by DAT scan imaging, the differential diagnosis of DRD in clinics makes use of the absence of signs of degeneration in these images (Albanese et al., 2011; Marshall and Grosset, 2003; Nygaard et al., 1992). Moreover, the good and sustained response to low doses of L-

dopa in DRD patients is suggestive of the maintenance of an appropriate population of mDA neurons, able to uptake and make use of this dopamine precursor to re-establish a normal dopamine production and correct the patient motor symptoms. These observations are supportive of a purely dopamine-associated impairment of BH4 functions in the DRD patients carrying this *GCH1* mutation. In PD the reduction in dopamine production, if present in carriers of a *GCH1* mutation, is insufficient to produce motor symptoms prior to decades of injuries to the dopaminergic cells of the substantia nigra and their ultimate degeneration. The appearance of the hallmark motor symptoms defined as the onset of the pathology is preceded by decades of slow progression of both non-motor and subtle motor prodromes, and defined pathology stages (Braak et al., 2003; Noyce et al., 2012). Hence, although insufficient to create a dopamine-related phenotype in early stages of the pathology, a *GCH1* mutation in a PD patient may be associated with decades of impairment of BH4-associated cell functions directly leading to, or increasing the susceptibility for, the ultimate degeneration of the midbrain dopaminergic neurons.

Based on these observations, I hypothesise that a single *GCH1* mutation can operate differently to generate a different functional phenotype: in DRD, causing a simple loss of dopamine which can be corrected by L-dopa supplementation; and in PD causing neuronal loss either through chronic lack of dopamine or through an alternative mechanism related to the other functions of the *GCH1*-BH4 pathway.
In order to understand the functional effect of a *GCH1* mutation in dopaminergic neurons, putative non-dopamine related BH4 functions are investigated in a midbrain dopaminergic cell model derived from both PD and DRD patients, from a single family carrying a heterozygous loss-of-function *GCH1* mutation.

GTPCH, the protein coded by the *GCH1* gene, catalyses the rate-limiting step of the production of BH4, the essential co-factor of tyrosine hydroxylase (*TH*) for the production of dopamine (DA). Besides this fundamental function in dopaminergic neurons, BH4 is involved in the maintenance of cytoplasmic redox balance but also specifically of the mitochondria, as well as in the coupling of all three isoforms of the nitric oxide synthase (NOS) (Figure 6).

1. Putative involvement of mitochondrial function

Mitochondria are highly dynamic cell organelles known as the 'powerhouse' of the cells as their main function is the production of energy in the form of ATP via the oxidative phosphorylation pathway. The electron transport chain (ETC), composed of protein complexes in the inner mitochondrial membrane, generates and maintains an electrochemical gradient across this membrane known as the mitochondrial membrane potential (MMP). Complexes I, III and IV produce and maintain the MMP through exchange of electrons and passage of protons through the inner mitochondrial membrane, which energy is harnessed for the synthesis of ATP by complex V, through a process known as oxidative phosphorylation which requires oxygen (reviewed in (Papa et al., 2012)). This process is normally associated with the production of ROS by the mitochondria (mtROS). Mitochondria are also involved in the metabolism of amino acids and lipids, as well as in the regulation of cellular calcium homeostasis, apoptosis, and free radicals scavenging (reviewed in: (Spinelli and Haigis, 2018)).
Neuronal cells rely heavily on their mitochondria to provide for their high energy demand necessary to maintain neuronal intracellular ion homeostasis despite the frequent opening of ion channels for the propagation of action potentials and neurosecretion (Halliwell, 2006). The pacing mechanism of dopaminergic neurons is based on frequent calcium influxes, requiring calcium buffering by the cell mitochondria. When mitochondrial dysfunction prevents calcium buffering, increased intracytoplasmic calcium increases NOS activity and NO production, which can react with the mitochondria-produced superoxide giving peroxinitrite. Peroxynitrite has a deleterious effect on ETC leading to further mitochondrial dysfunction (Radi et al., 1994). Moreover, superoxide produced at the mitochondria can be converted to H2O2 leading to increased oxidative damage in the cells (Angelova and Abramov, 2018). Due to the close association of the mitochondrial functions, disruption of either may affect all, leading to self-propagating deleterious cycles.

Ageing, the most common risk factor for PD, is associated with impaired mitochondrial function and quality associated to decreased ETC activity and increased mutational burden of mtDNA (Payne and Chinnery, 2015). The burden of mtDNA deletions is even more important in the surviving pigmented cells of the SN of PD patients compared to matched healthy controls, associated with a decreased ETC

activity and increased mtROS production in these cells (Bender et al., 2006; Kraytsberg et al., 2006). These may be even more relevant in mDA neurons which have high basal rates of oxidative phosphorylation, associated with higher mtROS production (Haddad and Nakamura, 2015). Moreover, impairments of the complex I of the mitochondrial respiratory chain have been described in PD patients platelets (Parker et al., 1989) and in human post-mortem substantia nigra tissue (Schapira et al., 1989). Inhibitors of complex I such as rotenone and MMP+ are routinely used in animal modelling of PD (Ballard et al., 1985; Martinez and Greenamyre, 2011) and mutations in genes such as Parkin and PINK1, which functions are directly associated with the mitochondria, have been associated to PD (Houlden and Singleton, 2012).
Finally BH4 is suggested to affect mitochondrial function. *GCH1* mutations associated with reduced BH4 availability in the cells may be associated with increased oxidative damage of the mitochondria through the reduced scavenging of mitochondrial-produced superoxide (Nakamura et al., 2001), or the increase of mitochondrial superoxide production probably through impairment of mitochondrial respiration and redox signalling (Bailey et al., 2017) ; and impaired mitochondrial activity by MPP+, leads to an important reduction in *GCH1* activity and resulting lower BH4 production (Ryan et al., 2014).

2. Putative involvement in NOS function

Nitric oxide (NO) is a highly diffusible and reactive molecule, able to travel several cell lengths, involved in cell-to-cell communication in the brain (Bredt and Snyder, 1994). NO is produced by all three isoforms of the nitric oxide synthase (NOS) enzyme: endothelial NOS (eNOS), inducible NOS (iNOS) and neuronal NOS (nNOS). All three isoforms catalyse the conversion of substrates L-arginine and molecular oxygen to NO and L-citrulline, and require the cofactors tetrahydrobiopterin (BH4), reduced nicotinamide-adenine-dinucleotide phosphate (NADPH), flavin adenine dinucleotide (FAD) and flavin mononucleotide (FMN). All NOS bind calmodulin and contain haem (reviewed in (Förstermann and Sessa, 2012)).

BH4, the downstream product of *GCH1*, is thus necessary to the normal function and activity of NOS as an essential cofactor of all three NOS isoforms. It is believed to act

in two ways: by allowing the dimerization of NOS to activate its activity and by increasing NOS affinity for L-Arginine. In the absence of BH4, NOS activity is uncoupled and the enzyme produces superoxide instead of NO (Vásquez-Vivar et al., 1998, 2003). Moreover, BH4, but not its reduced form BH2, is necessary for NOS coupling, as exampled by the effect of an imbalanced BH4:BH2 ratio in increasing NOS uncoupling and the rescue from this phenotype by the expression of dihydrofolate reductase, which reverts BH2 to BH4 (Crabtree et al., 2008, 2009b). And it is the limited availability of BH4 and not L-Arginine which is responsible for this uncoupling (Bevers et al., 2006).

In the brain of the *hph1* mouse, a model of GTPCH insufficiency associated with reduced BH4 levels, there is a reduced NOS activity which can be reverted to control levels when supplemented with exogenous BH4. This reduced activity is not associated with a lower NOS concentration in the *hph1* mouse brain and, as BH4 strongly increases the affinity of NOS for Arginine, lower BH4 results in severely limiting arginine availability for NOS activity (Brand et al., 1995).

3. The antioxidant function of BH4

While oxidants are constantly present in healthy cells, they are effectively buffered by the presence of antioxidants protection, molecules which are able to donate or accept an electron from ROS in order to stabilise the structure of the oxygen molecule which is in a highly unstable highly reactive partially reduced state. ROS include oxygen radicals such as superoxide, hydroxyl radical and hydrogen peroxide, as well as non-radical oxygen based molecules which can easily be converted to free radicals. BH4 is a powerful enough antioxidant to compensate for the absence of glutathione in dopaminergic neuron cells (Gramsbergen et al., 2002; Nakamura et al., 2000). Its ability to scavenge superoxide has been observed in dopaminergic neurons (Nakamura et al., 2001). It is thus possible that reduced BH4 content, secondary to decreased GTPCH activity, is associated with a limited ability for the dopaminergic neurons to cope with free radicals, including these produced by the synthesis of dopamine itself.

In addition to GSH and BH4, the brain is enriched in other low molecular mass antioxidants such as ascorbate which is found at millimolar intracellular concentration in neurons and astrocytes, thanks to their expression of specific transporters concentrating the molecule intracellularly (Rice, 2000).

4. Deleterious consequences of oxidative stress and NOS uncoupling

In the absence of an efficient antioxidant system, basal levels of ROS produced by mechanisms such as mitochondrial respiration and dopamine synthesis can accumulate, and ROS may be found in excess in these neurons. All free radicals are highly diffusible and reactive, giving them the capacity to oxidise all molecules around them. The accumulation of these injuries can result in the impairment of important cell mechanisms and may increase the basal production of ROS via cell metabolism. Eventually cells enter the deleterious state of oxidative stress, a self-renewable state in which ROS production and antioxidant protection are imbalanced, leading ROS to produce more ROS and to a significant increase in oxidative damage of the cells, potentially leading to apoptosis.

Oxidative stress is believed to play an important role in PD pathology, with extensive research multiplying evidence for the presence of oxidative stress in a large number of PD models and its involvement in many of the pathological processes associated with the development of PD pathophysiology. Oxidative stress markers are found systematically increased in the blood of PD patients compared to controls (Seet et al., 2010). Evidence for oxidative damage to proteins in the form of protein carbonyls is found in PD-associated brain regions such as substantia nigra and putamen in post-mortem tissue when compared to age-matched controls (Alam et al., 1997). Moreover in dopaminergic neurons, dopamine and L-DOPA can interact with oxygen to produce superoxide, increasing oxidation, and also quinones and semiquinones which decreases the antioxidant response to superoxide by depleting intracellular GSH, thus creating an oxidative environment for themselves (Halliwell, 2006). Finally the extreme requirement of mDA neurons on high quantities of energy results in higher basal rates of oxidative phosphorylation than VTA dopaminergic neurons unaffected by PD, probably an important source of ROS in itself (Mortiboys et al., 2018).

Lipid peroxidation is the result of the oxidation of the lipids of the cellular membrane by free radicals. Post-mortem studies demonstrate a significantly increased lipid peroxidation in the substantia nigra of PD patients compared to controls. In one study, evidence for higher lipid peroxidation intermediate (MDA - basal malondialdehyde) and lower availability of lipids available to lipid peroxidation (PUFA – poly-unsaturated fatty acid) is more largely observed in PD than control brains (Dexter et al., 1989). In another study, signs of lipid peroxidation are found in the substantia nigra of brains with early parkinsonian pathology in the absence of neurological symptom in life, as well as in other brain areas such as the frontal cortex, supporting a role for lipid peroxidation in the early stages of PD pathology (Dalfó et al., 2005).

In a situation of oxidative stress, the production of NO by neurons, is associated with a high risk of production of reactive nitrogen species, such as peroxynitrite. Peroxynitrite, produced by the reaction of NO with superoxide, is able to nitrate tyrosine protein residues, leading to impaired protein function (Gandhi and Abramov, 2012). It was also shown that nitrosative insult through stimulation of peroxynitrite production is associated with a-synuclein accumulation into perinuclear inclusions in HEK293 cells (Paxinou et al., 2001). Additionally, peroxynitrite is prompt to react with CO2 at physiological pH, an abundant molecule in cells, resulting in carbon radicals which act as oxidants in the cells. Peroxynitrite can also gain secondary oxidant properties by reacting with transition metal centres. These reactions are reviewed in (Radi, 2013). Finally, a main centre for the production of peroxynitrite in the cells is the mitochondrion, due to the mitochondrial production of superoxide and the capacity for NO to diffuse through the cytoplasm. There, peroxynitrite reacts with the proteins of the respiratory chain and affect their activity, leading to alterations to ATP production, calcium homeostasis and increased production of superoxide (Bringold et al., 2000; Radi et al., 1994).

Based on the known roles of BH4, and redox signalling in dopaminergic neurons and PD, I hypothesise that *GCH1* mutations may induce alterations in mitochondrial function, increased oxidative state of the cells, NOS activity through decoupling and increase the likelihood of cell death in PD cells. I investigated whether these were affected in mutants compared to controls and between disease phenotypes by making

use of molecular fluorescent probes and live functional imaging-based estimation of MMP (TMRM), NOS function (DAR-4M) and redox state of the cell (MitoROS, DHE, mCB and Bodipy). These were measured in the hiPSC-derived cultures at the mDA FP neural progenitor (NPC) and mDA neuronal stages. A summary of the investigations performed at various stages of the mDA induction protocol can be found in Figure 46.

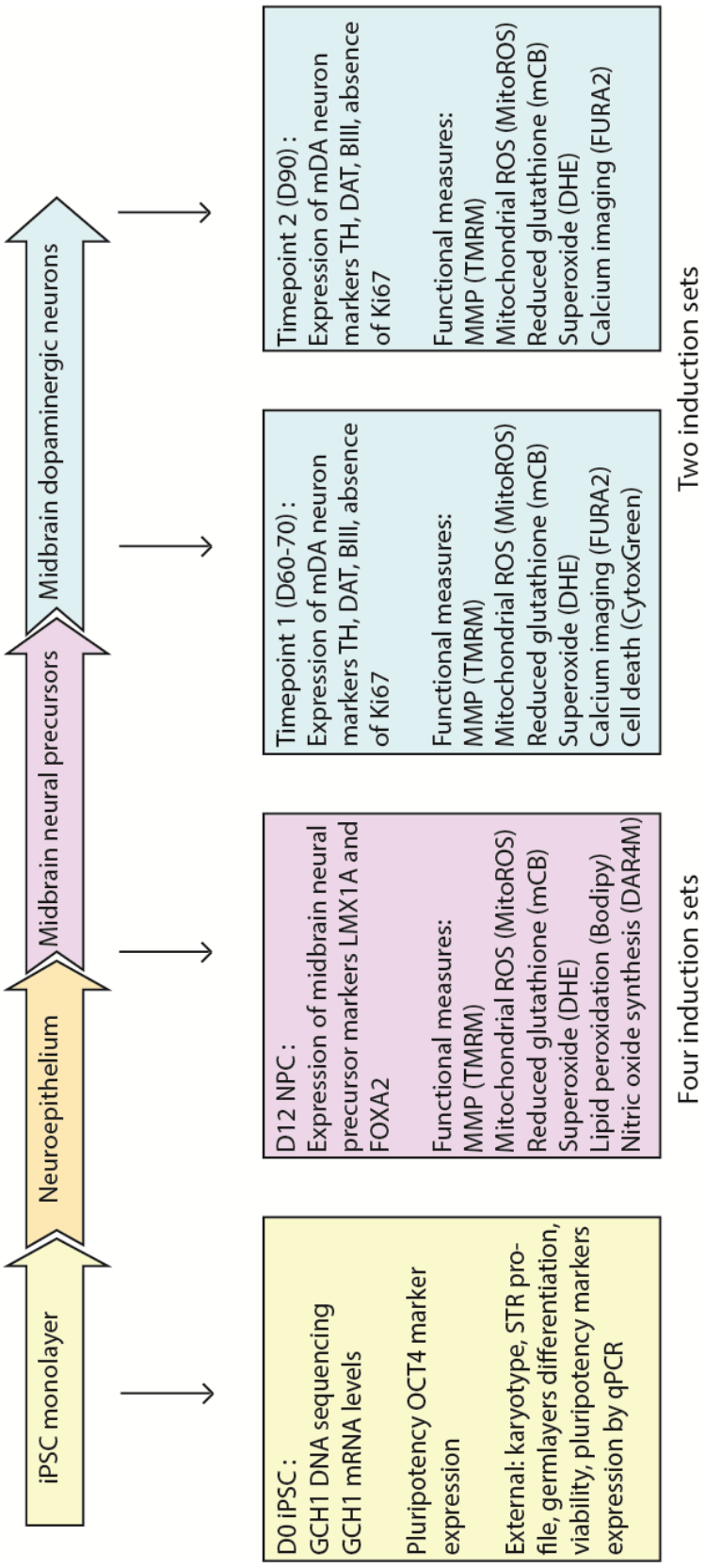

Figure 46: Sets of functional imaging. The different stages of cell differentiation are represented linearly. Each box describes the characterisation and the functional imaging performed at each timepoint in the number of induction sets indicated below.

II. Materials and Methods

1. Immunocytochemistry for identity validation

Immunocytochemistry (ICC) is used to ascertain cell type identity prior to functional imaging. NPC identity is determined by the nuclear co-expression of LMX1A and FOXA2. mDA neuron identity is determined with cytoplasmic co-expression of BIII-tubulin and TH, in the absence of Ki67. Briefly, ICC uses a primary antibody from a non-human species and specifically directed against the protein of interest. The signal is then amplified with the use of a secondary antibody from a third species directed against the species of the primary, associated with a fluorophore. Images are captured on an inverted Zeiss confocal fluorescence microscope (710, 780 or 880 pending availability). Images are manually quantified using Fiji (ImageJ). Results are presented as percentage of cells positively labelled with either antibody out of total number of nuclei as stained with DAPI. Details on used antibodies, conditions and ICC protocol can be found in the Materials and Methods chapter of this thesis.

2. GCH1 molecular analysis in the iPSC

DNA is extracted from iPSC cultures for all lines to validate the mutational status of the cells with regards to the *GCH1* gene. DNA is extracted using the Qiagen DNeasy mini kit (Qiagen). All exons are sequenced following the Sanger method, based on the use of in-house designed primers. Briefly, PCR for each exon and surrounding exon-intron boundaries is performed with the FastStart PCR method (Roche) and PCR product is cleaned using ExosAP-IT (Affymetrix). Sanger sequencing is performed separately for each amplicon in both forward and reverse directions using BigDye Terminator v3.1 sequencing chemistry and loaded on a ABI3730XL genetic analyser (Applied Biosystems). The sequences are then aligned and compared to the reference sequence (NM_000161.3) using CodonCode Aligner (CodonCode Corporation).

Additionally, transcription levels of wild-type *GCH1* are estimated by qPCR, and compared to levels of expression in untreated fibroblasts. Cells are lysed using lysis buffer and RNA extracted with the RNeasy Mini Kit (Qiagen). 0.5μg of RNA is

reverse transcribed to complementary DNA (cDNA) using SuperScript III Reverse Transcriptase (Invitrogen), dNTP Mix (Invitrogen) and Random Primers (Promega). The qPCR chemistry makes use of the TaqMan Fast Advanced Master Mix on QuantStudio 7 Flex Real-Time PCR System according to manufacturer's specifications (AppliedBiosystems). Pre-optimised *GCH1* primers spanning the exons 4-5 boundary with a VIC marker (Hs00609198_m1) and endogenous control primers for hypoxanthine phosphoribosyltransferase 1 with a FAM marker (HPRT1 - Hs02800695_m1) are used in the same well for internal control. All cDNA samples are run in triplicates using the FastProgram. Results are read on QuantStudio and analysed with Origin. Method for analysis employs the "Delta Delta CT" approach and calculates 2^-ΔΔCt for comparing the fold-change in expression of *GCH1* between samples.

Finally, western blots are attempted to estimate the presence and level of expression of *GCH1* in the cells using the method described in materials and methods, and similarly to the fibroblast chapter.

3. Preparation of cells for functional imaging

Functional imaging is performed on all three mutant *GCH1* lines, namely PD, DRD1 and DRD2, and variable combinations of the four control lines (CTRL1-4). hiPSC are cultured until complete confluence prior to the start of the mDA induction. Functional imaging is performed on both mDA neural precursors (NPC at D12) and midbrain dopaminergic neurons (mDA neurons at D70 and D90). Final plating is performed a minimum of two days prior to imaging for NPC, with cells being maintained in N2B27 with 0.1μM FGF; and around D35 for mDA neurons imaging, with cells being matured in D14+ media (20ng/mL BDNF, 20ng/mL GDNF, 0.2mM ascorbic acid, 0.5mM cAMP and 0.1μM compound E) until day of imaging. Cells are plated onto Matrigel-coated 8-wells ibidi chambers at a ratio of 1:6 for NPCs and 25-50k cells per well for mDA neurons supplementing media with 10μM RockI for the first 24 hours after the split. Description of the mDA induction protocol and exact media composition can be found in the previous chapter.

4. Mitochondrial membrane potential with TMRM & GSH content with mCB

Live cells are incubated for 30 minutes, in the dark, at room temperature with either 25nM TMRM or 50μM mCB, or both together, diluted in recording buffer (HBSS, 10mM HEPES, pH 7.4). Both dyes are kept in recording buffer during imaging. Maximum wavelength for excitation/emission fluorescence are 548/574 nm for TMRM and 394/490 nm for mCB. Image acquisition consists in complete cell z-stacks for both dyes. Positive control for specificity of TMRM fluorescence is performed by the observation of the loss of dye accumulation by adding 1μM FCCP (used here as a mitochondrial respiration chain uncoupler which leads to transport of the protons across the mitochondrial membrane and the release of the dye accumulated in the mitochondria due to the MMP). Z-stacks are analysed separately for each dye on Fiji (ImageJ) using maximum intensity projection of the z-stack to reduce the image to a two-dimensional format. Background is then removed with thresholding of the image and analyse particle is used for each dye separately to determine all areas containing a fluorescent particle in the image. An extra step to remove cells with a non-neuronal aspect from the field is added prior to thresholding for neuronal imaging analysis. Mean fluorescence intensity is measured across the ROIs defined as particles across each field. Results are presented as boxplots with n = number of z-stacks, and groups are compared using the appropriate statistical tests.

5. Mitochondrial ROS production with MitoTracker red CM-H2XROS

Live cells are incubated for 15 minutes at room temperature with 1 μM MitoTracker Red CM-H2XROS and 10nM Hoechst diluted in recording buffer. Loading of the dye is monitored on the confocal to ensure optimal starting conditions for each experiment. Hoechst nuclear staining is used to locate the cells. Dynamic change of fluorescence intensity in the mitochondria is captured with inverted Zeiss confocal microscope 880 Airyscan capturing one image every 10-20 seconds for 10 minutes. The MitoTracker Red CM-H2XROS dye, specifically targeted to the mitochondria, is non-fluorescent in its reduced form and fluoresces in its oxidised form with a maximum

excitation/emission fluorescence wavelength of 579⁄599 nm. The dye is specifically oxidised by ROS produced in the mitochondria, and its accumulation in the organelles is dependent on the mitochondrial membrane potential. Positive control for the experiment uses the addition 50-100μM rotenone to inhibit complex I of the mitochondrial respiratory chain, which would result in a drastic increase of the production of ROS by the mitochondria (and a depolarisation of the MMP), resulting in an increase in the dye fluorescence intensity. The specificity of the accumulation of the dye to the mitochondria is also tested by the addition of 1 μM FCCP at the end of each experiment. FCCP is a potent mitochondrial respiratory chain uncoupler able to completely depolarise the MMP and lead to the dissolution of fluorescence signal accumulation to the mitochondria.

Image analysis uses Fiji (ImageJ), with selection of all fluorescent areas with Analyse Particles after removal of the background fluorescence by setting background threshold. Mean fluorescence intensity value is recorded for each image along the time-series. These values are plotted using Origin (OriginLab) and a linear regression model used to estimate the slope of change of fluorescence in each field. These slopes are compared between groups (n = slope in one well) using the appropriate statistical test and presented as boxplots.

6. Superoxide production rate with DHE

Live cells are loaded for 3 minutes with 2 μM dihydroethidium (DHE) diluted in recording media, in the dark and at room temperature. Dynamic imaging of the rate of oxidation of the dye is measured as the emission fluorescence shift of DHE from 380nm in its reduced state to 530nm in its oxidised state, as well as its re-localisation in the nucleus when oxidised. Images are captured every 5 seconds for 8-10 minutes using a Cairn xenon arc light source and Optoscan monochromator (Cairn), associated with an Optiscan II stage system and custom filter wheel (Prior Scientific), and an Andor sCMOS camera (Oxford instruments). Positive control uses the addition of 100uM hydrogen peroxide 30 seconds prior to end of recording associated with a drastic increase in oxidised dye fluorescing at 530nm. At the NPC stage, images are extracted for the 530nm emission fluorescence only using AndorIQ, run through thresholding for background removal and mean fluorescent intensity is calculated

across the well using Fiji (ImageJ). At the neuronal stage, nuclei of cells with neuronal aspect only are selected manually and data extracted for both 380nm and 530nm channels using AndorIQ. Extracted data is then plotted and analysed on Origin. For NPCs, the rate of superoxide production is determined by linear regression through linear fit function on Origin of 530nm fluorescence intensity over time in the complete field and compared between groups using the appropriate statistical test with n = slope in one well. For mDA neurons, linear regression of 380:530nm ratio over time is used to establish rate of superoxide production in each cell and these are compared between groups using the appropriate statistical test.

7. Estimating lipid peroxidation using bodipy C11 dye

Live cells are incubated 20 minutes with 5μM Bodipy C11 591:581 solution diluted in N2B27 media at 37c 5% CO2. Bodipy C11 is a fluorescent derivative localising to the membranes which emission fluorescence shifts from 590nm (reduced form of the dye) to 510nm (oxidised form of the dye) when oxidised by free radicals. These free radicals can oxidise the dye while they are removing electrons from the membrane's lipids, an oxidative reaction called lipid peroxidation. The ratio of reduced to oxidised dye (510:590nm) is used to estimate the rate of lipid peroxidation in the cells. For NPCs, loading is difficult and areas central to the well and containing a large proportion of cells uptaking the dye in its reduced form (green) are selected for imaging. For neuronal cells, areas containing a large proportion of neuronal-looking cells with both processes and nuclei visible are selected. Image acquisition is performed on a Zeiss Confocal Inverted microscope (710 or 780 depending on set), with one image captured every 15-20 seconds at wavelengths of both 510nm and 590 nm for 10 minutes. Positive control is obtained by adding 100 μM hydrogen peroxide and observing a rapid increase in lipid peroxidation.

Image analysis for NPC uses Fiji (ImageJ) to establish an intensity threshold image and remove background fluorescence across the whole image. Then overall remaining areas are used to evaluate mean fluorescence intensity for each wavelength at each time-point. For mDA neurons, Fiji (ImageJ) is used to manually delimitate the border of neuronal-looking cells and these areas only are thresholded to remove background fluorescence and extract mean intensity fluorescence values for both wavelengths at

each time-points. In both cases, the Origin software is then used to calculate the ratio of 510:590 nm mean fluorescence intensity for each time-point and to normalise each of these time-series by their own minimum ratio value (most reduced state of the dye). Normalised values are plotted against time and a linear regression model is used to estimate the rate of change of the fluorescence ratio over time as a proxy for lipid peroxidation rate in these cells. These values are then compared between groups using the appropriate statistical tests.

8. Measuring nitric oxide production in the cells with DAR-4M

Diaminorhodamine-4M (DAR-4M) AM is a cell-permeant fluorescent NO indicator which exhibits an 840-fold increased fluorescence intensity when it reacts with NO in the cells in the presence of O2. Live cells are loaded for 40 minutes with 10 μM of DAR-4M in recording buffer in the dark, at room temperature, after rinsing with PBS. The dye is removed and cells placed in fresh recording buffer for imaging. DAR-4M is excited with the 561 nm laser as maximum absorption fluorescence of the molecule is 558nm in its triazole form and recording at maximal emission fluorescence of the compound at 574nm. Images are captured on a Zeiss inverted confocal with 3 z-stacks covering the complete depth of the cells recorded per well. Then time-series of one image every 5-10 seconds are captured. Baseline is recorded for about 3 minutes prior to the addition of 25mM L-Arginine, a necessary NOS substrate, to activate NO production and cells are further imaged for 2-3 minutes in their activated form.

Z-stacks are analysed by combining all images into the maximum intensity projection for each stack, then subtracting the background by thresholding and measuring the mean fluorescence intensity across remaining areas using Fiji (ImageJ). Results are plotted with n = number of z-stacks as representation of the basal intensity fluorescence of the cells.

Time-series are analysed by setting a set threshold to all images and measuring the mean fluorescence intensity for each time-point with Fiji (ImageJ). Data is then normalised to the starting fluorescence value and plotted against time. Data is analysed by subtracting baseline fluorescence from activated-state fluorescence intensity and comparing the extent of NO production burst associated with the supplementation of the cells with NOS substrate L-Arginine using Origin (OriginLab).

9. Physiological calcium signalling using the calcium indicator FURA-2

Live cells are loaded for 30 minutes with 5 μM FURA-2 and 0.005% pluronic acid in recording buffer, at room temperature, in the dark. Cells are then washed twice with PBS and covered with fresh recording buffer for imaging. Image acquisition is performed using a Cairn xenon arc light source and Optoscan monochromator (Cairn), associated with an Optiscan II stage system and custom filter wheel (Prior Scientific), and an Andor sCMOS camera (Oxford instruments). Baseline is recorded for 1.5-2 minutes before addition of stimulating molecules. At early neuronal timepoint, neurons are excited with 5μM glutamate then allowed to recover for a couple of minutes prior to astrocytic cells excitation with 100μM ATP. At late neuronal timepoint, KCl is substituted to glutamate for specific activation of neuronal depolarisation. However due to the reduced proportion of cells recovering from KCl compared to Glutamate, 100μM ATP is applied first to activate astrocytic cells, cells are then allowed to recover prior to addition of 50mM KCl to activate neuronal depolarisation. Data is extracted from the images by manually selecting the soma of calcium 'bursting' cells using AndorIQ, and this data is analysed on Origin. Ratio of calcium-bound FURA-2 (excitation at 340nm) to free FURA-2 (excitation at 380nm) image is used to detect calcium transients in the cells and select the soma of cells responding to any stimulus. Number of cells displaying a cytoplasmic calcium burst as a result of either or both stimuli is recorded and compared to the total number of cells in the field.

10. Cell death estimation with SytoxGreen

Live cells are incubated for 15 minutes with 250 nM Sytox Green and 10nM Hoechst diluted in N2B27 media at 37 degree 5%CO2. Media and dyes are rinsed with PBS and cells are placed in recording buffer for imaging. Image acquisition is performed on a Zeiss Confocal Inverted 880. Acquisition consisted in 5 z-stacks for each well, two wells per line at the mDA neuron stage. Areas for imaging are selected at random at the centre of and all around the well using Hoeschst staining to locate cells nuclei. Image analysis is performed by selecting the nuclei of cells with a neuronal aspect

using the brightfield image, and manually counting the number of Sytox Green positive nuclei out of all nuclei visible with Hoechst staining, using Fiji (ImageJ). Data is then entered in Origin (OriginLab) for data analysis and figures.

11. Statistical testing of data

Due to extremely high cell confluence necessary to survival and differentiation of the cells at the NPC stage, single cells cannot be delineated with certainty and all data analysis expressed as average fluorescence intensity across the complete z-stack field. At the neuronal stage, cells with a neuronal aspect are picked for analysis and results expressed either across wells or across individual cells.

For all comparisons between three or more groups, a Levene test for homogeneity of variances is used to determine whether these groups can be compared using a parametric One-way or two-way ANOVA (when Levene's test is non-significant) or a non-parametric Kruskal-Wallis ANOVA (when Levene's test is significant). This is to respect the assumption of homoscedacity or homogeneity of variances associated with the use of parametric ANOVA statistical tests. When the results of this comparison are significant, groups are compared to each other two by two using: parametric t-test with multiple testing Bonferroni correction as calculated by the Origin software, or the non-parametric Mann-Whitney U-test, with Bonferroni correction in the form of a manual re-adjustment of the p-value threshold for significance to 0.05/n with n = number of tests performed in both cases (Armstrong, 2014). Unless otherwise stated, non-parametric Mann-Whitney tests are used to compare each disease group to controls separately as well as between them, resulting in 3 independent t-tests and a new level of significance threshold at $p \leq 0.01667$.

III. Results

1. Validation of the iPSC lines

The 343+5C>G mutation carried by these patients, which affects the splicing site at the junction of exon 1 and intron 1 of *GCH1*, leads to the retention of intron 1 and the appearance of an early STOP codon during mRNA translation (Figure 13). It could also lead to nonsense-mediated decay of the abnormally spliced mRNA and the loss of half of the potential *GCH1* expression in the cells. This would result in a functional impairment similar to a heterozygous loss-of-function.

The maintenance of the mutation in the iPSC lines is assessed by Sanger sequencing on DNA extracted from these cells. It confirms the presence of the heterozygous 343+5G>C mutation in all three patient line and none of the controls. All other exons and exon-intron boundaries of the *GCH1* gene are also sequenced and no other variant could be identified in any of the cell lines used in this chapter.

As a heterozygous mutation, the retention of exon 1 may only occur in half of the *GCH1* mRNA in carriers compared to healthy controls. RNA extracted from all the iPSC lines is quantified for wildtype *GCH1* mRNA via qPCR using a primer at the junction of exons 4-5 boundary with HPRT1 as endogenous control in each well, and average of untreated control fibroblasts (same extraction as in fibroblasts chapter) for normalising expression. Results for separated cell lines are presented in Figure 47a. The relative amount of wildtype *GCH1* mRNA is two-fold higher in control iPSC than in untreated control fibroblasts, probably due to slight cell-type based variation in *GCH1* expression (Figure 47b); and levels of expression are almost halved in mutants compared to controls iPSCs (Figure 47c). These lines are thus used in further experiments.

In spite of numerous trials to analyse *GCH1* expression in the cells through western blots with two distinct commercially available anti-*GCH1* antibodies, various bands, none of which were at the expected size, are observed in both control and mutant cells.

The method is thus considered unreliable for the detection of the GTPCH protein as no antibody could be considered specific enough and abandoned (data not shown).

2. Functional imaging sets

The induction protocol for iPSC-derived mDA neurons is attempted a total of 13 times, with multiple attempts to variation and validation of the protocol not yielding functional imaging results (Table 28). Four sets of cells comprising of control and mutant cells, successfully reaching defined imaging time-points of the protocol, are used for functional analysis of the effect of the mutation in PD and DRD in this model. Results presented in this chapter are issued from all four sets of induction at the neuroprecursor stage (NPC) and two of these same sets which reached the neuronal stage at both early timepoint (around D60 of protocol) and late neuronal timepoint (around D90 of the protocol) (Figure 46). The sets imaged at the neuronal timepoints are obtained using the original protocol for one and a slightly modified version in which purmorphamine was delayed for the first 48 hours of the protocol (as described in the neurodevelopment chapter).

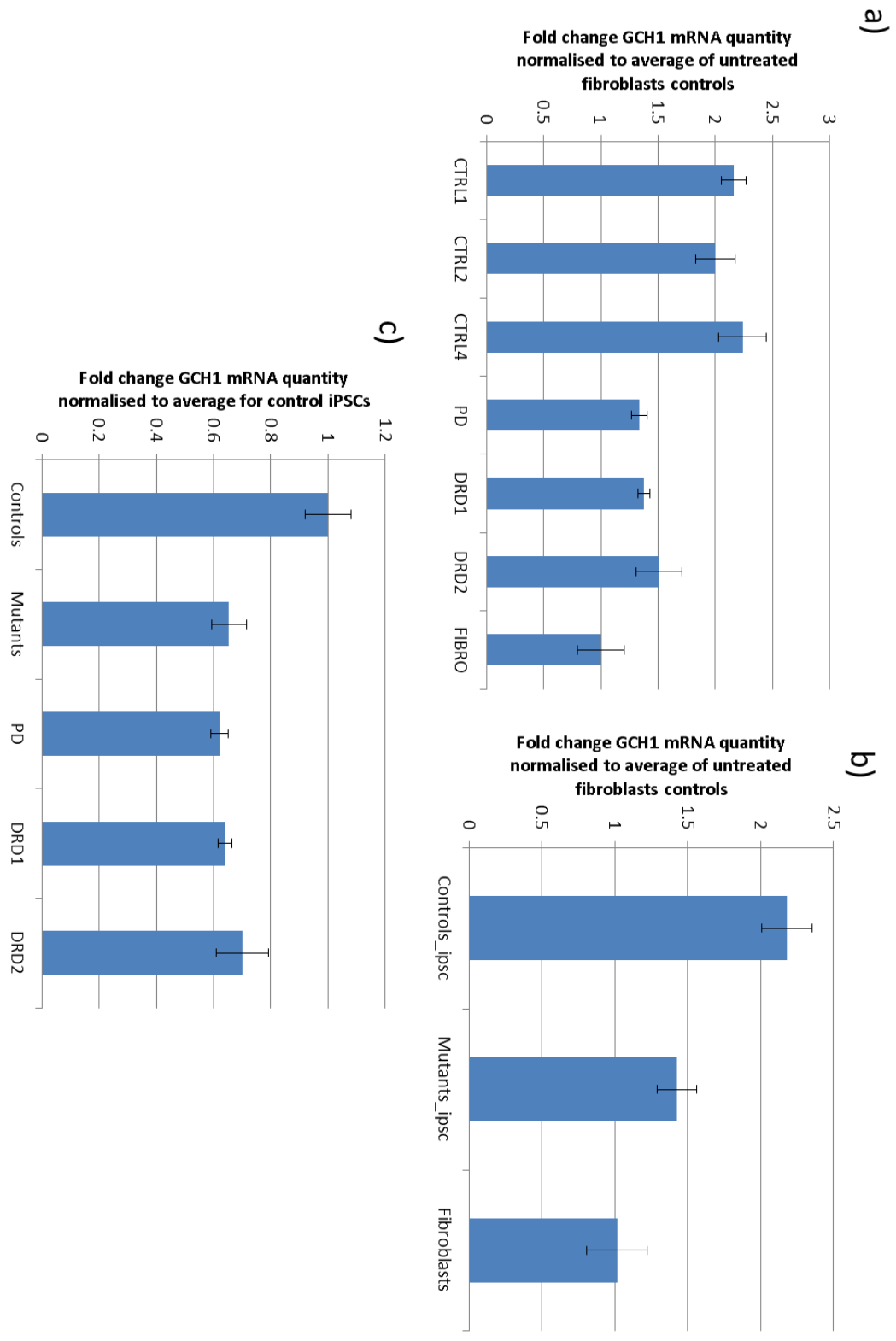

Figure 47: **qPCR for *GCH1* mRNA in iPSC normalised to average of untreated fibroblast controls.** 2^(-ΔΔCt) estimated using HPRT1 mRNA as endogenous control for each sample, each sample is run as triplicate, and corrected values are used to estimate an average for each cell line .(a) These are then normalised to untreated control fibroblasts expression. (b) Mutant and control cell lines are averaged and normalised to untreated control fibroblast expression . (c) Mutant iPSC as a group as well as separately are normalised to the average expression in iPSC controls.

3. Midbrain dopaminergic neuroprecursors

ICC results – Cells are NPCS

Immunocytochemistry is performed at D12 of induction protocol to confirm the patterning of iPSC to NPC via co-expression of the transcription factors LMX1A and FOXA2 (see neurodevelopment chapter for more detailed discussion of the markers) (Neurodevelopmental chapter Figure 36). Overall, co-expression of these factors is confirmed in 92% cells on average, with ~89% LMX1A+ cells (62.89-99.57%, n = 3848 cells analysed across 5 fields) and ~94% FOXA2+ cells (87.75-98.27%, n = 2503 cells analysed across 3 fields) on average respectively. By D12 of the mDA induction protocol, cells are thus patterned to become midbrain dopaminergic neurons and can be used for imaging as NPCs.

Tool validation for the simultaneous measurement of MMP and GSH

Changes in the MMP, reflecting changes in the function of the mitochondrial respiratory chain, can be associated with a variation in the production of ROS by the organelles. Although it is difficult to measure the MMP concomitantly with mitochondrial ROS production, as dyes for the measurement of the latter are dependent on the MMP, antioxidant levels in the complete cytoplasm can be used to approximate the oxidative state of the cell. To test these two functions together, MMP can be evaluated with TMRM and reduced glutathione (GSH) levels by mCB simultaneously, as both experimental paradigms consist in a similar loading duration (30 minutes) and imaging method (complete cell z-stacks in the presence of the dye). Moreover, the excitation and emission wavelengths of these dyes are different enough to avoid bleed-through which would affect both signals, with maximum fluorescence wavelength for excitation/emission of 548/574 nm for TMRM and 394/490 nm for mCB (Figure 48). However, there remains the possibility that when mCB conjugates with GSH, it limits its availability in the cell thus reducing the cell's capacity to buffer ROS. This may lead to a potentially increased oxidative state which needs to be compensated for by other antioxidants. In the absence of compensation, oxidative stress could affect the MMP and concomitant TMRM fluorescence intensity measurements could be affected and not represent basal levels in the undisturbed cell (Figure 48).

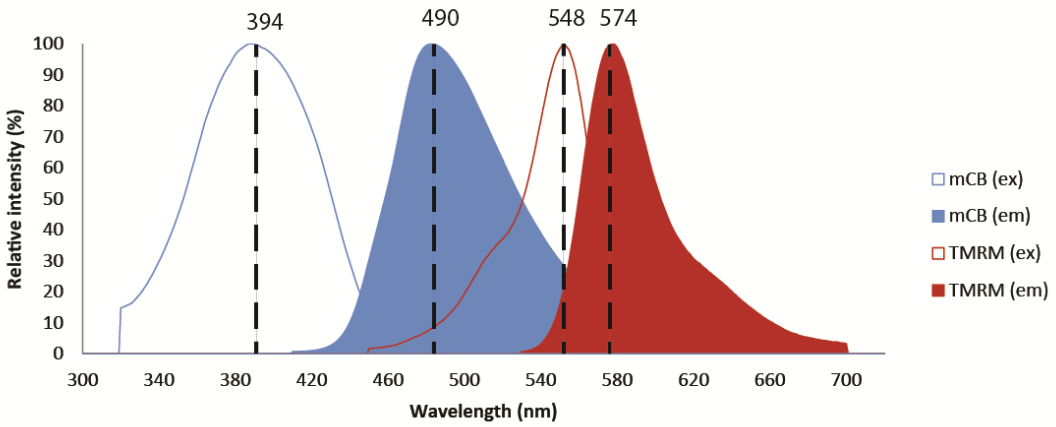

Figure 48: Excitation and emission spectra for TMRM and mCB dyes. Excitation spectra are represented as a line, emission spectra as filled areas. mCB spectra are in blue, TMRM spectra are in red. Values for maximum excitation/emission fluorescence wavelengths are represented as dashed vertical lines.

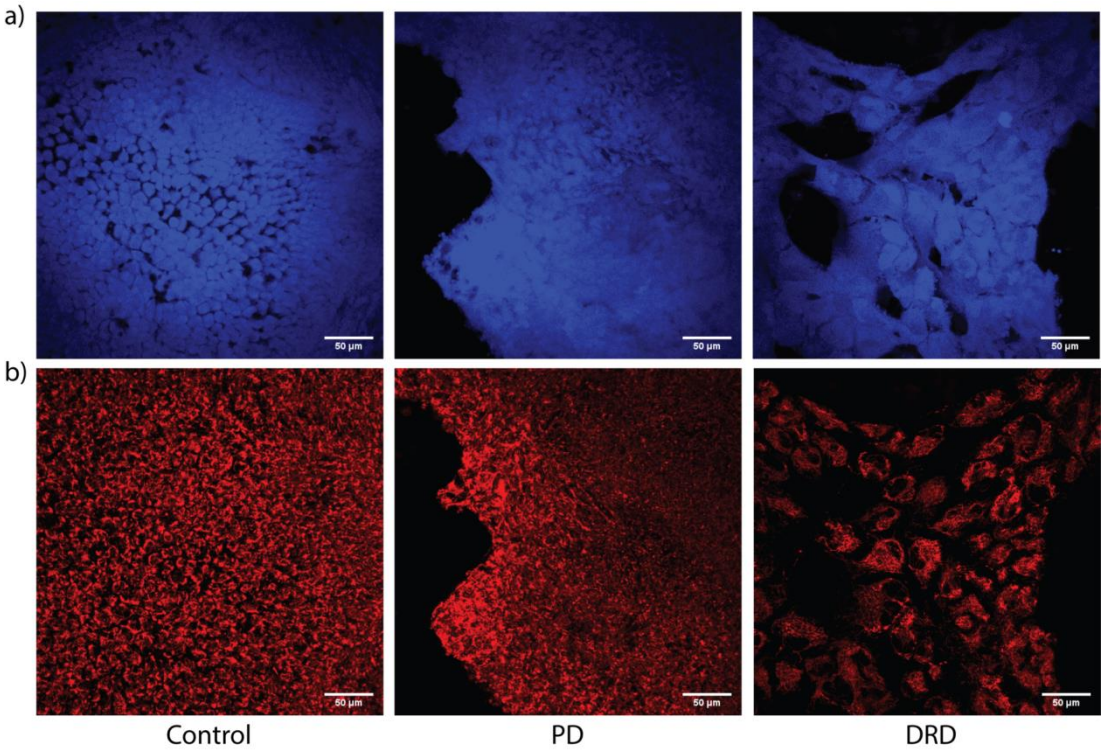

Figure 49: Examples of maximum intensity projection of whole-cell z-stacks for mCB and TMRM fluorescent dyes. Examples are shown in control line (left), PD line (middle) and DRD line (right) for both mCB (a) and TMRM (b).

To test whether the concomitant use of these dyes affects the corresponding biological measurements, mCB and TMRM are loaded together or separately and measured on the same day in a single set of NPC (Figure 49). This image analysis method is used across all experiments at this stage of the mDA induction protocol. Results are

compared between single-dye and paired-dyes experiments using mean fluorescence intensity measured for each dye separately. Both conditions (i.e. single or paired dyes) are compared across phenotypic groups (i.e. controls, PD and DRD) with a two-way ANOVA tests for TMRM and mCB fluorescence values separately. There is no significant effect of the association of the dyes on TMRM measurements ($p = 0.29103$; for two-way ANOVA) (Figure 50) or on mCB measurements ($p = 0.1304$; for two-way ANOVA) (Figure 51). Therefore, the sequestration of GSH by mCB does not significantly affect TMRM fluorescence in this experimental paradigm and both dyes can be used together to assess both biological functions simultaneously and compare these between cell lines or conditions.

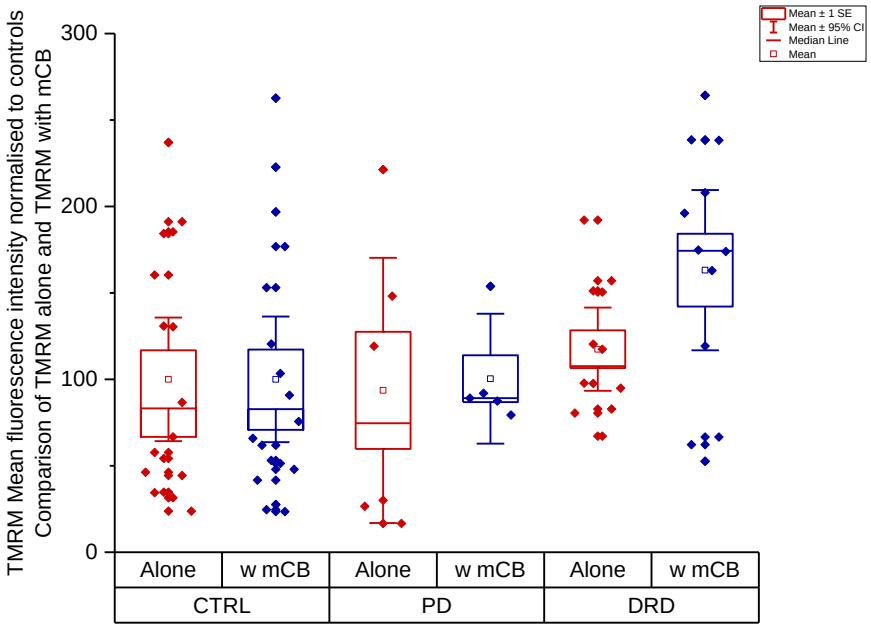

Figure 50: Testing the effect of co-imaging with mCB on TMRM: comparison of loading TMRM alone (red - Alone) or in conjunction with TMRM (blue – w mCB) for NPCs lines separated as controls (CTRL – 3 lines), PD (1 line) and DRD (2 lines) groups. Each point re-presents a z-stack. Box plot represents: mean (circle), median (line) median ± 1SE (standard error - box) and mean ± 95% CI (confidence interval – whiskers). Stars indicate statistically significant difference with $\alpha < 0.05$ between groups.

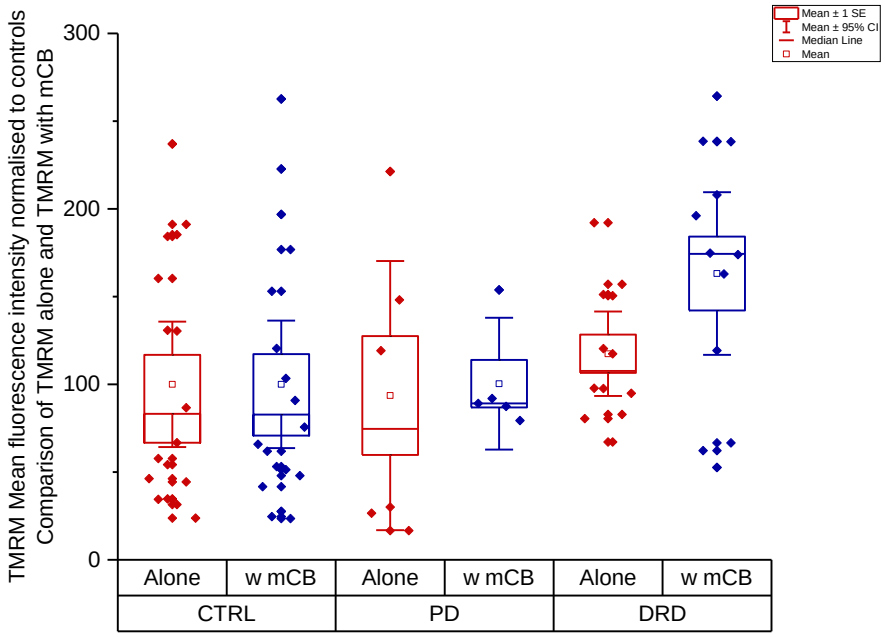

Figure 51: Testing the effect of co-imaging with TMRM on mCB: comparison of loading mCB alone (Blue - Alone) or in conjunction with TMRM (red – w TMRM) for NPCs lines separated as controls (CTRL – 3 lines), PD (1 line) and DRD (2 lines) groups. Each point re-presents a z-stack. Box plot represents: mean (circle), median (line) median ± 1SE (standard error - box) and mean ± 95% CI (confidence interval – whiskers). Stars indicate statistically significant difference with $\alpha < 0.05$ between groups.

Mitochondrial membrane potential – TMRM

Mitochondrial membrane potential is estimated using TMRM, a cell-permeant, cationic, fluorescent dye which accumulates in the mitochondria proportional to the MMP. TMRM is loaded with mCB and measured separately as z-stacks covering the entire depth of the cells. Mean fluorescence intensity across each field after threshold removal is normalised to average of controls for each set and sets are plotted together (Figure 52). TMRM fluorescence intensity is significantly different across the three groups ($p = 0.01755$; $F = 4.1894$; $df = 2$; One-Way ANOVA), with the difference between the means being statistically different for DRD and PD groups ($p = 0.01602$; 95% CI = 6.91227 - 88.77159; t-test with Bonferroni correction for multiple testing). There is no significant difference between mutant and control groups at the NPC stage ($p > 0.05$). However, median normalised values for controls, PD and DRD are 85.7, 79.8 and 98.1, respectively. This may indicate a depolarised MMP in PD compared to controls although under the significance threshold. Thus there is a significant difference in MMP polarisation between PD and DRD as early as the neuroprecursor

stage, and it seems to be associated with a depolarisation of the PD and a stronger polarisation of the DRD lines.

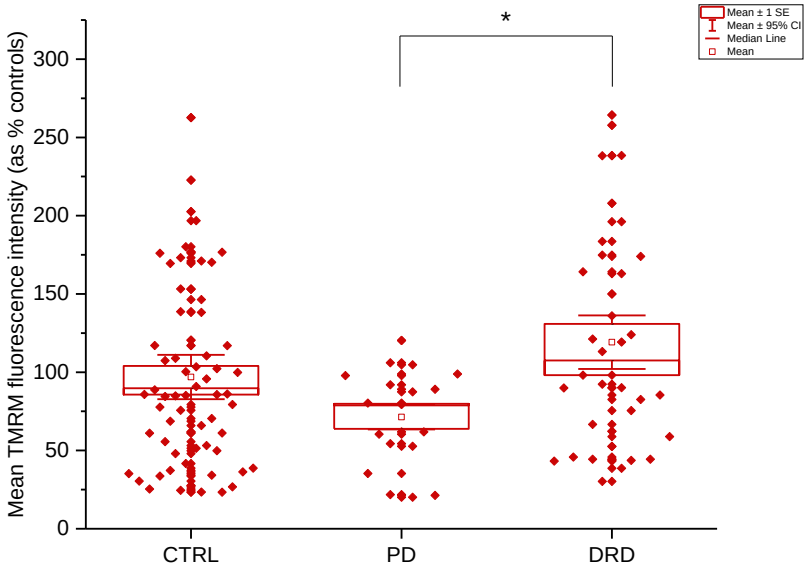

Figure 52: Boxplot of TMRM mean intensity in NPCs. Results from all sets of induction images at the NPC set. Each point represents a z-stack maximum intensity projection mean fluorescence intensity. Box plot represents: mean (circle), median (line) median ± 1SE (standard error - box) and mean ± 95% CI (confidence interval – whiskers). Means are compared by one-way ANOVA with multiple t-test with Bonferroni correction and stars indicate statistically significant difference with $\alpha < 0.05$ between groups.

Mitochondrial ROS production – MitoROS

The rate of production of ROS by the mitochondria is estimated by the rate of increase of fluorescence intensity of the MitoTracker CMH2XROS dye along time in unstimulated cells. Cells are co-loaded with Hoechst to locate cell nuclei. For the analysis, cells cannot be discriminated from each other with certainty (as can be seen in Figure 53). Discrimination between cells is not facilitated by a cell-filler dye as can be extrapolated from the use of mCB with TMRM in NPC cultures (Figure 49). Mean fluorescence intensity of the dye after removal of the background by thresholding is measured for each time-point. These values are plotted against time and the constant part of the resulting slope used to calculate the rate of increase of fluorescence intensity in each well. Representative plots for each group are shown in Figure 54, with an over-layer demonstrating the area of the curve used for slope calculation with a linear model (Originlab). Slope values are normalised to the average of control lines values and

plotted (Figure 55). There is no statistically significant difference between the three phenotype groups (p = 0.6291; F = 0.46838; df = 2; One-Way ANOVA).

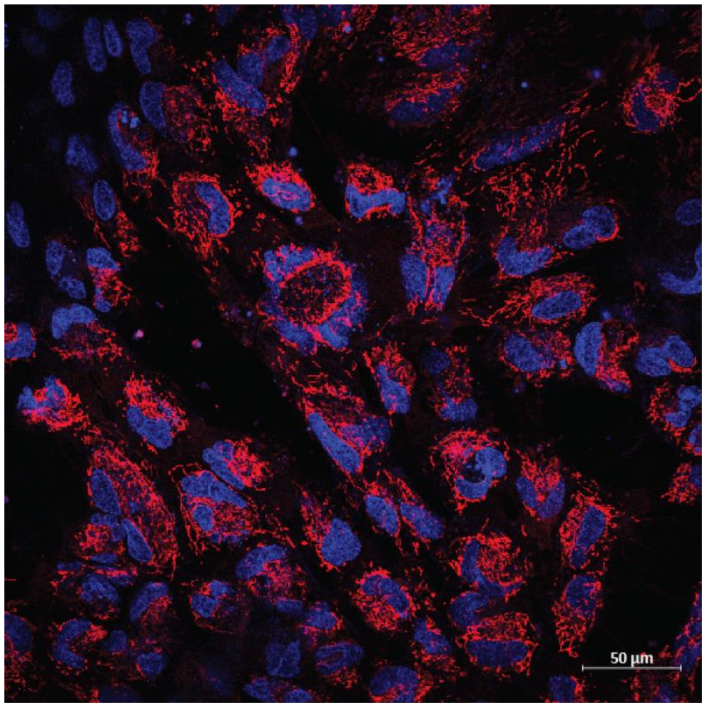

Figure 53: Representative image of MitoROS imaging of NPCs in association with Hoechst for nuclei staining. MitoROS is visualised in red in the mitochondria and nuclei are shown in blue. Time-series can be found in annexes as an image gallery.

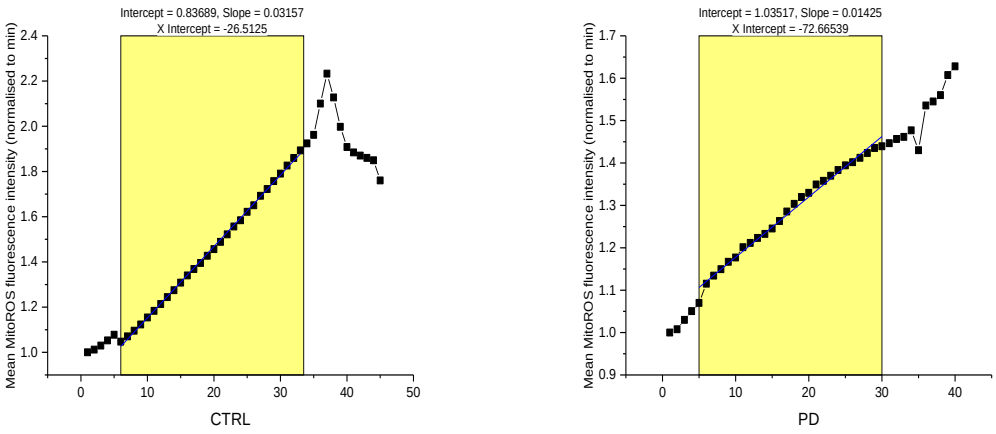

Figure 54: Representative traces of the MitoTracker CMH2XROS dye fluorescence evolution across time in NPCs for control and PD cells. The yellow area represents the time-span used to calculate rate of progression of fluorescence increase using a linear regression model.

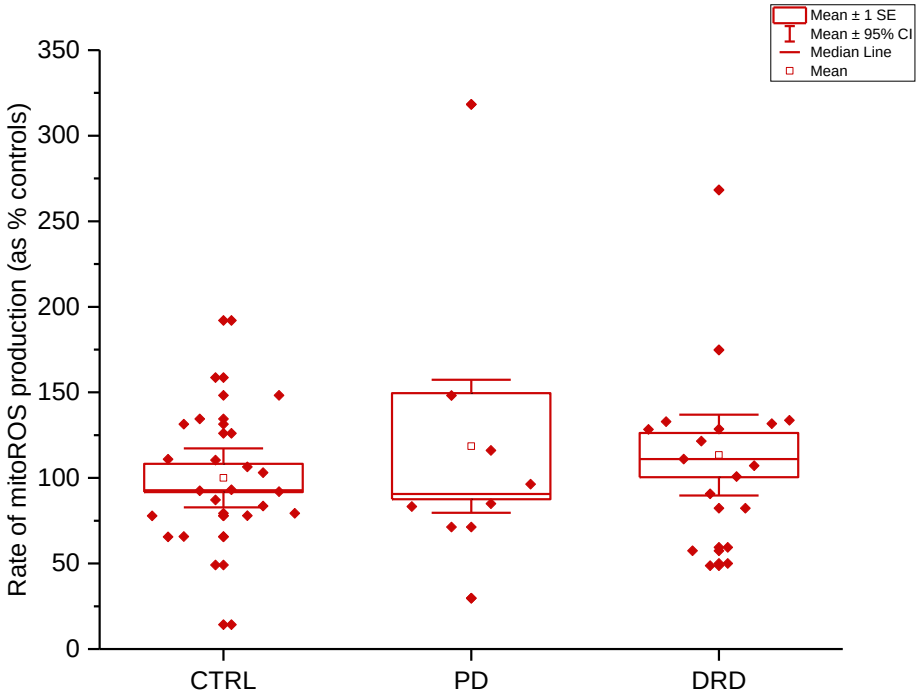

Figure 55: Boxplot of rate of ROS production by the mitochondria approximated by the increase in fluorescence intensity of the MitoTracker CMH2XROS dye in basal conditions. Each point represents a z-stack maximum intensity projection mean fluorescence intensity. Box plot represents: mean (circle), median (line) median ± 1SE (standard error - box) and mean ± 95% CI (confidence interval – whiskers). Means are compared by one-way ANOVA with multiple t-test with Bonferroni correction and stars indicate statistically significant difference with $\alpha < 0.05$ between groups.

These results suggest that the differences in MMP between cell groups are not associated with a change in mitochondrial ROS production. Of note, the MMP influences the capacity of MitoTracker to accumulate in the mitochondria, making it a potential confounder for these results.

Oxidative state of cell – GSH with mCB

Relative cell content in reduced glutathione (GSH) using the fluorescent form of the mCB dye allows to estimate the relative oxidative state of the cell as proportionally opposite to the levels of reduced antioxidants. mCB is loaded with TMRM and measured separately as z-stacks covering the entire depth of the cells. Mean fluorescence intensity across each field after threshold removal is normalised to average of controls for each set, and sets are plotted together (Figure 56). mCB mean fluorescence intensity is significantly different across the three groups (p =

0.000750588; Chi-square = 14.38931; df = 2; Kruskall-Wallis non-parametric ANOVA as assumption of homoscedasticity is not respected). Comparing groups two by two with Mann-Whitney tests (non-parametric t-tests), the DRD group contains significantly more GSH than the PD group (p = 0.00107; Z = -3.19308) and the control group (p = 0.00166; Z = -3.10748). There is no significant difference between PD and control groups at the NPC stage. These results may point at a lower depletion of glutathione, suggesting less need for ROS buffering and lower level of oxidative stress in DRD cells compared to both controls and PD cells at the neural precursor stage. It is important to note that another possible explanation for increased cell content in GSH may be due to the higher expression of the molecule in these cells. However, the differences observed in GSH content are not explained by variations in mitochondrial ROS production they may be due to the production of other major ROS in the cells.

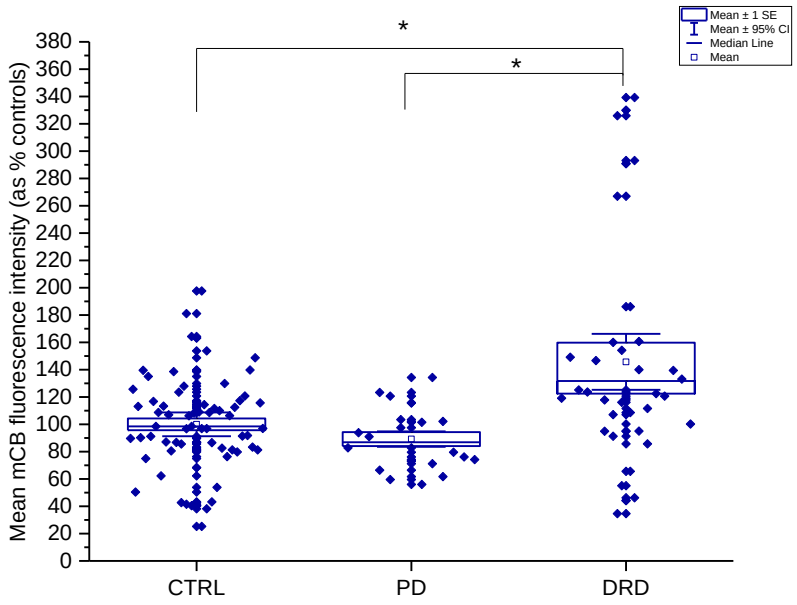

Figure 56: Boxplot of mCB mean intensity in NPCs. Results from all sets of induction images at the NPC stage. Each point represents a z-stack maximum intensity projection mean fluorescence intensity. Box plot represents: mean (circle), median (line) median ± 1SE (standard error - box) and mean ± 95% CI (confidence interval – whiskers). Means are compared by Kruskal-Wallis ANOVA with multiple Mann-Whitney tests with Bonferroni correction and stars indicate statistically significant difference with $\alpha < 0.05$ between groups.

Superoxide production – DHE

Superoxide is a potent and common ROS, notably produced by the mitochondrial respiratory chain. This free radical is obtained by the gain of an electron by a dioxygen

molecule. Superoxide production rate in a cell can be measured with dihydroethidium (DHE), a mainly reduced cell-permeant molecule which fluoresces at an emission wavelength of 380 nm. When specifically oxidised by superoxide, its fluorescence shifts to 530 nm and as an ethidium-based protein intercalates with nuclear DNA. At the neuroprecursor stage, mean fluorescence intensity of the oxidised dye across the complete field is measured at 530nm as nuclei could not clearly be differentiated for all cells in the field (Figure 57). Progression of the fluorescence intensity along time is estimated using a linear model (Figure 58), each slope value is normalised by the average of slopes for the control lines and results are plotted with each point representing a separate field or well of cells (Figure 59). There is no statistically significant difference between groups ($p = 0.84234$; $F = 0.17244$; $df = 2$; One-Way ANOVA test) suggesting the absence of a consequent difference in superoxide production between these cell lines at the NPC stage.

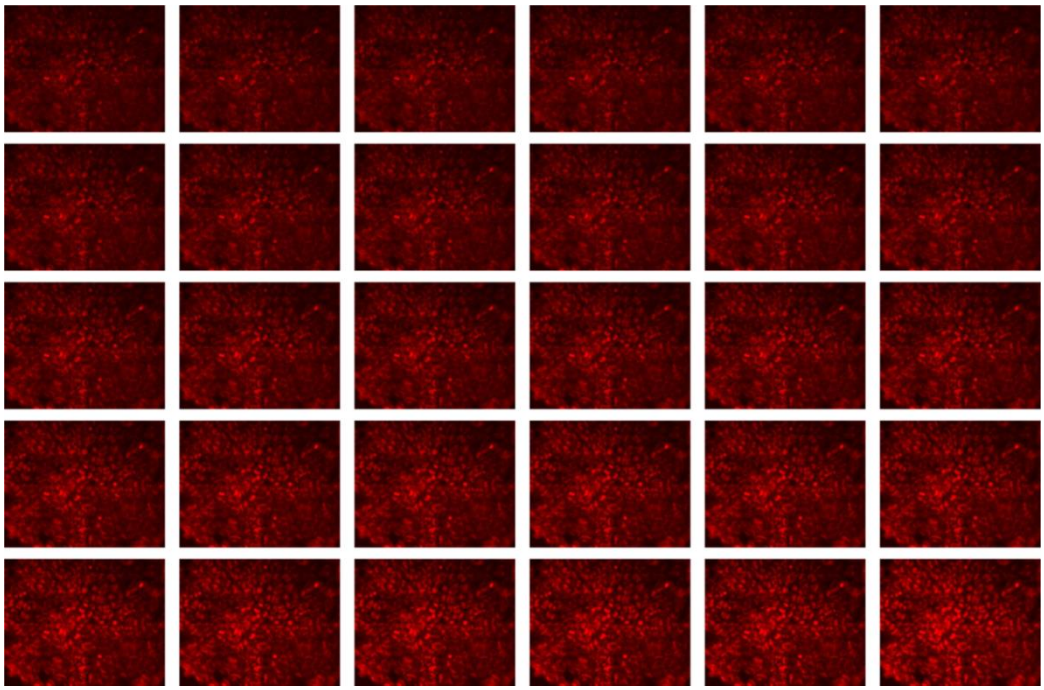

Figure 57: Time-series for DHE 530nm channel in neuroprecursors. Images are acquire every 5 seconds and one out of three images are selected for this panel (every 15 seconds).

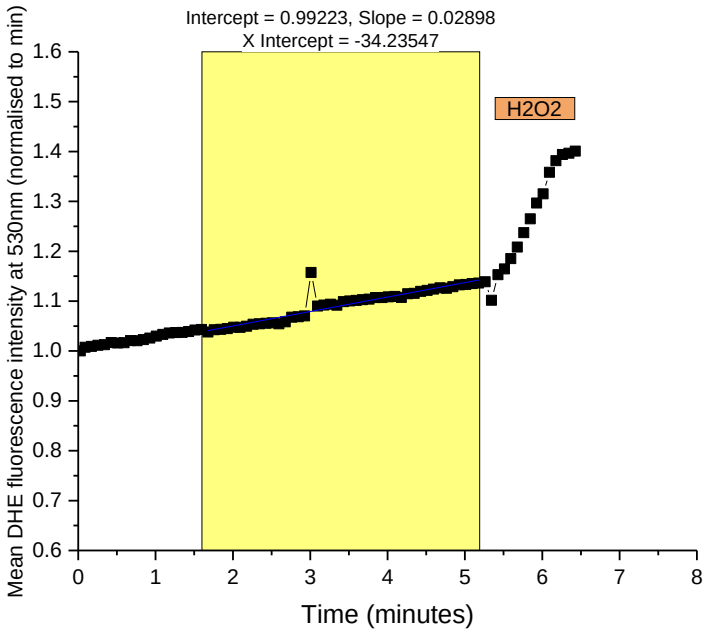

Figure 58: Example of mean fluorescence intensity of oxidised DHE (530nm) in control NPCs. Each point on the plot represents an image frame fluorescence intensity, with the yellow area representing the time section used for the calculation of the rate of progression of the intensity with time as calculated by linear regression. Addition of hydrogen peroxide (H2O2) at the end of the recording is marked by an orange rectangle.

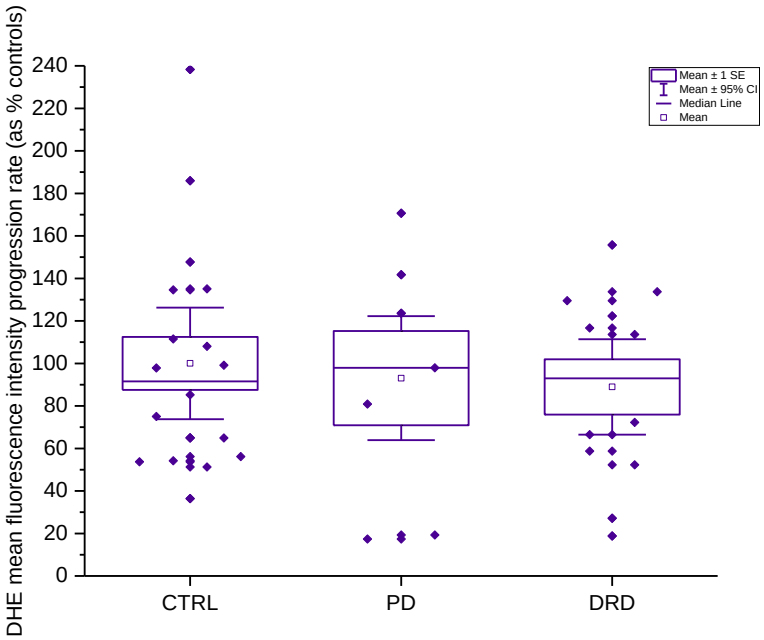

Figure 59: DHE results across all NPC sets. Fluorescence intensity of the oxidised form of the dye is measured at 530nm and rate of progression of fluorescence calculated and plotted for each well separately after results are normalised to the average of control lines for each experiment. Each point represents the slope in one well. Box plot represents: mean (circle), median (line) median ± 1SE (standard error - box) and mean ± 95% CI (confidence interval – whiskers). Means are compared by one-way ANOVA with multiple t-test with Bonferroni correction and stars indicate statistically significant difference with $\alpha < 0.05$ between groups.

Lipid peroxidation – Bodipy

Lipid peroxidation is due to the oxidation of lipids of the cellular membranes by ROS, and normally occurs when cells are in relative oxidative stress due and these free radicals cannot be buffered efficiently enough for the cells membrane to be spared this damage. Bodipy is used as a membrane-targeted molecule which fluorescence shifts from 510 nm when the dye is reduced to 590 nm when it is oxidised by the free radicals oxidising lipids of the cell membranes.

As can be seen on Figure 60, cells are too confluent and membranes moving too much to allow for the delineation of cell-to-cell limits along time and the comprehensive analysis of these images cell by cell, prompting the use of whole fields as unit of image analysis. Figure 61 shows the traces obtained by plotting the 510:590 nm fluorescence intensity ratio and the possible estimation of a rate of oxidation of the dye by linear regression. Results were not significantly different between phenotype groups (data not shown). Nevertheless, this constitutes a proof of principle experiment for the estimation of lipid peroxidation in NPCs.

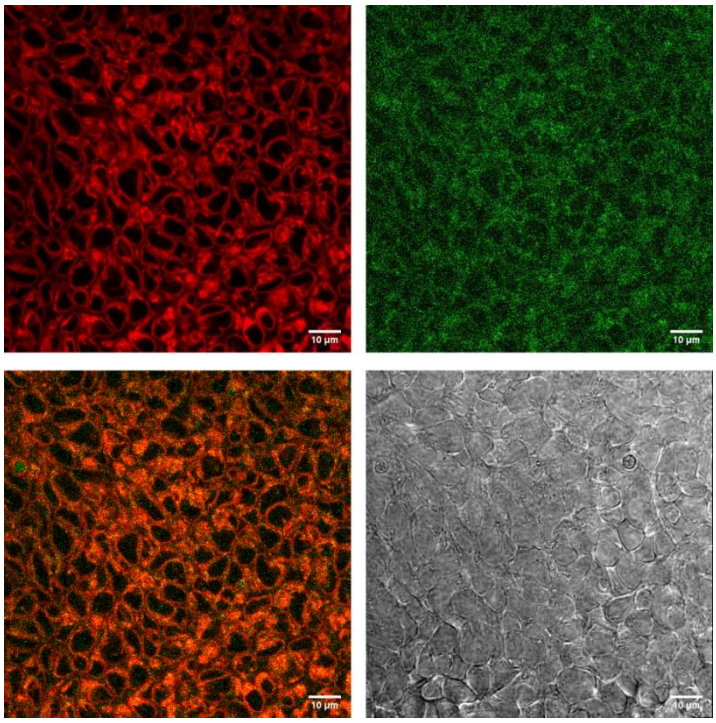

Figure 60: Bodipy C11 staining in neuroprecursors. Image shows bodipy fluorescence in PD cells at NPC stage, with 590nm image in red (upper left), 510nm image in green (upper right), merged 510nm and 590nm (lower left) and brightfield image of the cells (lower right).

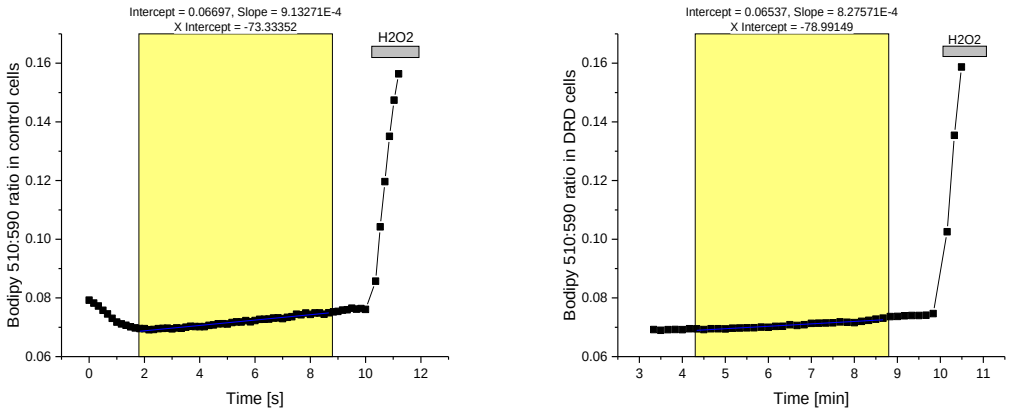

Figure 61: Representative traces of the ratio of bodipy dye fluorescence channels 581:591 evolution across time in NPCs for control, PD and DRD cells. The yellow area represents the time-span used to calculate rate of progression of fluorescence increase using a linear regression model. The grey box represents the addition of H2O2 as positive control for lipid peroxidation by increased dye oxidation at the membrane.

Nitric oxide – DAR-4M

BH4, the downstream product of GTPCH, is a coupler for all three isoforms of NOS, making the estimation of the rate of production of NO relevant in this model. DAR-4M AM dye is used here to report NO production in the NPCs. Baseline is measured for a few minutes then arginine is added to stimulate NOS activity in time series. An example of imaging gallery is presented in Figure 62 with the corresponding mean fluorescence intensity trace in Figure 63. There is a clear increase in DAR-4M AM intensity reflecting an increase of NO production when NOS are stimulated with arginine, supporting the feasibility of this experiment in the NPC model. However, some fluctuation of fluorescence across time is visible and cannot be appropriately reported with the image analysis method based on whole field to which cell confluence constrained these experiments to. Baseline NO production is first recorded by z-stack in unstimulated cells. The addition of L-arginine, an essential substrate of NOS which increases the production of NO in cells, is used to stimulate NOS activity in those cells. The effect of this stimulation is estimated using the ratio of stimulated fluorescence intensity to the baseline intensity, or deltaDAR-4M, according to a method used in the quality control of DAR-4M AM specificity for recording NO production in the cells (Kojima and Nagano, 2000).

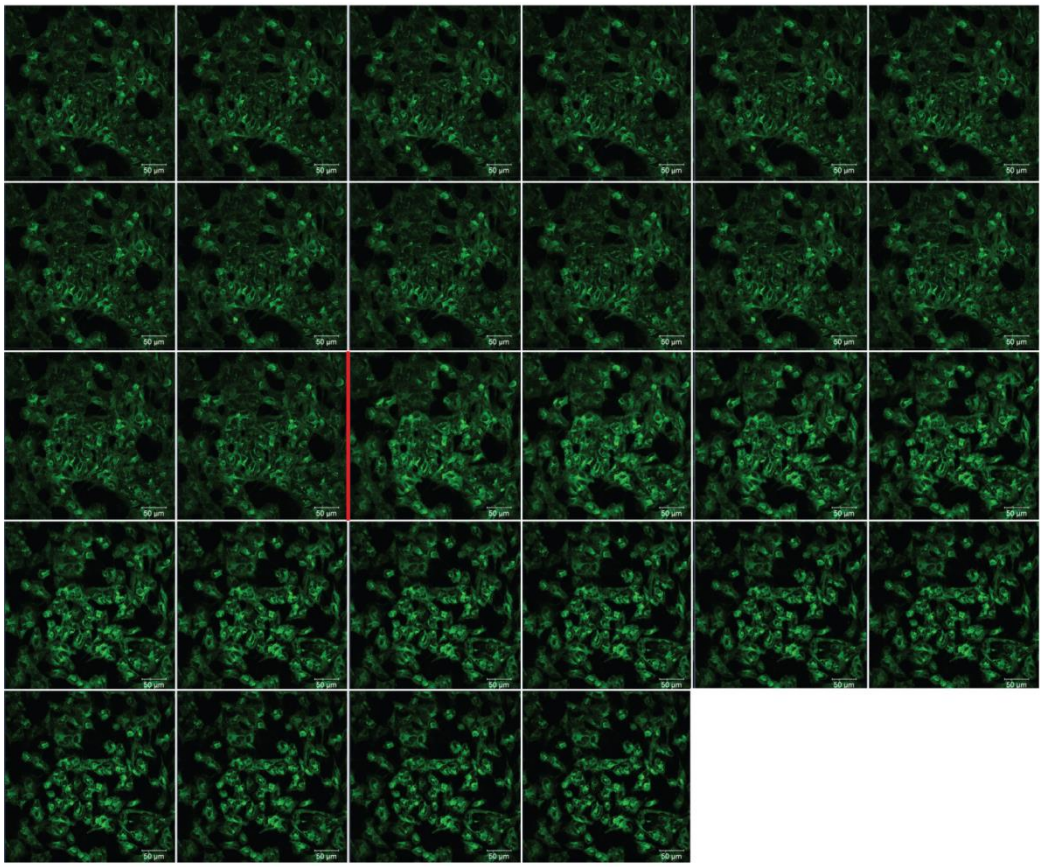

Figure 62: Representative time-series of DAR-4M imaging in NPCs. Images are sequential in time from top left to bottom right. The red line marks the time of addition of Arginin. The fluorescence plot of this well is found in **Figure 63**.

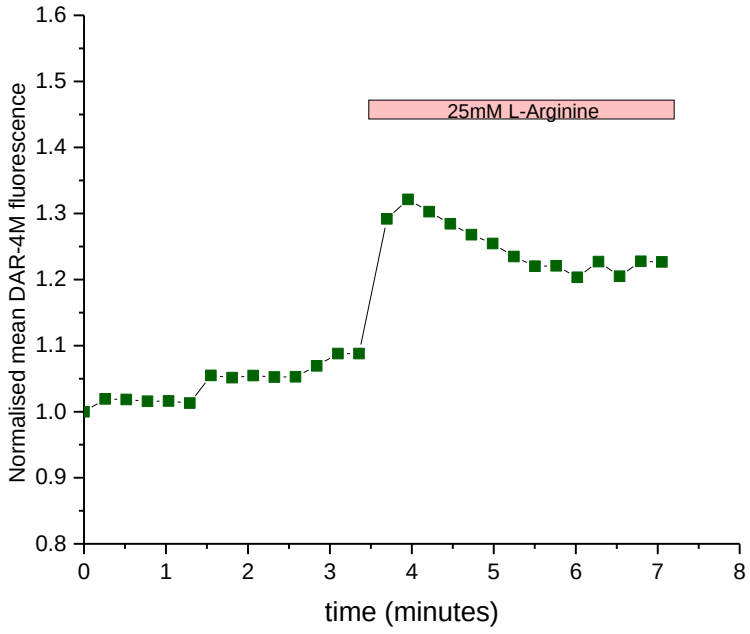

Figure 63: Basal rate of increase of DAR4M fluorescence in response to Arginine is visible on the corresponding plot of mean fluorescence intensity on time for the field shown in Figure 62.

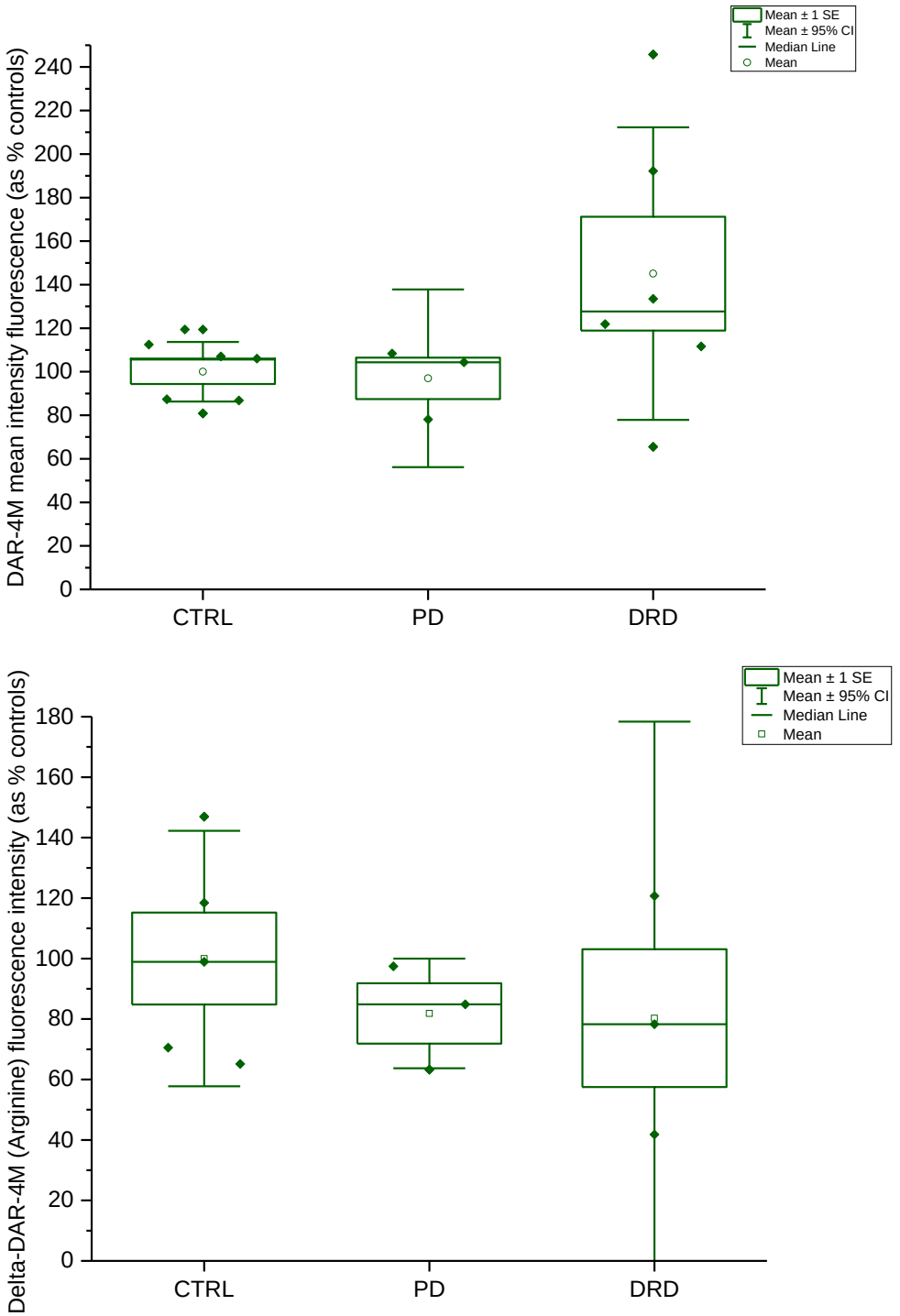

Figure 64: DAR-4M measurements in NPCs. DAR-4M z-stacks mean intensity fluorescence normalised to average of controls is shown on the top, with each point representing one z-stack. Basal rate of increase of DAR-4M fluorescence in response to Arginine-associated activation of NOS activity, or Delta-DAR-4M (Arginine), normalised to average controls, is shown on the bottom. Box plot represents: mean (circle), median (line) median ± 1SE (standard error - box) and mean ± 95% CI (confidence interval – whiskers). Means are compared by Kruskal-Wallis ANOVA and stars indicate statistically significant difference with $\alpha < 0.05$ between groups.

Results from these analyses are presented in Figure 64 for indication of the feasibility of the experiment in the NPC model. Number of observations is too small, due to the limitation of the analysis to whole fields and not individual cells, to conclude on variation in NOS activity between phenotypic groups at NPC stage.

Synthesis of NPC results

Live cell imaging experiments in the NPC demonstrate that these cells have an intact redox system, with the means to produce as well as to buffer ROS, and that these functions can be measured using fluorescent dyes and reporters such as mCB, TMRM, DHE and MitoROS in both control and mutant cell lines. Both the MMP and cellular GSH levels can be measured simultaneously with TMRM and mCB respectively, without one measure affecting the other in a significant way. Additionally, lipid peroxidation can be measured with Bodipy C11 and nitric oxide synthase activity with DAR-4M and Arginine stimulation in this model.

At the NPC stage, the *GCH1* mutation is associated with the increased polarisation of the MMP and elevated levels of cellular GSH in the DRD but not the PD cells. This effect of the mutation is not reflected by a measurable change in mitochondrial ROS production, cellular superoxide production or nitric oxide synthesis in the NPCs.

4. Midbrain dopaminergic neurons

Model validation

ICC is used to estimate the efficiency of the mDA induction protocol around D65, with the use of co-expression of BIII-tubulin (BIII), a neuronal marker, and tyrosine hydroxylase (TH), a necessary enzyme for the production of dopamine, are suggestive of the mDA neuronal phenotype in culture. The phenotype is further supported by the absence of Ki67 expression, a marker for cell proliferation present in the cell nuclei at all phases but quiescent G0 phase. Finally the absence of GFAP staining further supports cell phenotype as neuronal and not glial, as glial fibrillary acidic protein is a marker for intermediate filament protein in glial cells. Overall about 30-45% of the cells are expressing BIII and 3-12% cells express TH. None of these cells express Ki67 but 2-8% of the cells in culture are still cycling, and a small proportion of cells (1-5%) express GFAP, both suggestive of a mixed culture. Images for the co-expression of TH and BIII (Neurodevelopmental chapter Figure 38 & Figure 39).

FURA-2 is used to characterise the functionality of the neurons in this model through measuring cytosolic calcium fluxes in response to various stimuli. These include compounds such as KCl which promotes the opening of voltage-dependent calcium channels (VDCC) in neurons and ATP which mainly acts as a calcium-associated communication signal between glial cells, but can also modulate some neurons responses (Cotrina et al., 2000; Hammond and Michel, 2015; Kettenmann et al., 1984a, 1984b; Verderio and Matteoli, 2011; Verkhratsky and Kirchhoff, 2007). Representative traces for these cultures stimulated with KCl and ATP are shown in Figure 65. Mainly, response to stimuli by activation of calcium influx varies greatly between wells but is similar across all cell groups. The neurons in these cultures are thus expressing functional VDCC and glutamate receptors allowing calcium fluxes in response to stimuli. Response to ATP was observed in a proportion of cells, including some also having responded to either glutamate or KCl. The cells reacting to both types of stimuli are possibly leading to an over-estimation of the number of glial cells in these cultures as this can be linked to either the recording of two superposed cells, or to over-susceptibility of the cells to excitation rendering them reactive to all stimuli.

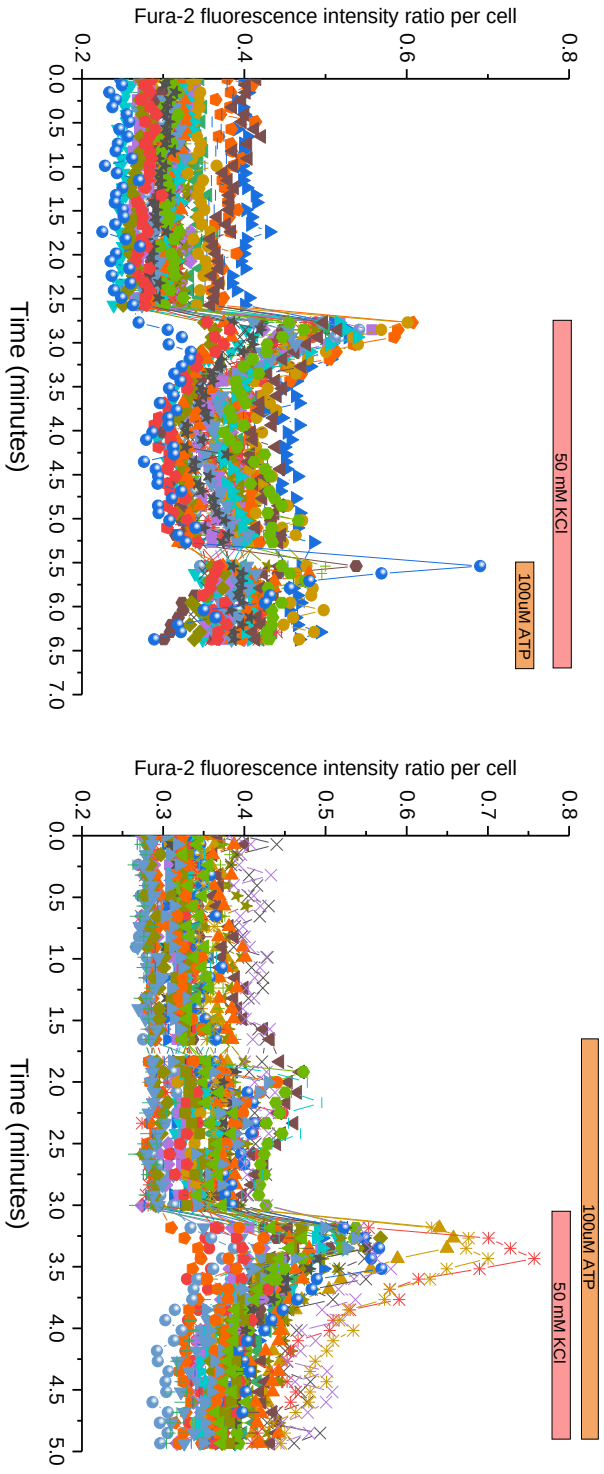

Figure 65: Characterisation of the cultures used for functional investigation of the mutation using calcium imaging. Changes in FURA-2 fluorescence intensity in single cells in response to stimuli (50 nM KCl and 100 µM ATP).

Based on these results, the presence of non-neuronal cells in the cultures prompts the necessity to visually select areas within the wells presenting an increased neuronal phenotype for functional imaging. Additionally, in experiments where cells could be clearly delimited, neuronal-looking cells only were used to measure the functional read-out of the experiment. Results are presented separately for each time-point at which functional experiments were performed in these neuronal cultures.

Mitochondrial membrane potential using TMRM

Mitochondrial membrane potential in neurons is estimated z-stack imaging after loading cells with TMRM. mCB is loaded together with TMRM as previously demonstrated not to significantly affect imaging results between cell lines (Figure 50&Figure 51). Mean TMRM fluorescence intensity is estimated across cells with a neuronal aspect. An example of TMRM fluorescence staining analysis in neuronal cultures is presented in Figure 66. Results from two separate inductions (1&2) at two distinct time points of the mDA induction protocol (early and late neuronal timepoints) are presented in Figure 67.

At early neuronal timepoint, both inductions show significant differences between their groups (Induction 1: $p = 0.00374$; $F = 11.08168$; Induction 2: $p = 0.02998$; $F = 3.95111$). This difference is associated with a significantly increased polarisation of the MMP in the PD compared to the DRD group for both inductions (Induction 1: $p = 0.00332$, 95% CI = 64.86426 - 279.31444; Induction 2: $p = 0.03974$, 95%CI = 17.15045 - 910.73844). These results are presented in the left column of Figure 67.

At late neuronal timepoint, MMP polarisation is significantly different in one induction (Induction 1: $p = 2.21936E\text{-}4$; $F = 15.52666$) but not in the other (Induction 2: $p = 0.34897$). For induction 1, this difference is associated with a significantly lower MMP in comparison to the control group in both PD group ($p = 5.44558E\text{-}4$, 95% CI = 251.36664 - 857.01503) and DRD group ($p = 8.29229E\text{-}4$, 95% CI = 227.22881 - 832.87719). These results are presented in the right column of Figure 67.

Results are pooled between inductions at early and late timepoint, with cells showing significant difference across all three phenotypic groups (early timepoint p = 1.46208E-4; F = 10.97714; df = 2; late timepoint p = 0.02462; chi-square = 5.05051; df = 1). At the early timepoint, this difference is associated with a significantly lower MMP in the DRD group than in the control group (p = 0.00984; 95% CI = 6.72831 - 60.4463) and in the PD group (p = 1.08498E-4; 95% CI = 26.58937 - 88.94838) (top of Figure 68). While at the late timepoint, it is associated with a significantly lower MMP in the PD compared to the control group (p = 0.02609; Z = 2.22486) (bottom of Figure 68). Additionally, although not significantly different from controls, the MMP in the DRD lines at the late timepoint is reduced.

Altogether, TMRM fluorescence intensity, reflective of MMP polarisation, is significantly reduced in DRD at early timepoint and PD at late timepoint (Figure 68), suggestive of a mutation-associated alteration of the MMP which affects the cells from the two disease groups differently in time. There may be a slower adaptation of the mitochondria with lowering of the MMP in the PD compared to the DRD group. This second observation needs to be confirmed in further induction sets.

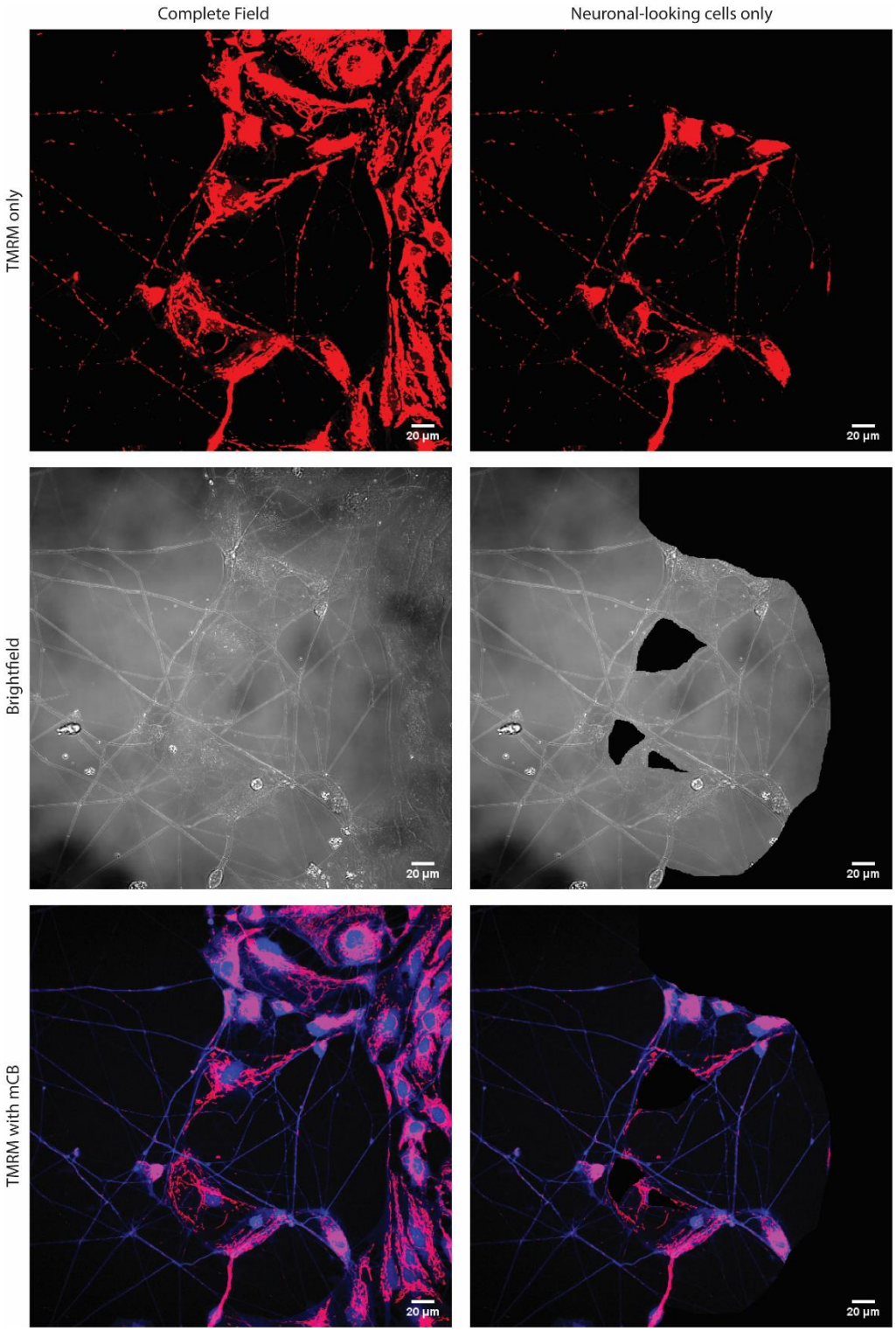

Figure 66: Example of TMRM image analysis. TMRM and mCB are loaded together (bottom row) and full-depth z-stacks are analysed by maximum intensity projection (left column). Areas with non-neuronal cells are removed from all layers (right column) prior to analysis of the TMRM channel only (top row).

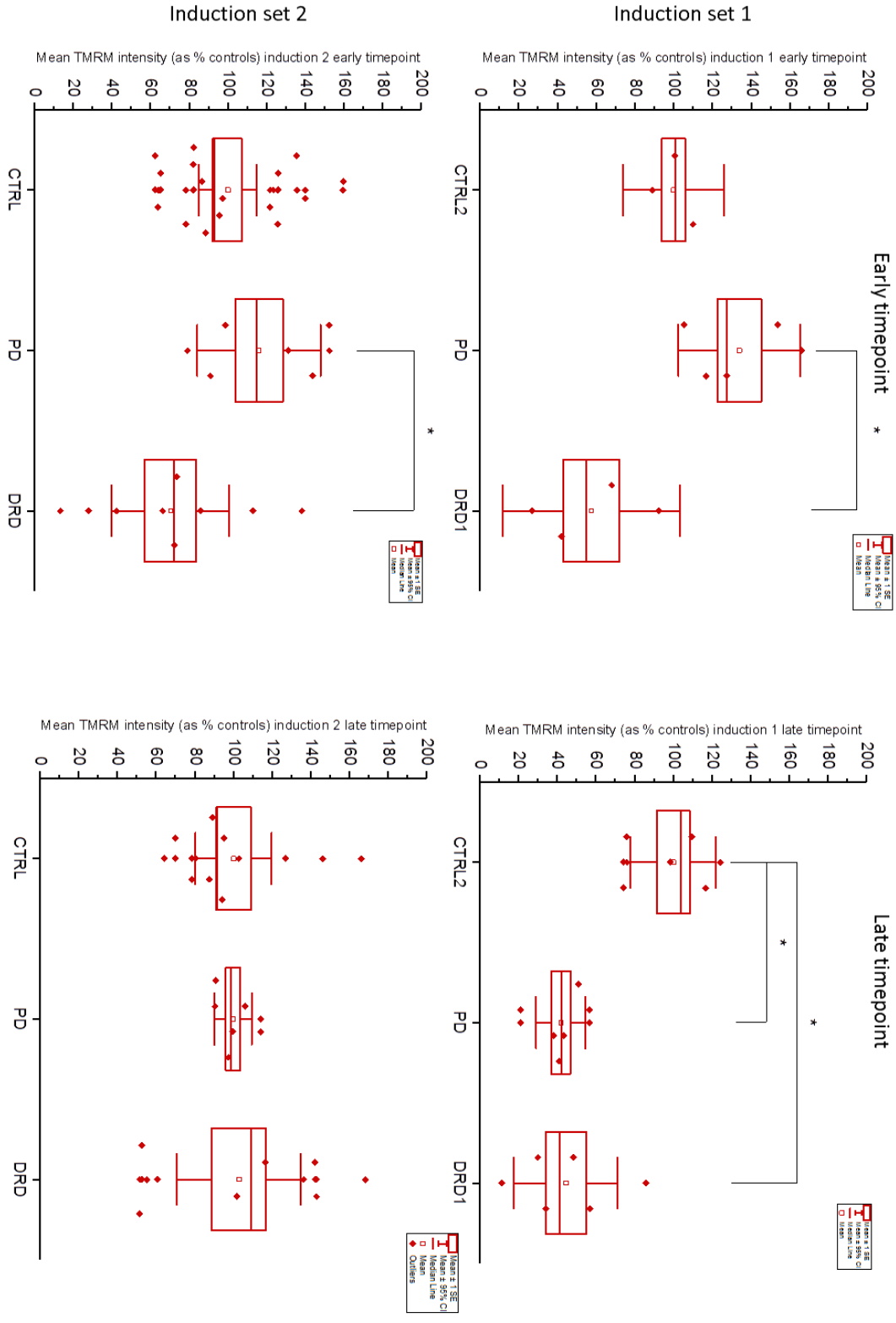

Figure 67: mean TMRM fluorescence intensity normalised to average of controls for whole-cell z-stacks. Results are presented for induction 1 (top row) and induction 2 (bottom row), at early neuronal timepoint (left column) and late neuronal timepoint (right column). Each data point represents a z-stack. Stars indicate significant difference between groups signalled by brackets. Box plot represents: mean (circle), median (line) median ± 1SE (standard error - box) and mean ± 95% CI (confidence interval – whiskers).

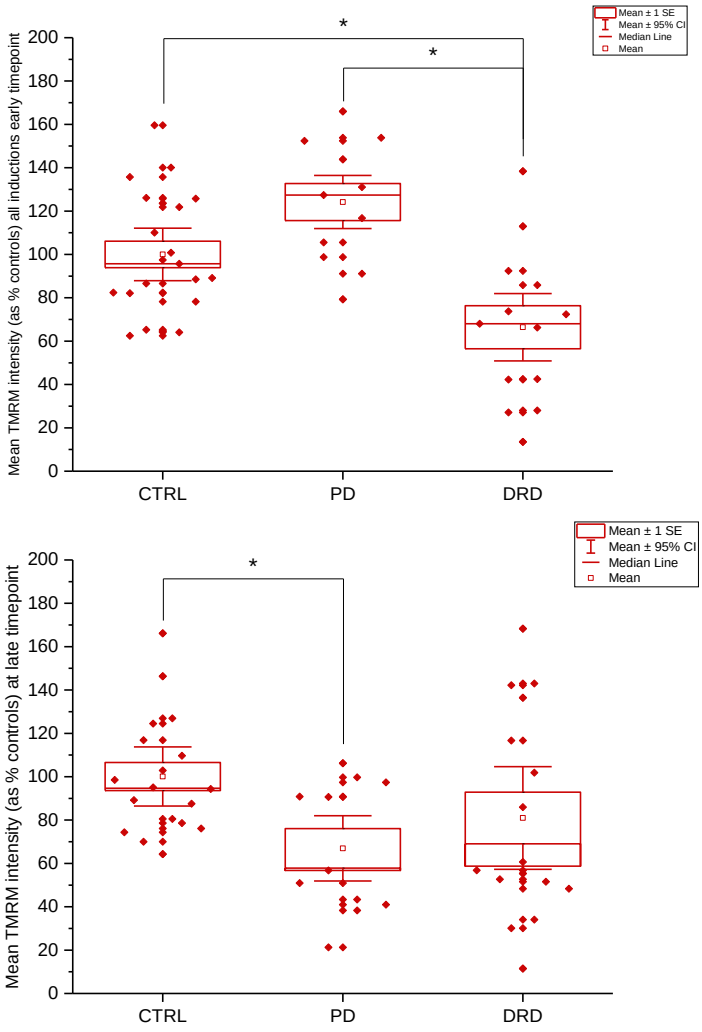

Figure 68: M**ean TMRM fluorescence intensity as percentage of controls pooled for each neuronal** timepoint: early on top, late on bottom. Each data point represents a z-stack. Box plot represents: mean (circle), median (line) median ± 1SE (standard error - box) and mean ± 95% CI (confidence interval – whiskers). Stars indicate statistically significant difference with $\alpha < 0.05$ between groups.

Mitochondrial ROS production using MitoTracker red CM-H2XROS

Mitochondrial ROS production rate is estimated by measuring the increase of fluorescence of MitoTracker red CM-H2XROS (MitoROS) in cells across time at the early neuronal timepoint. Image analysis for this experiment could not discriminate single cells with certainty (as can be seen in Figure 69), hence results are presented with one data point per field, one field per well. Example of a time-series with visible increase of MitoTracker CM-H2XROS fluorescence along time is presented in (Supplemental Material Figure 85). Representative plots for each clinical phenotype

group are shown in Figure 70, with an over-layer demonstrating the area of the curve used for slope calculation with linear model using Origin (Originlab). Results are plotted with each data point representing the slope value of one well. No significant difference can be observed between phenotypic groups ($p = 0.57031$) when pooling the results from both induction sets together Figure 71.

These results suggest that the differences in MMP between cell groups measured through TMRM intensity are not associated with a change in mitochondrial ROS production. Of note, the MMP influences the capacity of MitoTracker to accumulate in the mitochondria, potentially confounding these results. Additionally, due to the difficulty to discriminate the border between cells, these results are presented across all cells, neuronal and non-neuronal, in the field. This may be confounding the results by not enabling the observation of a neuronal phenotype in mitochondrial ROS production.

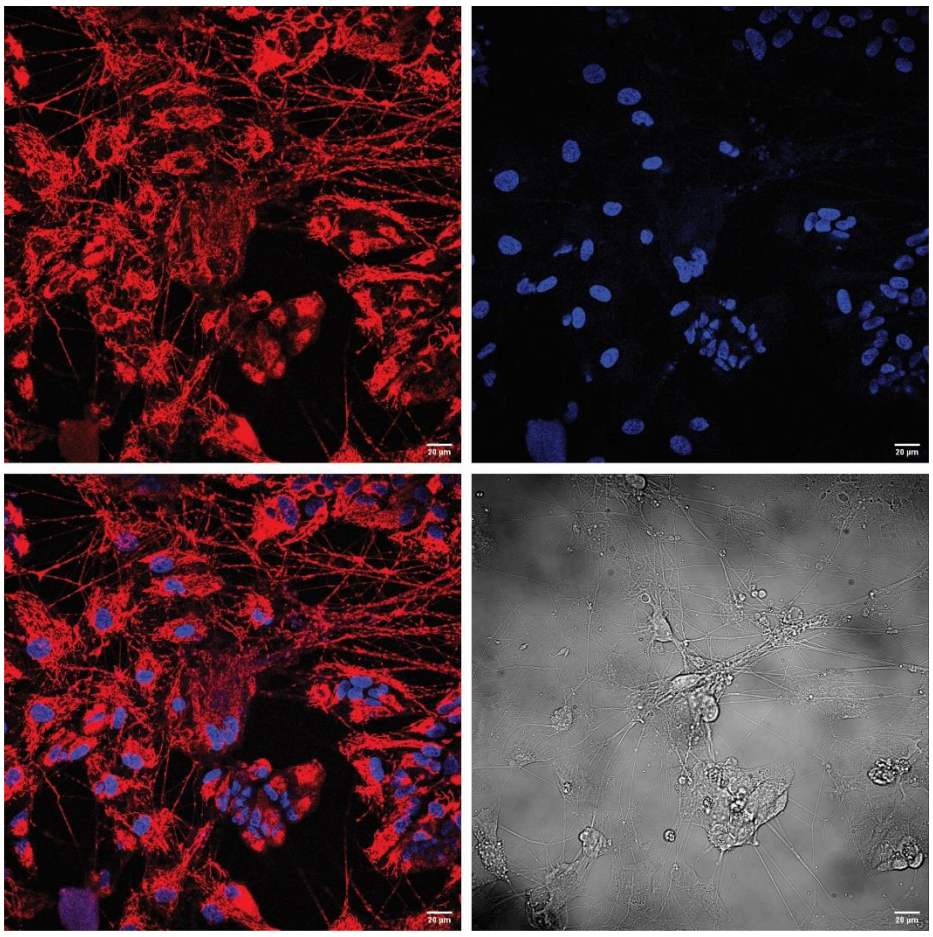

Figure 69: Representative image of MitoROS imaging of Neurons in association with Hoechst for nuclei staining. MitoROS is visualised in red in the mitochondria and nuclei are shown in blue.

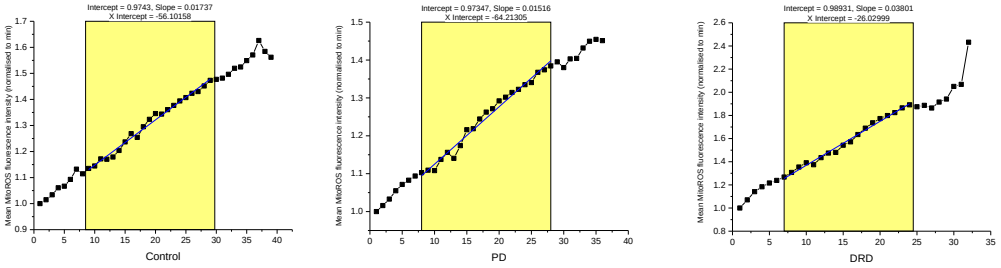

Figure 70: Representative traces of the MitoTracker CMH2XROS dye fluorescence evolution across time in neuronal cells for control, PD and DRD cells. The yellow area represents the time-span used to calculate rate of progression of fluorescence increase using a linear regression model.

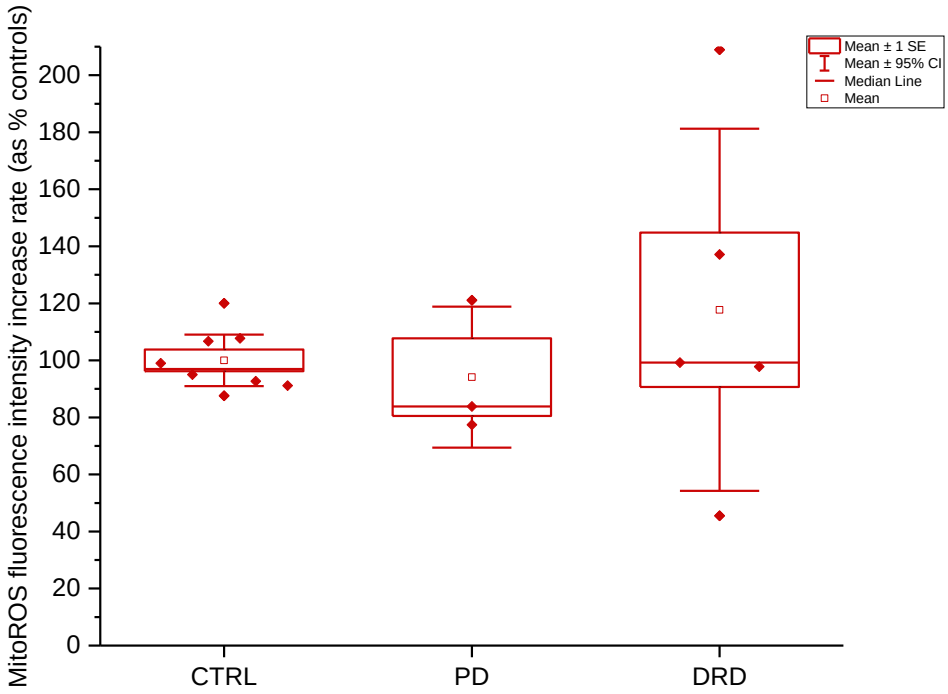

Figure 71: Boxplot of rate of ROS production by the mitochondria approximated by the increase in fluorescence intensity of the MitoTracker CMH2XROS dye in basal conditions at the early neuronal timepoint across both induction sets. Each data point represents a field. Box plot represents: mean (circle), median (line) median ± 1SE (standard error - box) and mean ± 95% CI (confidence interval – whiskers).

Oxidative state of cell – GSH with mCB

mCB is used to estimate cells content in GSH, which can be inversely correlated to the oxidative state of the cells. mCB is loaded and measured at the same time as TMRM in neuronal cells as this was previously demonstrated not to significantly affect

imaging results between cell lines. For each field, mean fluorescence intensity is measured after removal of all cells with a non-neuronal aspect from the imaging field.

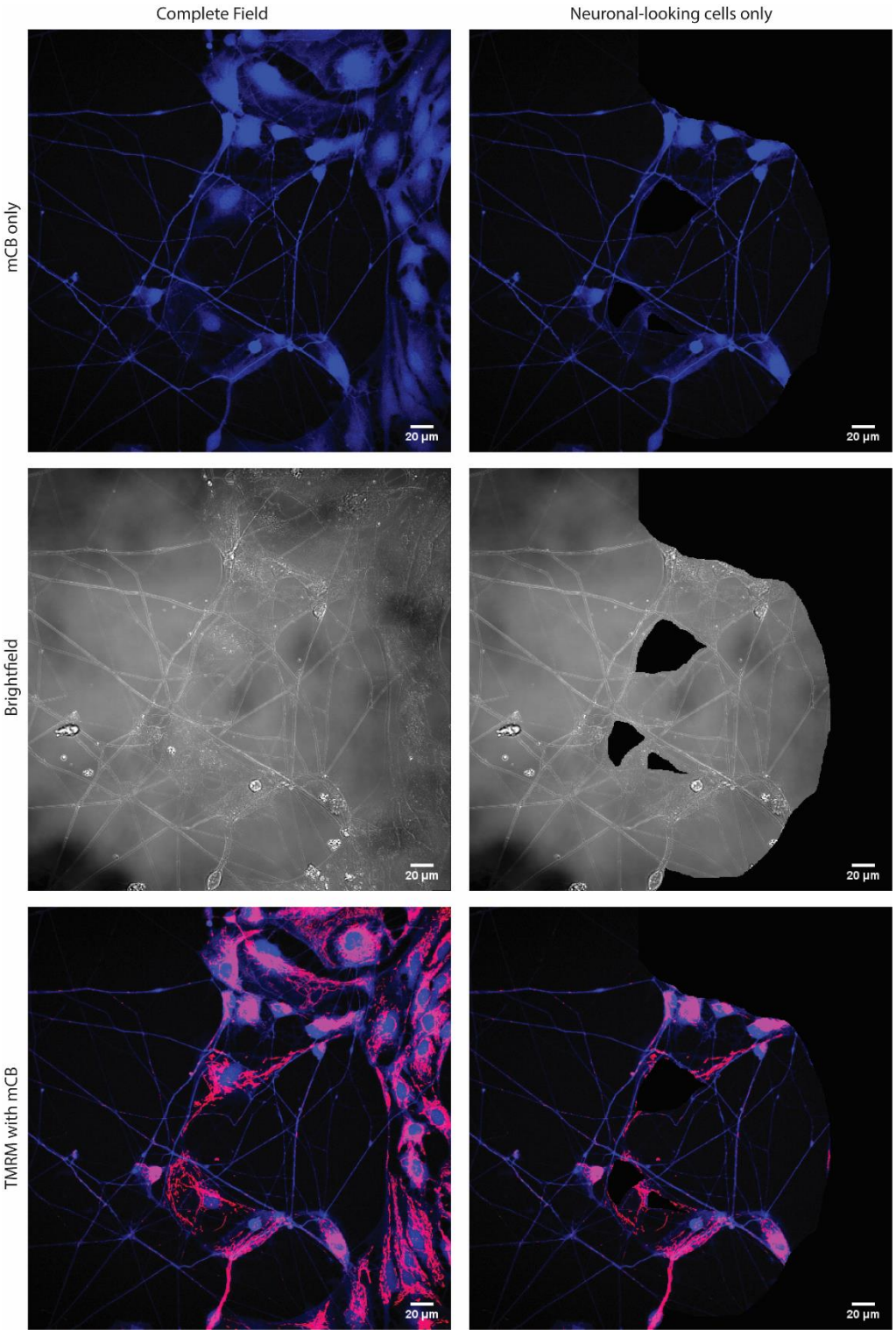

Figure 72: Example of mCB image analysis. TMRM and mCB are loaded together (bottom row) and full-depth z-stacks are analysed by maximum intensity projection (left column). Areas with non-neuronal cells are removed from all layers (right column) prior to analysis of the mCB channel only (top row).

An example of mCB fluorescent staining in neuronal cultures and selection of cells for analysis by deletion is found in Figure 72. The experiment was performed at two time points and results pooled between inductions are presented at both time-points (Figure 73). There is no significant difference in GSH content between the disease groups at either timepoint.

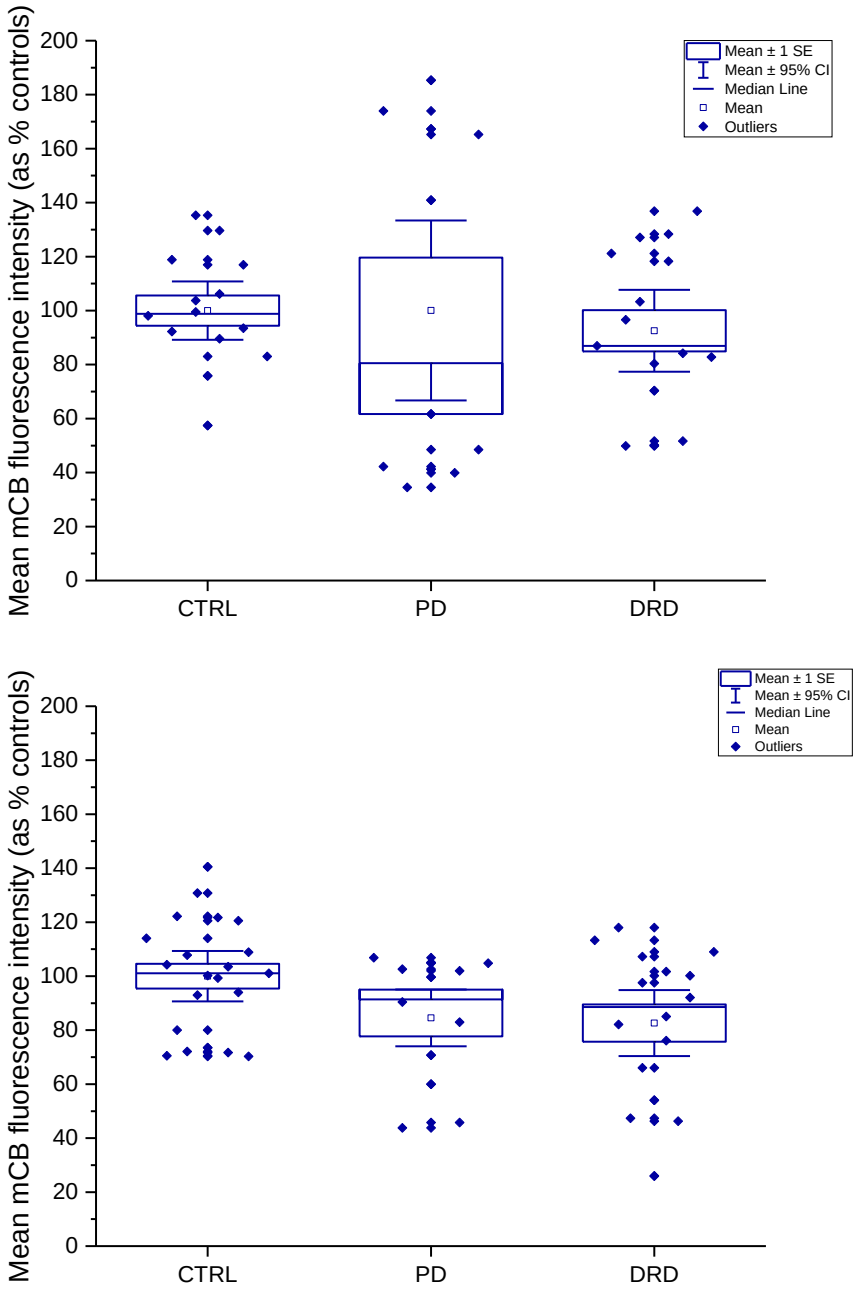

Figure 73: Mean mCB fluorescence intensity normalised to average of controls for whole-cell z-stacks. Results are presented for both inductions pooled at early (top) and late (bottom) timepoints. Each data point represents a field. Box plot represents: mean (circle), median (line) median ± 1SE (standard error - box) and mean ± 95% CI (confidence interval – whiskers).

Superoxide production with DHE, cell by cell analysis

DHE is used to estimate the rate of production of superoxide in neuronal cells, by using slope of progression of DHE oxidised:reduced ratio. An example of a time series is presented in (Supplementary Material Figure 86). An example of the observed fluorescence at each wavelength separately, for a time-point when oxidation of the dye and its relocation to the nuclei has started is presented in Figure 74 and demonstrates the possibility to clearly delimitate each nucleus for image analysis. Images are analysed by manually selecting the nuclei of cells with a neuronal aspect and measuring the fluorescence intensity at both wavelengths for each nucleus. Ratio of fluorescence intensity as 530:380nm is calculated for each time-point and plotted against time. A linear model is used to estimate the rate of change of the ratio along time for each nucleus separately (Figure 75). Nuclear slopes are normalised to the average of slopes for control cells and plotted in either of three groups: controls, PD or DRD (Figure 76).

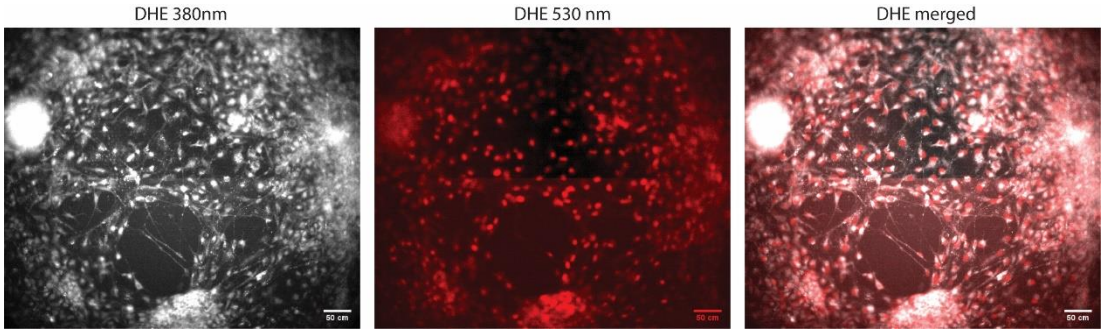

Figure 74: Example of DHE 380nm and 530 nm channels. Image was selected towards the end of the experiment to illustrate the relocalisation of the dye to the nucleus after its shift from 380nm to 530nm fluorescence wavelength.

At the early neuronal timepoint, the assumption for homogeneity of variances is not respected and the three phenotypic groups are compared with non-parametric Kruskal-Wallis test, resulting in a significant difference between groups in both induction sets (Induction 1: p = 2.14433E-6; Chi-Square = 26.10537; df = 2 & Induction 2: p = 0.00106; Chi Square = 13.69829; df = 2). Comparisons of these groups by pairs are performed using Mann-Whitney U-test with Bonferroni correction. The rate of production of superoxide by the PD group is significantly lower than in controls in both inductions (Induction 1: p = 3.0595E-5; Induction 2: p = 0.00253). Superoxide production is found significantly lower in DRD than in controls in induction 1 (p =

1.16759E-5) but not induction 2 ($p > 0.0167$). Finally superoxide production is significantly lower in PD group than DRD group in one induction 2 ($p = 0.0046$) but not induction1 ($p > 0.0167$). Results of the first time point are presented in the left column of Figure 76.

At the late neuronal timepoint, the assumption for homogeneity of variances is not respected either and the same statistical tests applied. There is a significant difference between groups in both induction sets (Induction 1: $p = 3.60705E-5$; Chi-Square = 20.46007; df = 2 - Induction 2: $p = 2.32175E-12$; Chi Square = 53.5774; df = 2). For both inductions, the rate of production of superoxide is found significantly higher in the DRD group than in the control group (Induction 1: $p = 2.00442E-4$; Induction 2: $p = 1.44151E-9$) and in DRD group than in PD group (Induction 1: $p = 5.20613E-6$; Induction 2: $p = 5.62792E-11$). However, there is no statistically significant difference between the PD and control group in either induction set at the later timepoint ($p > 0.0167$). Results of the second time-point are presented in the right column of Figure 76.

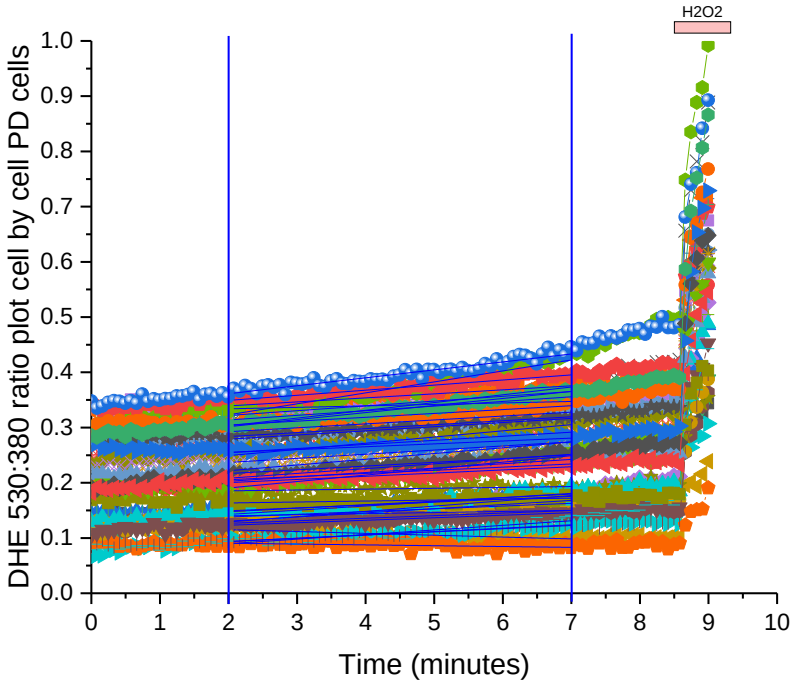

Figure 75: Example of slopes for DHE oxidised:reduced ratio in neurons. Each set of data represents the progression of the ratio with time at the nucleus of a neuronal-looking cell. Blue lines represent the linear regression for best fit for each of these and is used to calculate the slope.

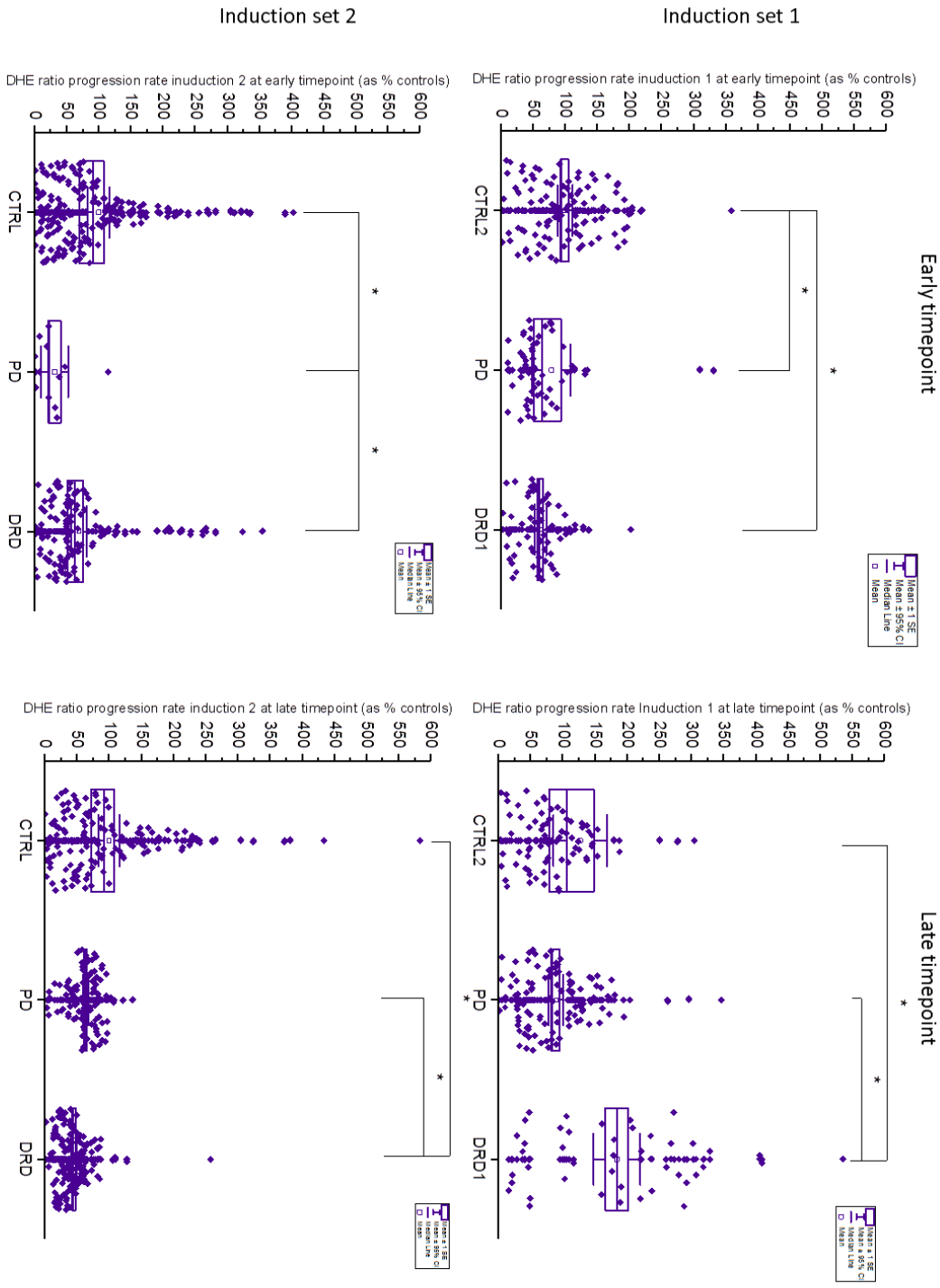

Figure 76: DHE 530:380 slope normalised to average of controls for whole-cells z-stacks. Results are presented for induction 1 (top row) and induction 2 (bottom row), at early neuronal timepoint (left column) and late neuronal timepoint (right column). Each data point represents a cell. Box plot represents: mean (circle), median (line) median ± 1SE (standard error - box) and mean ± 95% CI (confidence interval – whiskers). Means are compared by Kruskal-Wallis ANOVA and stars indicate statistically significant difference with $\alpha < 0.05$ between groups.

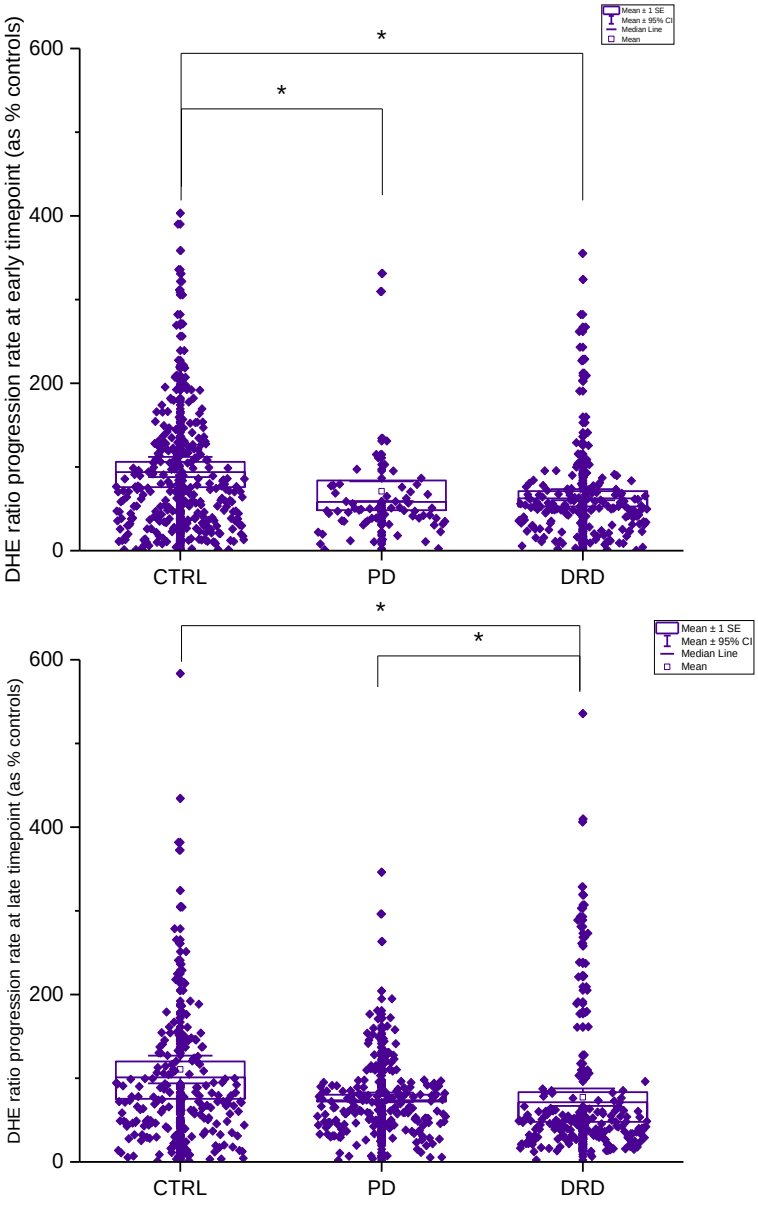

Figure 77: Pooled data from induction sets for DHE 530:380 slope normalised to average of controls for whole-cell z-stacks. Results are presented for both early neuronal timepoint (top) and late neuronal timepoint (bottom). Each data point represents a cell. Box plot represents: mean (circle), median (line) median ± 1SE (standard error - box) and mean ± 95% CI (confidence interval – whiskers). Means are compared by Kruskal-Wallis ANOVA and stars indicate statistically significant difference with $\alpha < 0.05$ between groups.

As the results from both inductions are similar at each time-point, these are pooled to compare superoxide production in the mDA neurons between induction timepoints (Figure 77). At both time-points, there is a significant difference between the three groups (Early neuronal timepoint: p = 8.63685E-6; Chi-square = 23.31895; df = 2 & Late neuronal timepoint: p = 7.21584E-7; Chi-square = 28.28363; df = 2). At the early neuronal timepoint, the rate of superoxide production is significantly lower in the PD

group (p = 6.94872E-4) and in the DRD group (p = 2.43768E-5) than in the control group. There is no significant difference between the disease groups (p > 0.0167 in DRD vs PD). At late neuronal timepoint, the rate of superoxide production is similar in the PD and control groups (p > 0.0167) but significantly lower in the DRD group when compared to both control group (p = 9.42213E-6) and PD group (p = 2.55186E-6).

Thus superoxide production rate appears significantly lower in all *GCH1* mutation carriers at the early neuronal timepoint and in DRD in the late neuronal timepoint. However, there is a trend, albeit non-significant, for the maintenance of this low level production in the PD cell at the later timepoint.

Measuring NO production in neurons – DAR-4M experiments

Basal NOS activity as well as deltaDAR-4M(L-arginine) activated NOS activity are measured via NO production associated with DAR-4M emission fluorescence intensity changes in dynamic live-cell imaging in the neuronal cultures. Fluorescence intensity fluctuated greatly in cells, both in basal and arginine-activated states, with variable rhythm between neighbouring cells, as can be observed in Figure 78. Overall field fluorescence intensity also fluctuated greatly with time as visualised in Figure 79, making the interpretation of dye intensity changes and the response to arginine stimulation virtually impossible. This fluctuating pattern may be associated with the transient increases of intracellular Ca2+ levels associated with neuron action potentials due to mechanisms similar to mDA pace-making activity, thus reflecting the calcium-dependent fraction of NOS activity in these cells (Fleming et al., 1997).

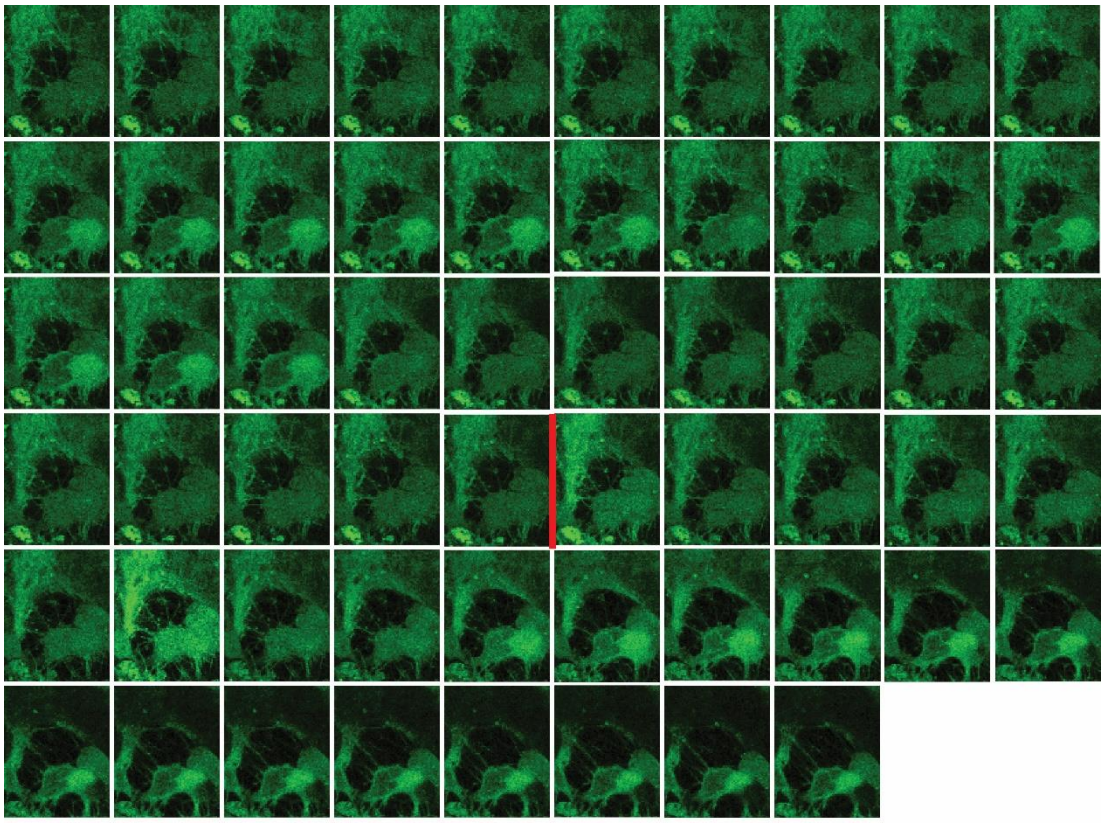

Figure 78: Representative detail of a time-series of DAR-4M imaging in control neurons. Images are sequential in time from top left to bottom right. The red line marks the time of addition of L-arginine. The fluorescence plot of this well is found in **Figure 79**

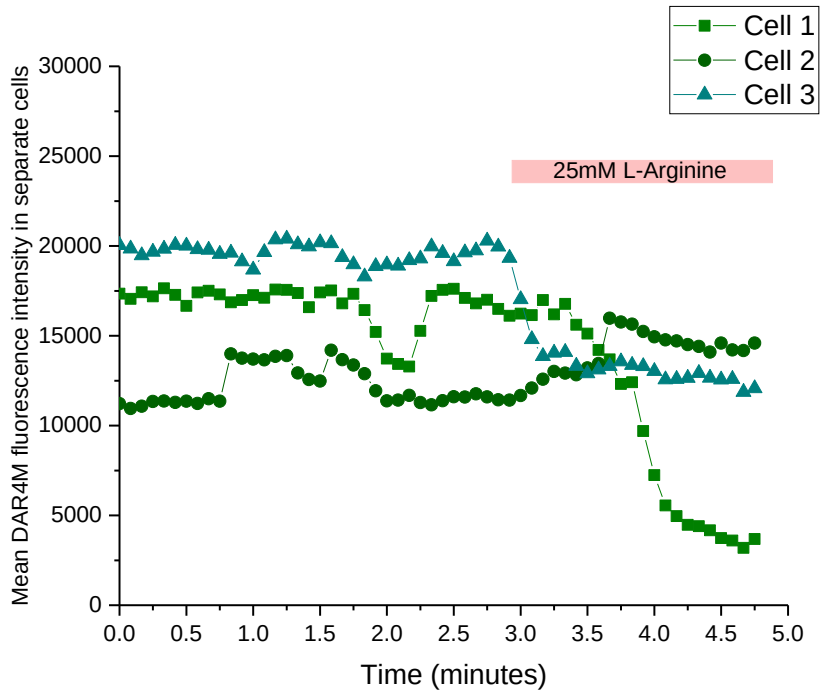

Figure 79: Fluctuation in DAR4M fluorescence is visible on the corresponding plot of mean fluorescence intensity on time for the field shown in Figure 78. Three cells from detail are selected and plotted separately.

Sytox Green for cell death in neurons

Sytox Green is a non-cell permeant nuclear marker which only accesses and marks the nuclei of dead cells, with an important increase in its fluorescence intensity upon binding to nucleic acids. Cells are loaded with Sytox Green and Hoehst and 5 z-stacks are acquired for each well. Images are analysed by counting Hoechst-positive nuclei belonging to cells with a neuronal aspect (total nuclei) and determine the proportion of these which are SytoxGreen positive (dead cells). An example for these staining is found in Figure 80. The experiment was conducted in two separate inductions at the early neuronal timepoint, with each data-point representing the proportion of dead cell in each z-stack, and the pooled results presented in Figure 81.

Population means are found significantly different across the three phenotypic groups ($p = 0.00647$; $F = 5.34372$; $df = 2$). This difference is associated with a significantly higher proportion of cell death in the PD group compared to both the control group ($p = 0.01187$; 95% CI = 14.20956 – 147.73695) and the DRD group ($p = 0.00985$; 95% CI = 16.87755 – 158.36479).

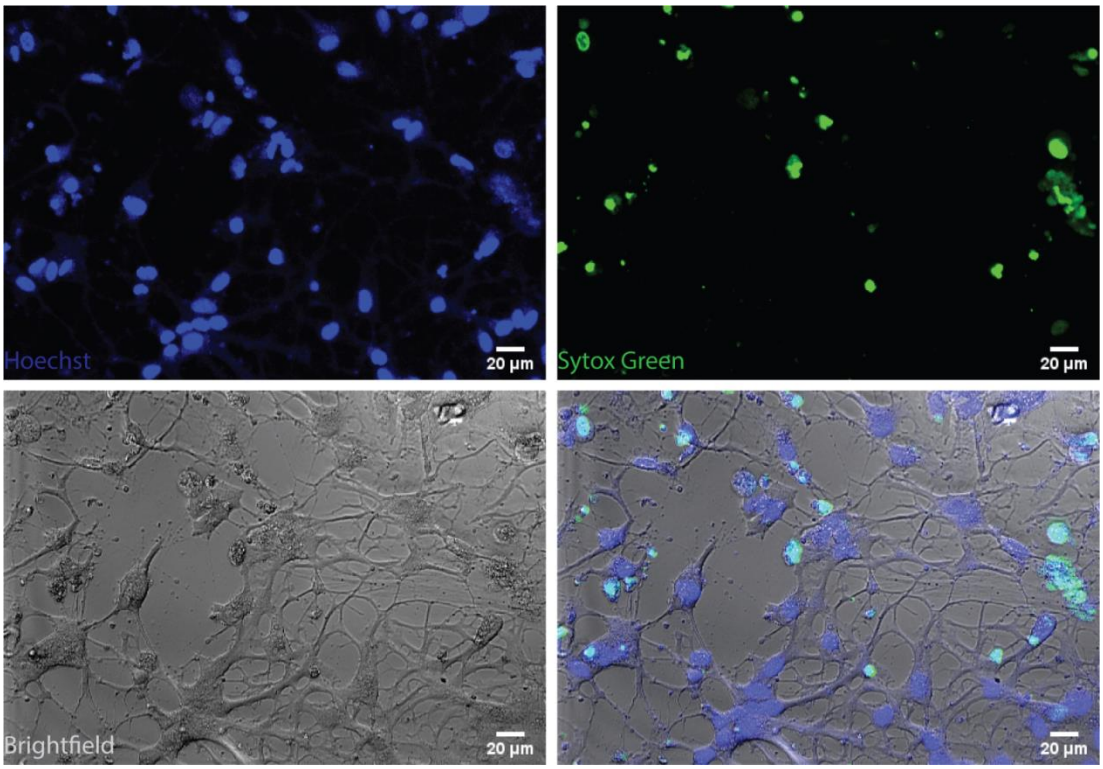

Figure 80: Cell death staining with Sytox Green. All nuclei are stained with Hoechst (upper left) and nuclei from dead cells with Sytox Green (upper right). Neuronal looking cells are visualised and used for counts based on brightfield image (bottom left).

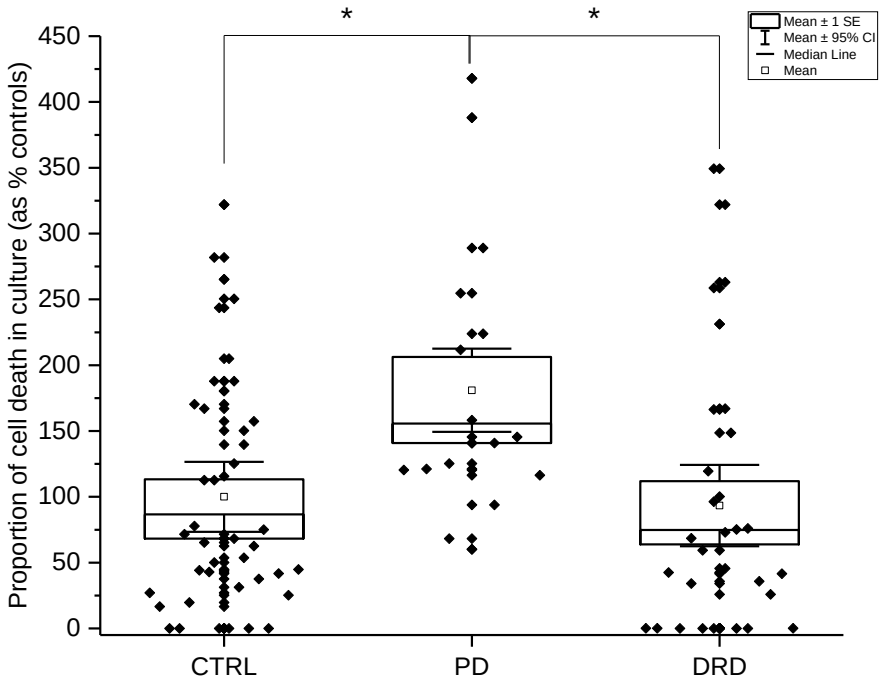

Figure 81: Proportion of cell death across all imaged neurons for both induction sets at the early neuronal timepoint, normalised to average of controls. Each data point represents a field of view. Box plot represents: mean (circle), median (line) median ± 1SE (standard error - box) and mean ± 95% CI (confidence interval – whiskers). Means are compared by one-way ANOVA with multiple t-test with Bonferroni correction and stars indicate statistically significant difference with $\alpha < 0.05$ between groups.

These results demonstrate an important increase of cell death in PD cells compared to the control and DRD ones, reminiscent of the neurodegenerative aspect of the pathology in the human brain. This is visible in the mDA neuronal cultures from the early neuronal timepoint and needs to be confirmed at different time-points. This result is hinting at a mDA neuron-specific susceptibility to cell death in a PD patient-derived model in culture that is absent from the DRD cells. This may underlie the differences observed in the presentation of the pathology in individuals carrying the studied *GCH1* mutation.

Synthesis of neuronal results

Live cell imaging experiments in the mDA neuron stage demonstrate that, similarly to the NPC stage, the use of TMRM for the estimation of MMP, mCB for GSH content, DHE for superoxide production and MitoROS for mitochondrial ROS are possible live in this model, although with some variation apparent between induction sets and some difficulties in performing single cell analyses due to confluence. Additionally, FURA-2 can be used to visualise calcium fluxes both spontaneously and in response to stimuli and that these are influencing NOS activity as visualised with DAR-4M staining. Finally, proportion of cell death in the cultures can be estimated with the concomitant use of DAPI and SytoxGreen.

At the early neuronal timepoint, cell death is significantly increased in the PD line compared to controls and DRD, and this is associated with lower content in GSH and lower superoxide production, but no changes in mitochondrial function (either MMP or mitochondrial ROS production). The DRD cells present with a depolarised MMP compared to controls and PD at this stage, associated with a lower superoxide production than controls, but no change in GSH content or cell death percentage. Cell death in the PD cells may thus be independent of mitochondrial function at that stage but associated with changes in the redox balance of the cells.

At the later timepoint, data on cell death is unavailable but a reduction in the MMP is observed in the PD cells, suggestive of a progressive deficit in mitochondrial function associated to the mutation that emerges with time in culture. As results are less consistent between sets, repetitions are warranted to draw any conclusions on these. Overall results are summarised in Table 29.

Time	Early Timepoint			Late Timepoint		
Experiments	**Induction 1**	**Induction 2**	**Overall**	**Induction 1**	**Induction 2**	**Overall**
MMP	Depolarised in DRD			Depolarised in mutants v/s controls	no change	Depolarised in PD
GSH	Lower in PD v/s DRD	Increased in PD v/s DRD and controls	No difference	Lower in DRD than controls	no change	No difference
Superoxide	Lower in mutants v/s controls	Lower in DRD and v/s controls	Lower in mutants v/s controls	Higher in DRD than PD and controls	Lower in DRD than PD and controls	Lower in DRD than PD and controls
Cell death	Higher in PD than DRD and controls			n/a		

Table 29: Overall neuronal results in both inductions and at early and late timepoints

IV. Discussion

Results from the functional analysis of the *GCH1*-BH4 pathway in *GCH1* mutant cells, compared to healthy controls, provide insights into the cellular functions associated with the phenotypic differences observed between PD and DRD patients.

The control group has measurable MMP, basal mitochondrial ROS production, antioxidant (GSH) levels, superoxide production, lipid peroxidation at the membranes, and NOS activity from an early neural precursor stage. These, with the exception of the last two parameters, can be measured at the later neuronal stage of the induction protocol. Additionally, the proportion of cell death in culture can be determined in the neuronal cells.

The DRD cells demonstrate an increased polarisation of their MMP as well as higher GSH content at the NPC stage, which are not reflected by a change in mitochondrial ROS or overall superoxide production. Upon becoming neurons, their MMP is significantly depolarised, from which they only partially recover at a more mature timepoint. These changes are associated with a decrease of their production of superoxide with no effect on mitochondrial ROS production, GSH content or neuronal cell death in the DRD model.

The PD cells do not demonstrate significant differences in MMP polarisation, mitochondrial ROS, GSH levels, superoxide production or NOS activity compared to controls at the NPC stage, although they have a significantly depolarised MMP compared to DRD cells. When becoming neurons, the MMP of PD cells is first slightly polarised (early timepoint) and later significantly depolarised compared to controls. These cells also demonstrate a decreased superoxide production with no effect on mitochondrial ROS production or GSH content measurements. These alterations are associated with a significant increase of neuronal cell death compared to both DRD and control cells.

The difference in MMP observed between the mutant groups at the NPC stage may be associated with the concomitant increased polarisation of the MMP in DRD cells and

depolarisation of the MMP in PD cells in comparison to controls. These may be indicative of a difference in the timing with which the mutation affects the MMP between the disease groups, as is also observed at the early neuronal timepoint with an increased polarisation of the MMP in PD cells and a depolarisation in the DRD cells. It appears that this *GCH1* mutation causes a progressive decrease in mitochondrial health and function in PD cells which may be relevant to the vulnerability of these cells to death. The maturity achieved by these cells with longer times in culture may reveal phenotypes relevant to ageing diseases.

The increased GSH content of DRD cells at the NPC stage may be the result of its decreased use for buffering ROS or by an increased expression of glutathione to buffer larger quantities of ROS compared to the other groups. To determine which mechanism is at stake, it would be important to capture the level of expression of glutathione and other antioxidants such as BH4, ascorbate or superoxide dismutase in these cell groups using qPCR and western blots.

The progression in the production of superoxide overtime, from a baseline similar between all groups at NPC stage to an early decreased production in DRD (only a trend for PD) and a lower production in both PD and DRD compared to controls in neurons at a later stage, may be explained in many different ways. First, it could reflect the length the cells have spent in culture or second, the maturation stage of the cells, hinting at a possible cell-type specific superoxide metabolism in this model. Both could be affecting the lines differently due to the inter-line variability of the donor's phenotype or of the induction process. A third possible explanation is molecular competition between DHE and NO for reacting with superoxide in these cells. Due to the nature of the studied *GCH1* mutation, BH4 levels may be reduced in mutant cells compared to healthy controls, leading to an imbalance of the BH4:BH2 ratio and the uncoupling of a proportion of NOS in these cells: coupled NOS would produce NO while uncoupled NOS would produce superoxide. Additionally, fluctuations in intracellular calcium are associated with waves of activation of NOS in the neuronal cells but not in the NPC, potentially increasing the demand of mDA neurons for BH4. Both highly reactive molecules can interact extremely fast to produce peroxynitrite, which may limit the availability of superoxide to be measured by DHE, hence be

associated with an under-estimated superoxide production rate in the mutant cells (Beckman and Koppenol, 1996). Indeed, superoxide reacts with DHE at a reaction rate constant k ~ 10^3 $M^{-1}s^{-1}$ (Chen et al., 2013), while the reaction of superoxide with NO occurs with a constant k ~10^{10} M^{-1} s^{-1} and produces peroxynitrite which is permeant to cell membranes, can travel ~10μm from its site of formation (the equivalent of 1-2 cell diameters) and has a biological half-life of ~5-20ms (Radi, 2013). Measuring the production of peroxinitrite in these cells could confirm this hypothesis. However, peroxinitrite measurement is extremely difficult in live cells as most of the existing probes are reporting oxidation which can be confounded by the presence of other oxidants in the cells, such as the commonly used dihydrorhodamine which can be oxidised by hydroxyl radicals or nitrogen dioxide (Kalyanaraman et al., 2012; Wardman, 2008). A promising alternative could be the use of boronate-containing fluorophores, as these boronate species are oxidised to stable fluorescent molecules by rapid and stoichiometric reaction with peroxynitrite (Sikora et al., 2009; Zielonka et al., 2010). Additionally, it is recommended to confirm DHE results by HPLC in order to confirm the superoxide-specific nature of the observed signal, as other intracellular oxidants such as cytochrome or iron with H2O2 may interact with the molecule, forming ethidium instead of 2-hydroethidium, which presents with similar fluorescence spectral characteristics (Kalyanaraman et al., 2012).

Interestingly, cell death is significantly increased in PD compared to both DRD and control groups at the neuronal stage, reminiscent of the mDA neuronal degeneration observed in PD patients. Interestingly, this result is obtained when focussing analysis on neuronal cells: overall cell death in the imaging fields is decreased in DRD compared to both PD and control lines (data not shown). These observation may support the hypothesis that dopaminergic-specific cell death associated with PD and/or that the presence of supportive mechanisms in DRD which support overall survival in vitro.

Finally, proof-of-principle experiments demonstrate that lipid peroxidation and NOS activity can be measured in these iPSC-derived models using Bodipy C11 and DAR-4M AM fluorescent dyes respectively, using the adapted methods described in this chapter. The first provides a proxy for the alteration of cellular membranes associated

to oxidative stress and lipid peroxidation has been described in human PD brains (Dalfó et al., 2005; Dexter et al., 1989). Using bodipy C11 in the neuronal cells showed rapid oxidation of the dye and consequent loss of dynamic range for the measurement of lipid peroxidation; hence the loading method needs to be optimised in these cells.
The latter provides an alternative for measuring NO production in this model to the commonly used DAF-FM AM dye, routinely used in our lab on different cell models, but which lacks the ability to load in these cells (example in Supplementary Material Figure 87). In the *GCH1* model, reduced BH4 levels affect NOS coupling leading to the production of superoxide instead of NO; and the importance of this disease mechanism may vary between disease groups. Measuring NO production is thus important in the context of this study. Although DAR-4M is successfully loaded in the neuronal cultures, its fluorescence fluctuates greatly in the absence of glutamine, potentially due to intracellular calcium fluctuations activating eNOS and nNOS in this cell type (Fleming et al., 1997). Due to these oscillations in NOS activity, z-stacks cannot be used to measure basal NOS activity and measuring the amplitude of NOS activation post-arginine stimulation becomes difficult in these cultures. These may also be the reflection of cell-to-cell communication in vitro since NO is involved in neuronal signalling (Garthwaite, 2008).

1. Limitations

Technical difficulties need to be overcome, mainly through the improvement of the method to increase the yield of mDA neurons by the end-point stage. One achievement of this method is the quasi-purity of patterned mDA FP neural progenitors obtained at the NPC timepoint, which suggests a later variation in further maturation of these cells. The use of a method for selecting the cells committed to becoming mDA neurons at an intermediate stage between NPC and early neuronal timepoint could improve these yields. Magnetic-activated cell sorting (MACS), a less stringent variation of the fluorescence-activated cell sorting (FACS) for the cells, could provide a solution should extracellular markers for these neurogenic cells be identified. Current candidate markers include N-CAM and CD166 (Kirkeby et al., 2017; Paik et al., 2018). Increasing yields will also promote the use of non-fluorescent-based methods for the analysis of metabolites such as HPLC. Finally, the lack of enrichment in mDA

neuronal cells may be accounting for much of the observed well to well and induction to induction variability.

Another issue inherent to the method is the need for extreme confluency of the cells for differentiation and survival during most of the induction, leading to difficulties for loading dyes and for image analysis. The necessity for high density plating in mDA differentiation has been observed by team attempting mDA neurons differentiation from primary mesencephalic precursor cultures (Ko et al., 2005). Using sparser densities of NPCs in my experiments led to massive cell death and loss of cultures. Such high density of cells limits the ability for the dye to load uniformly. Moreover, imaging areas with lower cell densities which are not representative of the cultures risks to include bias in results. At the NPC stage, the use of whole-fields results is warranted. At the neuronal stage, the use of live TH-staining for the identification of the mDA neurons in culture, via the use of *TH* promoter-dependent expression of fluorescent markers or extracellular markers and specific live-staining antibodies, is considered to allow improvement and automatization of whole-single cell image analysis.

Overall, the validation of these results requires their replication, which can be achieved at different levels. First, these results are obtained using one iPSC clone for each line, 4 controls and 2 DRD and 1 PD, allowing for the potential risk of describing a clone-specific phenotype in the PD line due to the absence of replication. The next inductions could be performed in different clones to overcome this caveat. Second, these results describe the diseases phenotypes in a single family carrying a single *GCH1* mutation, and thus may be mutation- or family-specific. Replication of these results in cells from different *GCH1* families associated with the same mutation (removing family-specific confounding effects) and with a different *GCH1* mutation (removing both mutation and family specific confounding effects) is warranted to overcome this caveat. Third, as control lines were obtained from unrelated healthy individuals, the differences observed in mutant vs control groups may be associated with differences between the genetic backgrounds of these individuals. Validation of the association of the observed phenotype with the *GCH1* point mutation (c.343+5C>G) will necessitate the production of isogenic lines from the disease cells in which the point mutation is

corrected. Consistent differences between mutant lines and their corresponding isogenic controls as well as healthy controls and their mutated version would allow the differentiation of mutation-induced phenotypes from family genetic background phenotypes.

2. Further experiments

To my knowledge, this chapter constitutes the first observation of basal functional alterations in hiPSC-derived midbrain neural progenitors in the absence of deleterious stimulus in PD and the first investigation of these cells in DRD patient-derived cells. A previous study found that hiPSC-derived early forebrain progenitors from PARK2 patients have a higher susceptibility to exposure to copper (Aboud et al., 2015). Using human fetal midbrain NPCs and siRNA one team studied the effect of LRRK2 KD on apoptosis and differentiation (Milosevic et al., 2009). Another investigated the neuronal-progenitor subtype specificity of MPTP, 6-OHDA and H2O2 toxicity in rat primary midbrain neuroprogenitor cultures (Sabolek et al., 2008). However these studies all use external stimuli to induce a phenotype.

All the results described in this chapter are obtained in unstimulated cells, with the exception of NO synthesis measurement and calcium imaging. The use of specific stimuli may be used to provide further insights into the aetiology of these diseases by observing the coping ability of the cells. Mitochondrial ETC complex I inhibitors such as rotenone could be used to further impact mitochondrial function and increase ROS production in the cells. The latter could have a more visible effect in mutant cells which partially lack antioxidant defences and allow the measurement of a greater difference in MitoROS production, GSH content, lipid peroxidation and superoxide production between mutants and controls. These differences could in turn be corrected by increasing the expression of *GCH1* in all cells, with the use of TNF-alpha and/or IFN-gamma similarly to the fibroblast chapter, thus supporting the role of the mutation, or lead to further impairments. Moreover, increasing neuronal activity in cultures with short, low concentration treatment with KCL may reveal further mutant phenotypes associated with their reduced ability to release dopamine as a result from this

stimulation. It may also trigger excitotoxicity in these neurons, to which the mutant cells might have different coping ability than controls.

In a related approach, supplementing the cells with L-DOPA, in order to support dopamine production independently of *GCH1* and BH4 in these cells, could focus the observed effects of the mutation on non-dopamine-related mechanisms. Sepiapterin can be transformed into BH4 by sepiapterin reductase in the salvage-pathway of BH4, independently of *GCH1* expression. By supplementing the mutant cells with sepiapterin and observing at least a partial rescue of their phenotype could further narrow down functional observation to the effects of the *GCH1* mutation only in this model. This has been used in a previous publication (Ishikawa et al., 2016). However, the use of these molecules need to be validated first: both levodopa and TNF-alpha are suggested to have toxic effects on mDA cells in vitro (McGuire et al., 2001; Mytilineou et al., 2003), and toxicity needs to be established prior to the use of this molecule. For instance, the use of ascorbic acid, a powerful antioxidant, or of deprenyl, an inhibitor of monoamine oxidase type B, in cultures seem to limit the toxicity of levodopa (Mena et al., 1992; Pardo et al., 1993).

Observations of a phenotype and of phenotypic differences between *GCH1*-associated PD and DRD patient-derived cell model constitute a strong support for the discovery of underlying mechanisms in both pathologies. Using patient-derived cell models is of the outmost importance in the research into genetic causes of these diseases. However, this *in vitro* cell model comes with the essential caveat of focussing on a single cell-type model which is not representative of a complete organism. Confirmation of these results would also be necessary in animal models: there are currently at least two mice models fully characterised and validated for loss-of-function analyses of *GCH1* in October 2018 by the international mouse phenotype consortium (Dickinson et al., 2016). *GCH1* mutations are also being modelled in zebrafish, with a focus on dystonia so far (Vaz et al., 2018), but some research groups are now turning their focus on PD-related mechanisms in *GCH1*-zebrafish models.

Chapter 7: Conclusions and future directions

Investigating the role of *GCH1* mutations and the downstream BH4 pathway in Parkinson's disease, I have used a multidisciplinary approach to fulfil four aims.

Aim 1 – I have demonstrated an accumulated burden for variants in the complete *GCH1*-BH4 pathway on the risk for PD (chapter 3), and more precisely in the genes involved in DRD and BH4-deficiency aetiology (*GCH1*, *SPR* and *PTS*), suggesting a stronger link between the disorders than previously thought. This analysis uses the largest available PD exome cohort and first requires its appropriate quality control filtering, however the exclusion criteria used for the development of this cohort may have limited my ability to discern the effect of other genes such as *TH* (rather associated with early onset PD). In future research, the use of larger cohorts with a better definition of indels, as well as wider criteria of inclusion, would provide a more complete picture of the role of the *GCH1*-BH4 pathway in the risk for PD.

Aim 2 – fibroblasts derived from skin biopsies of patients carrying a heterozygous c.343+5G>C *GCH1* mutation have a depolarised mitochondrial membrane potential and a higher content in GSH than control cells. When treated with cytokines to induce the expression of *GCH1*, the mutant form fails to increase the polarisation of the MMP and to decrease GSH content of the cells to levels comparable to wild-type. Investigations in the fibroblast use a species and ageing relevant model, but is limited to the observation of non-dopamine related functions of the GCH1-BH4 pathway and the model necessitates cytokine treatment to induce *GCH1* expression, which may have secondary effects on the studied functions. The development of a neuronal model is thus necessary to validate these observations in a dopaminergic model.

Aim 3 – I have used patient-derived induced pluripotent stem cells (iPSC) to develop a human midbrain dopaminergic (mDA) neuronal model *in vitro*. The method is based on the recapitulation of neurodevelopmental cues for the differentiation of mDA neurons using small molecules. Technical difficulties limited the yield of the method, similarly to other published methods, and future research should focus on the finer

tuning of these cues or the selection of successfully differentiated cells for higher purity of the cultures.

Aim 4 – I find that in FP neural progenitors and mDA neurons, the c.343+5G>C *GCH1* mutation is associated with mitochondrial impairment, associated to increased GSH content in DRD neural precursors and with decreased superoxide production in all mutants at the neuronal stage. Importantly, neuronal cell death is significantly increased in PD mDA neurons compared to both DRD and controls, supporting the ability of the model to recapitulate hallmark aspects of the disease.

Reconciling the final yield of our induction method and the results from the functional analyses, the presence of non-mDA neuron cells in the cultures may be supportive of a more physiologically-relevant model. Indeed, cultures containing a single cell type derived from iPSC lack the presence of support and target cells for the neurons, potentially hindering their behaviour. Moreover, the presence of visible functional differences in the mutants compared to control cultures points at two intriguing hypotheses: either the presence of non-neuronal cells is associated with greater stress for the iPSC-derived mDA neurons and allow for the earlier observation of phenotypes; or these phenotypic impairments may involve more cell types than believed in the current consensus.

Further investigations into the effect of the mutation on some of these cellular functions need to be considered. First, using TMRM in dynamic measurements to observe the effect of inhibition of separate complexes of the ETC on MMP can be considered to evaluate the relative health of these complexes and their ability to cope with increased stress in the model. Second, the observed impairment of the MMP may be associated with changes in mitochondrial oxidative phosphorylation and ATP production rate which can be measured directly and independently to the MMP using: NADH/FAD autofluorescence measurements (Bartolomé and Abramov, 2015), measuring basal and activated ATP concentration using genetically engineered markers or enzymatic assays, and measuring oxygen consumption with probes in a O2 controlled environment (Bartolome et al., 2013; Lesage et al., 2016). Third, NOS activity measurement with DAR-4M dye can be supplemented by the stimulation of

NOS by increasing intracellular Ca2+ levels using 1μM bradykinin and suppression of NOS activity using 1mM L-NAME, a potent NOS inhibitor, to validate that the observation of fluctuation in the neuronal cultures is associated to bursts of NO production linked to the bursts of increased intracellular calcium associated to neuronal cells depolarisation (Kojima and Nagano, 2000). Third, HPLC to precisely measure the amount of BH4, dopamine and their metabolites in the cultures (de la Fuente et al., 2017) would, in hand with the functional assays presented here, complete the picture of the impairments of the GCH1-BH4 pathway associated to this GCH1 mutation.

Using patient hiPSC-derived model presents with the advantage of recapitulating disease and observations in an in vitro human model carrying the complete genetic information of patients affected by either disease. However, improvement of the differentiation method as well as appropriate ageing of cultures, which may recapitulate a rather foetal stage of maturity in its current form, will require further optimisation of timing and developmental cues used in the protocol. Additionally, the use of sorting methods such as FACS or MACS can be optimised in these cells to increase the purity of the final cultures (Paik et al., 2018). Alternatively, use of genetically encoded live-cell markers of cell type, such as fluorescence markers under the TH promoter, can help focusing the data analysis of these functional fluorescence assays on mDA neurons only for analysis (Calatayud et al., 2019).
Hence, the early biochemical pathology modelled in these iPSC-derived cultures remains to be confirmed in separate lines and models. As these effects may be specific to the mutation and family studied, a genome editing method such as CRISPR-Cas9 could be used to correct the mutation in patient lines or induce the mutation in healthy control lines. Comparing the original to the genetically engineered lines would offer a clear definition of the effect of the mutation irrespective of the familial background. Additionally, lines from families carrying different GCH1 mutations could also be used to confirm these effects in a variety of setups. Finally, animal models such as mouse models can be developed with human-relevant mutations or protein knockdown and mDA neurons which have developed in a physiological environment can be harvested at several stages of maturation, ageing and disorder development, all advantages compared to human subjects.

Bibliography

Abeling, N.G., Duran, M., Bakker, H.D., Stroomer, L., Thöny, B., Blau, N., Booij, J., and Poll-The, B.T. (2006). Sepiapterin reductase deficiency an autosomal recessive DOPA-responsive dystonia. Mol. Genet. Metab. *89*, 116–120.

Aboud, A.A., Tidball, A.M., Kumar, K.K., Neely, M.D., Han, B., Ess, K.C., Hong, C.C., Erikson, K.M., Hedera, P., and Bowman, A.B. (2015). PARK2 patient neuroprogenitors show increased mitochondrial sensitivity to copper. Neurobiol. Dis. *73*, 204–212.

Abraham, G., and Inouye, M. (2014). Fast Principal Component Analysis of Large-Scale Genome-Wide Data. PLoS ONE *9*.

Abraham, G., Qiu, Y., Inouye, M., and Stegle, O. (2017). FlashPCA2: principal component analysis of Biobank-scale genotype datasets. Bioinformatics *33*, 2776–2778.

Abramov, A.Y., Gegg, M., Grunewald, A., Wood, N.W., Klein, C., and Schapira, A.H.V. (2011). Bioenergetic consequences of PINK1 mutations in Parkinson disease. PloS One *6*, e25622.

Agid, Y. (1991). Parkinson's disease: pathophysiology. The Lancet *337*, 1321–1324.

Alam, Z.I., Daniel, S.E., Lees, A.J., Marsden, D.C., Jenner, P., and Halliwell, B. (1997). A Generalised Increase in Protein Carbonyls in the Brain in Parkinson's but Not Incidental Lewy Body Disease. J. Neurochem. *69*, 1326–1329.

Albanese, A., Asmus, F., Bhatia, K.P., Elia, A.E., Elibol, B., Filippini, G., Gasser, T., Krauss, J.K., Nardocci, N., Newton, A., et al. (2011). EFNS guidelines on diagnosis and treatment of primary dystonias. Eur. J. Neurol. *18*, 5–18.

Allen, S.P., Rajan, S., Duffy, L., Mortiboys, H., Higginbottom, A., Grierson, A.J., and Shaw, P.J. (2014). Superoxide dismutase 1 mutation in a cellular model of amyotrophic lateral sclerosis shifts energy generation from oxidative phosphorylation to glycolysis. Neurobiol. Aging *35*, 1499–1509.

Andersson, E., Tryggvason, U., Deng, Q., Friling, S., Alekseenko, Z., Robert, B., Perlmann, T., and Ericson, J. (2006). Identification of Intrinsic Determinants of Midbrain Dopamine Neurons. Cell *124*, 393–405.

Ang, S.-L., and Rossant, J. (1994). HNF-3β is essential for node and notochord formation in mouse development. Cell *78*, 561–574.

Angelova, P.R., and Abramov, A.Y. (2018). Role of mitochondrial ROS in the brain: from physiology to neurodegeneration. FEBS Lett. *592*, 692–702.

Antelmi, E., Stamelou, M., Liguori, R., and Bhatia, K.P. (2015). Nonmotor Symptoms in Dopa-Responsive Dystonia. Mov. Disord. Clin. Pract. *2*, 347–356.

Antoniades, C., Shirodaria, C., Van Assche, T., Cunnington, C., Tegeder, I., Lötsch, J., Guzik, T.J., Leeson, P., Diesch, J., Tousoulis, D., et al. (2008). GCH1 Haplotype Determines Vascular and Plasma Biopterin Availability in Coronary Artery Disease: Effects on Vascular Superoxide Production and Endothelial Function. J. Am. Coll. Cardiol. *52*, 158–165.

Armata, I.A., Balaj, L., Kuster, J.K., Zhang, X., Tsai, S., Armatas, A.A., Multhaupt-Buell, T.J., Soberman, R., Breakefield, X.O., Ichinose, H., et al. (2013). Dopa-Responsive Dystonia: Functional Analysis of Single Nucleotide Substitutions within the 5' Untranslated GCH1 Region. PLoS ONE *8*.

Armstrong, R.A. (2014). When to use the Bonferroni correction. Ophthalmic Physiol. Opt. *34*, 502–508.

Assmann, B., Surtees, R., and Hoffmann, G.F. (2003). Approach to the diagnosis of neurotransmitter diseases exemplified by the differential diagnosis of childhood-onset dystonia. Ann. Neurol. *54*, S18–S24.

Baba, M., Nakajo, S., Tu, P.H., Tomita, T., Nakaya, K., Lee, V.M., Trojanowski, J.Q., and Iwatsubo, T. (1998). Aggregation of alpha-synuclein in Lewy bodies of sporadic Parkinson's disease and dementia with Lewy bodies. Am. J. Pathol. *152*, 879–884.

Bademci, G., Edwards, T.L., Torres, A.L., Scott, W.K., Züchner, S., Martin, E.R., Vance, J.M., and Wang, L. (2010). A rare novel deletion of the tyrosine hydroxylase gene in Parkinson disease. Hum. Mutat. *31*, E1767–E1771.

Badenes, S.M., Fernandes, T.G., Cordeiro, C.S.M., Boucher, S., Kuninger, D., Vemuri, M.C., Diogo, M.M., and Cabral, J.M.S. (2016). Defined Essential 8™ Medium and Vitronectin Efficiently Support Scalable Xeno-Free Expansion of Human Induced Pluripotent Stem Cells in Stirred Microcarrier Culture Systems. PLOS ONE *11*, e0151264.

Bagga, V., Dunnett, S.B., and Fricker-Gates, R.A. (2008). Ascorbic Acid Increases the Number of Dopamine Neurons In Vitro and in Transplants to the 6-OHDA-Lesioned Rat Brain. Cell Transplant. *17*, 763–773.

Bai, C.B., Stephen, D., and Joyner, A.L. (2004). All Mouse Ventral Spinal Cord Patterning by Hedgehog Is Gli Dependent and Involves an Activator Function of Gli3. Dev. Cell *6*, 103–115.

Bailey, J., Shaw, A., Fischer, R., Ryan, B.J., Kessler, B.M., McCullagh, J., Wade-Martins, R., Channon, K.M., and Crabtree, M.J. (2017). A novel role for endothelial tetrahydrobiopterin in mitochondrial redox balance. Free Radic. Biol. Med. *104*, 214–225.

Balint, B., Mencacci, N.E., Valente, E.M., Pisani, A., Rothwell, J., Jankovic, J., Vidailhet, M., and Bhatia, K.P. (2018). Dystonia. Nat. Rev. Dis. Primer *4*, 25.

Ballard, P.A., Tetrud, J.W., and Langston, J.W. (1985). Permanent human parkinsonism due to 1-methy 1-4-phenyl-1,2,3,6-tetrahydropyridine (MPTP): Seven cases. Neurology *35*, 949–956.

Bamshad, M.J., Ng, S.B., Bigham, A.W., Tabor, H.K., Emond, M.J., Nickerson, D.A., and Shendure, J. (2011). Exome sequencing as a tool for Mendelian disease gene discovery. Nat. Rev. Genet. *12*, 745–755.

Bandmann, O., Nygaard, T.G., Surtees, R., Marsden, C.D., Wood, N.W., and Harding, A.E. (1996a). Dopa-Responsive Dystonia in British Patients: New Mutations of the GTP-Cyclohydrolase I Gene and Evidence for Genetic Heterogeneity. Hum. Mol. Genet. *5*, 403–406.

Bandmann, O., Daniel, S., Marsden, C.D., Wood, N.W., and Harding, A.E. (1996b). The GTP-cyclohydrolase I gene in atypical Parkinsonian patients: a clinico-genetic study. J. Neurol. Sci. *141*, 27–32.

Bandmann, O., Goertz, M., Zschocke, J., Deuschl, G., Jost, W., Hefter, H., Muller, U., Zofel, P., Hoffmann, G., and Oertel, W. (2003). The phenylalanine loading test in the differential diagnosis of dystonia. Neurology *60*, 700–702.

Bandrés-Ciga, S., Mencacci, N.E., Durán, R., Barrero, F.J., Escamilla-Sevilla, F., Morgan, S., Hehir, J., Vives, F., Hardy, J., and Pittman, A.M. (2016). Analysis of the genetic variability in Parkinson's disease from Southern Spain. Neurobiol. Aging *37*, 210.e1-210.e5.

Barker, R.A., Parmar, M., Studer, L., and Takahashi, J. (2017). Human Trials of Stem Cell-Derived Dopamine Neurons for Parkinson's Disease: Dawn of a New Era. Cell Stem Cell *21*, 569–573.

Bartholomé, K., and Lüdecke, B. (1997). Mutations in the Tyrosine Hydroxylase Gene Cause Various Forms of L-Dopa-Responsive Dystonia. In Advances in Pharmacology, D.S. Goldstein, G. Eisenhofer, and R. McCarty, eds. (Academic Press), pp. 48–49.

Bartolomé, F., and Abramov, A.Y. (2015). Measurement of Mitochondrial NADH and FAD Autofluorescence in Live Cells. In Mitochondrial Medicine: Volume I, Probing Mitochondrial Function, V. Weissig, and M. Edeas, eds. (New York, NY: Springer), pp. 263–270.

Bartolome, F., Wu, H.-C., Burchell, V.S., Preza, E., Wray, S., Mahoney, C.J., Fox, N.C., Calvo, A., Canosa, A., Moglia, C., et al. (2013). Pathogenic VCP Mutations Induce Mitochondrial Uncoupling and Reduced ATP Levels. Neuron *78*, 57–64.

Basson, M.A., Echevarria, D., Ahn, C.P., Sudarov, A., Joyner, A.L., Mason, I.J., Martinez, S., and Martin, G.R. (2008). Specific regions within the embryonic midbrain and cerebellum require different levels of FGF signaling during development. Development *135*, 889–898.

Beckman, J.S., and Koppenol, W.H. (1996). Nitric oxide, superoxide, and peroxynitrite: the good, the bad, and ugly. Am. J. Physiol.-Cell Physiol. *271*, C1424–C1437.

Bell, S.M., Barnes, K., Clemmens, H., Al-Rafiah, A.R., Al-ofi, E.A., Leech, V., Bandmann, O., Shaw, P.J., Blackburn, D.J., Ferraiuolo, L., et al. (2018). Ursodeoxycholic Acid Improves Mitochondrial Function and Redistributes Drp1 in Fibroblasts from Patients with Either Sporadic or Familial Alzheimer's Disease. J. Mol. Biol. *430*, 3942–3953.

Benamer, H.T.S., Patterson, J., Grosset, D.G., Booij, J., Bruin, K. de, Royen, E. van, Speelman, J.D., Horstink, M.H.I.M., Sips, H.J.W.A., Dierckx, R.A., et al. (2000). Accurate differentiation of parkinsonism and essential tremor using visual assessment of [123I]-FP-CIT SPECT imaging: The [123I]-FP-CIT study group. Mov. Disord. *15*, 503–510.

Bencsics, C., Wachtel, S.R., Milstien, S., Hatakeyama, K., Becker, J.B., and Kang, U.J. (1996). Double Transduction with GTP Cyclohydrolase I and Tyrosine Hydroxylase Is Necessary for Spontaneous Synthesis ofl-DOPA by Primary Fibroblasts. J. Neurosci. *16*, 4449–4456.

Bender, A., Krishnan, K.J., Morris, C.M., Taylor, G.A., Reeve, A.K., Perry, R.H., Jaros, E., Hersheson, J.S., Betts, J., Klopstock, T., et al. (2006). High levels of mitochondrial DNA deletions in substantia nigra neurons in aging and Parkinson disease. Nat. Genet. *38*, 515–517.

Bendi, V.S., Shou, J., Joy, S., and Torres-Russotto, D. (2018). Motor fluctuations and levodopa-induced dyskinesias in dopa-responsive dystonia. Parkinsonism Relat. Disord. *50*, 126–127.

Benjamini, Y., and Hochberg, Y. (1995). Controlling the False Discovery Rate: A Practical and Powerful Approach to Multiple Testing. J. R. Stat. Soc. Ser. B Methodol. *57*, 289–300.

Berardelli, A., Wenning, G.K., Antonini, A., Berg, D., Bloem, B.R., Bonifati, V., Brooks, D., Burn, D.J., Colosimo, C., Fanciulli, A., et al. (2013). EFNS/MDS-ES recommendations for the diagnosis of Parkinson's disease. Eur. J. Neurol. *20*, 16–34.

Bernheimer, H., Birkmayer, W., Hornykiewicz, O., Jellinger, K., and Seitelberger, F. (1973). Brain dopamine and the syndromes of Parkinson and Huntington Clinical, morphological and neurochemical correlations. J. Neurol. Sci. *20*, 415–455.

Betarbet, R., Sherer, T.B., MacKenzie, G., Garcia-Osuna, M., Panov, A.V., and Greenamyre, J.T. (2000). Chronic systemic pesticide exposure reproduces features of Parkinson's disease. Nat. Neurosci. *3*, 1301–1306.

Bevers, L.M., Braam Branko, Post Jan Andries, van Zonneveld Anton Jan, Rabelink Ton J., Koomans Hein A., Verhaar Marianne C., and Joles Jaap A. (2006). Tetrahydrobiopterin, but Not l-Arginine, Decreases NO Synthase Uncoupling in Cells Expressing High Levels of Endothelial NO Synthase. Hypertension *47*, 87–94.

Bissonette, G.B., and Roesch, M.R. (2016). Development and function of the midbrain dopamine system: what we know and what we need to. Genes Brain Behav. *15*, 62–73.

Blandini, F., Levandis, G., Bazzini, E., Nappi, G., and Armentero, M.-T. (2007). Time-course of nigrostriatal damage, basal ganglia metabolic changes and behavioural alterations following intrastriatal injection of 6-hydroxydopamine in the rat: new clues from an old model. Eur. J. Neurosci. *25*, 397–405.

Blau, N., Bonafé, L., and Thöny, B. (2001). Tetrahydrobiopterin Deficiencies without Hyperphenylalaninemia: Diagnosis and Genetics of DOPA-Responsive Dystonia and Sepiapterin Reductase Deficiency. Mol. Genet. Metab. *74*, 172–185.

Bock, C., Kiskinis, E., Verstappen, G., Gu, H., Boulting, G., Smith, Z.D., Ziller, M., Croft, G.F., Amoroso, M.W., Oakley, D.H., et al. (2011). Reference Maps of Human ES and iPS Cell Variation Enable High-Throughput Characterization of Pluripotent Cell Lines. Cell *144*, 439–452.

Bonafé, L., Thöny, B., Leimbacher, W., Kierat, L., and Blau, N. (2001a). Diagnosis of Dopa-responsive Dystonia and Other Tetrahydrobiopterin Disorders by the Study of Biopterin Metabolism in Fibroblasts. Clin. Chem. *47*, 477–485.

Bonafé, L., Thöny, B., Penzien, J.M., Czarnecki, B., and Blau, N. (2001b). Mutations in the Sepiapterin Reductase Gene Cause a Novel Tetrahydrobiopterin-Dependent Monoamine-Neurotransmitter Deficiency without Hyperphenylalaninemia. Am. J. Hum. Genet. *69*, 269–277.

Bonifati, V., Rizzu, P., Baren, M.J. van, Schaap, O., Breedveld, G.J., Krieger, E., Dekker, M.C.J., Squitieri, F., Ibanez, P., Joosse, M., et al. (2003). Mutations in the DJ-1 Gene Associated with Autosomal Recessive Early-Onset Parkinsonism. Science *299*, 256–259.

Bonilla, S., Hall, A.C., Pinto, L., Attardo, A., Götz, M., Huttner, W.B., and Arenas, E. (2008). Identification of midbrain floor plate radial glia-like cells as dopaminergic progenitors. Glia *56*, 809–820.

Borghese, L., Dolezalova, D., Opitz, T., Haupt, S., Leinhaas, A., Steinfarz, B., Koch, P., Edenhofer, F., Hampl, A., and Brüstle, O. (2010). Inhibition of Notch Signaling in Human Embryonic Stem Cell–Derived Neural Stem Cells Delays G1/S Phase Transition and Accelerates Neuronal Differentiation In Vitro and In Vivo. STEM CELLS *28*, 955–964.

Bose, A., and Beal, M.F. (2019). Mitochondrial dysfunction and oxidative stress in induced pluripotent stem cell models of Parkinson's disease. Eur. J. Neurosci. *49*, 525–532.

Braak, H., and Braak, E. (2000). Pathoanatomy of Parkinson's disease. J. Neurol. *247*, II3–II10.

Braak, H., Braak, E., Yilmazer, D., de Vos, R.A.I., Jansen, E.N.H., Bohl, J., and Jellinger, K. (1994). Amygdala pathology in Parkinson's disease. Acta Neuropathol. (Berl.) *88*, 493–500.

Braak, H., Rüb, U., Sandmann-Keil, D., Gai, W.P., de Vos, R.A.I., Jansen Steur, E.N.H., Arai, K., and Braak, E. (2000). Parkinson's disease: affection of brain stem nuclei controlling premotor and motor neurons of the somatomotor system. Acta Neuropathol. (Berl.) *99*, 489–495.

Braak, H., Del Tredici, K., Rüb, U., de Vos, R.A.I., Jansen Steur, E.N.H., and Braak, E. (2003). Staging of brain pathology related to sporadic Parkinson's disease. Neurobiol. Aging *24*, 197–211.

Braak, H., de Vos, R.A.I., Bohl, J., and Del Tredici, K. (2006). Gastric α-synuclein immunoreactive inclusions in Meissner's and Auerbach's plexuses in cases staged for Parkinson's disease-related brain pathology. Neurosci. Lett. *396*, 67–72.

Brand, M.P., Heales, S.J.R., Land, J.M., and Clark, J.B. (1995). Tetrahydrobiopterin deficiency and brain nitric oxide synthase in thehph1 mouse. J. Inherit. Metab. Dis. *18*, 33–39.

Bras, J.M., and Singleton, A. (2009). Genetic susceptibility in Parkinson's disease. Biochim. Biophys. Acta BBA - Mol. Basis Dis. *1792*, 597–603.

Bras, J., Guerreiro, R., and Hardy, J. (2012). Use of next-generation sequencing and other whole-genome strategies to dissect neurological disease. Nat. Rev. Neurosci. *13*, 453–464.

Bräutigam, C., Wevers, R.A., Jansen, R.J.T., Smeitink, J.A.M., Andel, J.F. de R., Gabreëls, F.J.M., and Hoffmann, G.F. (1998). Biochemical hallmarks of tyrosine hydroxylase deficiency. Clin. Chem. *44*, 1897–1904.

Bredt, D.S., and Snyder, S.H. (1994). Nitric oxide: a physiologic messenger molecule. Annu. Rev. Biochem. *63*, 175–195.

Bringold, U., Ghafourifar, P., and Richter, C. (2000). Peroxynitrite formed by mitochondrial NO synthase promotes mitochondrial Ca2+ release. Free Radic. Biol. Med. *29*, 343–348.

Broccoli, V., Boncinelli, E., and Wurst, W. (1999). The caudal limit of *Otx2* expression positions the isthmic organizer. Nature *401*, 164–168.

Bromberg-Martin, E.S., Matsumoto, M., and Hikosaka, O. (2010). Dopamine in Motivational Control: Rewarding, Aversive, and Alerting. Neuron *68*, 815–834.

Brown, T.P., Rumsby, P.C., Capleton, A.C., Rushton, L., and Levy, L.S. (2006). Pesticides and Parkinson's disease - Is there a link? Environ. Health Perspect. *114*, 156–164.

Buchman, A.S., Shulman, J.M., Nag, S., Leurgans, S.E., Arnold, S.E., Morris, M.C., Schneider, J.A., and Bennett, D.A. (2012). Nigral pathology and parkinsonian signs in elders without Parkinson disease. Ann. Neurol. *71*, 258–266.

Caiazzo, M., Dell'Anno, M.T., Dvoretskova, E., Lazarevic, D., Taverna, S., Leo, D., Sotnikova, T.D., Menegon, A., Roncaglia, P., Colciago, G., et al. (2011). Direct generation of functional dopaminergic neurons from mouse and human fibroblasts. Nature *476*, 224–227.

Calatayud, C., Carola, G., Fernández-Carasa, I., Valtorta, M., Jiménez-Delgado, S., Díaz, M., Soriano-Fradera, J., Cappelletti, G., García-Sancho, J., Raya, Á., et al. (2019). CRISPR/Cas9-mediated generation of a tyrosine hydroxylase reporter iPSC line for live imaging and isolation of dopaminergic neurons. Sci. Rep. *9*.

Carcamo-Orive, I., Hoffman, G.E., Cundiff, P., Beckmann, N.D., D'Souza, S.L., Knowles, J.W., Patel, A., Papatsenko, D., Abbasi, F., Reaven, G.M., et al. (2017). Analysis of Transcriptional Variability in a Large Human iPSC Library Reveals Genetic and Non-genetic Determinants of Heterogeneity. Cell Stem Cell *20*, 518-532.e9.

Chambers, S.M., Fasano, C.A., Papapetrou, E.P., Tomishima, M., Sadelain, M., and Studer, L. (2009). Highly efficient neural conversion of human ES and iPS cells by dual inhibition of SMAD signaling. Nat. Biotechnol. *27*, 275–280.

Chang, D., Nalls, M.A., Hallgrímsdóttir, I.B., Hunkapiller, J., van der Brug, M., Cai, F., International Parkinson's Disease Genomics Consortium, 23andMe Research Team, Kerchner,

G.A., Ayalon, G., et al. (2017). A meta-analysis of genome-wide association studies identifies 17 new Parkinson's disease risk loci. Nat. Genet. *49*, 1511–1516.

Charcot, J.-M. (1825-1893) A. du texte (1875). Leçons sur les maladies du système nerveux : faites à la Salpêtrière. Tome 2 / par J.-M. Charcot,... ; recueillies et publ. par Bourneville,...

Chartier-Harlin, M.-C., Kachergus, J., Roumier, C., Mouroux, V., Douay, X., Lincoln, S., Levecque, C., Larvor, L., Andrieux, J., Hulihan, M., et al. (2004). α-synuclein locus duplication as a cause of familial Parkinson's disease. The Lancet *364*, 1167–1169.

Chatterjee, S., Noack, H., Possel, H., Keilhoff, G., and Wolf, G. (1999). Glutathione levels in primary glial cultures: Monochlorobimane provides evidence of cell type-specific distribution. Glia *27*, 152–161.

Chen, C.-M., Chen, Y.-C., Chiang, M.-C., Fung, H.-C., Chang, K.-H., Lee-Chen, G.-J., and Wu, Y.-R. (2016). Association of GCH1 and MIR4697, but not SIPA1L2 and VPS13C polymorphisms, with Parkinson's disease in Taiwan. Neurobiol. Aging *39*, 221.e1-221.e5.

Chen, J., Rogers, S.C., and Kavdia, M. (2013). Analysis of Kinetics of Dihydroethidium Fluorescence with Superoxide Using Xanthine Oxidase and Hypoxanthine Assay. Ann. Biomed. Eng. *41*, 327–337.

Chiba, K., Peterson, L.A., Castagnoli, K.P., and Trevor, A.J. (1985). Studies on the molecular mechanism of bioactivation of the selective nigrostriatal toxin 1-methyl-4-phenyl-1,2,3,6-tetrahydropyridine. Drug Metab. Dispos. *13*, 342–347.

Cingolani, P., Platts, A., Wang, L.L., Coon, M., Nguyen, T., Wang, L., Land, S.J., Lu, X., and Ruden, D.M. (2012a). A program for annotating and predicting the effects of single nucleotide polymorphisms, SnpEff: SNPs in the genome of Drosophila melanogaster strain w ^{1118} ; iso-2; iso-3. Fly (Austin) *6*, 80–92.

Cingolani, P., Patel, V.M., Coon, M., Nguyen, T., Land, S.J., Ruden, D.M., and Lu, X. (2012b). Using Drosophila melanogaster as a Model for Genotoxic Chemical Mutational Studies with a New Program, SnpSift. Front. Genet. *3*.

Claassen, D.A., Desler, M.M., and Rizzino, A. (2009). ROCK Inhibition Enhances the Recovery and Growth of Cryopreserved Human Embryonic Stem Cells and Human Induced Pluripotent Stem Cells. Mol. Reprod. Dev. *76*, 722–732.

Clot, F., Grabli, D., Cazeneuve, C., Roze, E., Castelnau, P., Chabrol, B., Landrieu, P., Nguyen, K., Ponsot, G., Abada, M., et al. (2009). Exhaustive analysis of BH4 and dopamine biosynthesis genes in patients with Dopa-responsive dystonia. Brain *132*, 1753–1763.

Cobb, S.A., Wider, C., Ross, O.A., Mata, I.F., Adler, C.H., Rajput, A., Rajput, A.H., Wu, R.-M., Hauser, R., Josephs, K.A., et al. (2009). GCH1 in early-onset Parkinson's disease. Mov. Disord. *24*, 2070–2075.

Cohen, J.Y., Haesler, S., Vong, L., Lowell, B.B., and Uchida, N. (2012). Neuron-type-specific signals for reward and punishment in the ventral tegmental area. Nature *482*, 85–88.

Collins, L.M., Drouin-Ouellet, J., Kuan, W.-L., Cox, T., and Barker, R.A. (2018). Dermal fibroblasts from patients with Parkinson's disease have normal GCase activity and autophagy compared to patients with PD and GBA mutations. F1000Research *6*.

Cooper, O., Hargus, G., Deleidi, M., Blak, A., Osborn, T., Marlow, E., Lee, K., Levy, A., Perez-Torres, E., Yow, A., et al. (2010). Differentiation of human ES and Parkinson's disease iPS cells

into ventral midbrain dopaminergic neurons requires a high activity form of SHH, FGF8a and specific regionalization by retinoic acid. Mol. Cell. Neurosci. *45*, 258–266.

Cotrina, M.L., Lin, J.H.-C., Alves-Rodrigues, A., Liu, S., Li, J., Azmi-Ghadimi, H., Kang, J., Naus, C.C.G., and Nedergaard, M. (1998). Connexins regulate calcium signaling by controlling ATP release. Proc. Natl. Acad. Sci. *95*, 15735–15740.

Cotrina, M.L., Lin, J.H.-C., López-García, J.C., Naus, C.C.G., and Nedergaard, M. (2000). ATP-Mediated Glia Signaling. J. Neurosci. *20*, 2835–2844.

Crabtree, M.J., Smith, C.L., Lam, G., Goligorsky, M.S., and Gross, S.S. (2008). Ratio of 5,6,7,8-tetrahydrobiopterin to 7,8-dihydrobiopterin in endothelial cells determines glucose-elicited changes in NO vs. superoxide production by eNOS. Am. J. Physiol. Heart Circ. Physiol. *294*, H1530-1540.

Crabtree, M.J., Tatham, A.L., Al-Wakeel, Y., Warrick, N., Hale, A.B., Cai, S., Channon, K.M., and Alp, N.J. (2009a). Quantitative Regulation of Intracellular Endothelial Nitric-oxide Synthase (eNOS) Coupling by Both Tetrahydrobiopterin-eNOS Stoichiometry and Biopterin Redox Status INSIGHTS FROM CELLS WITH TET-REGULATED GTP CYCLOHYDROLASE I EXPRESSION. J. Biol. Chem. *284*, 1136–1144.

Crabtree, M.J., Tatham, A.L., Hale, A.B., Alp, N.J., and Channon, K.M. (2009b). Critical Role for Tetrahydrobiopterin Recycling by Dihydrofolate Reductase in Regulation of Endothelial Nitric-oxide Synthase Coupling RELATIVE IMPORTANCE OF THE DE NOVO BIOPTERIN SYNTHESIS VERSUS SALVAGE PATHWAYS. J. Biol. Chem. *284*, 28128–28136.

Creese, I., Stewart, K., and Snyder, S.H. (1979). Species variations in dopamine receptor binding. Eur. J. Pharmacol. *60*, 55–66.

Crossley, P.H., Martinez, S., and Martin, G.R. (1996). Midbrain development induced by FGF8 in the chick embryo. Nature *380*, 66–68.

Currie, L.J., Harrison, M.B., Trugman, J.M., Bennett, J.P., and Wooten, G.F. (2004). Postmenopausal Estrogen Use Affects Risk for Parkinson Disease. Arch. Neurol. *61*, 886–888.

Dahlstrom, A., and Fuxe, K. (1964). Evidence for the existence of monoamine-containing neurons in the central nervous system. I. Demonstration of monoamines in the cell bodies of brain stem neurons. Acta Physiol. Scand. *62*, 1–55.

Dalfó, E., Portero-Otín, M., Ayala, V., Martínez, A., Pamplona, R., and Ferrer, I. (2005). Evidence of Oxidative Stress in the Neocortex in Incidental Lewy Body Disease. J. Neuropathol. Exp. Neurol. *64*, 816–830.

De Rijk, M.C., Launer, L.J., Berger, K., Breteler, M.M.B., Dartigues, J.-F., Baldereschi, M., Fratiglioni, L., Lobo, A., Martinez-Lage, J., Trenkwalder, C., et al. (2000). Prevalence of Parkinson's disease in Europe: A collaborative study of population-based cohorts. Neurology *54*, S21–S23.

Denham, M., Bye, C., Leung, J., Conley, B.J., Thompson, L.H., and Dottori, M. (2012). Glycogen Synthase Kinase 3β and Activin/Nodal Inhibition in Human Embryonic Stem Cells Induces a Pre-Neuroepithelial State That Is Required for Specification to a Floor Plate Cell Lineage. STEM CELLS *30*, 2400–2411.

Dexter, D.T., Carter, C.J., Wells, F.R., Javoy-Agid, F., Agid, Y., Lees, A., Jenner, P., and Marsden, C.D. (1989). Basal Lipid Peroxidation in Substantia Nigra Is Increased in Parkinson's Disease. J. Neurochem. *52*, 381–389.

Dhawan, V., Ma, Y., Pillai, V., Spetsieris, P., and al, et (2002). Comparative analysis of striatal FDOPA uptake in Parkinson's disease: Ratio method versus graphical approach. J. Nucl. Med. N. Y. *43*, 1324–1330.

Di Fonzo, A., Rohé, C.F., Ferreira, J., Chien, H.F., Vacca, L., Stocchi, F., Guedes, L., Fabrizio, E., Manfredi, M., Vanacore, N., et al. (2005). A frequent LRRK2 gene mutation associated with autosomal dominant Parkinson's disease. The Lancet *365*, 412–415.

Dick, F.D., De Palma, G., Ahmadi, A., Scott, N.W., Prescott, G.J., Bennett, J., Semple, S., Dick, S., Counsell, C., Mozzoni, P., et al. (2007). Environmental risk factors for Parkinson's disease and parkinsonism: the Geoparkinson study. Occup. Environ. Med. *64*, 666–672.

Dickinson, M.E., Flenniken, A.M., Ji, X., Teboul, L., Wong, M.D., White, J.K., Meehan, T.F., Weninger, W.J., Westerberg, H., Adissu, H., et al. (2016). High-throughput discovery of novel developmental phenotypes. Nature *537*, 508–514.

Ding, Q., Motoyama, J., Gasca, S., Mo, R., Sasaki, H., Rossant, J., and Hui, C.C. (1998). Diminished Sonic hedgehog signaling and lack of floor plate differentiation in Gli2 mutant mice. Development *125*, 2533–2543.

Dressler, D., Altenmueller, E., Bhidayasiri, R., Bohlega, S., Chana, P., Chung, T.M., Frucht, S., Garcia-Ruiz, P.J., Kaelin, A., Kaji, R., et al. (2016). Strategies for treatment of dystonia. J. Neural Transm. *123*, 251–258.

Du, F., Yu, Q., Chen, A., Chen, D., and Yan, S.S. (2018). Astrocytes Attenuate Mitochondrial Dysfunctions in Human Dopaminergic Neurons Derived from iPSC. Stem Cell Rep. *10*, 366–374.

van Duijn, C.M., Dekker, M.C.J., Bonifati, V., Galjaard, R.J., Houwing-Duistermaat, J.J., Snijders, P.J.L.M., Testers, L., Breedveld, G.J., Horstink, M., Sandkuijl, L.A., et al. (2001). PARK7, a Novel Locus for Autosomal Recessive Early-Onset Parkinsonism, on Chromosome 1p36. Am. J. Hum. Genet. *69*, 629–634.

Eggers, C., Volk, A.E., Kahraman, D., Fink, G.R., Leube, B., Schmidt, M., and Timmermann, L. (2012). Are dopa-responsive dystonia and Parkinson's disease related disorders? A case report. Parkinsonism Relat. Disord. *18*, 666–668.

Esteras, N., Rohrer, J.D., Hardy, J., Wray, S., and Abramov, A.Y. (2017). Mitochondrial hyperpolarization in iPSC-derived neurons from patients of FTDP-17 with 10+16 MAPT mutation leads to oxidative stress and neurodegeneration. Redox Biol. *12*, 410–422.

Evans, J.R., Mason, S.L., and Barker, R.A. (2012). Chapter 9 - Current status of clinical trials of neural transplantation in Parkinson's disease. In Progress in Brain Research, S.B. Dunnett, and A. Björklund, eds. (Elsevier), pp. 169–198.

Farkas, L.M., Dünker, N., Roussa, E., Unsicker, K., and Krieglstein, K. (2003). Transforming Growth Factor-βs Are Essential for the Development of Midbrain Dopaminergic Neurons In Vitro and In Vivo. J. Neurosci. *23*, 5178–5186.

Fearnley, J.M., and Lees, A.J. (1991). Ageing and Parkinson's Disease: Substantia Nigra Regional Selectivity. Brain *114*, 2283–2301.

Felten, D.L., and Sladek, J.R. (1983). Monoamine distribution in primate brain V. Monoaminergic nuclei: Anatomy, pathways and local organization. Brain Res. Bull. *10*, 171–284.

Feng, B., Sun, G., Kong, Q., and Li, Q. (2018). Compound heterozygous mutations in the TH gene in a Chinese family with autosomal-recessive dopa-responsive dystonia. Medicine (Baltimore) *97*.

Ferri, A.L.M., Lin, W., Mavromatakis, Y.E., Wang, J.C., Sasaki, H., Whitsett, J.A., and Ang, S.-L. (2007). Foxa1 and Foxa2 regulate multiple phases of midbrain dopaminergic neuron development in a dosage-dependent manner. Development *134*, 2761–2769.

Fleming, I., Bauersachs, J., and Busse, R. (1997). Calcium-Dependent and Calcium-Independent Activation of the Endothelial NO Synthase. J. Vasc. Res. *34*, 165–174.

Fleming, J.E., Quattrocki, E., Latter, G., Miquel, J., Marcuson, R., Zuckerkandl, E., and Bensch, K.G. (1986). Age-dependent changes in proteins of Drosophila melanogaster. Science *231*, 1157–1159.

Flurkey, K., M. Currer, J., and Harrison, D.E. (2007). Chapter 20 - Mouse Models in Aging Research. In The Mouse in Biomedical Research (Second Edition), J.G. Fox, M.T. Davisson, F.W. Quimby, S.W. Barthold, C.E. Newcomer, and A.L. Smith, eds. (Burlington: Academic Press), pp. 637–672.

Forno, L.S., Sternberger, L.A., Sternberger, N.H., Strefling, A.M., Swanson, K., and Eng, L.F. (1986). Reaction of Lewy bodies with antibodies to phosphorylated and non-phosphorylated neurofilaments. Neurosci. Lett. *64*, 253–258.

Förstermann, U., and Sessa, W.C. (2012). Nitric oxide synthases: regulation and function. Eur. Heart J. *33*, 829–837.

Freeman, T.B., Spence, M.S., Boss, B.D., Spector, D.H., Strecker, R.E., Olanow, C.W., and Kordower, J.H. (1991). Development of dopaminergic neurons in the human substantia nigra. Exp. Neurol. *113*, 344–353.

de la Fuente, C., Burke, D.G., Eaton, S., and Heales, S.J.R. (2017). Inhibition of neuronal mitochondrial complex I or lysosomal glucocerebrosidase is associated with increased dopamine and serotonin turnover. Neurochem. Int. *109*, 94–100.

Fujishiro, K., Hagihara, M., Takahashi, A., and Nagatsu, T. (1990). Concentrations of neopterin and biopterin in the cerebrospinal fluid of patients with Parkinson's disease. Biochem. Med. Metab. Biol. *44*, 97–100.

Funayama, M., Hasegawa, K., Kowa, H., Saito, M., Tsuji, S., and Obata, F. (2002). A new locus for Parkinson's disease (PARK8) maps to chromosome 12p11.2–q13.1. Ann. Neurol. *51*, 296–301.

Furukawa, Y., Lang, A.E., Trugman, J.M., Bird, T.D., Hunter, A., Sadeh, M., Tagawa, T., George-Hyslop, P.H.S., Guttman, M., Morris, L.W., et al. (1998). Gender-related penetrance and de novo GTP-cyclohydrolase I gene mutations in dopa-responsive dystonia. Neurology *50*, 1015–1020.

Furukawa, Y., Nygaard, T.G., Gütlich, M., Rajput, A.H., Pifl, C., DiStefano, L., Chang, L.J., Price, K., Shimadzu, M., Hornykiewicz, O., et al. (1999). Striatal biopterin and tyrosine hydroxylase protein reduction in dopa-responsive dystonia. Neurology *53*, 1032–1032.

Furukawa, Y., Guttman, M., Sparagana, S.P., Trugman, J.M., Hyland, K., Wyatt, P., Lang, A.E., Rouleau, G.A., Shimadzu, M., and Kish, S.J. (2000). Dopa-responsive dystonia due to a large deletion in the GTP cyclohydrolase I gene. Ann. Neurol. *47*, 517–520.

Furukawa, Y., Graf, W.D., Wong, H., Shimadzu, M., and Kish, S.J. (2001). Dopa-responsive dystonia simulating spastic paraplegia due to tyrosine hydroxylase (TH) gene mutations. Neurology *56*, 260–263.

Furukawa, Y., Kapatos, G., Haycock, J.W., Worsley, J., Wong, H., Kish, S.J., and Nygaard, T.G. (2002). Brain biopterin and tyrosine hydroxylase in asymptomatic dopa-responsive dystonia. Ann. Neurol. *51*, 637–641.

Furukawa, Y., Rajput, A.H., Tong, J., Tomizawa, Y., Hornykiewicz, O., and Kish, S.J. (2016). A marked contrast between serotonergic and dopaminergic changes in dopa-responsive dystonia. Neurology *87*, 1060–1061.

Gai, W.P., Blumbergs, P.C., and Blessing, W.W. (1995). Microtubule-associated protein 5 is a component of Lewy bodies and Lewy neurites in the brainstem and forebrain regions affected in Parkinson's disease. Acta Neuropathol. (Berl.) *91*, 78–81.

Galloway, P.G., Mulvihill, P., and Perry, G. (1992). Filaments of Lewy bodies contain insoluble cytoskeletal elements. Am. J. Pathol. *140*, 809–822.

Gandhi, S., and Abramov, A.Y. (2012). Mechanism of Oxidative Stress in Neurodegeneration. Oxid. Med. Cell. Longev. *2012*, e428010.

Garavaglia, B., Invernizzi, F., Carbone, M.L.A., Viscardi, V., Saracino, F., Ghezzi, D., Zeviani, M., Zorzi, G., and Nardocci, N. (2004). GTP-cyclohydrolase I gene mutations in patients with autosomal dominant and recessive GTP-CH1 deficiency: Identification and functional characterization of four novel mutations. J. Inherit. Metab. Dis. *27*, 455–463.

Garthwaite, J. (2008). Concepts of neural nitric oxide-mediated transmission. Eur. J. Neurosci. *27*, 2783–2802.

Gerencser, A.A., Chinopoulos, C., Birket, M.J., Jastroch, M., Vitelli, C., Nicholls, D.G., and Brand, M.D. (2012). Quantitative measurement of mitochondrial membrane potential in cultured cells: calcium-induced de- and hyperpolarization of neuronal mitochondria. J. Physiol. *590*, 2845–2871.

German, D.C., Manaye, K.F., White, C.L., Woodward, D.J., McIntire, D.D., Smith, W.K., Kalaria, R.N., and Mann, D.M.A. (1992). Disease-specific patterns of locus coeruleus cell loss. Ann. Neurol. *32*, 667–676.

Gibb, W., and Lees, A.J. (1988). The relevance of the Lewy body to the pathogenesis of idiopathic Parkinson's disease.

Gibb, W., and Lees, A.J. (1994). Pathological clues to the cause of Parkinson's disease. In Movement Disorders 3, (Oxford), pp. 147–166.

Gibb, W.R., and Lees, A.J. (1991). Anatomy, pigmentation, ventral and dorsal subpopulations of the substantia nigra, and differential cell death in Parkinson's disease. J. Neurol. Neurosurg. Psychiatry *54*, 388–396.

Gibb, W.R.G., and Lees, A.J. (1989). The Significance of the Lewy Body in the Diagnosis of Idiopathic Parkinson's Disease. Neuropathol. Appl. Neurobiol. *15*, 27–44.

Giorgi, C., Marchi, S., and Pinton, P. (2018). The machineries, regulation and cellular functions of mitochondrial calcium. Nat. Rev. Mol. Cell Biol. *19*, 713–730.

Goeman, J.J., and Solari, A. (2014). Multiple hypothesis testing in genomics. Stat. Med. *33*, 1946–1978.

Golbe, L.I., Di Iorio, G., Bonavita, V., Miller, D.C., and Duvoisin, R.C. (1990). A large kindred with autosomal dominant Parkinson's disease. Ann. Neurol. *27*, 276–282.

Golbe, L.I., Lazzarini, A.M., Duvoisin, R.C., Iorio, G.D., Sanges, G., Bonavita, V., and Sala, S. la (1996). Clinical genetic analysis of Parkinson's disease in the contursi kindred. Ann. Neurol. *40*, 767–775.

Goldman, M. Why is multiple testing a problem? 5.

Goldman, J.E., Yen, S.-H., Chiu, F.-C., and Peress, N.S. (1983). Lewy Bodies of Parkinson's Disease Contain Neurofilament Antigens. Science *221*, 1082–1084.

Goldstein, D.B., Holmes, C., Li, S.-T., Bruce, S., Verhagen Metman, L., and Cannon, R.O.I. (2000). Cardiac Sympathetic Denervation in Parkinson Disease. Ann. Intern. Med. *133*, 338–347.

Goldstein, D.S., Sharabi, Y., Karp, B.I., Bentho, O., Saleem, A., Pacak, K., and Eisenhofer, G. (2007). Cardiac sympathetic denervation preceding motor signs in Parkinson disease. Clin. Auton. Res. *17*, 118–121.

Goldstein, D.S., Holmes, C., Lopez, G.J., Wu, T., and Sharabi, Y. (2018). Cardiac sympathetic denervation predicts PD in at-risk individuals. Parkinsonism Relat. Disord. *52*, 90–93.

Goldwurm, S., Fonzo, A.D., Simons, E.J., Rohé, C.F., Zini, M., Canesi, M., Tesei, S., Zecchinelli, A., Antonini, A., Mariani, C., et al. (2005). The G6055A (G2019S) mutation in LRRK2 is frequent in both early and late onset Parkinson's disease and originates from a common ancestor. J. Med. Genet. *42*, e65–e65.

Goodrich, L.V., Milenković, L., Higgins, K.M., and Scott, M.P. (1997). Altered Neural Cell Fates and Medulloblastoma in Mouse patched Mutants. Science *277*, 1109–1113.

Gowers, W.R. (William R. (1886). A manual of diseases of the nervous system (London : J. & A. Churchill).

Gramsbergen, J.B., Sandberg, M., Møller Dall, A., Kornblit, B., and Zimmer, J. (2002). Glutathione depletion in nigrostriatal slice cultures: GABA loss, dopamine resistance and protection by the tetrahydrobiopterin precursor sepiapterin. Brain Res. *935*, 47–58.

Grealish, S., Jönsson, M.E., Li, M., Kirik, D., Björklund, A., and Thompson, L.H. (2010). The A9 dopamine neuron component in grafts of ventral mesencephalon is an important determinant for recovery of motor function in a rat model of Parkinson's disease. Brain *133*, 482–495.

Grötzsch, H., Pizzolato, G.-P., Ghika, J., Schorderet, D., Vingerhoets, F.J., Landis, T., and Burkhard, P.R. (2002). Neuropathology of a case of dopa-responsive dystonia associated with a new genetic locus, DYT14. Neurology *58*, 1839–1842.

Grynkiewicz, G., Poenie, M., and Tsien, R.Y. (1985). A new generation of Ca2+ indicators with greatly improved fluorescence properties. J. Biol. Chem. *260*, 3440–3450.

Guella, I., Sherman, H.E., Appel-Cresswell, S., Rajput, A., Rajput, A.H., and Farrer, M.J. (2015). Parkinsonism in GTP cyclohydrolase 1 mutation carriers. Brain *138*, e349–e349.

Guthrie, P.B., Knappenberger, J., Segal, M., Bennett, M.V.L., Charles, A.C., and Kater, S.B. (1999). ATP Released from Astrocytes Mediates Glial Calcium Waves. J. Neurosci. *19*, 520–528.

Haddad, D., and Nakamura, K. (2015). Understanding the susceptibility of dopamine neurons to mitochondrial stressors in Parkinson's disease. FEBS Lett. *589*, 3702–3713.

Hagenah, J., Saunders-Pullman, R., Hedrich, K., Kabakci, K., Habermann, K., Wiegers, K., Mohrmann, K., Lohnau, T., Raymond, D., Vieregge, P., et al. (2005). High mutation rate in dopa-responsive dystonia: Detection with comprehensive GCHI screening. Neurology *64*, 908–911.

Hall, C.E., Yao, Z., Choi, M., Tyzack, G.E., Serio, A., Luisier, R., Harley, J., Preza, E., Arber, C., Crisp, S.J., et al. (2017). Progressive Motor Neuron Pathology and the Role of Astrocytes in a Human Stem Cell Model of VCP-Related ALS. Cell Rep. *19*, 1739–1749.

Halliwell, B. (2006). Oxidative stress and neurodegeneration: where are we now? J. Neurochem. *97*, 1634–1658.

Hammond, C., and Michel, F. (2015). Chapter 5 - The voltage-gated channels of Ca2+ action potentials: Generalization. In Cellular and Molecular Neurophysiology (Fourth Edition), C. Hammond, ed. (Boston: Academic Press), pp. 93–120.

Hanaway, J., McConnell, J.A., and Netsky, M.G. (1971). Histogenesis of the substantia nigra, ventral tegmental area of Tsai and interpeduncular nucleus: An autoradiographic study of the mesencephalon in the rat. J. Comp. Neurol. *142*, 59–73.

Hay, R.J., Macy, M.L., and Chen, T.R. (1989). Mycoplasma infection of cultured cells. Nature *339*, 487.

Hayashi, J., Ohta, S., Kikuchi, A., Takemitsu, M., Goto, Y., and Nonaka, I. (1991). Introduction of disease-related mitochondrial DNA deletions into HeLa cells lacking mitochondrial DNA results in mitochondrial dysfunction. Proc. Natl. Acad. Sci. *88*, 10614–10618.

Healy, D.G., Falchi, M., O'Sullivan, S.S., Bonifati, V., Durr, A., Bressman, S., Brice, A., Aasly, J., Zabetian, C.P., Goldwurm, S., et al. (2008). Phenotype, genotype, and worldwide genetic penetrance of LRRK2-associated Parkinson's disease: a case-control study. Lancet Neurol. *7*, 583–590.

Hebsgaard, J.B., Nelander, J., Sabelström, H., Jönsson, M.E., Stott, S., and Parmar, M. (2009). Dopamine neuron precursors within the developing human mesencephalon show radial glial characteristics. Glia *57*, 1648–1659.

Heitzer, T., Krohn, K., Albers, S., and Meinertz, T. (2000). Tetrahydrobiopterin improves endothelium-dependent vasodilation by increasing nitric oxide activity in patients with Type II diabetes mellitus. Diabetologia *43*, 1435–1438.

Hertz, J.M., Østergaard, K., Juncker, I., Pedersen, S., Romstad, A., Møller, L.B., Güttler, F., and Dupont, E. (2006). Low frequency of Parkin, Tyrosine Hydroxylase, and GTP Cyclohydrolase I gene mutations in a Danish population of early-onset Parkinson's Disease. Eur. J. Neurol. *13*, 385–390.

Higashi, Y., Sasaki, S., Nakagawa, K., Fukuda, Y., Matsuura, H., Oshima, T., and Chayama, K. (2002). Tetrahydrobiopterin enhances forearm vascular response to acetylcholine in both normotensive and hypertensive individuals. Am. J. Hypertens. *15*, 326–332.

Hirano, M., Yanagihara, T., and Ueno, S. (1998). Dominant negative effect of GTP cyclohydrolase I mutations in dopa-responsive hereditary progressive dystonia. Ann. Neurol. *44*, 365–371.

Hirsch, L., Jette, N., Frolkis, A., Steeves, T., and Pringsheim, T. (2016). The Incidence of Parkinson's Disease: A Systematic Review and Meta-Analysis. Neuroepidemiology *46*, 292–300.

Hodge, G.K., and Butcher, L.L. (1980). Pars compacta of the substantia nigra modulates motor activity but is not involved importantly in regulating food and water intake. Naunyn. Schmiedebergs Arch. Pharmacol. *313*, 51–67.

Hong, H.J., Hsiao, G., Cheng, T.H., and Yen, M.H. (2001). Supplemention with tetrahydrobiopterin suppresses the development of hypertension in spontaneously hypertensive rats. Hypertens. Dallas Tex 1979 *38*, 1044–1048.

Hoofwijk, D.M.N., van Reij, R.R.I., Rutten, B.P., Kenis, G., Buhre, W.F., and Joosten, E.A. (2016). Genetic polymorphisms and their association with the prevalence and severity of chronic postsurgical pain: a systematic review. Br. J. Anaesth. *117*, 708–719.

Horn, A.S. (1990). Dopamine uptake: A review of progress in the last decade. Prog. Neurobiol. *34*, 387–400.

Hornykiewicz, O. (2010). A brief history of levodopa. J. Neurol. *257*, 249–252.

Houlden, H., and Singleton, A.B. (2012). The genetics and neuropathology of Parkinson's disease. Acta Neuropathol. (Berl.) *124*, 325–338.

del Hoyo, P., García-Redondo, A., de Bustos, F., Molina, J.A., Sayed, Y., Alonso-Navarro, H., Caballero, L., Arenas, J., Agúndez, J.A., and Jiménez-Jiménez, F.J. (2010). Oxidative stress in skin fibroblasts cultures from patients with Parkinson's disease. BMC Neurol. *10*, 95.

Hu, B.-Y., Weick, J.P., Yu, J., Ma, L.-X., Zhang, X.-Q., Thomson, J.A., and Zhang, S.-C. (2010). Neural differentiation of human induced pluripotent stem cells follows developmental principles but with variable potency. Proc. Natl. Acad. Sci. *107*, 4335–4340.

Huang, D., Xu, J., Wang, J., Tong, J., Bai, X., Li, H., Wang, Z., Huang, Y., Wu, Y., Yu, M., et al. (2017a). Dynamic Changes in the Nigrostriatal Pathway in the MPTP Mouse Model of Parkinson's Disease.

Huang, T.-S., Li, L., Moalim-Nour, L., Jia, D., Bai, J., Yao, Z., Bennett, S.A.L., Figeys, D., and Wang, L. (2017b). A Regulatory Network Involving β-Catenin, e-Cadherin, PI3k/Akt, and Slug Balances Self-Renewal and Differentiation of Human Pluripotent Stem Cells In Response to Wnt Signaling. STEM CELLS 1419–1433.

Hughes, A.J., Daniel, S.E., Kilford, L., and Lees, A.J. (1992). Accuracy of clinical diagnosis of idiopathic Parkinson's disease: a clinico-pathological study of 100 cases. J. Neurol. Neurosurg. Psychiatry *55*, 181–184.

Hughes, A.J., Daniel, S.E., Ben-Shlomo, Y., and Lees, A.J. (2002). The accuracy of diagnosis of parkinsonian syndromes in a specialist movement disorder service. Brain *125*, 861–870.

Huisman, E., Uylings, H.B.M., and Hoogland, P.V. (2008). Gender-related changes in increase of dopaminergic neurons in the olfactory bulb of Parkinson's disease patients. Mov. Disord. *23*, 1407–1413.

Hussein, S.M., Batada, N.N., Vuoristo, S., Ching, R.W., Autio, R., Närvä, E., Ng, S., Sourour, M., Hämäläinen, R., Olsson, C., et al. (2011). Copy number variation and selection during reprogramming to pluripotency. Nature *471*, 58–62.

Hwang, W.J., Calne, D.B., Tsui, J.K.C., and de la Fuente-Fernández, R. (2001). The long-term response to levodopa in dopa-responsive dystonia. Parkinsonism Relat. Disord. *8*, 1–5.

Hwu, W.-L., Wang, P.-J., Hsiao, K.-J., Wang, T.-R., Chiou, Y.-W., and Lee, Y.-M. (1999). Dopa-responsive dystonia induced by a recessive GTP cyclohydrolase I mutation. Hum. Genet. *105*, 226–230.

Hwu, W.-L., Chiou, Y.-W., Lai, S.-Y., and Lee, Y.-M. (2000). Dopa-responsive dystonia is induced by a dominant-negative mechanism. Ann. Neurol. *48*, 609–613.

Hynes, M., Porter, J.A., Chiang, C., Chang, D., Tessier-Lavigne, M., Beachy, P.A., and Rosenthal, A. (1995). Induction of midbrain dopaminergic neurons by Sonic hedgehog. Neuron *15*, 35–44.

Ichinose, H., Ohye, T., Takahashi, E., Seki, N., Hori, T., Segawa, M., Nomura, Y., Endo, K., Tanaka, H., Tsuji, S., et al. (1994). Hereditary progressive dystonia with marked diurnal fluctuation caused by mutations in the GTP cyclohydrolase I gene. Nat. Genet. *8*, 236–242.

Ichinose, H., Ohye, T., Matsuda, Y., Hori, T., Blau, N., Burlina, A., Rouse, B., Matalon, R., Fujita, K., and Nagatsu, T. (1995). Characterization of Mouse and Human GTP Cyclohydrolase I Genes MUTATIONS IN PATIENTS WITH GTP CYCLOHYDROLASE I DEFICIENCY. J. Biol. Chem. *270*, 10062–10071.

Ichinose, H., Homma, D., Sumi-Ichinose, C., Nomura, T., and Kondo, K. (2013). Chapter Three - GTP Cyclohydrolase Regulation: Implications for Brain Development and Function. In Advances in Pharmacology, L.E. Eiden, ed. (Academic Press), pp. 23–35.

Incardona, J.P., Gaffield, W., Kapur, R.P., and Roelink, H. (1998). The teratogenic Veratrum alkaloid cyclopamine inhibits sonic hedgehog signal transduction. Development *125*, 3553–3562.

Inman, G.J., Nicolás, F.J., Callahan, J.F., Harling, J.D., Gaster, L.M., Reith, A.D., Laping, N.J., and Hill, C.S. (2002). SB-431542 Is a Potent and Specific Inhibitor of Transforming Growth Factor-β Superfamily Type I Activin Receptor-Like Kinase (ALK) Receptors ALK4, ALK5, and ALK7. Mol. Pharmacol. *62*, 65–74.

Irie, S., Kanazawa, N., Ryoh, M., Mochizuki, H., Nomura, Y., and Segawa, M. (2011). A case of parkinsonism and dopa-induced severe dyskinesia associated with novel mutation in the GTP cyclohydrolase I gene. Parkinsonism Relat. Disord. *17*, 769–770.

Ishikawa, T., Imamura, K., Kondo, T., Koshiba, Y., Hara, S., Ichinose, H., Furujo, M., Kinoshita, M., Oeda, T., Takahashi, J., et al. (2016). Genetic and pharmacological correction of aberrant dopamine synthesis using patient iPSCs with BH4 metabolism disorders. Hum. Mol. Genet. *25*, 5188–5197.

Iwanaga, K., Wakabayashi, K., Yoshimoto, M., Tomita, I., Satoh, H., Takashima, H., Satoh, A., Seto, M., Tsujihata, M., and Takahashi, H. (1999). Lewy body–type degeneration in cardiac plexus in Parkinson's and incidental Lewy body diseases. Neurology *52*.

Iwatsubo, T., Nakano, I., Fukunaga, K., and Miyamoto, E. (1991). Ca2+/calmodulin-dependent protein kinase II immunoreactivity in Lewy bodies. Acta Neuropathol. (Berl.) *82*, 159–163.

Jaeschke, H. (2010). 9.14 - Antioxidant Defense Mechanisms. In Comprehensive Toxicology (Second Edition), C.A. McQueen, ed. (Oxford: Elsevier), pp. 319–337.

Jakes, R., Spillantini, M.G., and Goedert, M. (1994). Identification of two distinct synucleins from human brain. FEBS Lett. *345*, 27–32.

Jellinger, K.A. (1991). Pathology of Parkinson's disease. Mol. Chem. Neuropathol. *14*, 153–197.

Jiang, H., Xu, Z., Zhong, P., Ren, Y., Liang, G., Schilling, H.A., Hu, Z., Zhang, Y., Wang, X., Chen, S., et al. (2015). Cell cycle and p53 gate the direct conversion of human fibroblasts to dopaminergic neurons. Nat. Commun. *6*, 10100.

Johnson, J.L. (2017). Genetic Association Study (GAS) Power Calculator (University of Michigan School of Public Health Department of Biostatistics Center for Statistical Genetics).

Johnson, M.E., Salvatore, M.F., Maiolo, S.A., and Bobrovskaya, L. (2018). Tyrosine hydroxylase as a sentinel for central and peripheral tissue responses in Parkinson's progression: Evidence from clinical studies and neurotoxin models. Prog. Neurobiol. *165–167*, 1–25.

Jones, L., Goode, L., Davila, E., Brown, A., McCarthy, D.M., Sharma, N., Bhide, P.G., and Armata, I.A. (2017). Translational effects and coding potential of an upstream open reading frame associated with DOPA Responsive Dystonia. Biochim. Biophys. Acta BBA - Mol. Basis Dis. *1863*, 1171–1182.

Kalir, H.H., and Mytilineou, C. (1991). Ascorbic Acid in Mesencephalic Cultures: Effects on Dopaminergic Neuron Development. J. Neurochem. *57*, 458–464.

Kalyanaraman, B., Darley-Usmar, V., Davies, K.J.A., Dennery, P.A., Forman, H.J., Grisham, M.B., Mann, G.E., Moore, K., Roberts, L.J., and Ischiropoulos, H. (2012). Measuring reactive oxygen and nitrogen species with fluorescent probes: challenges and limitations. Free Radic. Biol. Med. *52*, 1–6.

Kee, N., Volakakis, N., Kirkeby, A., Dahl, L., Storvall, H., Nolbrant, S., Lahti, L., Björklund, Å.K., Gillberg, L., Joodmardi, E., et al. (2017). Single-Cell Analysis Reveals a Close Relationship between Differentiating Dopamine and Subthalamic Nucleus Neuronal Lineages. Cell Stem Cell *20*, 29–40.

Kettenmann, H., Backus, K.H., and Schachner, M. (1984a). Aspartate, glutamate and γ-aminobutyric acid depolarize cultured astrocytes. Neurosci. Lett. *52*, 25–29.

Kettenmann, H., Gilbert, P., and Schachner, M. (1984b). Depolarization of cultured oligodendrocytes by glutamate and GABA. Neurosci. Lett. *47*, 271–276.

Kim, H.-S., Kim, J., Jo, Y., Jeon, D., and Cho, Y.S. (2014). Direct lineage reprogramming of mouse fibroblasts to functional midbrain dopaminergic neuronal progenitors. Stem Cell Res. *12*, 60–68.

Kim, J., Su, S.C., Wang, H., Cheng, A.W., Cassady, J.P., Lodato, M.A., Lengner, C.J., Chung, C.-Y., Dawlaty, M.M., Tsai, L.-H., et al. (2011). Functional Integration of Dopaminergic Neurons Directly Converted from Mouse Fibroblasts. Cell Stem Cell *9*, 413–419.

Kim, R., Jeon, B., and Lee, W.-W. (2016). A Systematic Review of Treatment Outcome in Patients with Dopa-responsive Dystonia (DRD) and DRD-Plus. Mov. Disord. Clin. Pract. *3*, 435–442.

Kingsbury, A.E., Bandopadhyay, R., Silveira-Moriyama, L., Ayling, H., Kallis, C., Sterlacci, W., Maeir, H., Poewe, W., and Lees, A.J. (2010). Brain stem pathology in Parkinson's disease: An evaluation of the Braak staging model. Mov. Disord. *25*, 2508–2515.

Kircher, M., Witten, D.M., Jain, P., O'Roak, B.J., Cooper, G.M., and Shendure, J. (2014). A general framework for estimating the relative pathogenicity of human genetic variants. Nat. Genet. *46*, 310–315.

Kirkeby, A., Grealish, S., Wolf, D.A., Nelander, J., Wood, J., Lundblad, M., Lindvall, O., and Parmar, M. (2012). Generation of Regionally Specified Neural Progenitors and Functional Neurons from Human Embryonic Stem Cells under Defined Conditions. Cell Rep. *1*, 703–714.

Kirkeby, A., Nelander, J., and Parmar, M. (2013). Generating regionalized neuronal cells from pluripotency, a step-by-step protocol. Front. Cell. Neurosci. *6*.

Kirkeby, A., Nolbrant, S., Tiklova, K., Heuer, A., Kee, N., Cardoso, T., Ottosson, D.R., Lelos, M.J., Rifes, P., Dunnett, S.B., et al. (2017). Predictive Markers Guide Differentiation to Improve Graft Outcome in Clinical Translation of hESC-Based Therapy for Parkinson's Disease. Cell Stem Cell *20*, 135–148.

Kitada, T., Asakawa, S., Hattori, N., Matsumine, H., Yamamura, Y., Minoshima, S., Yokochi, M., Mizuno, Y., and Shimizu, N. (1998). Mutations in the *parkin* gene cause autosomal recessive juvenile parkinsonism. Nature *392*, 605–608.

Klein, C., Hedrich, K., Kabakçi, K., Mohrmann, K., Wiegers, K., Landt, O., Hagenah, J., Schwinger, E., Pramstaller, P.P., Ozelius, L.J., et al. (2002). Exon deletions in the GCHI gene in two of four Turkish families with dopa-responsive dystonia. Neurology *59*, 1783–1786.

Ko, J.-Y., Lee, J.-Y., Park, C.-H., and Lee, S.-H. (2005). Effect of cell-density on in-vitro dopaminergic differentiation of mesencephalic precursor cells. NeuroReport *16*, 499.

Kojima, H., and Nagano, T. (2000). Fluorescent Indicators for Nitric Oxide. Adv. Mater. *12*, 763–765.

Kojima, H., Hirotani, M., Nakatsubo, N., Kikuchi, K., Urano, Y., Higuchi, T., Hirata, Y., and Nagano, T. (2001). Bioimaging of Nitric Oxide with Fluorescent Indicators Based on the Rhodamine Chromophore. Anal. Chem. *73*, 1967–1973.

Kordower, J.H., Olanow, C.W., Dodiya, H.B., Chu, Y., Beach, T.G., Adler, C.H., Halliday, G.M., and Bartus, R.T. (2013). Disease duration and the integrity of the nigrostriatal system in Parkinson's disease. Brain *136*, 2419–2431.

Korotkova, T.M., Ponomarenko, A.A., Haas, H.L., and Sergeeva, O.A. (2005). Differential expression of the homeobox gene Pitx3 in midbrain dopaminergic neurons. Eur. J. Neurosci. *22*, 1287–1293.

Korte-Bouws, G.A.H., Albers, E., Voskamp, M., Hendriksen, H., De Leeuw, L.R., Güntürkün, O., De Roock, S., Vastert, S.J., and Korte, S.M. (2019). Juvenile Arthritis Patients Suffering from Chronic Inflammation Have Increased Activity of Both IDO and GTP-CH1 Pathways But Decreased BH4 Efficacy: Implications for Well-Being, Including Fatigue, Cognitive Impairment, Anxiety, and Depression. Pharmaceuticals *12*, 9.

Kraytsberg, Y., Kudryavtseva, E., McKee, A.C., Geula, C., Kowall, N.W., and Khrapko, K. (2006). Mitochondrial DNA deletions are abundant and cause functional impairment in aged human substantia nigra neurons. Nat. Genet. *38*, 518–520.

Kriks, S., Shim, J.-W., Piao, J., Ganat, Y.M., Wakeman, D.R., Xie, Z., Carrillo-Reid, L., Auyeung, G., Antonacci, C., Buch, A., et al. (2011). Dopamine neurons derived from human ES cells efficiently engraft in animal models of Parkinson/'s disease. Nature *480*, 547–551.

Krüger, R., Kuhn, W., Müller, T., Woitalla, D., Graeber, M., Kösel, S., Przuntek, H., Epplen, J.T., Schöls, L., and Riess, O. (1998). Ala30Pro mutation in the gene encoding alpha-synuclein in Parkinson's disease. Nat. Genet. *18*, 106–108.

Kurian, M.A., Gissen, P., Smith, M., Heales, S.J., and Clayton, P.T. (2011). The monoamine neurotransmitter disorders: an expanding range of neurological syndromes. Lancet Neurol. *10*, 721–733.

Kuzkaya, N., Weissmann, N., Harrison, D.G., and Dikalov, S. (2003). Interactions of Peroxynitrite, Tetrahydrobiopterin, Ascorbic Acid, and Thiols IMPLICATIONS FOR UNCOUPLING ENDOTHELIAL NITRIC-OXIDE SYNTHASE. J. Biol. Chem. *278*, 22546–22554.

Lammel, S., Lim, B.K., Ran, C., Huang, K.W., Betley, M.J., Tye, K.M., Deisseroth, K., and Malenka, R.C. (2012). Input-specific control of reward and aversion in the ventral tegmental area. Nature *491*, 212–217.

Landmesser, U., Dikalov, S., Price, S.R., McCann, L., Fukai, T., Holland, S.M., Mitch, W.E., and Harrison, D.G. (2003). Oxidation of tetrahydrobiopterin leads to uncoupling of endothelial cell nitric oxide synthase in hypertension. J. Clin. Invest. *111*, 1201–1209.

Langston, J.W., Ballard, P., Tetrud, J.W., and Irwin, I. (1983). Chronic Parkinsonism in humans due to a product of meperidine-analog synthesis. Science *219*, 979–980.

Lapasset, L., Milhavet, O., Prieur, A., Besnard, E., Babled, A., Aït-Hamou, N., Leschik, J., Pellestor, F., Ramirez, J.-M., Vos, J.D., et al. (2011). Rejuvenating senescent and centenarian human cells by reprogramming through the pluripotent state. Genes Dev. *25*, 2248–2253.

Lapointe, N., St-Hilaire, M., Martinoli, M.-G., Blanchet, J., Gould, P., Rouillard, C., and Cicchetti, F. (2004). Rotenone induces non-specific central nervous system and systemic toxicity. FASEB J. *18*, 717–719.

de Lau, L.M., and Breteler, M.M. (2006). Epidemiology of Parkinson's disease. Lancet Neurol. *5*, 525–535.

Laurent, L.C., Ulitsky, I., Slavin, I., Tran, H., Schork, A., Morey, R., Lynch, C., Harness, J.V., Lee, S., Barrero, M.J., et al. (2011). Dynamic Changes in the Copy Number of Pluripotency and Cell Proliferation Genes in Human ESCs and iPSCs during Reprogramming and Time in Culture. Cell Stem Cell *8*, 106–118.

Laurie, S., Fernandez-Callejo, M., Marco-Sola, S., Trotta, J.-R., Camps, J., Chacón, A., Espinosa, A., Gut, M., Gut, I., Heath, S., et al. (2016). From Wet-Lab to Variations: Concordance and Speed of Bioinformatics Pipelines for Whole Genome and Whole Exome Sequencing. Hum. Mutat. *37*, 1263–1271.

Laursen, J.B., Somers, M., Kurz, S., McCann, L., Warnholtz, A., Freeman, B.A., Tarpey, M., Fukai, T., and Harrison, D.G. (2001). Endothelial regulation of vasomotion in apoE-deficient mice: implications for interactions between peroxynitrite and tetrahydrobiopterin. Circulation *103*, 1282–1288.

Law, S.W., Conneely, O.M., DeMayo, F.J., and O'Malley, B.W. (1992). Identification of a new brain-specific transcription factor, NURR1. Mol. Endocrinol. *6*, 2129–2135.

Lazzarini, A.M.M., Myers, R.H., Zimmerman, T.R.J., Mark, M.H., Golbe, L.I., Sage, J.I., Johnson, W.G., and Duvoisin, R.C. (1994). A clinical genetic study of Parkinson's disease: Evidence for dominant transmission. Neurology 499–506.

Lee, S., Wright, F.A., and Zou, F. (2011). Control of Population Stratification by Correlation-Selected Principal Components. Biometrics *67*, 967–974.

Lee, S., Emond, M.J., Bamshad, M.J., Barnes, K.C., Rieder, M.J., Nickerson, D.A., Christiani, D.C., Wurfel, M.M., and Lin, X. (2012). Optimal Unified Approach for Rare-Variant Association Testing with Application to Small-Sample Case-Control Whole-Exome Sequencing Studies. Am. J. Hum. Genet. *91*, 224–237.

Lee, S., Abecasis, G.R., Boehnke, M., and Lin, X. (2014). Rare-Variant Association Analysis: Study Designs and Statistical Tests. Am. J. Hum. Genet. *95*, 5–23.

Lees, A.J., Hardy, J., and Revesz, T. (2009). Parkinson's disease. The Lancet *373*, 2055–2066.

Lesage, S., Drouet, V., Majounie, E., Deramecourt, V., Jacoupy, M., Nicolas, A., Cormier-Dequaire, F., Hassoun, S.M., Pujol, C., Ciura, S., et al. (2016). Loss of VPS13C Function in Autosomal-Recessive Parkinsonism Causes Mitochondrial Dysfunction and Increases PINK1/Parkin-Dependent Mitophagy. Am. J. Hum. Genet. *98*, 500–513.

Lewthwaite, A.J., Lambert, T.D., Rolfe, E.B., Olgiati, S., Quadri, M., Simons, E.J., Morrison, K.E., Bonifati, V., and Nicholl, D.J. (2015). Novel GCH1 variant in Dopa-responsive dystonia and Parkinson's disease. Parkinsonism Relat. Disord. *21*, 394–397.

Lewy, F.H. (1912). Paralysis agitans. I. Pathologische Anatomie. In Handbuch der Neurologie, (Berlin: Springer), pp. 920–933.

Li, B., and Leal, S.M. (2008). Methods for Detecting Associations with Rare Variants for Common Diseases: Application to Analysis of Sequence Data. Am. J. Hum. Genet. *83*, 311–321.

Liang, G., and Zhang, Y. (2013). Genetic and Epigenetic Variations in iPSCs: Potential Causes and Implications for Application. Cell Stem Cell *13*, 149–159.

Liu, R., Baird, D., Park, Y., Freedman, N.D., Huang, X., Hollenbeck, A., Blair, A., and Chen, H. (2014). Female reproductive factors, menopausal hormone use, and Parkinson's disease. Mov. Disord. Off. J. Mov. Disord. Soc. *29*, 889–896.

Livak, K.J., and Schmittgen, T.D. (2001). Analysis of Relative Gene Expression Data Using Real-Time Quantitative PCR and the 2−ΔΔCT Method. Methods *25*, 402–408.

Lloyd, K., and Hornykiewicz, O. (1970). Parkinson's Disease: Activity of L-Dopa Decarboxylase in Discrete Brain Regions. Science *170*, 1212–1213.

López-Laso, E., Sánchez-Raya, A., Moriana, J.A., Martínez-Gual, E., Camino-León, R., Mateos-González, M.E., Pérez-Navero, J.L., Ochoa-Sepúlveda, J.J., Ormazabal, A., Opladen, T., et al. (2011). Neuropsychiatric symptoms and intelligence quotient in autosomal dominant Segawa disease. J. Neurol. *258*, 2155–2162.

Louis, E.D., Ottman, R., and Hauser, W.A. (1998). How common is the most common adult movement disorder? estimates of the prevalence of essential tremor throughout the world. Mov. Disord. Off. J. Mov. Disord. Soc. *13*, 5–10.

Lovenberg, W., Levine, R.A., Robinson, D.S., Ebert, M., Williams, A.C., and Calne, D.B. (1979). Hydroxylase cofactor activity in cerebrospinal fluid of normal subjects and patients with Parkinson's disease. Science *204*, 624–626.

Lüdecke, B., Dworniczak, B., and Bartholomé, K. (1995). A point mutation in the tyrosine hydroxylase gene associated with Segawa's syndrome. Hum. Genet. *95*, 123–125.

Lüdecke, B., Knappskog, P.M., Clayton, P.T., Surtees, R.A.H., Clelland, J.D., Heales, S.J.R., Brand, M.P., Bartholomé, K., and Flatmark, T. (1996). Recessively Inherited L-DOPA-Responsive Parkinsonism In Infancy Caused by A Point Mutation (L205p) in the Tyrosine Hydroxylase Gene. Hum. Mol. Genet. *5*, 1023–1028.

Ma, W., Tavakoli, T., Derby, E., Serebryakova, Y., Rao, M.S., and Mattson, M.P. (2008). Cell-extracellular matrix interactions regulate neural differentiation of human embryonic stem cells. BMC Dev. Biol. *8*, 90.

Macdonald, R., Barnes, K., Hastings, C., and Mortiboys, H. (2018). Mitochondrial abnormalities in Parkinson's disease and Alzheimer's disease: can mitochondria be targeted therapeutically? Biochem. Soc. Trans. *46*, 891–909.

Madsen, B.E., and Browning, S.R. (2009). A Groupwise Association Test for Rare Mutations Using a Weighted Sum Statistic. PLOS Genet. *5*, e1000384.

Mahlknecht, P., Hotter, A., Hussl, A., Esterhammer, R., Schocke, M., and Seppi, K. (2010). Significance of MRI in Diagnosis and Differential Diagnosis of Parkinson's Disease. Neurodegener. Dis. *7*, 300–318.

Manfredi, G., Yang, L., Gajewski, C.D., and Mattiazzi, M. (2002). Measurements of ATP in mammalian cells. Methods *26*, 317–326.

Manolio, T.A. (2010). Genomewide Association Studies and Assessment of the Risk of Disease. N. Engl. J. Med. *363*, 166–176.

Marion, R.M., Strati, K., Li, H., Tejera, A., Schoeftner, S., Ortega, S., Serrano, M., and Blasco, M.A. (2009). Telomeres Acquire Embryonic Stem Cell Characteristics in Induced Pluripotent Stem Cells. Cell Stem Cell *4*, 141–154.

Maroteaux, L., and Scheller, R.H. (1991). The rat brain synucleins; family of proteins transiently associated with neuronal membrane. Mol. Brain Res. *11*, 335–343.

Marras, C., Beck, J.C., Bower, J.H., Roberts, E., Ritz, B., Ross, G.W., Abbott, R.D., Savica, R., Eeden, S.K.V.D., Willis, A.W., et al. (2018). Prevalence of Parkinson's disease across North America. Npj Park. Dis. *4*, 21.

Marshall, V., and Grosset, D. (2003). Role of dopamine transporter imaging in routine clinical practice. Mov. Disord. *18*, 1415–1423.

Martignoni, M., Groothuis, G.M.M., and Kanter, R. de (2006). Species differences between mouse, rat, dog, monkey and human CYP-mediated drug metabolism, inhibition and induction. Expert Opin. Drug Metab. Toxicol. *2*, 875–894.

Martinez, T.N., and Greenamyre, J.T. (2011). Toxin Models of Mitochondrial Dysfunction in Parkinson's Disease. Antioxid. Redox Signal. *16*, 920–934.

Martinez-Martin, P. (2011). The importance of non-motor disturbances to quality of life in Parkinson's disease. J. Neurol. Sci. *310*, 12–16.

Marton, R.M., and Ioannidis, J.P.A. (2018). A Comprehensive Analysis of Protocols for Deriving Dopaminergic Neurons from Human Pluripotent Stem Cells. STEM CELLS Transl. Med. *0*.

Mastick, G.S., and Andrews, G.L. (2001). Pax6 Regulates the Identity of Embryonic Diencephalic Neurons. Mol. Cell. Neurosci. *17*, 190–207.

Matise, M.P., Epstein, D.J., Park, H.L., Platt, K.A., and Joyner, A.L. (1998). Gli2 is required for induction of floor plate and adjacent cells, but not most ventral neurons in the mouse central nervous system. Development *125*, 2759–2770.

Matsumine, H., Saito, M., Shimoda-Matsubayashi, S., Tanaka, H., Ishikawa, A., Nakagawa-Hattori, Y., Yokochi, M., Kobayashi, T., Igarashi, S., Takano, H., et al. (1997). Localization of a gene for an autosomal recessive form of juvenile Parkinsonism to chromosome 6q25.2-27. Am. J. Hum. Genet. *60*, 588–596.

Matsumine, H., Yamamura, Y., Hattori, N., Kobayashi, T., Kitada, T., Yoritaka, A., and Mizuno, Y. (1998). A Microdeletion of D6S305 in a Family of Autosomal Recessive Juvenile Parkinsonism (PARK2). Genomics *49*, 143–146.

McGuire, S.O., Ling, Z.D., Lipton, J.W., Sortwell, C.E., Collier, T.J., and Carvey, P.M. (2001). Tumor Necrosis Factor α Is Toxic to Embryonic Mesencephalic Dopamine Neurons. Exp. Neurol. *169*, 219–230.

McMahon, A.P., and Bradley, A. (1990). The Wnt-1 (int-1) proto-oncogene is required for development of a large region of the mouse brain. Cell *62*, 1073–1085.

McMahon, A.P., Joyner, A.L., Bradley, A., and McMahon, J.A. (1992). The midbrain-hindbrain phenotype of Wnt-1−Wnt-1− mice results from stepwise deletion of engrailed-expressing cells by 9.5 days postcoitum. Cell *69*, 581–595.

McRitchie, D. a., Hardman, C. d., and Halliday, G. m. (1996). Cytoarchitectural distribution of calcium binding proteins in midbrain dopaminergic regions of rats and humans. J. Comp. Neurol. *364*, 121–150.

Mena, M.A., Pardo, B., Casarejos, M.J., Fahn, S., and Yébenes, J.G. de (1992). Neurotoxicity of levodopa on catecholamine-rich neurons. Mov. Disord. *7*, 23–31.

Mencacci, N.E., Isaias, I.U., Reich, M.M., Ganos, C., Plagnol, V., Polke, J.M., Bras, J., Hersheson, J., Stamelou, M., Pittman, A.M., et al. (2014). Parkinson's disease in GTP cyclohydrolase 1 mutation carriers. Brain *137*, 2480–2492.

Mencacci, N.E., Pittman, A.M., Isaias, I.U., Hardy, J., Klebe, S., Bhatia, K.P., and Wood, N.W. (2015). Reply: Parkinson's disease in GTP cyclohydrolase 1 mutation carriers. Brain *138*, e352–e352.

Miller, J.D., Ganat, Y.M., Kishinevsky, S., Bowman, R.L., Liu, B., Tu, E.Y., Mandal, P.K., Vera, E., Shim, J., Kriks, S., et al. (2013). Human iPSC-Based Modeling of Late-Onset Disease via Progerin-Induced Aging. Cell Stem Cell *13*, 691–705.

Millet, S., Campbell, K., Epstein, D.J., Losos, K., Harris, E., and Joyner, A.L. (1999). A role for *Gbx2* in repression of *Otx2* and positioning the mid/hindbrain organizer. Nature *401*, 161–164.

Milosevic, J., Schwarz, S.C., Ogunlade, V., Meyer, A.K., Storch, A., and Schwarz, J. (2009). Emerging role of LRRK2 in human neural progenitor cell cycle progression, survival and differentiation. Mol. Neurodegener. *4*, 25.

Milstien, S., Kaufman, S., and Sakai, N. (1993). Tetrahydrobiopterin biosynthesis defects examined in cytokine-stimulated fibroblasts. J. Inherit. Metab. Dis. *16*, 975–981.

Mizuno, Y., Shimoda, S., and Origasa, H. (2018). Long-term treatment of Parkinson's disease with levodopa and other adjunctive drugs. J. Neural Transm. *125*, 35–43.

Moisan, F., Kab, S., Mohamed, F., Canonico, M., Le Guern, M., Quintin, C., Carcaillon, L., Nicolau, J., Duport, N., Singh-Manoux, A., et al. (2016). Parkinson disease male-to-female ratios increase with age: French nationwide study and meta-analysis. J. Neurol. Neurosurg. Psychiatry *87*, 952–957.

Monti, J.M., and Jantos, H. (2008). The roles of dopamine and serotonin, and of their receptors, in regulating sleep and waking. In Progress in Brain Research, G. Di Giovann, V. Di Matteo, and E. Esposito, eds. (Elsevier), pp. 625–646.

Morris, A.P., and Zeggini, E. (2010). An evaluation of statistical approaches to rare variant analysis in genetic association studies. Genet. Epidemiol. *34*, 188–193.

Morrish, P.K., Rakshi, J.S., Bailey, D.L., Sawle, G.V., and Brooks, D.J. (1998). Measuring the rate of progression and estimating the preclinical period of Parkinson's disease with [18F]dopa PET. J. Neurol. Neurosurg. Psychiatry *64*, 314–319.

Mortiboys, H., Thomas, K.J., Koopman, W.J.H., Klaffke, S., Abou-Sleiman, P., Olpin, S., Wood, N.W., Willems, P.H.G.M., Smeitink, J.A.M., Cookson, M.R., et al. (2008). Mitochondrial function and morphology are impaired in parkin-mutant fibroblasts. Ann. Neurol. *64*, 555–565.

Mortiboys, H., Macdonald, R., Payne, T., Sassani, M., Jenkins, T., and Bandmann, O. (2018). Translational approaches to restoring mitochondrial function in Parkinson's disease. FEBS Lett. *592*, 776–792.

Motono, M., Ioroi, Y., Ogura, T., and Takahashi, J. (2016). WNT-C59, a Small-Molecule WNT Inhibitor, Efficiently Induces Anterior Cortex That Includes Cortical Motor Neurons From Human Pluripotent Stem Cells. Stem Cells Transl. Med. *5*, 552–560.

Mullis, K.B. (1990). The unusual origin of the polymerase chain reaction. Sci. Am. *262*, 56–61, 64–65.

Mytilineou, C., Werner, P., Molinari, S., Di Rocco, A., Cohen, G., and Yahr, M.D. (1994). Impaired oxidative decarboxylation of pyruvate in fibroblasts from patients with Parkinson's disease. J. Neural Transm. Park. Dis. Dement. Sect. *8*, 223–228.

Mytilineou, C., Walker, R.H., JnoBaptiste, R., and Olanow, C.W. (2003). Levodopa Is Toxic to Dopamine Neurons in an in Vitro but Not an in Vivo Model of Oxidative Stress. J. Pharmacol. Exp. Ther. *304*, 792–800.

Naguib, Y.M.A. (1998). A Fluorometric Method for Measurement of Peroxyl Radical Scavenging Activities of Lipophilic Antioxidants. Anal. Biochem. *265*, 290–298.

Nakamura, K., Wright, D.A., Wiatr, T., Kowlessur, D., Milstien, S., Lei, X.G., and Kang, U.J. (2000). Preferential Resistance of Dopaminergic Neurons to the Toxicity of Glutathione Depletion Is Independent of Cellular Glutathione Peroxidase and Is Mediated by Tetrahydrobiopterin. J. Neurochem. *74*, 2305–2314.

Nakamura, K., Bindokas, V.P., Kowlessur, D., Elas, M., Milstien, S., Marks, J.D., Halpern, H.J., and Kang, U.J. (2001). Tetrahydrobiopterin Scavenges Superoxide in Dopaminergic Neurons. J. Biol. Chem. *276*, 34402–34407.

Nakashima, S., and Ikuta, F. (1984). Tyrosine hydroxylase protein in Lewy bodies of parkinsonian and senile brains. J. Neurol. Sci. *66*, 91–96.

Nalls, M.A., Pankratz, N., Lill, C.M., Do, C.B., Hernandez, D.G., Saad, M., DeStefano, A.L., Kara, E., Bras, J., Sharma, M., et al. (2014). Large-scale meta-analysis of genome-wide association data identifies six new risk loci for Parkinson's disease. Nat. Genet. *46*, 989–993.

Nasser, A., and Møller, L.B. (2014). GCH1 variants, tetrahydrobiopterin and their effects on pain sensitivity. Scand. J. Pain *5*, 121–128.

Nelander, J., Hebsgaard, J.B., and Parmar, M. (2009). Organization of the human embryonic ventral mesencephalon. Gene Expr. Patterns *9*, 555–561.

Newman, J.R.B., Todorovic, M., Silburn, P.A., Sutherland, G.T., and Mellick, G.D. (2014). Lack of reproducibility in re-evaluating associations between GCH1 polymorphisms and Parkinson's disease and isolated dystonia in an Australian case–control group. Parkinsonism Relat. Disord. *20*, 668–670.

Nicholls, D.G. (2006). Simultaneous Monitoring of Ionophore- and Inhibitor-mediated Plasma and Mitochondrial Membrane Potential Changes in Cultured Neurons. J. Biol. Chem. *281*, 14864–14874.

Nichols, W.C., Pankratz, N., Hernandez, D., Paisán-Ruíz, C., Jain, S., Halter, C.A., Michaels, V.E., Reed, T., Rudolph, A., Shults, C.W., et al. (2005). Genetic screening for a single common LRRK2 mutation in familial Parkinson's disease. The Lancet *365*, 410–412.

Nishioka, K., Hayashi, S., Farrer, M.J., Singleton, A.B., Yoshino, H., Imai, H., Kitami, T., Sato, K., Kuroda, R., Tomiyama, H., et al. (2006). Clinical heterogeneity of α-synuclein gene duplication in Parkinson's disease. Ann. Neurol. *59*, 298–309.

Nolbrant, S., Heuer, A., Parmar, M., and Kirkeby, A. (2017). Generation of high-purity human ventral midbrain dopaminergic progenitors for in vitro maturation and intracerebral transplantation. Nat. Protoc. *12*, 1962.

Nordström, U., Jessell, T.M., and Edlund, T. (2002). Progressive induction of caudal neural character by graded Wnt signaling. Nat. Neurosci. *5*, 525.

Noyce, A.J., Bestwick, J.P., Silveira-Moriyama, L., Hawkes, C.H., Giovannoni, G., Lees, A.J., and Schrag, A. (2012). Meta-analysis of early nonmotor features and risk factors for Parkinson disease. Ann. Neurol. *72*, 893–901.

Noyce, A.J., R'Bibo, L., Peress, L., Bestwick, J.P., Adams-Carr, K.L., Mencacci, N.E., Hawkes, C.H., Masters, J.M., Wood, N., Hardy, J., et al. (2017). PREDICT-PD: An online approach to prospectively identify risk indicators of Parkinson's disease. Mov. Disord. n/a-n/a.

Noyce, A.J., Dickson, J., Rees, R.N., Bestwick, J.P., Isaias, I.U., Politis, M., Giovannoni, G., Warner, T.T., Lees, A.J., and Schrag, A. (2018). Dopamine reuptake transporter–single-photon emission computed tomography and transcranial sonography as imaging markers of prediagnostic Parkinson's disease. Mov. Disord. *33*, 478–482.

Nunnari, J., and Suomalainen, A. (2012). Mitochondria: In Sickness and in Health. Cell *148*, 1145–1159.

Nygaard, T.G. (1993). An analysis of North American families with dopa-responsive dystonia. In Hereditary Progressive Dystonia, (London), pp. 97–106.

Nygaard, T.G., Marsden, C.D., and Duvoisin, R.C. (1988). Dopa-responsive dystonia. Adv. Neurol. *50*, 377–384.

Nygaard, T.G., Trugman, J.M., de Yebenes, J.G., and Fahn, S. (1990). Dopa-responsive dystonia: The spectrum of clinical manifestations in a large North American family. Neurology *40*, 66–69.

Nygaard, T.G., Takahashi, H., Heiman, G.A., Snow, B.J., Fahn, S., and Calne, D.B. (1992). Long-term treatment response and fluorodopa positron emission tomographic scanning of parkinsonism in a family with dopa-responsive dystonia. Ann. Neurol. *32*, 603–608.

Nygaard, T.G., Wilhelmsen, K.C., Risch, N.J., Brown, D.L., Trugman, J.M., Conrad Gilliam, T., Fahn, S., and Weeks, D.E. (1993). Linkage mapping of dopa–responsive dystonia (DRD) to chromosome 14q. Nat. Genet. *5*, 386–391.

Nygaard, T.G., Waran, S.P., Levine, R.A., Naini, A.B., and Chutorian, A.M. (1994). Dopa-responsive dystonia simulating cerebral palsy. Pediatr. Neurol. *11*, 236–240.

Olson, L., Seiger, Å., and Fuxe, K. (1972). Heterogeneity of striatal and limbic dopamine innervation: Highly fluorescent islands in developing and adult rats. Brain Res. *44*, 283–288.

Olson, L., Boréus, L.O., and Seiger, Å. (1973). Histochemical demonstration and mapping of 5-hydroxytryptamine- and catecholamine-containing neuron systems in the human fetal brain. Z. Für Anat. Entwicklungsgeschichte *139*, 259–282.

O'Malley, K.L., and Rotwein, P. (1988). Human tyrosine hydroxylase and insulin genes are contiguous on chromosome 11. Nucleic Acids Res. *16*, 4437–4446.

Ono, Y., Nakatani, T., Sakamoto, Y., Mizuhara, E., Minaki, Y., Kumai, M., Hamaguchi, A., Nishimura, M., Inoue, Y., Hayashi, H., et al. (2007). Differences in neurogenic potential in floor plate cells along an anteroposterior location: midbrain dopaminergic neurons originate from mesencephalic floor plate cells. Development *134*, 3213–3225.

Opladen, T., Hoffmann, G., Hörster, F., Hinz, A.-B., Neidhardt, K., Klein, C., and Wolf, N. (2011). Clinical and biochemical characterization of patients with early infantile onset of autosomal

recessive GTP cyclohydrolase I deficiency without hyperphenylalaninemia. Mov. Disord. *26*, 157–161.

Orimo, S., Takahashi, A., Uchihara, T., Mori, F., Kakita, A., Wakabayashi, K., and Takahashi, H. (2007). Degeneration of Cardiac Sympathetic Nerve Begins in the Early Disease Process of Parkinson's Disease. Brain Pathol. *17*, 24–30.

Paik, E.J., O'Neil, A.L., Ng, S.-Y., Sun, C., and Rubin, L.L. (2018). Using intracellular markers to identify a novel set of surface markers for live cell purification from a heterogeneous hIPSC culture. Sci. Rep. *8*, 804.

Paisán-Ruíz, C., Jain, S., Evans, E.W., Gilks, W.P., Simón, J., van der Brug, M., de Munain, A.L., Aparicio, S., Gil, A.M., Khan, N., et al. (2004). Cloning of the Gene Containing Mutations that Cause PARK8-Linked Parkinson's Disease. Neuron *44*, 595–600.

Pakkenberg, B., Møller, A., Gundersen, H.J., Dam, A.M., and Pakkenberg, H. (1991). The absolute number of nerve cells in substantia nigra in normal subjects and in patients with Parkinson's disease estimated with an unbiased stereological method. J. Neurol. Neurosurg. Psychiatry *54*, 30–33.

Pap, E.H.W., Drummen, G.P.C., Winter, V.J., Kooij, T.W.A., Rijken, P., Wirtz, K.W.A., Kamp, J.A.F.O. den, Hage, W.J., and Post, J.A. (1999). Ratio-fluorescence microscopy of lipid oxidation in living cells using C11-BODIPY581/591. FEBS Lett. *453*, 278–282.

Papa, S., Martino, P.L., Capitanio, G., Gaballo, A., De Rasmo, D., Signorile, A., and Petruzzella, V. (2012). The Oxidative Phosphorylation System in Mammalian Mitochondria. In Advances in Mitochondrial Medicine, R. Scatena, P. Bottoni, and B. Giardina, eds. (Dordrecht: Springer Netherlands), pp. 3–37.

Pardo, B., Mena, M.A., Fahn, S., and Yébenes, J.G. de (1993). Ascorbic acid protects against levodopa-induced neurotoxicity on a catecholamine-rich human neuroblastoma cell line. Mov. Disord. *8*, 278–284.

Parker, W.D., Boyson, S.J., and Parks, J.K. (1989). Abnormalities of the electron transport chain in idiopathic parkinson's disease. Ann. Neurol. *26*, 719–723.

Parkinson, J. (1817). An Essay on the Shaking Palsy. Whittingham Rowland Lond.

Parkinson's UK (2018). The incidence and prevalence of Parkinson's in the UK - Results from the Clinical Practice Research Datalink. Summary Report.

Patani, R., Lewis, P.A., Trabzuni, D., Puddifoot, C.A., Wyllie, D.J.A., Walker, R., Smith, C., Hardingham, G.E., Weale, M., Hardy, J., et al. (2012a). Investigating the utility of human embryonic stem cell-derived neurons to model ageing and neurodegenerative disease using whole-genome gene expression and splicing analysis. J. Neurochem. *122*, 738–751.

Patani, R., Lewis, P.A., Trabzuni, D., Puddifoot, C.A., Wyllie, D.J.A., Walker, R., Smith, C., Hardingham, G.E., Weale, M., Hardy, J., et al. (2012b). Investigating the utility of human embryonic stem cell-derived neurons to model ageing and neurodegenerative disease using whole-genome gene expression and splicing analysis. J. Neurochem. *122*, 738–751.

Patterson, M., Chan, D.N., Ha, I., Case, D., Cui, Y., Handel, B.V., Mikkola, H.K., and Lowry, W.E. (2012). Defining the nature of human pluripotent stem cell progeny. Cell Res. *22*, 178–193.

Paudel, R., Hardy, J., Revesz, T., Holton, J.L., and Houlden, H. (2012). Review: Genetics and neuropathology of primary pure dystonia. Neuropathol. Appl. Neurobiol. *38*, 520–534.

Pawitan, Y., Seng, K.C., and Magnusson, P.K.E. (2009). How Many Genetic Variants Remain to Be Discovered? PLOS ONE *4*, e7969.

Paxinou, E., Chen, Q., Weisse, M., Giasson, B.I., Norris, E.H., Rueter, S.M., Trojanowski, J.Q., Lee, V.M.-Y., and Ischiropoulos, H. (2001). Induction of α-Synuclein Aggregation by Intracellular Nitrative Insult. J. Neurosci. *21*, 8053–8061.

Payami, H., Larsen, K., Bernard, S., and Nutt, J. (1994). Increased risk of Parkinson's disease in parents and siblings of patients. Ann. Neurol. *36*, 659–661.

Payne, B.A.I., and Chinnery, P.F. (2015). Mitochondrial dysfunction in aging: Much progress but many unresolved questions. Biochim. Biophys. Acta BBA - Bioenerg. *1847*, 1347–1353.

Perry, S.W., Norman, J.P., Barbieri, J., Brown, E.B., and Gelbard, H.A. (2011). Mitochondrial membrane potential probes and the proton gradient: a practical usage guide. BioTechniques *50*, 98–115.

Pfisterer, U., Kirkeby, A., Torper, O., Wood, J., Nelander, J., Dufour, A., Björklund, A., Lindvall, O., Jakobsson, J., and Parmar, M. (2011). Direct conversion of human fibroblasts to dopaminergic neurons. Proc. Natl. Acad. Sci. *108*, 10343–10348.

Phukan, J., Albanese, A., Gasser, T., and Warner, T. (2011). Primary dystonia and dystonia-plus syndromes: clinical characteristics, diagnosis, and pathogenesis. Lancet Neurol. *10*, 1074–1085.

Pickel, V.M., Specht, L.A., Sumal, K.K., Joh, T.H., Reis, D.J., and Hervonen, A. (1980). Immunocytochemical localization of tyrosine hydroxylase in the human fetal nervous system. J. Comp. Neurol. *194*, 465–474.

Pickrell, A.M., and Youle, R.J. (2015). The Roles of PINK1, Parkin, and Mitochondrial Fidelity in Parkinson's Disease. Neuron *85*, 257–273.

Pittman, A., and Hardy, J. (2013). Genetic Analysis in Neurology: The Next 10 Years. JAMA Neurol. *70*, 696–702.

Placzek, M., and Briscoe, J. (2005). The floor plate: multiple cells, multiple signals. Nat. Rev. Neurosci. *6*, 230–240.

Placzek, M., and Briscoe, J. (2018). Sonic hedgehog in vertebrate neural tube development. Int. J. Dev. Biol. *62*, 225–234.

Plagnol, V., Nalls, M.A., Bras, J., Hernandez, D., Sharma, M., Sheerin, U.-M., IPDGC, and WTCCC2 (2011). A Two-Stage Meta-Analysis Identifies Several New Loci for Parkinson's Disease. PLoS Genet. *7*.

Polymeropoulos, M.H., Higgins, J.J., Golbe, L.I., Johnson, W.G., Ide, S.E., Iorio, G.D., Sanges, G., Stenroos, E.S., Pho, L.T., Schaffer, A.A., et al. (1996). Mapping of a Gene for Parkinson's Disease to Chromosome 4q21-q23. Science *274*, 1197–1199.

Polymeropoulos, M.H., Lavedan, C., Leroy, E., Ide, S.E., Dehejia, A., Dutra, A., Pike, B., Root, H., Rubenstein, J., Boyer, R., et al. (1997). Mutation in the α-Synuclein Gene Identified in Families with Parkinson's Disease. Science *276*, 2045–2047.

Popat, R.A., Van Den Eeden, S.K., Tanner, C.M., McGuire, V., Bernstein, A.L., Bloch, D.A., Leimpeter, A., and Nelson, L.M. (2005). Effect of reproductive factors and postmenopausal hormone use on the risk of Parkinson disease. Neurology 383–390.

Postuma, R.B., Berg, D., Stern, M., Poewe, W., Olanow, C.W., Oertel, W., Obeso, J., Marek, K., Litvan, I., Lang, A.E., et al. (2015). MDS clinical diagnostic criteria for Parkinson's disease. Mov. Disord. *30*, 1591–1601.

Prakash, N., Brodski, C., Naserke, T., Puelles, E., Gogoi, R., Hall, A., Panhuysen, M., Echevarria, D., Sussel, L., Weisenhorn, D.M.V., et al. (2006). A Wnt1-regulated genetic network controls the identity and fate of midbrain-dopaminergic progenitors in vivo. Development *133*, 89–98.

Price, A.L., Patterson, N.J., Plenge, R.M., Weinblatt, M.E., Shadick, N.A., and Reich, D. (2006). Principal components analysis corrects for stratification in genome-wide association studies. Nat. Genet. *38*, 904–909.

Price, A.L., Zaitlen, N.A., Reich, D., and Patterson, N. (2010). New approaches to population stratification in genome-wide association studies. Nat. Rev. Genet. *11*, 459–463.

Pruitt, K.D., Harrow, J., Harte, R.A., Wallin, C., Diekhans, M., Maglott, D.R., Searle, S., Farrell, C.M., Loveland, J.E., Ruef, B.J., et al. (2009). The consensus coding sequence (CCDS) project: Identifying a common protein-coding gene set for the human and mouse genomes. Genome Res. *19*, 1316–1323.

Purcell, S., Neale, B., Todd-Brown, K., Thomas, L., Ferreira, M.A.R., Bender, D., Maller, J., Sklar, P., de Bakker, P.I.W., Daly, M.J., et al. (2007). PLINK: A Tool Set for Whole-Genome Association and Population-Based Linkage Analyses. Am. J. Hum. Genet. *81*, 559–575.

R Core Team (2014). R: A language and environment for statistical computing.

Radi, R. (2013). Peroxynitrite, a Stealthy Biological Oxidant. J. Biol. Chem. *288*, 26464–26472.

Radi, R., Rodriguez, M., Castro, L., and Telleri, R. (1994). Inhibition of mitochondrial electron transport by peroxynitrite. Arch. Biochem. Biophys. *308*, 89–95.

Rajput, A.H., Gibb, W.R.G., Zhong, X.H., Shannak, K.S., Kish, S., Chang, L.G., and Hornykiewicz, O. (1994). Dopa-responsive dystonia: Pathological and biochemical observations in a case. Ann. Neurol. *35*, 396–402.

Ramjit, A.L., Sedig, L., Leibner, J., Wu, S.S., Dai, Y., Okun, M.S., Rodriguez, R.L., Malaty, I.A., and Fernandez, H.H. (2010). The Relationship Between Anosmia, Constipation, and Orthostasis and Parkinson's Disease Duration: Results of a Pilot Study. Int. J. Neurosci. *120*, 67–70.

Renart, J., Reiser, J., and Stark, G.R. (1979). Transfer of proteins from gels to diazobenzyloxymethyl-paper and detection with antisera: a method for studying antibody specificity and antigen structure. Proc. Natl. Acad. Sci. U. S. A. *76*, 3116–3120.

Rengmark, A., Pihlstrøm, L., Linder, J., Forsgren, L., and Toft, M. (2016). Low frequency of GCH1 and TH mutations in Parkinson's disease. Parkinsonism Relat. Disord. *29*, 109–111.

Rice, M.E. (2000). Ascorbate regulation and its neuroprotective role in the brain. Trends Neurosci. *23*, 209–216.

Robinson, B.H., Petrova-Benedict, R., Buncic, J.R., and Wallace, D.C. (1992). Nonviability of cells with oxidative defects in galactose medium: A screening test for affected patient fibroblasts. Biochem. Med. Metab. Biol. *48*, 122–126.

Robinson, R., McCarthy, G., Bandmann, O., Dobbie, M., Surtees, R., and Wood, N. (1999). GTP cyclohydrolase deficiency; intrafamilial variation in clinical phenotype, including levodopa responsiveness. J. Neurol. Neurosurg. Psychiatry *66*, 86–89.

Rodriguez-Pallares, J., Parga, J.A., Muñoz, A., Rey, P., Guerra, M.J., and Labandeira-Garcia, J.L. (2007). Mechanism of 6-hydroxydopamine neurotoxicity: the role of NADPH oxidase and microglial activation in 6-hydroxydopamine-induced degeneration of dopaminergic neurons. J. Neurochem. *103*, 145–156.

Rosenkranz-Weiss, P., Sessa, W.C., Milstien, S., Kaufman, S., Watson, C.A., and Pober, J.S. (1994). Regulation of nitric oxide synthesis by proinflammatory cytokines in human umbilical vein endothelial cells. Elevations in tetrahydrobiopterin levels enhance endothelial nitric oxide synthase specific activity. J. Clin. Invest. *93*, 2236–2243.

Rottem, S., and Naot, Y. (1998). Subversion and exploitation of host cells by mycoplasmas. Trends Microbiol. *6*, 436–440.

Roussa, E., and Krieglstein, K. (2004). Induction and specification of midbrain dopaminergic cells: focus on SHH, FGF8, and TGF-β. Cell Tissue Res. *318*, 23–33.

Rudakou, U., Ouled Amar Bencheikh, B., Ruskey, J.A., Krohn, L., Laurent, S.B., Spiegelman, D., Liong, C., Fahn, S., Waters, C., Monchi, O., et al. (2018). Common and rare GCH1 variants are associated with Parkinson's disease. Neurobiol. Aging.

Rudow, G., O'Brien, R., Savonenko, A.V., Resnick, S.M., Zonderman, A.B., Pletnikova, O., Marsh, L., Dawson, T.M., Crain, B.J., West, M.J., et al. (2008). Morphometry of the human substantia nigra in ageing and Parkinson's disease. Acta Neuropathol. (Berl.) *115*, 461.

Ryan, B.J., Lourenço-Venda, L.L., Crabtree, M.J., Hale, A.B., Channon, K.M., and Wade-Martins, R. (2014). α-Synuclein and mitochondrial bioenergetics regulate tetrahydrobiopterin levels in a human dopaminergic model of Parkinson disease. Free Radic. Biol. Med. *67*, 58–68.

Ryan, B.J., Crabtree, M.J., Channon, K.M., and Wade-Martins, R. (2015). Parkinson's disease in GTP cyclohydrolase 1 mutation carriers. Brain *138*, e348–e348.

Sabolek, M., Mieskes, I., Lenk, T., Lehmensiek, V., Hermann, A., Schwarz, J., and Storch, A. (2008). Stage-dependent vulnerability of fetal mesencephalic neuroprogenitors towards dopaminergic neurotoxins. NeuroToxicology *29*, 714–721.

Safaralizadeh, T., Jamshidi, J., Esmaili Shandiz, E., Movafagh, A., Fazeli, A., Emamalizadeh, B., Manafi, N., Taghavi, S., Tafakhori, A., and Darvish, H. (2016). SIPA1L2, MIR4697, GCH1 and VPS13C loci and risk of Parkinson's diseases in Iranian population: A case-control study. J. Neurol. Sci. *369*, 1–4.

Sanderson, M.J., Smith, I., Parker, I., and Bootman, M.D. (2014). Fluorescence Microscopy. Cold Spring Harb. Protoc. *2014*, pdb.top071795.

Sanger, F., Nicklen, S., and Coulson, A.R. (1977). DNA sequencing with chain-terminating inhibitors. Proc. Natl. Acad. Sci. U. S. A. *74*, 5463–5467.

Sasaki, H., Hui, C., Nakafuku, M., and Kondoh, H. (1997). A binding site for Gli proteins is essential for HNF-3beta floor plate enhancer activity in transgenics and can respond to Shh in vitro. Development *124*, 1313–1322.

Saucedo-Cardenas, O., Quintana-Hau, J.D., Le, W.-D., Smidt, M.P., Cox, J.J., Mayo, F.D., Burbach, J.P.H., and Conneely, O.M. (1998). Nurr1 is essential for the induction of the dopaminergic phenotype and the survival of ventral mesencephalic late dopaminergic precursor neurons. Proc. Natl. Acad. Sci. *95*, 4013–4018.

Sautter, J., Meyer, M., Spenger, C., Seiler, R.W., and Widmer, H.R. (1998). Effects of combined BDNF and GDNF treatment on cultured dopaminergic midbrain neurons. NeuroReport *9*, 1093.

Schapira, A.H.V., Cooper, J.M., Dexter, D., Jenner, P., Clark, J.B., and Marsden, C.D. (1989). Mitochondrial complex I deficiency in Parkinson's disease. The Lancet *333*, 1269.

Schapira, A.H.V., Chaudhuri, K.R., and Jenner, P. (2017). Non-motor features of Parkinson disease. Nat. Rev. Neurosci. *18*, 435–450.

Scherfler, C., Schwarz, J., Antonini, A., Grosset, D., Valldeoriola, F., Marek, K., Oertel, W., Tolosa, E., Lees, A.J., and Poewe, W. (2007). Role of DAT-SPECT in the diagnostic work up of Parkinsonism. Mov. Disord. *22*, 1229–1238.

Schöndorf, D.C., Aureli, M., McAllister, F.E., Hindley, C.J., Mayer, F., Schmid, B., Sardi, S.P., Valsecchi, M., Hoffmann, S., Schwarz, L.K., et al. (2014). iPSC-derived neurons from GBA1-associated Parkinson's disease patients show autophagic defects and impaired calcium homeostasis. Nat. Commun. *5*.

Seet, R.C.S., Lee, C.-Y.J., Lim, E.C.H., Tan, J.J.H., Quek, A.M.L., Chong, W.-L., Looi, W.-F., Huang, S.-H., Wang, H., Chan, Y.-H., et al. (2010). Oxidative damage in Parkinson disease: Measurement using accurate biomarkers. Free Radic. Biol. Med. *48*, 560–566.

Segawa, M., Hosaka, A., Miyagawa, F., Nomura, Y., and Imai, H. (1976). Hereditary progressive dystonia with marked diurnal fluctuation. Adv. Neurol. *14*, 215–233.

Segawa, M., Nomura, Y., and Hayashi, M. (2013). Dopa-Responsive Dystonia Is Caused by Particular Impairment of Nigrostriatal Dopamine Neurons Different from Those Involved in Parkinson Disease: Evidence Observed in Studies on Segawa Disease. Neuropediatrics *44*, 061–066.

Semina, E.V., Ferrell, R.E., Mintz-Hittner, H.A., Bitoun, P., Alward, W.L.M., Reiter, R.S., Funkhauser, C., Daack-Hirsch, S., and Murray, J.C. (1998). A novel homeobox gene PITX3 is mutated in families with autosomal-dominant cataracts and ASMD. Nat. Genet. *19*, 167–170.

Šestan, N., Artavanis-Tsakonas, S., and Rakic, P. (1999). Contact-Dependent Inhibition of Cortical Neurite Growth Mediated by Notch Signaling. Science *286*, 741–746.

Shalash, A.S., Rösler, T.W., Müller, S.H., Salama, M., Deuschl, G., Müller, U., Opladen, T., Petersen, B.-S., Franke, A., Hopfner, F., et al. (2017). c.207C>G mutation in sepiapterin reductase causes autosomal dominant dopa-responsive dystonia. Neurol. Genet. *3*, e197.

Sharma, M., Mueller, J.C., Zimprich, A., Lichtner, P., Hofer, A., Leitner, P., Maass, S., Berg, D., Dürr, A., Bonifati, V., et al. (2006). The sepiapterin reductase gene region reveals association in the PARK3 locus: analysis of familial and sporadic Parkinson's disease in European populations. J. Med. Genet. *43*, 557–562.

Sharma, N., Armata, I.A., Multhaupt-Buell, T.J., Ozelius, L.J., Xin, W., and Sims, K.B. (2011). Mutation in 5′ upstream region of GCHI gene causes familial dopa-responsive dystonia. Mov. Disord. *26*, 2140–2141.

Sherer, T.B., Betarbet, R., Testa, C.M., Seo, B.B., Richardson, J.R., Kim, J.H., Miller, G.W., Yagi, T., Matsuno-Yagi, A., and Greenamyre, J.T. (2003). Mechanism of Toxicity in Rotenone Models of Parkinson's Disease. J. Neurosci. *23*, 10756–10764.

Shibata, M., Morita, Y., Shimizu, T., Takahashi, K., and Suzuki, N. (2009). Cardiac parasympathetic dysfunction concurrent with cardiac sympathetic denervation in Parkinson's disease. J. Neurol. Sci. *276*, 79–83.

Shigemizu, D., Miya, F., Akiyama, S., Okuda, S., Boroevich, K.A., Fujimoto, A., Nakagawa, H., Ozaki, K., Niida, S., Kanemura, Y., et al. (2018). IMSindel: An accurate intermediate-size indel

detection tool incorporating de novo assembly and gapped global-local alignment with split read analysis. Sci. Rep. *8*, 1–9.

Shimoji, M., Zhang, L., Mandir, A.S., Dawson, V.L., and Dawson, T.M. (2005). Absence of inclusion body formation in the MPTP mouse model of Parkinson's disease. Mol. Brain Res. *134*, 103–108.

Shimura, H., Hattori, N., Kubo, S., Mizuno, Y., Asakawa, S., Minoshima, S., Shimizu, N., Iwai, K., Chiba, T., Tanaka, K., et al. (2000). Familial Parkinson disease gene product, parkin, is a ubiquitin-protein ligase. Nat. Genet. *25*, 302.

Shinozaki, K., Kashiwagi, A., Nishio, Y., Okamura, T., Yoshida, Y., Masada, M., Toda, N., and Kikkawa, R. (1999). Abnormal biopterin metabolism is a major cause of impaired endothelium-dependent relaxation through nitric oxide/O2- imbalance in insulin-resistant rat aorta. Diabetes *48*, 2437–2445.

Sikora, A., Zielonka, J., Lopez, M., Joseph, J., and Kalyanaraman, B. (2009). Direct oxidation of boronates by peroxynitrite: Mechanism and implications in fluorescence imaging of peroxynitrite. Free Radic. Biol. Med. *47*, 1401–1407.

Singleton, A.B., Farrer, M., Johnson, J., Singleton, A., Hague, S., Kachergus, J., Hulihan, M., Peuralinna, T., Dutra, A., Nussbaum, R., et al. (2003). α-Synuclein Locus Triplication Causes Parkinson's Disease. Science *302*, 841–841.

Singleton, A.B., Hardy, J., Traynor, B.J., and Houlden, H. (2010). Towards a complete resolution of the genetic architecture of disease. Trends Genet. *26*, 438–442.

Sinha, S., and Chen, J.K. (2006). Purmorphamine activates the Hedgehog pathway by targeting Smoothened. Nat. Chem. Biol. Camb. *2*, 29–30.

Skol, A.D., Scott, L.J., Abecasis, G.R., and Boehnke, M. (2006). Joint analysis is more efficient than replication-based analysis for two-stage genome-wide association studies. Nat. Genet. *38*, 209–213.

Smidt, M.P., Schaick, H.S.A. van, Lanctôt, C., Tremblay, J.J., Cox, J.J., Kleij, A.A.M. van der, Wolterink, G., Drouin, J., and Burbach, J.P.H. (1997). A homeodomain gene Ptx3 has highly restricted brain expression in mesencephalic dopaminergic neurons. Proc. Natl. Acad. Sci. *94*, 13305–13310.

Smidt, M.P., Asbreuk, C.H.J., Cox, J.J., Chen, H., Johnson, R.L., and Burbach, J.P.H. (2000). A second independent pathway for development of mesencephalic dopaminergic neurons requires Lmx1b. Nat. Neurosci. *3*, 337–341.

Smidt, M.P., Smits, S.M., and Burbach, J.P.H. (2004a). Homeobox gene Pitx3 and its role in the development of dopamine neurons of the substantia nigra. Cell Tissue Res. *318*, 35–43.

Smidt, M.P., Smits, S.M., Bouwmeester, H., Hamers, F.P.T., Linden, A.J.A. van der, Hellemons, A.J.C.G.M., Graw, J., and Burbach, J.P.H. (2004b). Early developmental failure of substantia nigra dopamine neurons in mice lacking the homeodomain gene Pitx3. Development *131*, 1145–1155.

Smith, C.D., Carney, J.M., Starke-Reed, P.E., Oliver, C.N., Stadtman, E.R., Floyd, R.A., and Markesbery, W.R. (1991). Excess brain protein oxidation and enzyme dysfunction in normal aging and in Alzheimer disease. Proc. Natl. Acad. Sci. *88*, 10540–10543.

Smith, L.M., Sanders, J.Z., Kaiser, R.J., Hughes, P., Dodd, C., Connell, C.R., Heiner, C., Kent, S.B.H., and Hood, L.E. (1986). Fluorescence detection in automated DNA sequence analysis. Nature *321*, 674–679.

Smits, S.M., Ponnio, T., Conneely, O.M., Burbach, J.P.H., and Smidt, M.P. (2003). Involvement of Nurr1 in specifying the neurotransmitter identity of ventral midbrain dopaminergic neurons. Eur. J. Neurosci. *18*, 1731–1738.

Smits, S.M., Burbach, J.P.H., and Smidt, M.P. (2006). Developmental origin and fate of meso-diencephalic dopamine neurons. Prog. Neurobiol. *78*, 1–16.

Sonntag, K.-C., Pruszak, J., Yoshizaki, T., Arensbergen, J. van, Sanchez-Pernaute, R., and Isacson, O. (2007). Enhanced Yield of Neuroepithelial Precursors and Midbrain-Like Dopaminergic Neurons from Human Embryonic Stem Cells Using the Bone Morphogenic Protein Antagonist Noggin. STEM CELLS *25*, 411–418.

Speed, D., Hemani, G., Johnson, M.R., and Balding, D.J. (2012). Improved Heritability Estimation from Genome-wide SNPs. Am. J. Hum. Genet. *91*, 1011–1021.

Spillantini, M.G., Divane, A., and Goedert, M. (1995). Assignment of Human α-Synuclein (SNCA) and β-Synuclein (SNCB) Genes to Chromosomes 4q21 and 5q35. Genomics *27*, 379–381.

Spillantini, M.G., Schmidt, M.L., Lee, V.M.-Y., Trojanowski, J.Q., Jakes, R., and Goedert, M. (1997). α-Synuclein in Lewy bodies. Nature *388*, 839–840.

Spinelli, J.B., and Haigis, M.C. (2018). The multifaceted contributions of mitochondria to cellular metabolism. Nat. Cell Biol. *20*, 745–754.

Stein, J.L., de la Torre-Ubieta, L., Tian, Y., Parikshak, N.N., Hernández, I.A., Marchetto, M.C., Baker, D.K., Lu, D., Hinman, C.R., Lowe, J.K., et al. (2014). A Quantitative Framework to Evaluate Modeling of Cortical Development by Neural Stem Cells. Neuron *83*, 69–86.

Steinberger, D., Blau, N., Goriuonov, D., Bitsch, J., Zuker, M., Hummel, S., and Müller, U. (2004). Heterozygous mutation in 5'-untranslated region of sepiapterin reductase gene (SPR) in a patient with dopa-responsive dystonia. Neurogenetics *5*, 187–190.

Steinberger, D., Trübenbach, J., Zirn, B., Leube, B., Wildhardt, G., and Müller, U. (2007). Utility of MLPA in deletion analysis of GCH1 in dopa-responsive dystonia. Neurogenetics *8*, 69–69.

Stenson, P.D., Mort, M., Ball, E.V., Shaw, K., Phillips, A.D., and Cooper, D.N. (2013). The Human Gene Mutation Database: building a comprehensive mutation repository for clinical and molecular genetics, diagnostic testing and personalized genomic medicine. Hum. Genet. *133*, 1–9.

Stothard, P. (2000). The sequence manipulation suite: JavaScript programs for analyzing and formatting protein and DNA sequences. BioTechniques *28*, 1102–1104.

Stroes, E., Kastelein, J., Cosentino, F., Erkelens, W., Wever, R., Koomans, H., Lüscher, T., and Rabelink, T. (1997). Tetrahydrobiopterin restores endothelial function in hypercholesterolemia. J. Clin. Invest. *99*, 41–46.

Suhr, S.T., Chang, E.A., Tjong, J., Alcasid, N., Perkins, G.A., Goissis, M.D., Ellisman, M.H., Perez, G.I., and Cibelli, J.B. (2010). Mitochondrial Rejuvenation After Induced Pluripotency. PLOS ONE *5*, e14095.

Sun, M., Kong, L., Wang, X., Lu, X., Gao, Q., and Geller, A.I. (2005). Comparison of the capability of GDNF, BDNF, or both, to protect nigrostriatal neurons in a rat model of Parkinson's disease. Brain Res. *1052*, 119–129.

Swaans, R.J.M., Rondot, P., Renier, W.O., Heuvel, L.P.W.J.V.D., Steenbergen-Spanjers, G.C.H., and Wevers, R.A. (2000). Four novel mutations in the Tyrosine Hydroxylase gene in patients with infantile parkinsonism. Ann. Hum. Genet. *64*, 25–31.

Swistowski, A., Peng, J., Liu, Q., Mali, P., Rao, M.S., Cheng, L., and Zeng, X. (2010). Efficient Generation of Functional Dopaminergic Neurons from Human Induced Pluripotent Stem Cells Under Defined Conditions. STEM CELLS *28*, 1893–1904.

Tachi, N., Takahashi, S., Jo, M., and Shinoda, M. (2011). A new mutation of GCH1 in triplets family with dopa-responsive dystonia. Eur. J. Neurol. *18*, 1191–1193.

Tadic, V., Kasten M, Brüggemann N, Stiller S, Hagenah J, and Klein C (2012). Dopa-responsive dystonia revisited: Diagnostic delay, residual signs, and nonmotor signs. Arch. Neurol. *69*, 1558–1562.

Takahashi, K., and Yamanaka, S. (2006). Induction of Pluripotent Stem Cells from Mouse Embryonic and Adult Fibroblast Cultures by Defined Factors. Cell *126*, 663–676.

Takahashi, K., Tanabe, K., Ohnuki, M., Narita, M., Ichisaka, T., Tomoda, K., and Yamanaka, S. (2007). Induction of Pluripotent Stem Cells from Adult Human Fibroblasts by Defined Factors. Cell *131*, 861–872.

Takaoka, K., Yamamoto, M., and Hamada, H. (2007). Origin of body axes in the mouse embryo. Curr. Opin. Genet. Dev. *17*, 344–350.

Tanner, C.M., Ottman, R., Goldman, S.M., Ellenberg, J., Chan, P., Mayeux, R., and Langston, J.W. (1999). Parkinson Disease in Twins: An Etiologic Study. JAMA *281*, 341–346.

Tassin, J., Dürr, A., Bonnet, A.-M., Gil, R., Vidailhet, M., Lücking, C.B., Goas, J.-Y., Durif, F., Abada, M., Echenne, B., et al. (2000). Levodopa-responsive dystoniaGTP cyclohydrolase I or parkin mutations? Brain *123*, 1112–1121.

Teitelman, G., Jaeger, C., Albert, V., Joh, T., and Reis, D. (1983). Expression of amino acid decarboxylase in proliferating cells of the neural tube and notochord of developing rat embryo. J. Neurosci. *3*, 1379–1388.

The International HapMap Consortium (2005). A haplotype map of the human genome. Nature *437*, 1299–1320.

The Jackson Laboratory (2019). The Jackson Laboratory.

Thomas, K.R., and Capecchi, M.R. (1990). Targeted disruption of the murine int-1 proto-oncogene resulting in severe abnormalities in midbrain and cerebellar development. Nature *346*, 847–850.

Thompson, L., Barraud, P., Andersson, E., Kirik, D., and Björklund, A. (2005). Identification of Dopaminergic Neurons of Nigral and Ventral Tegmental Area Subtypes in Grafts of Fetal Ventral Mesencephalon Based on Cell Morphology, Protein Expression, and Efferent Projections. J. Neurosci. *25*, 6467–6477.

Thöny, B., Auerbach, G., and Blau, N. (2000). Tetrahydrobiopterin biosynthesis, regeneration and functions. Biochem. J. *347*, 1–16.

Tilokani, L., Nagashima, S., Paupe, V., and Prudent, J. (2018). Mitochondrial dynamics: overview of molecular mechanisms. Essays Biochem. *62*, 341–360.

Trender-Gerhard, I., Sweeney, M.G., Schwingenschuh, P., Mir, P., Edwards, M.J., Gerhard, A., Polke, J.M., Hanna, M.G., Davis, M.B., Wood, N.W., et al. (2009). Autosomal-dominant GTPCH1-deficient DRD: clinical characteristics and long-term outcome of 34 patients. J. Neurol. Neurosurg. Psychiatry *80*, 839–845.

Tsika, E., and Moore, D.J. (2012). Mechanisms of LRRK2-Mediated Neurodegeneration. Curr. Neurol. Neurosci. Rep. *12*, 251–260.

Tu, P., Galvin, J.E., Baba, M., Giasson, B., Tomita, T., Leight, S., Nakajo, S., Iwatsubo, T., Trojanowski, J.Q., and Lee, V.M.-Y. (1998). Glial cytoplasmic inclusions in white matter oligodendrocytes of multiple system atrophy brains contain insoluble α-synuclein. Ann. Neurol. *44*, 415–422.

Tukey, J.W. (1949). Comparing Individual Means in the Analysis of Variance. Biometrics *5*, 99–114.

Turcano, P., Mielke, M.M., Bower, J.H., Parisi, J.E., Cutsforth-Gregory, J.K., Ahlskog, J.E., and Savica, R. (2018). Levodopa-induced dyskinesia in Parkinson disease: A population-based cohort study. Neurology *91*, e2238–e2243.

Twelves, D., Perkins, K.S.M., and Counsell, C. (2003). Systematic review of incidence studies of Parkinson's disease. Mov. Disord. *18*, 19–31.

Uhlén, M., Fagerberg, L., Hallström, B.M., Lindskog, C., Oksvold, P., Mardinoglu, A., Sivertsson, Å., Kampf, C., Sjöstedt, E., Asplund, A., et al. (2015). Tissue-based map of the human proteome. Science *347*, 1260419.

Ulloa, F., and Martí, E. (2010). Wnt won the war: Antagonistic role of Wnt over Shh controls dorso-ventral patterning of the vertebrate neural tube. Dev. Dyn. *239*, 69–76.

Ungerstedt, U., Ljungberg, T., and Steg, G. (1974). Behavioral, physiological, and neurochemical changes after 6-hydroxydopamine-induced degeneration of the nigro-striatal dopamine neurons. Adv. Neurol. *5*, 421–426.

Valente, E.M., Bentivoglio, A.R., Dixon, P.H., Ferraris, A., Ialongo, T., Frontali, M., Albanese, A., and Wood, N.W. (2001). Localization of a Novel Locus for Autosomal Recessive Early-Onset Parkinsonism, PARK6, on Human Chromosome 1p35-p36. Am. J. Hum. Genet. *68*, 895–900.

Valente, E.M., Abou-Sleiman, P.M., Caputo, V., Muqit, M.M.K., Harvey, K., Gispert, S., Ali, Z., Turco, D.D., Bentivoglio, A.R., Healy, D.G., et al. (2004). Hereditary Early-Onset Parkinson's Disease Caused by Mutations in PINK1. Science *304*, 1158–1160.

Van Hove, J.L.K., Steyaert, J., Matthijs, G., Legius, E., Theys, P., Wevers, R., Romstad, A., Møller, L.B., Hedrich, K., Goriounov, D., et al. (2006). Expanded motor and psychiatric phenotype in autosomal dominant Segawa syndrome due to GTP cyclohydrolase deficiency. J. Neurol. Neurosurg. Psychiatry *77*, 18–23.

Vásquez-Vivar, J., Kalyanaraman, B., Martásek, P., Hogg, N., Masters, B.S.S., Karoui, H., Tordo, P., and Pritchard, K.A. (1998). Superoxide generation by endothelial nitric oxide synthase: The influence of cofactors. Proc. Natl. Acad. Sci. *95*, 9220–9225.

Vásquez-Vivar, J., Kalyanaraman, B., and Martásek, P. (2003). The Role of Tetrahydrobiopterin in Superoxide Generation from eNOS: Enzymology and Physiological Implications. Free Radic. Res. *37*, 121–127.

Vaz, R.L., Outeiro, T.F., and Ferreira, J.J. (2018). Zebrafish as an Animal Model for Drug Discovery in Parkinson's Disease and Other Movement Disorders: A Systematic Review. Front. Neurol. *9*.

Verderio, C., and Matteoli, M. (2011). ATP in neuron–glia bidirectional signalling. Brain Res. Rev. *66*, 106–114.

Verkhratsky, A., and Kirchhoff, F. (2007). Glutamate-mediated neuronal–glial transmission. J. Anat. *210*, 651–660.

Vierbuchen, T., Ostermeier, A., Pang, Z.P., Kokubu, Y., Südhof, T.C., and Wernig, M. (2010). Direct conversion of fibroblasts to functional neurons by defined factors. Nature *463*, 1035–1041.

Wagner, G.C., Jarvis, M.F., and Carelli, R.M. (1985). Ascorbic acid reduces the dopamine depletion induced by MPTP. Neuropharmacology *24*, 1261–1262.

Wakabayashi, K., Takahashi, H., Takeda, S., Ohama, E., and Ikuta, F. (1988). Parkinson's disease: the presence of Lewy bodies in Auerbach's and Meissner's plexuses. Acta Neuropathol. (Berl.) *76*, 217–221.

Wakabayashi, K., Takahashi, H., Obata, K., and Ikuta, F. (1992). Immunocytochemical localization of synaptic vesicle-specific protein in lewy body-containing neurons in Parkinson's disease. Neurosci. Lett. *138*, 237–240.

Wang, K., Li, M., and Hakonarson, H. (2010). ANNOVAR: functional annotation of genetic variants from high-throughput sequencing data. Nucleic Acids Res. *38*, e164–e164.

Wang, M.Z., Jin, P., Bumcrot, D.A., Marigo, V., Mcmahon, A.P., Wang, E.A., Woolf, T., and Pang, K. (1995). Induction of dopaminergic neuron phenotype in the midbrain by Sonic hedgehog protein. Nat. Med. *1*, 1184–1188.

Wardman, P. (2008). Methods to measure the reactivity of peroxynitrite-derived oxidants toward reduced fluoresceins and rhodamines. Methods Enzymol. *441*, 261–282.

Warner, T.T., and Bressman, S.B. (2007). Clinical Diagnosis and Management of Dystonia (CRC Press).

Warner, T.T., and Schapira, A.H.V. (2003). Genetic and environmental factors in the cause of Parkinson's disease. Ann. Neurol. *53*, S16–S25.

van de Warrenburg, B.P., Schouten, M.I., de Bot, S.T., Vermeer, S., Meijer, R., Pennings, M., Gilissen, C., Willemsen, M.A., Scheffer, H., and Kamsteeg, E.-J. (2016). Clinical exome sequencing for cerebellar ataxia and spastic paraplegia uncovers novel gene–disease associations and unanticipated rare disorders. Eur. J. Hum. Genet. *24*, 1460–1466.

Wassarman, K.M., Lewandoski, M., Campbell, K., Joyner, A.L., Rubenstein, J.L., Martinez, S., and Martin, G.R. (1997). Specification of the anterior hindbrain and establishment of a normal mid/hindbrain organizer is dependent on Gbx2 gene function. Development *124*, 2923–2934.

Weber, Y., Steinberger, D., Deuschl, G., Benecke, R., and Müller, U. (1997). Two previously unrecognized splicing mutations of GCH1 in Dopa-responsive dystonia: exon skipping and one base insertion. Neurogenetics *1*, 125–127.

Wevers, R.A., de Rijk-van Andel, J.F., Bräutigam, C., Geurtz, B., van den Heuvel, L.P., Steenbergen-Spanjers, G.C., Smeitink, J.A., Hoffmann, G.F., and Gabreëls, F.J. (1999). A review of biochemical and molecular genetic aspects of tyrosine hydroxylase deficiency including a novel mutation (291delC). J. Inherit. Metab. Dis. *22*, 364–373.

Wider, C., Melquist, S., Hauf, M., Solida, A., Cobb, S.A., Kachergus, J.M., Gass, J., Coon, K.D., Baker, M., Cannon, A., et al. (2008). Study of a Swiss dopa-responsive dystonia family with a deletion in GCH1 Redefining DYT14 as DYT5. Neurology *70*, 1377–1383.

Wiedemann, F.R., Winkler, K., Lins, H., Wallesch, C.-W., and Kunz, W.S. (1999). Detection of Respiratory Chain Defects in Cultivated Skin Fibroblasts and Skeletal Muscle of Patients with Parkinson's Disease. Ann. N. Y. Acad. Sci. *893*, 426–429.

Wijemanne, S., and Jankovic, J. (2015). Dopa-responsive dystonia—clinical and genetic heterogeneity. Nat. Rev. Neurol. *11*, 414–424.

Wijgerde, M., McMahon, J.A., Rule, M., and McMahon, A.P. (2002). A direct requirement for Hedgehog signaling for normal specification of all ventral progenitor domains in the presumptive mammalian spinal cord. Genes Dev. *16*, 2849–2864.

Witte, M.B., and Barbul, A. (2002). Role of nitric oxide in wound repair. Am. J. Surg. *183*, 406–412.

Wu, M.C., Lee, S., Cai, T., Li, Y., Boehnke, M., and Lin, X. (2011). Rare-Variant Association Testing for Sequencing Data with the Sequence Kernel Association Test. Am. J. Hum. Genet. *89*, 82–93.

Wu-Chou, Y.-H., Yeh, T.-H., Wang, C.-Y., Lin, J.-J., Huang, C.-C., Chang, H.-C., Lai, S.-C., Chen, R.-S., Weng, Y.-H., Huang, C.-L., et al. (2010). High frequency of multiexonic deletion of the GCH1 gene in a Taiwanese cohort of dopa-response dystonia. Am. J. Med. Genet. B Neuropsychiatr. Genet. *153B*, 903–908.

Xi, J., Liu, Y., Liu, H., Chen, H., Emborg, M.E., and Zhang, S.-C. (2012). Specification of Midbrain Dopamine Neurons from Primate Pluripotent Stem Cells. STEM CELLS *30*, 1655–1663.

Xia, N., Zhang, P., Fang, F., Wang, Z., Rothstein, M., Angulo, B., Chiang, R., Taylor, J., and Reijo Pera, R.A. (2016). Transcriptional comparison of human induced and primary midbrain dopaminergic neurons. Sci. Rep. *6*, 20270.

Xie, Y., Schutte, R.J., Ng, N.N., Ess, K.C., Schwartz, P.H., and O'Dowd, D.K. (2018). Reproducible and efficient generation of functionally active neurons from human hiPSCs for preclinical disease modeling. Stem Cell Res. *26*, 84–94.

Xu, Q., Li, K., Sun, Q., Ding, D., Zhao, Y., Yang, N., Luo, Y., Liu, Z., Zhang, Y., Wang, C., et al. (2017). Rare GCH1 heterozygous variants contributing to Parkinson's disease. Brain *140*, e41–e41.

Yamada, T., McGeer, P.L., and McGeer, E.G. (1992). Lewy bodies in Parkinson's disease are recognized by antibodies to complement proteins. Acta Neuropathol. (Berl.) *84*, 100–104.

Yan, J., Studer, L., and McKay, R.D.G. (2001). Ascorbic acid increases the yield of dopaminergic neurons derived from basic fibroblast growth factor expanded mesencephalic precursors. J. Neurochem. *76*, 307–311.

Yang, X., Zheng, J., An, R., Tian, S., Zhao, Q., Chen, Y., Huang, H., Ning, P.P., Song, Y., and Xu, Y. (2017). Polymorphism in MIR4697 but not VPS13C, GCH1, or SIPA1L2 is associated with risk of Parkinson's disease in a Han Chinese population. Neurosci. Lett. *650*, 8–11.

Ye, W., Shimamura, K., Rubenstein, J.L.R., Hynes, M.A., and Rosenthal, A. (1998). FGF and Shh Signals Control Dopaminergic and Serotonergic Cell Fate in the Anterior Neural Plate. Cell *93*, 755–766.

Young, L., Sung, J., Stacey, G., and Masters, J.R. (2010). Detection of Mycoplasma in cell cultures. Nat. Protoc. *5*, 929–934.

Yu, P.B., Hong, C.C., Sachidanandan, C., Babitt, J.L., Deng, D.Y., Hoyng, S.A., Lin, H.Y., Bloch, K.D., and Peterson, R.T. (2008). Dorsomorphin inhibits BMP signals required for embryogenesis and iron metabolism. Nat. Chem. Biol. *4*, 33–41.

Yuan, S.H., Martin, J., Elia, J., Flippin, J., Paramban, R.I., Hefferan, M.P., Vidal, J.G., Mu, Y., Killian, R.L., Israel, M.A., et al. (2011). Cell-Surface Marker Signatures for the Isolation of Neural Stem Cells, Glia and Neurons Derived from Human Pluripotent Stem Cells. PLOS ONE *6*, e17540.

Zarow, C., Lyness, S.A., Mortimer, J.A., and Chui, H.C. (2003). Neuronal Loss Is Greater in the Locus Coeruleus Than Nucleus Basalis and Substantia Nigra in Alzheimer and Parkinson Diseases. Arch. Neurol. *60*, 337–341.

Zarranz, J.J., Alegre, J., Gómez-Esteban, J.C., Lezcano, E., Ros, R., Ampuero, I., Vidal, L., Hoenicka, J., Rodriguez, O., Atarés, B., et al. (2004). The new mutation, E46K, of α-synuclein causes parkinson and Lewy body dementia. Ann. Neurol. *55*, 164–173.

Zetterström, R.H., Solomin, L., Jansson, L., Hoffer, B.J., Olson, L., and Perlmann, T. (1997). Dopamine Neuron Agenesis in Nurr1-Deficient Mice. Science *276*, 248–250.

Zhan, X., Hu, Y., Li, B., Abecasis, G.R., and Liu, D.J. (2016). RVTESTS: an efficient and comprehensive tool for rare variant association analysis using sequence data. Bioinformatics *32*, 1423–1426.

Zhao, H., Kalivendi, S., Zhang, H., Joseph, J., Nithipatikom, K., Vásquez-Vivar, J., and Kalyanaraman, B. (2003). Superoxide reacts with hydroethidine but forms a fluorescent product that is distinctly different from ethidium: potential implications in intracellular fluorescence detection of superoxide. Free Radic. Biol. Med. *34*, 1359–1368.

Zhao, S., Maxwell, S., Jimenez-Beristain, A., Vives, J., Kuehner, E., Zhao, J., O'Brien, C., Felipe, C.D., Semina, E., and Li, M. (2004). Generation of embryonic stem cells and transgenic mice expressing green fluorescence protein in midbrain dopaminergic neurons. Eur. J. Neurosci. *19*, 1133–1140.

Zielonka, J., Sikora, A., Joseph, J., and Kalyanaraman, B. (2010). Peroxynitrite is the major species formed from different flux ratios of co-generated nitric oxide and superoxide: direct reaction with boronate-based fluorescent probe. J. Biol. Chem. *285*, 14210–14216.

Zimprich, A., Biskup, S., Leitner, P., Lichtner, P., Farrer, M., Lincoln, S., Kachergus, J., Hulihan, M., Uitti, R.J., Calne, D.B., et al. (2004). Mutations in LRRK2 Cause Autosomal-Dominant Parkinsonism with Pleomorphic Pathology. Neuron *44*, 601–607.

Zirn, B., Steinberger, D., Troidl, C., Brockmann, K., Hagen, M. von der, Feiner, C., Henke, L., and Müller, U. (2008). Frequency of GCH1 deletions in Dopa-responsive dystonia. J. Neurol. Neurosurg. Psychiatry *79*, 183–186.

Zook, J.M., Chapman, B., Wang, J., Mittelman, D., Hofmann, O., Hide, W., and Salit, M. (2014). Integrating human sequence data sets provides a resource of benchmark SNP and indel genotype calls. Nat. Biotechnol. *32*, 246–251.

Zou, M., Li, R., Wang, J.-Y., Wang, K., Wang, Y.-N., Li, Y., Ji, F.-X., Sun, S.-N., Huang, S.-S., Fan, H.-H., et al. (2018). Association analyses of variants of SIPA1L2, MIR4697, GCH1, VPS13C, and DDRGK1 with Parkinson's disease in East Asians. Neurobiol. Aging *0*.

(2019). Reverse transcription PCR: Principle, Procedure, Applications, Advantages and Disadvantages.

ZEISS Microscopy Online Campus | Live-Cell Imaging | Microscopy Techniques.

Supplementary material

Reference	Sequencing method	N cases	N controls	Comment
Bandmann et al., 1996b	Sanger sequencing	29 FPD with akinetic-rigid presentation	0	Selection of rare PD subtype, with small numbers and no controls
Cobb et al., 2009	Direct sequencing	53 familial EOPD	0	Selection of rare PD subtype, with small numbers and no controls
		(21 w associated dystonia)		
Hertz et al., 2006	Direct sequencing	87 EOPD	0	Selection of rare PD subtype with small numbers and no controls
Newmann et al., 2014	Targeted SNP sequencing	233 dystonia	1,090	Limited sequencing to 5 *GCH1* SNPs
		1,337 PD		
Bandrés-Ciga et al., 2016	Sanger sequencing	97 LOPD	0	Selection of rare and common PD subtypes, with small numbers and no controls
		28 EOPD		
		9 FPD		
Rengmark et al., 2016	Deep targeted sequencing	509 LOPD	230	May be a population-specific observation and coverage gaps
Yang et al., 2017	Targeted SNP sequencing	589 sporadic PD	634	Limited sequencing to a single SNP in *GCH1*

Table 30: Negative genetic association of GCH1 with PD risk in literature review.

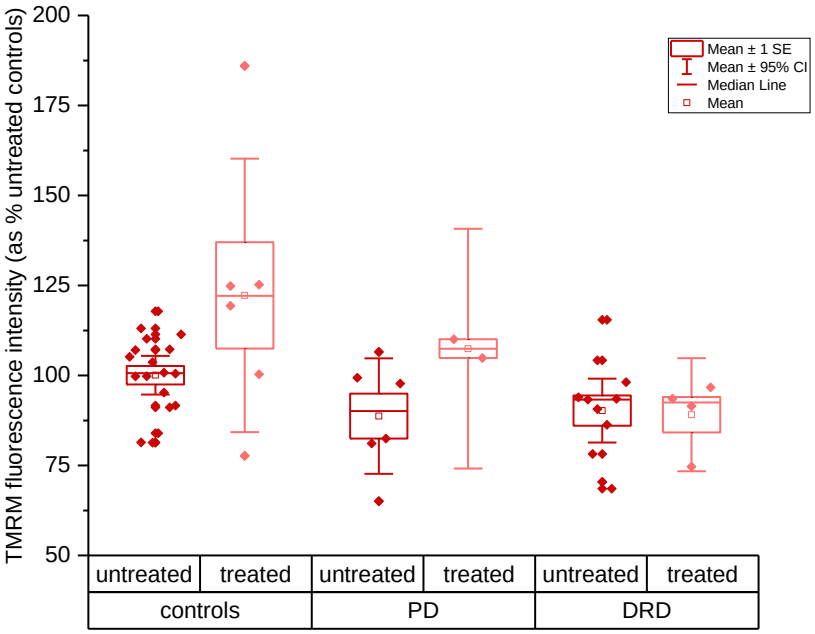

Figure 82: MMP polarisation estimated by TMRM fluorescence intensity normalised to the average of untreated controls, as a proxy for MMP polarisation. Groups are separated as controls, PD and DRD. Untreated groups are in dark red, treated groups are in pink. Box plot represents: mean (circle), median (line) median ± 1SE (standard error - box) and mean ± 95% CI (confidence interval – whiskers).

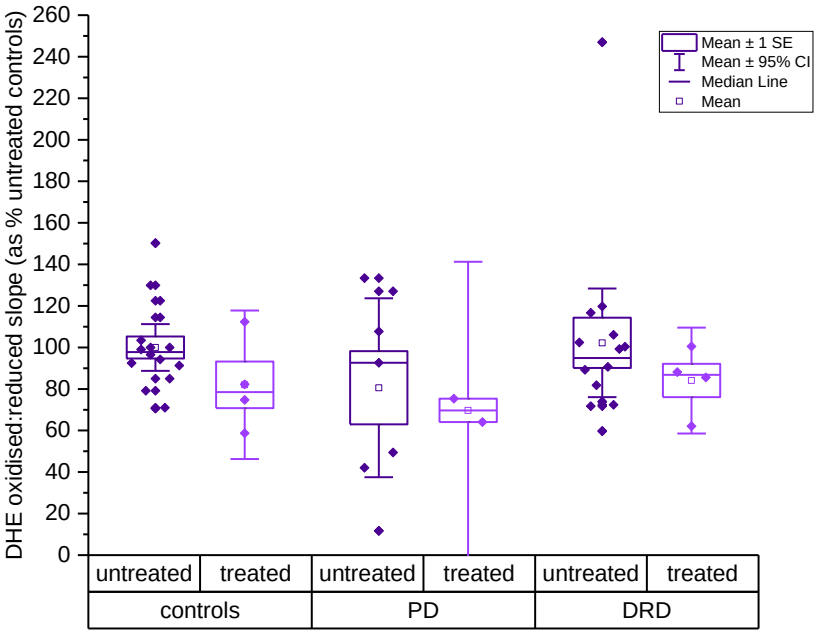

Figure 83: Rate of production of superoxide estimated by slope of DHE oxidised:reduced ratio, normalised to untreated controls. Results are presented comparing controls to PD and DRD separately. Untreated groups are in dark purple, treated groups in light purple. Box plot represents: mean (circle), median (line) median ± 1SE (standard error - box) and mean ± 95% CI (confidence interval – whiskers).

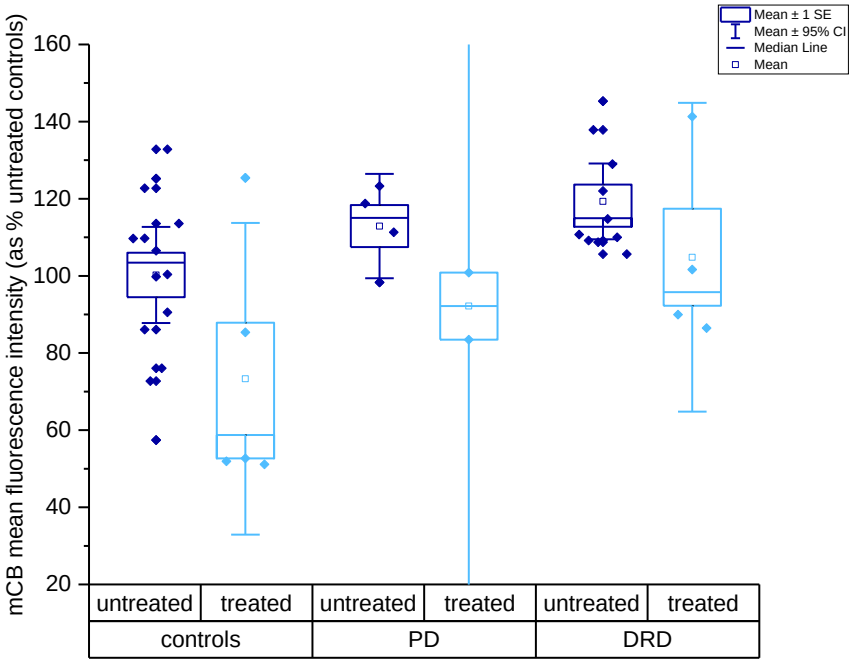

Figure 84: Cellular GSH content estimated by mean mCB fluorescence intensity normalised to control. Results are presented comparing controls to PD and DRD separately. Untreated are in dark blue, treated are in light blue. Box plot represents: mean (circle), median (line) median ± 1SE (standard error - box) and mean ± 95% CI (confidence interval – whiskers).

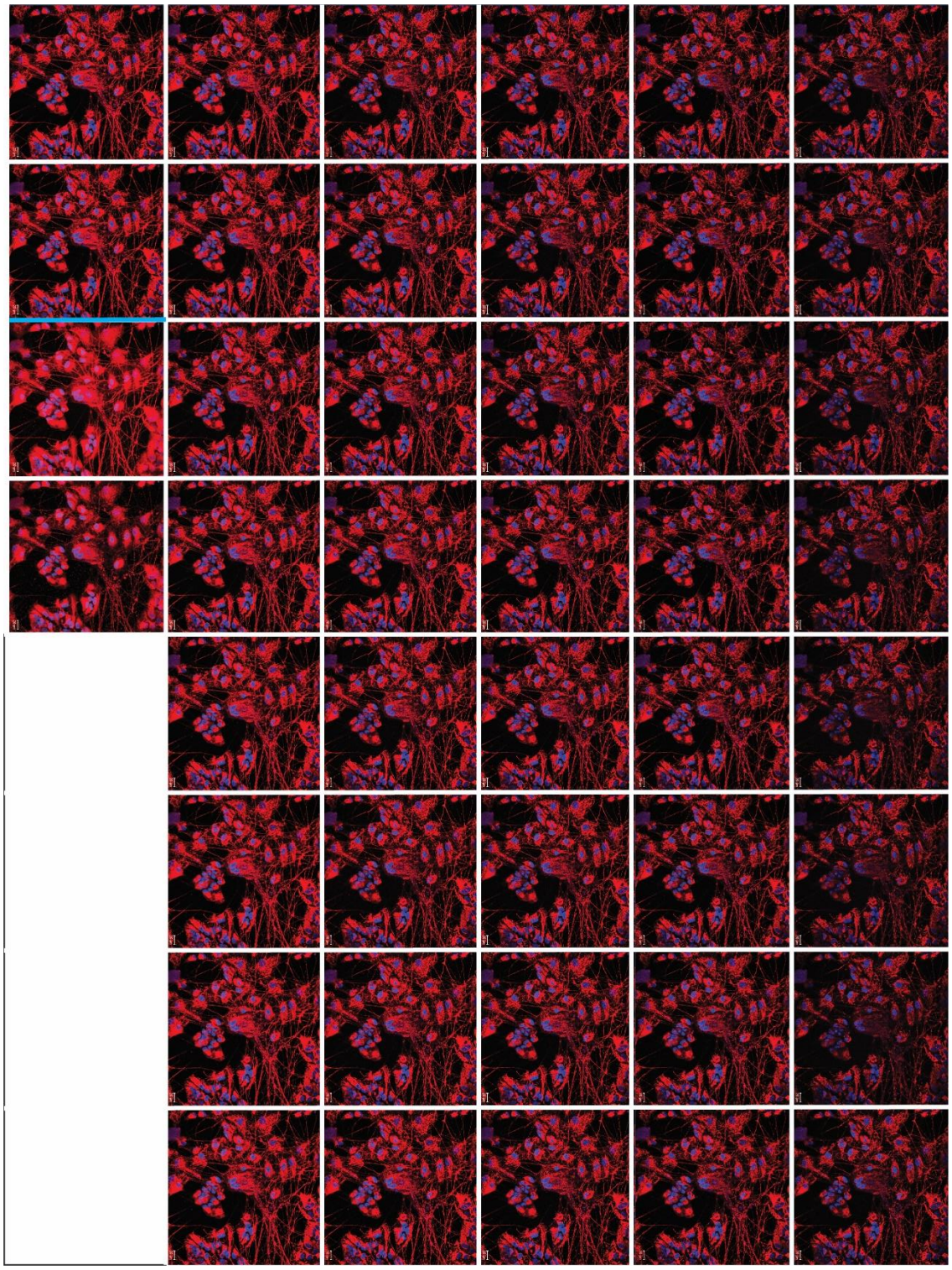

Figure 85: Representative time-series of the MitoTracker CMH2XROS dye fluorescence evolution across time in neuronal cells. The blue marker indicates the addition of FCCP which uncouples the mitochondria and leads to leakage of the dye around them.

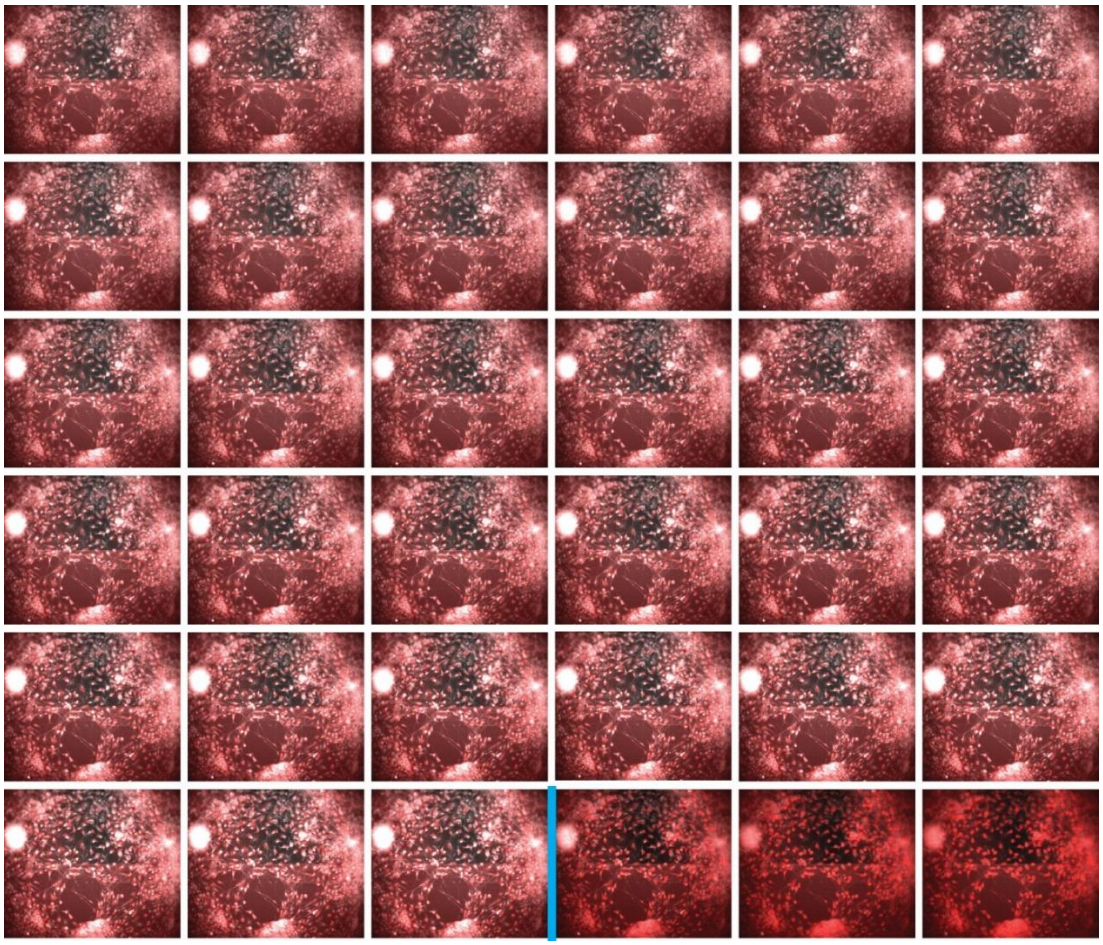

Figure 86: Example of a time-series of DHE with both channels 380nm (grey) and 530 nm (red) merged. The blue bar represents the point of addition of positive control for oxidation of the dye H2O2.

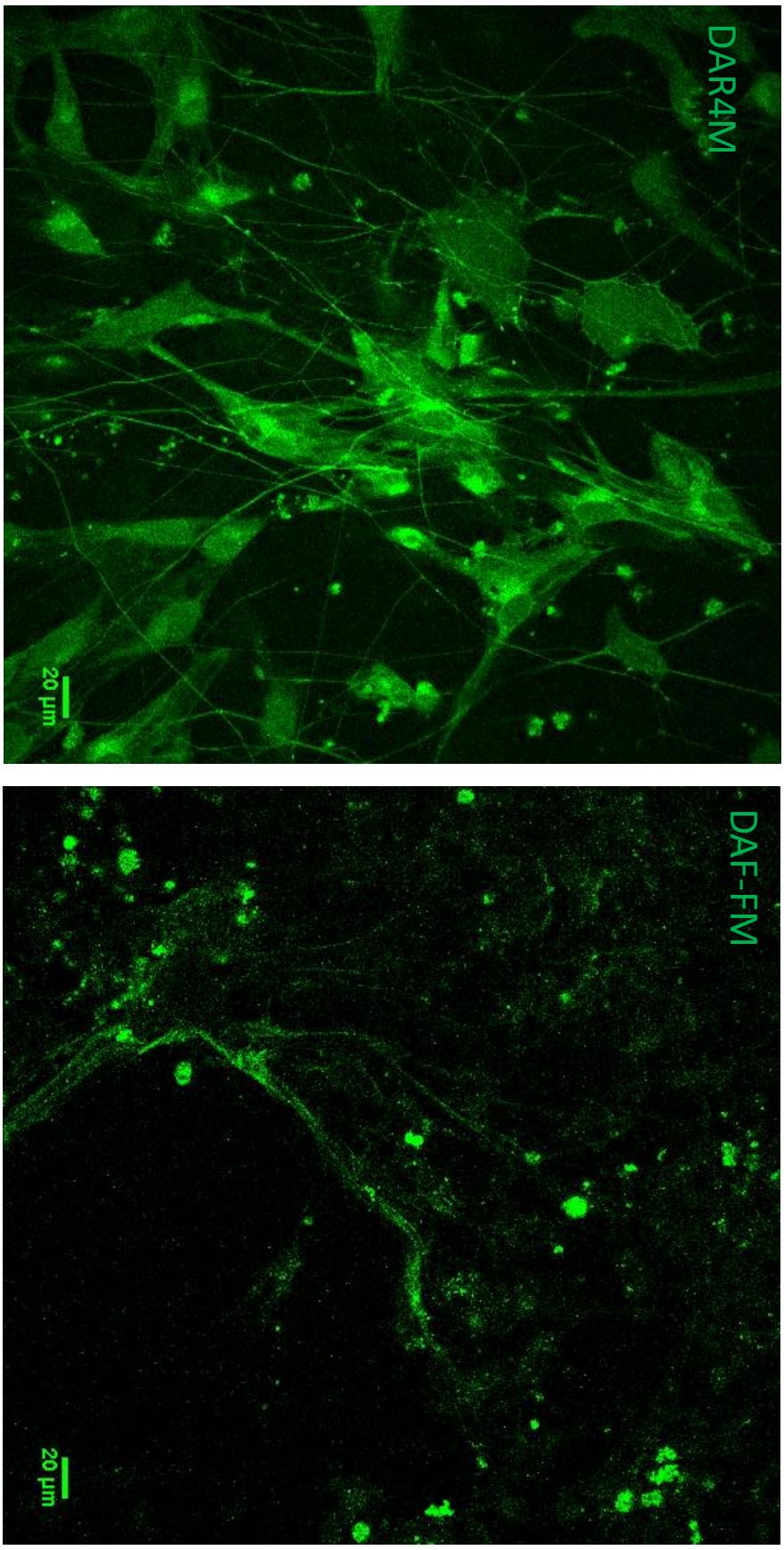

Figure 87: DAR-4M v/s DAF-FM loading in neuronal cultures